

Tuna-Inspired Experimental Platforms

Exploring High-Performance Fish Swimming

A dissertation presented to the
School of Engineering and Applied Science
in candidacy for the degree of
Doctor of Philosophy
in the subject of
Mechanical and Aerospace Engineering

By
Carl Henry White

University of Virginia

December 2022

APPROVAL SHEET

This dissertation is submitted in partial fulfillment of the requirements for the degree of
Doctor of Philosophy in Mechanical and Aerospace Engineering

Carl H. White, Author

This dissertation has been read and approved by the Examination Committee:

Hilary Bart-Smith, Advisor

Department of Mechanical and Aerospace Engineering
University of Virginia

Daniel B. Quinn, Chairperson

Department of Mechanical and Aerospace Engineering
University of Virginia

George V. Lauder

Department of Organismic and Evolutionary Biology
Harvard University

Haibo Dong

Department of Mechanical and Aerospace Engineering
University of Virginia

Harry C. Powell

Department of Electrical and Computer Engineering
University of Virginia

And accepted for the University of Virginia School of Engineering and Applied Science:

Jennifer L. West, Dean

Copyright © 2022 by Carl H. White

All rights reserved

Abstract

Autonomous underwater vehicles perform a growing variety of missions including exploration, surveillance, and defense. Their conventional designs feature rigid hulls and rotary propellers which contrast the flexible bodies and undulatory tails of fish. As a result, fish exhibit exceptional speed, efficiency, and maneuverability often surpassing that of conventional vehicles. This performance difference motivates the design of vehicles taking inspiration from biology. However, a significant gap in performance exists between such bio-inspired vehicles and the high-performance capabilities of fish. Bio-inspired vehicles typically focus on low-speed locomotion with low tail-beat frequencies. The few systems that do achieve high frequencies often remain limited to low speeds. Consequently, current robotic fish are unable to access the high-frequency, high-speed performance space of fish. Furthermore, the energetic costs of most robotic fish exceed those of fish by orders of magnitude while at a fraction of the speed.

Here we design and test robotic fish able to explore the high-performance space of fish with biologically realistic energy efficiencies. Our bio-inspired systems achieve this by modeling the morphology and kinematics of yellowfin tuna (*Thunnus albacares*), which are open-ocean swimmers with extraordinary speed and endurance. We present five generations of fish robots inspired by tuna and compare our results with data for tuna and a diversity of fish species. These Tunabots are research platforms that improve our understanding of high-performance fish swimming. The fifth generation, Tunabot Flex, demonstrates that body flexibility improves speed and efficiency. Our work provides a new baseline for the development of state-of-the-art underwater vehicles that aim to explore a fish-like, high-performance space and close the gap between robotic systems and fish swimming ability.

Acknowledgements

I would not have achieved this dissertation without the company of those who chose to walk beside me. First and foremost, thank you to my family and loved ones. Your encouragement sustained me even when your eyes understandably glazed over while listening about data sets. Thank you to my sister, Lauren, for lighting the doctoral path ahead of me. I am deeply grateful to my grandfather, Papa, for your persistent interest in my success and career. I know you would have pressed me about my retirement plans before I could even remove my doctoral hood. I sincerely thank my advisor, Hilary Bart-Smith, for giving me the creative freedom and experienced mentorship to pursue my research interests. Joining your lab eight years ago as a second-year undergraduate student has been a life-changing opportunity, and I am forever grateful. Similarly, I owe a great deal to Prof. Chris Goynes for his role in the beginning of my graduate career. I wholeheartedly thank George Lauder for his patient guidance and high spirits while being the consummate collaborator and like a second advisor to me. I appreciate my other collaborators as well, especially Dr. Joe Zhu, Dr. Roger Zhu, Dr. Robin Thandiackal, Dr. Dylan Wainwright, Dr. Valentina Di Santo, Dr. Junshi Wang, Prof. Haibo Dong, Prof. Keith Moored, Prof. Lex Smits, the MURI team, Prof. Shawn Russell, Dr. Trevor Kemp, Gregory Lewis, Sebring Smith, and many others. I am indebted to my examination committee for their selfless contributions of precious time to provide helpful feedback. I also acknowledge and thank Dr. Bob Brizzolara, the Office of Naval Research, the David and Lucile Packard Foundation, Prof. George Lauder, and the MAE Department for their generous financial support. Finally, a warm thank you to the talented and wonderfully unique friends I met along the way both here and abroad.

*This dissertation is dedicated to
the memories of my grandfathers*

Contents

List of Figures	xi
List of Tables	xiv
Nomenclature	xv
Notation	xvii
Chapter 1 — Introduction	1
Chapter 2 — Tunabots V1–V3: Proofs of Concept and Prototypes	9
2.1 Overview.....	9
2.2 Tunabot V1	11
2.2.1 Actuation Mechanism Theory.....	11
2.2.2 Design and Fabrication.....	20
2.2.3 Waterproofing Methods	30
2.2.4 Free-Swimming Results	34
2.3 Tunabot V2: Free-Swimming Experiments.....	35
2.3.1 Design and Fabrication.....	35
2.3.2 Waterproofing Methods	40
2.3.3 Methodology for Free-Swimming Experiments	42
2.3.4 Free-Swimming Wake Visualization Results	45
2.3.5 Free-Swimming Performance and Kinematic Results	50
2.3.6 Free-Swimming Peduncle Stiffness Results	52
2.4 Tunabot V2: Tethered Experiment	54
2.4.1 Design and Fabrication.....	54
2.4.2 Speed Control and Power Measurement	57

2.4.3	Methodology for Tethered Testing	61
2.4.4	Tethered Performance Results	64
2.5	Tunabot V3	69
2.5.1	Design and Fabrication.....	69
2.5.2	Waterproofing Methods	75
2.5.3	Tethered Results	78
Chapter 3 — Tunabot V4: Exploring the Performance Space of Fish Swimming.....		81
3.1	Overview.....	81
3.2	Tunabot V4	82
3.2.1	Design and Fabrication.....	82
3.2.2	Waterproofing Methods	87
3.3	Materials and Methods	88
3.3.1	Performance Testing Protocol.....	88
3.3.2	Speed Control and Power Measurement	91
3.3.3	Swimming Kinematics of Tuna, Mackerel, and Tunabot V4	92
3.3.4	Drag Forces and Coefficients.....	94
3.3.5	Static Thrust Measurement.....	98
3.3.6	Added Mass, Lift-Based Propulsion, and Effective Angle of Attack	100
3.3.7	Flow Visualization	109
3.3.8	Statistical Analysis	110
3.4	Results.....	111
3.4.1	Drag Forces and Coefficients.....	111
3.4.2	Swimming Kinematics	113
3.4.3	Swimming Speed and Tail-Beat Frequency.....	115
3.4.4	Cost of Transport.....	116
3.4.5	Stride Length.....	117
3.4.6	Head and Tail-Beat Amplitudes.....	118
3.4.7	Strouhal Number	119
3.4.8	Static Thrust and the Effective Angle of Attack	119
3.4.9	Thrust after Caudal Fin Removal.....	124
3.4.10	Caudal Fin Wake Flow Patterns.....	126
3.5	Discussions	128
3.5.1	Complications of the Elastomer Skin.....	128

3.5.2	Peduncle Stiffness	129
3.5.3	Caudal Fin Flexibility.....	130
3.5.4	Static Thrust and the Effective Angle of Attack	131
Chapter 4 — Tunabot V5: Body Flexibility Improves High-Performance Swimming.....		136
4.1	Overview.....	136
4.2	Tunabot V5: ‘Tunabot Flex’	137
4.2.1	Design and Fabrication.....	137
4.2.2	Waterproofing Methods	143
4.3	Body Flexibility Experiment: Materials and Methods	145
4.3.1	Performance Testing Protocol.....	145
4.3.2	Speed Control and Power Measurement	148
4.3.3	Swimming Kinematics of Tuna and Tunabot V5.....	151
4.3.4	Biological Comparison of Energy Efficiency: Cost of Transport.....	153
4.3.5	Drag Forces and Coefficients	155
4.3.6	Motor Efficiency	159
4.3.7	Statistical Analysis	162
4.4	Body Flexibility Experiment: Results	163
4.4.1	Center of Mass	163
4.4.2	Drag Forces and Coefficients.....	163
4.4.3	Swimming Kinematics	165
4.4.4	Swimming Speed and Tail-Beat Frequency.....	168
4.4.5	Cost of Transport.....	170
4.4.6	Stride Length.....	172
4.4.7	Strouhal Number	173
4.4.8	Motor Efficiency	173
4.5	Tunabots V4 and V5 Comparison Experiment: Materials and Methods.....	175
4.5.1	Specialized Configuration of Tunabot V5	175
4.5.2	Performance Testing Protocol.....	177
4.6	Tunabots V4 and V5 Comparison Experiment: Results.....	178
4.6.1	Drag Forces and Coefficients	178
4.6.2	Swimming Kinematics	179
4.6.3	Swimming Speed and Tail-Beat Frequency.....	180
4.6.4	Cost of Transport.....	180

4.6.5	Stride Length	182
4.6.6	Head and Tail-Beat Amplitudes	182
4.6.7	Strouhal Number	183
4.7	Biological Comparisons and Detailed Discussions	183
4.7.1	Normalizing by Length When Making Comparisons	183
4.7.2	Center of Mass	185
4.7.3	Dead-Drag Coefficients and Forces	185
4.7.4	Swimming Kinematics	188
4.7.5	Swimming Speed and Tail-Beat Frequency	192
4.7.6	Cost of Transport.....	194
4.7.7	Work per Meter	198
4.7.8	Stride Length	199
4.7.9	Strouhal Number	200
4.7.10	Optimal Number of Joints	201
4.7.11	Tunabot V5 Outperformed Tunabot V4: Design Improvements	205
4.7.12	Performance Implications: Closing the Performance Gap	207
4.7.13	Tethered Tunabots.....	208
Chapter 5 — Concluding Remarks		210
5.1	Closing the Gap: Robotic vs. Biological Swimming Performance	210
5.2	Future Work.....	215
5.2.1	Demonstrate Tunabot V5’s Full Capabilities.....	215
5.2.2	Improve Motor Efficiency.....	215
5.2.3	Investigate Fin-Fin Interactions	216
5.2.4	Explore Caudal Fin Flexibility	217
5.2.5	Investigate Peduncle Stiffness with Tunabot V5	218
5.2.6	Apply Bio-Inspired Flow Sensing.....	219
References		221
Appendix.....		245

List of Figures

Figure 1-1: Significant performance gap between robotic fish and fish swimming ability.....	2
Figure 1-2: Overview of the Tunabots.....	5
Figure 1-3: Overview of the design progression from Tunabot V1 through Tunabot V5.....	6
Figure 2-1: Actuation mechanism diagram.....	13
Figure 2-2: Plotted equations of motion of the peduncle’s horizontal component.....	18
Figure 2-3: Design of Tunabot V1.....	21
Figure 2-4: CAD model of Tunabot V1.....	24
Figure 2-5: Tunabot V1’s design inspired by yellowfin tuna.....	25
Figure 2-6: 3D-printed whale fluke with nonhomogeneous stiffness.....	26
Figure 2-7: Internal ballast of Tunabot V1.....	30
Figure 2-8: Waterproofing methods of Tunabot V1.....	31
Figure 2-9: Design of Tunabot V2.....	36
Figure 2-10: CAD model of Tunabot V2.....	37
Figure 2-11: Design and fabrication of Tunabot V2’s skin.....	38
Figure 2-12: Modular peduncle stiffness of Tunabot V2.....	40
Figure 2-13: Motor housing of Tunabot V2.....	41
Figure 2-14: Flow visualization of free-swimming Tunabot V2.....	46
Figure 2-15: Swimming kinematics of free-swimming Tunabot V2.....	51
Figure 2-16: Tethered configuration of Tunabot V2.....	54
Figure 2-17: Speed control and power measurement system of Tunabot V2.....	58

Figure 2-18: Experimental setup for Tunabot V2’s tethered performance testing	62
Figure 2-19: Performance results of Tunabot V2	67
Figure 2-20: Design of Tunabot V3.....	70
Figure 2-21: CAD model of Tunabot V3.....	71
Figure 2-22: Design and fabrication of Tunabot V3.....	73
Figure 3-1: Design of Tunabot V4.....	83
Figure 3-2: CAD model of Tunabot V4.....	85
Figure 3-3: Experimental setup for Tunabot V4’s performance testing.....	90
Figure 3-4: Video capture of freely swimming yellowfin tuna	93
Figure 3-5: Experimental setup for Tunabot V4’s drag measurement	95
Figure 3-6: Experimental setup for Tunabot V4’s static thrust measurement	98
Figure 3-7: Theory of lift-based propulsion generated by caudal fin	105
Figure 3-8: Experimental setup for visualizing the flow field around Tunabot V4.....	109
Figure 3-9: Drag forces and coefficients of Tunabot V4.....	112
Figure 3-10: Swimming kinematics of Tunabot V4, yellowfin tuna, and mackerel.....	114
Figure 3-11: Performance results of Tunabot V4	116
Figure 3-12: Static thrust and the associated electrical power consumption of Tunabot V4	120
Figure 3-13: Static thrust and the effective angle of attack of Tunabot V4 and mackerel	121
Figure 3-14: No propulsion without the caudal fin of Tunabot V4	124
Figure 3-15: Visualized flow field in the wake and around the tail of Tunabot V4.....	127
Figure 4-1: Design of Tunabot V5.....	138
Figure 4-2: CAD model of Tunabot V5.....	141
Figure 4-3: Design comparisons of Tunabot V5’s three body flexibility configurations.....	145

Figure 4-4: Experimental setup for Tunabot V5’s performance testing	147
Figure 4-5: Speed control and power measurement system of Tunabot V5.....	148
Figure 4-6: LabVIEW controller and data acquisition software.....	150
Figure 4-7: Midline tracking of Tunabot V5 to determine swimming kinematics.....	152
Figure 4-8: Experimental setup for Tunabot V5’s drag measurement	156
Figure 4-9: Drag forces and coefficients of Tunabot V5.....	164
Figure 4-10: Swimming kinematics of Tunabot V5 and yellowfin tuna	166
Figure 4-11: Head and tail-beat amplitudes of Tunabot V5	167
Figure 4-12: Phase difference of Tunabot V5.....	168
Figure 4-13: Performance results of Tunabot V5	169
Figure 4-14: Electrical power consumption of Tunabot V5	171
Figure 4-15: Motor characteristics of Tunabot V5 (4 DOF Flex)	174
Figure 4-16: Maximum motor characteristics of Tunabots V4 and V5.....	174
Figure 4-17: Design comparisons of Tunabots V4 and V5	176
Figure 4-18: Swimming kinematics comparison between Tunabots V4 and V5	179
Figure 4-19: Performance results comparison between Tunabots V4 and V5	181
Figure 5-1: Closing the performance gap between fish robots and high-performance fish.....	211
Figure 5-2: Tunabot Fin.....	217
Figure 5-3: Artificial flow sensor inspired by fish neuromasts	220

List of Tables

Table 1-1: Swimming speed and tail-beat frequency of bio-inspired robots.....	7
Table 1-2: Swimming efficiency of bio-inspired robots.....	8
Table 2-1: Design parameters of Tunabots V1–V5	22
Table 4-1: Joint parameters of Tunabot V5’s three body flexibility configurations	139
Table 4-2: Wetted and projected areas of Tunabot V5.....	158
Table 4-3: Comparison of design parameters between Tunabots V4 and V5	176
Table 4-4: Comparison of wetted and projected areas between Tunabots V4 and V5.....	178
Table 5-1: Maximum swimming speed of Tunabots V1–V5	212
Table 5-2: Minimum cost of transport (COT) of Tunabots V4 and V5.....	212
Table A-1: Performance space of a diversity of fish species.....	245

Nomenclature

Acronyms are listed in alphabetical order.

2D	two-dimensional
3D	three-dimensional
AAS	absolute aerobic scope, or net cost of transport (COT_{net})
ABS	acrylonitrile butadiene styrene
AMR	active metabolic rate
AUV	autonomous underwater vehicle
BL	body length
CAD	computer-aided design
CFD	computational fluid dynamics
CI	confidence interval
CNC	computer numerical control
COM	center of mass
COT	cost of transport
COT_{net}	net cost of transport, or absolute aerobic scope (AAS)
DC	direct current
DEA	dielectric elastomer actuator
DMLS	direct metal laser sintering
DOF	degrees of freedom

EAP	electroactive polymer
FDM	fused deposition modeling
FL	fork length
GCOT	gross cost of transport
HDD	hard disk drive
IPMC	ionic polymer-metal composite
MFC	macro-fiber composite
MRI	magnetic resonance imaging
NI-DAQ	National Instruments data acquisition device
PFC	piezoelectric fiber composite
PIV	particle image velocimetry
PPy	polypyrrole
PWM	pulse-width modulation
<i>Re</i>	Reynolds number
SEM	standard error of the mean
SL	stride length
SLS	selective laser sintering
SMA	shape memory alloy
SMR	standard metabolic rate
<i>St</i>	Strouhal number
V	version (e.g., V1 is ‘Version 1’)
WPM	work per meter
μ CT	micro-computed tomography

Notation

Variables are listed in order of appearance without repetition.

Section 2.2.1 Actuation Mechanism Theory

R^2	coefficient of determination
θ	bend angle of the rotating bent shaft
φ	angular displacement of the rotating bent shaft
r	length of the bent portion of the rotating bent shaft
x_{shaft}	x-component of the rotating bent shaft's tip location
y_{shaft}	y-component of the rotating bent shaft's tip location
z_{shaft}	z-component of the rotating bent shaft's tip location
d	distance in the z-direction from the rotating bent shaft's bend location to the rotational axis of the two pinned joints
l	length of the arm
h	height of the slot
k	depth of the slot
x_{trace}	x-component of the shaft tip's trace within the slot projected onto the x-z plane
z_{trace}	z-component of the shaft tip's trace within the slot projected onto the x-z plane
β	angle between the z-axis and bent portion of the shaft
ζ	angle between the z-axis and flapper centerline

y_{slot}	y-component of the parametric curve of the flapper at the point of spar attachment
z_{slot}	z-component of the parametric curve of the flapper at the point of spar attachment
L	length of the spar
y_{peduncle}	y-component of the parametric curve of the peduncle's displacement
z_{peduncle}	z-component of the parametric curve of the peduncle's displacement
$v_{y_{\text{peduncle}}}$	y-component of the peduncle's velocity
$a_{y_{\text{peduncle}}}$	y-component of the peduncle's acceleration
$(y_{\text{peduncle}})_{\text{global extrema}}$	maximum and minimum values of the y-component of the peduncle's displacement
$(v_{y_{\text{peduncle}}})_{\text{global extrema}}$	maximum and minimum values of the y-component of the peduncle's velocity
$(a_{y_{\text{peduncle}}})_{\text{local extrema}}$	maximum and minimum values of the y-component of the peduncle's acceleration

Section 2.3.3 Methodology for Free-Swimming Experiments

Re	Reynolds number
ρ	density of fluid
U	velocity of fluid, free-swimming speed, or self-propelled speed
BL	body length
μ	dynamic viscosity of fluid
SL	stride length
f	tail-beat frequency

St	Strouhal number
A_{tb}	tail-beat amplitude
$\kappa(x)$	midline curvature as a function of x
x	position along the body's length from snout to tail tip
$c(x)$	midline curve as a function of x

Section 2.4.3 Methodology for Tethered Testing

COT	cost of transport
P	total electrical power consumption
m_u	unsubmerged mass
WPM	work per meter

Section 3.3.4 Drag Forces and Coefficients

C_D	drag coefficient
F_D	hydrodynamic drag force
A	reference area

Section 3.3.6 Added Mass, Lift-Based Propulsion, and Effective Angle of Attack

F_{am}	added mass force
m_f	added fluid mass
$\frac{\partial U}{\partial t}$	acceleration of fluid
a	point of location of both the peduncle joint and leading edge of the caudal fin
b	point of location of the trailing edge of the caudal fin

m	slope of the foil's chord in a ventral-view frame of reference
α	angle of attack of the foil
v_∞	freestream flow velocity
U_{rel}	incoming velocity seen by the foil
\bar{v}_{caudal}	average velocity of the caudal fin
t_0	initial time
t_1	subsequent time step
Δx_a	change in position of point a in the x-direction
Δx_b	change in position of point b in the x-direction
Δy_a	change in position of point a in the y-direction
Δy_b	change in position of point b in the y-direction
dt	amount of time between the initial time and subsequent time step
v_{ax}	x-component of the velocity of point a
v_{ay}	y-component of the velocity of point a
v_{bx}	x-component of the velocity of point b
v_{by}	y-component of the velocity of point b
v_a	velocity of point a
v_b	velocity of point b
$\bar{v}_{\text{caudal}_x}$	x-component of the average velocity of the caudal fin
$\bar{v}_{\text{caudal}_y}$	y-component of the average velocity of the caudal fin
ε	angle between the freestream flow velocity and the incoming velocity from the reference frame of the foil

$U_{rel,x}$	x-component of the incoming velocity seen by the foil
$v_{\infty,x}$	x-component of the freestream flow velocity
$U_{rel,y}$	y-component of the incoming velocity seen by the foil
$v_{\infty,y}$	y-component of the freestream flow velocity
α_e	effective angle of attack
F_L	hydrodynamic lift force
S	planform area of the caudal fin from a lateral viewpoint
C_L	lift coefficient of the foil
$F_{L,x}$	x-component of the hydrodynamic lift force
$F_{L,y}$	y-component of the hydrodynamic lift force
$F_{D,x}$	x-component of the hydrodynamic drag force
$F_{D,y}$	y-component of the hydrodynamic drag force
F_H	hydrodynamic force generated by the pitching-heaving foil
$F_{H,x}$	x-component of the hydrodynamic force; lift-generated, forward thrust force
$F_{H,y}$	y-component of the hydrodynamic force

Section 3.3.8 Statistical Analysis

δ	uncertainty
σ_x	sample standard deviation
n	sample size
x_i	i^{th} value of the sample
\bar{x}	mean of the sample

$\sigma_{\bar{x}}$	standard error of the mean
CI	confidence interval
t	t-statistic

Section 4.3.4 Biological Comparison of Energy Efficiency: Cost of Transport

$S\dot{V}O_2$	standard metabolic rate (SMR)
$\dot{V}O_2$	active metabolic rate (AMR)
$\dot{M}O_2$	oxygen consumption rate
g	gravitational acceleration
ϵ	dimensionless metric of efficiency for locomotion

Section 4.3.6 Motor Efficiency

τ	torque
m_{load}	mass of lifted load
r_{spool}	radius of spool
P_{rot}	rotational mechanical power
ω	angular velocity
η	efficiency of motor
I_{stall}	stall current
τ_{stall}	stall torque

Chapter 1

Introduction

Significant effort in autonomous underwater vehicle (AUV) research is focused on replicating aspects of biological swimming to improve locomotor performance (Table 1-1) [1]–[70]. Traditional propeller-driven systems are well-modeled and rigid, whereas biological propulsion is less understood and features complex, undulatory flexibility. If this gap in understanding were to close, the potential for high-performance systems would be significant. Designing bio-inspired systems requires knowledge of the biological features contributing to high performance, and how these features can then be applied to artificial systems in order to capture the performance benefits. Just as biology can inform the design of robotic systems, so mechanical devices can in turn serve as a research platform to explore aspects of fish swimming. This circular feedback between bio-inspired robotics and robotics-inspired biology [71] advances our understanding of how to optimize robotic platforms through bio-inspired design in ways that may eventually exceed biological capabilities.

Many species of fish swim by undulating their flexible body from head to tail in a wave-like motion. With each tail beat, oscillation of the body generates thrust by accelerating surrounding water and forming vortices which are then shed from the caudal fin's trailing edge

[72]–[74]. The subsequent fluid wake pattern is termed a ‘reverse von Kármán street’, which features counter-rotating, linked ring vortices, each with a central jet directed downstream [75], [76]. Both the velocity of the thrust jet and frequency of vorticity shedding increase with the tail-beat frequency, resulting in faster swimming speeds. In effect, fish swimming speed is largely a function of tail-beat frequency, though not exclusively [77], [78]. The tail-beat frequency of a single species may range from 0.1 to 20 Hz and beyond (Figure 1-1(A)) with corresponding swimming speeds surpassing 15 body lengths per second (BL/s). This broad biological performance space demonstrates the attractive versatility of flexible, undulatory-body propulsion.

In contrast, robotic systems designed for bio-inspired swimming typically focus on low-frequency, low-speed locomotion (Figure 1-1(A)). Some systems closely emulate the

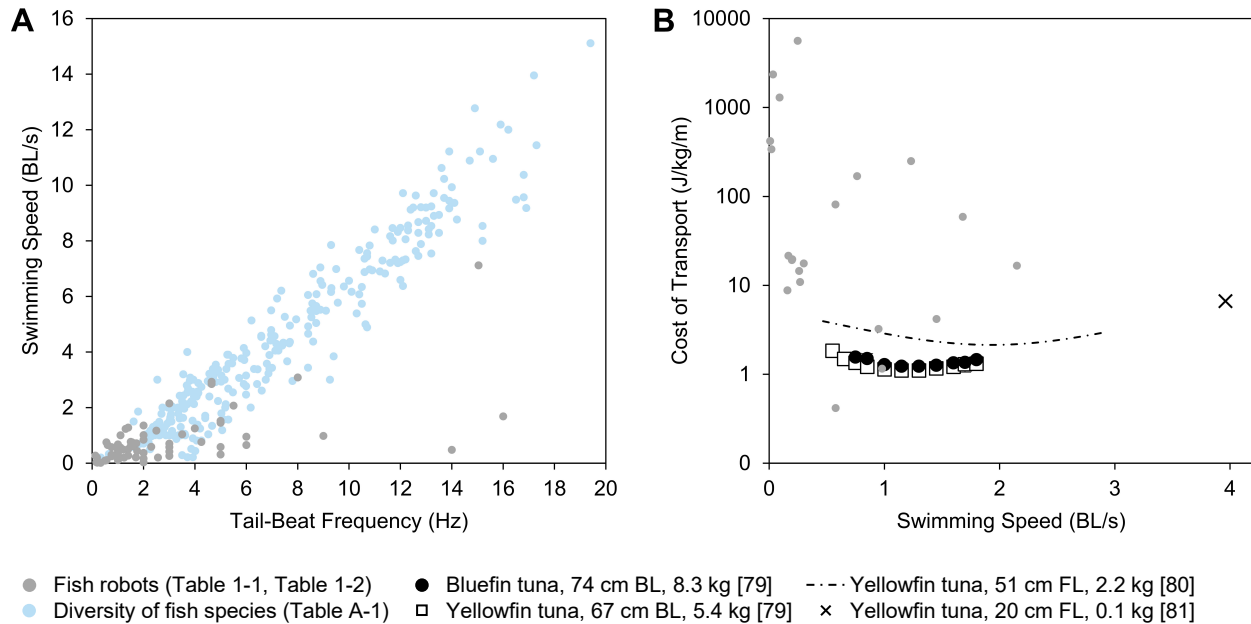


Figure 1-1: Significant performance gap between robotic fish and fish swimming ability. Fish robots are unable to match both the swimming speed *and* energy efficiency of high-performance fish. **(A)** We compare the maximum swimming speed and corresponding tail-beat frequency of 70 fish robots (Table 1-1) with 300 observations of a diversity of fish species (see Table A-1). Current robotic fish are unable to access this high-speed, high-frequency performance space of fish with few exceptions: [12], [59], [66]. **(B)** We compare the maximum swimming speed and corresponding cost of transport (COT) of 24 fish robots (Table 1-2) with literature data of tunas [79]–[81]. The logarithmic y-axis illustrates how the COT of fish robots is one to four orders of magnitude higher than that of tunas with few exceptions: [5], [31], [37], [44].

morphology and kinematics of fishes, while others are not directly comparable with any particular species. Together these systems exemplify the remarkable diversity and accomplishments of bio-inspired robotic swimming research to date, as well as the challenges that lie ahead. Most robotic swimmers operate at frequencies below 3 Hz, resulting in swimming speeds below 1.5 BL/s (Figure 1-1(A)). The few systems that do achieve high frequencies often remain limited to low speeds. Current robotic fish designs are unable to access the high-frequency, high-speed performance space occupied by fishes.

Furthermore, robotic fish often exhibit unreasonably high energetic costs from a biological perspective (Figure 1-1(B)). Energy efficiency of fish swimming is most often quantified in terms of the cost of transport (COT), which describes the energy spent to move a body over a unit distance. For example, the COT of tunas ranges 1.1–1.8 J/kg/m for swimming speeds up to 1.8 BL/s [79]. Conversely, the COT of most robotic swimmers (Table 1-2) is one to four orders of magnitude higher than this at a fraction of the speed. Additionally, presentation of COT data in the fish robotics community is rare, and comparisons with biology are even scarcer. In Table 1-2, we review the fish robotics literature from the Robotuna in 1999 [3] to the time of this dissertation’s defense. This table includes papers that enabled us to calculate COT with their included data and contains, to our knowledge, all papers available to us that directly report COT. Both the brevity of this list and magnitude of COT values convey how the progress towards energy-efficient fish-like systems has lagged behind the development of their undulatory mechanisms.

In this dissertation, we design and test robotic fish able to explore the high-performance space of fish with biologically realistic energy efficiencies. Our bio-inspired systems achieve this by modeling the morphology and kinematics of yellowfin tuna (*Thunnus albacares*). Tunas are

an ideal group for studying high-performance swimming [82] because they are open-ocean swimmers with extraordinary speed and endurance. Tunas are also endothermic (i.e., warm-bodied) which enables faster cruising speeds than ectotherms [83]. We present five generations of fish robots inspired by tuna (Figure 1-2, Figure 1-3) and compare our results with data for tuna and a diversity of fish species. These Tunabots are research platforms that improve our understanding of high-performance fish swimming. In Chapter 2, we develop the foundational designs and methodologies for exploring the high-performance space of fish over three generations: Tunabot V1, Tunabot V2, and Tunabot V3. In Chapter 3, we test Tunabot V4's full range of tail-beat frequencies and compare our results with yellowfin tuna and Atlantic mackerel (*Scomber scombrus*). In Chapter 4, Tunabot V5 ('Tunabot Flex') demonstrates that body flexibility improves swimming speed and lowers COT. Our work provides a new baseline for the development of state-of-the-art underwater vehicles that aim to explore a fish-like, high-performance space and close the gap between robotic systems and fish swimming ability.

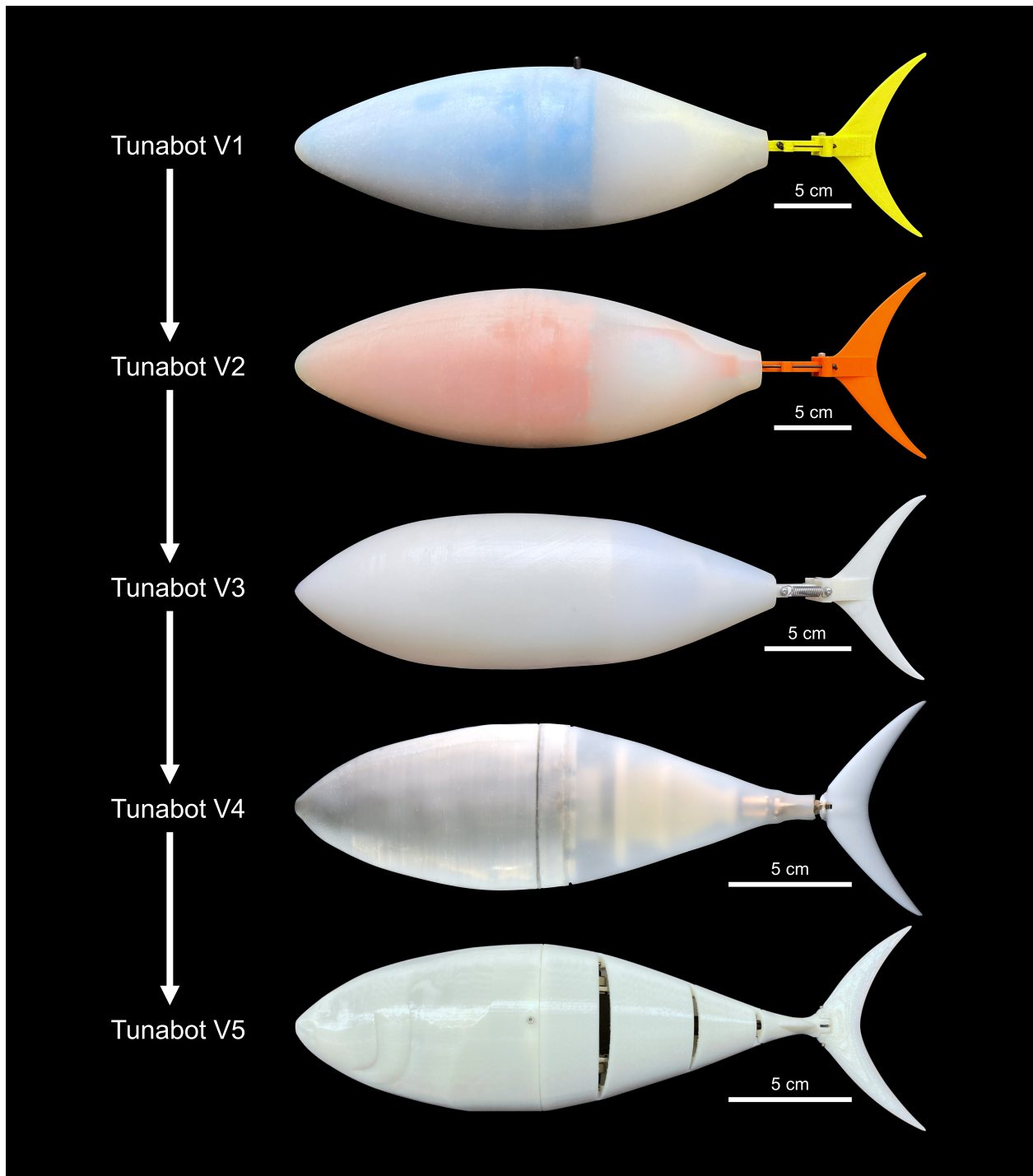


Figure 1-2: Overview of the Tunabots. Photographs of the five Tunabot generations. The tuna-inspired design and subsequent swimming performance improved as each generation built upon the last. Tunabots V1 and V2 freely swam in a stationary water tank. Tethers and external power cables (not shown) were later added to Tunabot V2 for flow tank testing. Tunabots V3, V4, and V5 were similarly tethered.

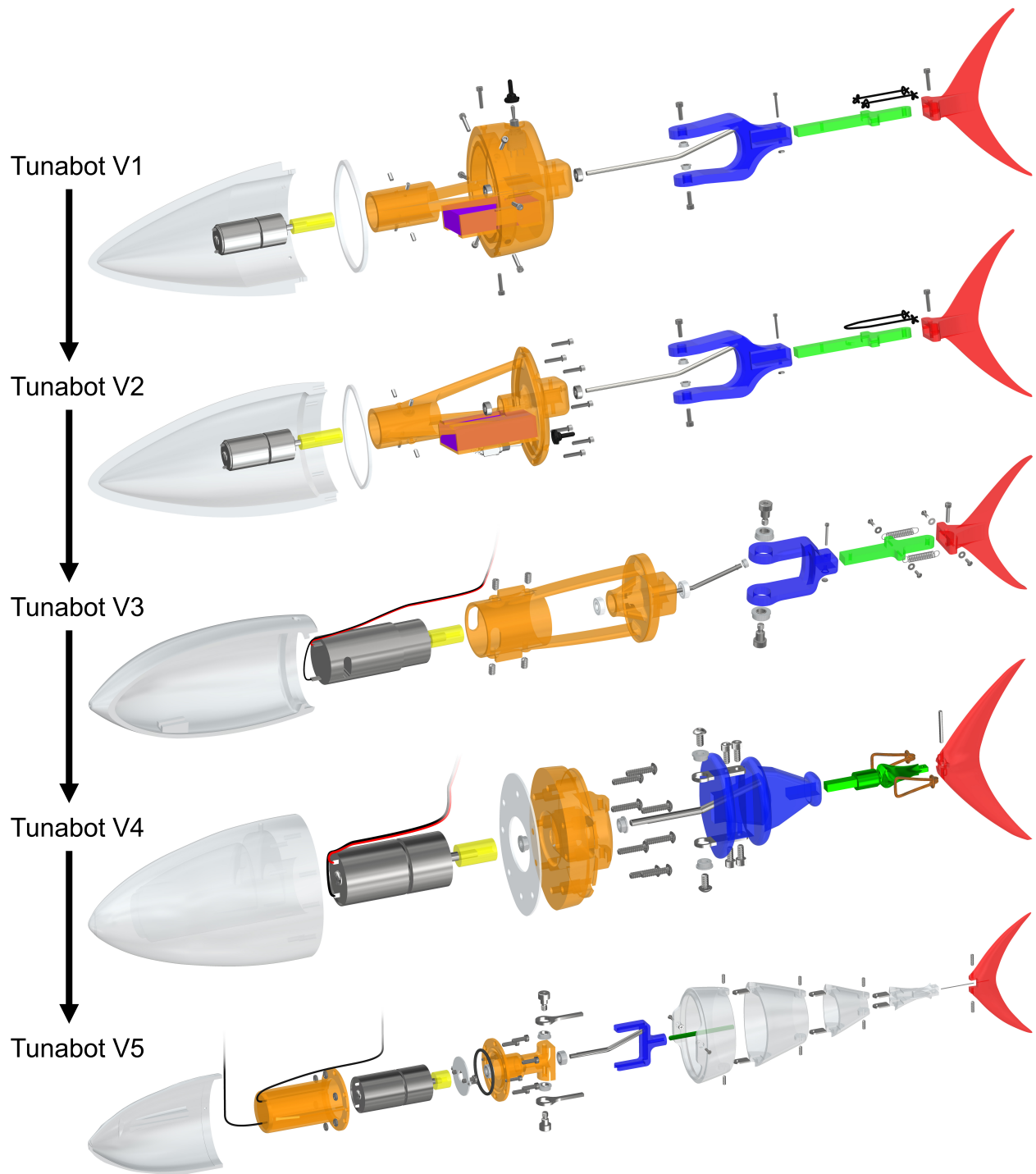


Figure 1-3: Overview of the design progression from Tunabot V1 through Tunabot V5. The five generations of Tunabots were designed and tested in succession. The pictured sequence of computer-aided design (CAD) models with exploded views shows the linear design progression as each generation built upon the last. Components with similar functions are shaded the same color across generations so that the evolution of individual parts is also evident. Further details such as labeled part names are provided in Figure 2-4 (Tunabot V1), Figure 2-10 (Tunabot V2), Figure 2-21 (Tunabot V3), Figure 3-2 (Tunabot V4), and Figure 4-2 (Tunabot V5). Images are not to scale relative to one another.

Table 1-1: Swimming speed and tail-beat frequency of bio-inspired robots. Here we review the field of bio-inspired underwater robots from 1999 [3] to the time of this dissertation’s defense. We emphasize high-performance systems and provide their maximum reported speed and corresponding actuation frequency (i.e., tail-beat frequency in the case of systems with tails). We plot this data set in Figure 1-1(A). To reasonably compare existing systems with our Tunabots, we only include systems that were physical, whole-bodied, and self-propelled; we exclude studies that were simulations (e.g., [84]), flapping foils (e.g., [85]), single body parts (e.g., [86]), and non-self-propelled (e.g., [87]). This list of 70 systems is comprehensive but not all-inclusive. Entries are alphabetized by author.

Reference	Description	Speed (m/s)	Body Length, BL (m)	Speed (BL/s)	Actuation Frequency (Hz)
Ahmad Mazlan (2015)	RoboSalmon	0.143	0.90	0.16	1.0
Anderson & Chhabra (2002)	VUUUV	1.25	2.4	0.52	1.0
Barrett et al. (1999)	Robotuna	0.70	1.25	0.56	1.1
Berlinger et al. (2021)	Finbot	0.122	0.160	0.763	4.25
Bujard et al. (2021)	Robotic squid	0.26	0.266	0.98	9.0
Butail et al. (2015)	Robotic zebrafish	0.04	0.154	0.26	3.0
Cai et al. (2010)	Robo-ray II	0.157	0.32	0.49	1.2
Cai et al. (2015)	Robotic cownose ray	0.30	0.46	0.65	0.6
Chen & Jiang (2019)	Tensegrity robotic fish	0.30	0.420	0.72	1.72
Chen et al. (2015)	IPMC robotic cownose ray	0.007	0.21	0.034	0.157
Chen et al. (2019)	IPMC robotic fish	0.12	0.27	0.45	1.0
Chen et al. (2022)	Leaping fish robot	1.88	0.264	7.12	15.04
Christianson et al. (2018)	DEA robotic leptocephali	0.0019	0.22	0.0086	0.33
Christianson et al. (2019)	DEA robotic jellyfish	0.0032	0.163	0.020	0.2
Cianchetti et al. (2015)	OCTOPUS	0.05	0.17	0.3	0.75
Curet et al. (2011)	Robotic knifefish	0.30	0.459	0.65	6.0
Du et al. (2019)	CasiTuna	0.80	0.52	1.52	5.0
Erturk (2015)	MFC piezoelectric fish	0.075	0.243	0.31	5.0
Farideddin Masoomi et al. (2014)	UC-Ika 1	0.29	0.70	0.41	3.0
Fish et al. (2017)	MantaBot	0.43	0.428	1.00	1.1
Fujiwara & Yamaguchi (2017)	Single-motor-actuated fish	0.58	0.345	1.7	16.0
Gibouin et al. (2018)	Flexible robotic fish	0.104	0.17	0.61	1.6
Hirata et al. (2000)	Robotic sea bream	0.20	0.34	0.59	2.3
Jusufi et al. (2017)	Pneumatic swimmer	0.13	0.17	0.75	0.55
Katzschmann et al. (2018)	SoFi	0.235	0.47	0.50	1.4
Kumph (2000)	Robopike	0.09	0.82	0.1	1.0
Kwak & Bae (2017)	Robotic water beetle	0.117	0.095	1.2	1.3
Leftwich & Smits (2011)	Robotic lamprey	0.115	1.14	0.10	0.55
Leftwich et al. (2012)	Robotic lamprey	0.10	0.90	0.11	0.56
Li et al. (2013)	Underactuated robotic fish	0.15	0.425	0.35	1.0
Li et al. (2017)	Electro-ionic robotic fish	0.135	0.093	1.5	5.0
Li et al. (2019)	Group of robotic fish	0.575	0.45	1.28	1.4
Li et al. (2021)	Mariana Trench soft robot	0.0519	0.22	0.24	1.0
Liao et al. (2014)	Wire-driven robotic fish	0.333	0.495	0.67	1.0
Liu & Curet (2018)	KnifeBot	0.325	0.462	0.703	3.0
Long et al. (2006)	BEA swimmer	0.069	0.33	0.21	1.7
Long Jr. et al. (2006)	Madeleine	0.74	0.78	0.95	6.0
Mazumdar et al. (2008)	Compliant Robotic Tuna (CRT)	0.10	0.27	0.37	2.0
McGovern et al. (2009)	NEMO-propelled fish	0.033	0.125	0.26	0.8
Mohammadshahi et al. (2008)	ADCSL robotic fish	0.75	0.6	1.25	4.0
Neely et al. (2016)	Robotic stingray	0.094	0.35	0.27	1.4
Nguyen & Ho (2022)	Pneumatic eel robot	0.105	0.530	0.198	1.25
Paschal et al. (2017)	Reconfigurable armed robot	0.1	0.6	0.2	2.0
Pham et al. (2019)	Pectoral fin-propelled fish	0.231	0.4	0.58	0.75
Robertson et al. (2019)	RoboScallop	0.16	0.8	0.20	2.56
Saadat et al. (2021)	Finbot with foil	0.091	0.209	0.44	1.75
Sfakiotakis et al. (2015)	Robotic octopus	0.0986	0.38	0.26	0.9
Shao & Xu (2019)	MFC piezoelectric fish	0.1645	0.345	0.48	14.0
Shintake et al. (2018)	DEA robotic fish	0.0372	0.15	0.25	0.75
Shintake et al. (2020)	Tensegrity trout robot	0.23	0.400	0.58	3.0
Tan et al. (2006)	IPMC robotic fish	0.0063	0.23	0.03	2.0
Valdivia y Alvarado & Youcef-Toumi (2015)	Soft robotic shark	n/a	n/a	0.579	5.0
Van den Berg (2019)	Single-motor-actuated fish	0.85	0.41	2.07	5.5

Villanueva et al. (2011)	Robojelly	0.0542	0.6	0.1	0.5
Villanueva et al. (2013)	Cyro	0.0847	0.316	0.268	0.12
Wang et al. (2010)	SPC-3 UUV	1.87	1.6	1.2	2.5
Wang et al. (2019a)	Breastroke-inspired robot	0.0767	0.1	0.8	1.5
Wang et al. (2019b)	Gait optimized swimmer	0.4042	0.40	1.0	2.0
Wang et al. (2021)	Robotic larval zebrafish	0.133	0.0043	31	83
Wen et al. (2018)	Median finned-robot	0.353	0.58	0.61	1.5
Wu et al. (2015)	Robotic <i>Esox lucius</i>	0.46	0.614	0.75	1.55
Xie et al. (2020)	Wire-driven robotic fish	0.43	0.506	0.84	2.0
Yang et al. (2021)	Origami cephalopod robot	0.067	0.335	0.20	0.18
Yu & Tan (2015)	Pectoral fin-propelled fish	0.71	0.68	1.04	3.5
Yu et al. (2016a)	Leaping robotic dolphin	2.05	0.72	2.85	4.65
Yu et al. (2016b)	Single-motor-actuated fish	1.14	0.37	3.1	8.0
Yu et al. (2019)	Leaping robotic dolphin	2.11	0.72	2.93	4.65
Zhong et al. (2013)	Wire-driven robotic fish	0.365	0.555	0.66	1.0
Zhong et al. (2017)	Wire-driven robotic fish	0.67	0.31	2.15	3.0
Zhong et al. (2018)	Wire-driven robotic fish	0.42	0.31	1.4	2.0

Table 1-2: Swimming efficiency of bio-inspired robots. Here we provide all publications to our knowledge of bio-inspired underwater robots from 1999 [3] to the time of this dissertation’s defense that directly reported the cost of transport (COT). To thoroughly characterize the field, we also include publications that included sufficient data for us to calculate their COT ourselves, which constitute the majority of entries in this table. For publications with multiple values, we provide the COT corresponding to the maximum reported speed. This review demonstrates how energy efficiency is rarely investigated, and when it is, energy expenditure is often orders of magnitude higher than biological systems. We plot this data set in Figure 1-1(B). COT is mass-specific and thus uncalculable for the six entries that did not report mass. All 30 entries are included in Table 1-1. Entries are sorted by COT.

Reference	Description	Speed (m/s)	Body Length, BL (m)	Speed (BL/s)	Actuation Frequency (Hz)	Power (W)	Work per Meter (J/m)	Mass (kg)	COT (J/kg/m)
Pham et al. (2019)	Pectoral fin-propelled robot	0.231	0.4	0.58	0.75	0.102	0.44	1.059	0.42
Bujard et al. (2021)	Robotic squid	0.26	0.266	0.98	9.0	0.115	0.44	0.380	1.2
Long Jr. et al. (2006)	Madeleine	0.74	0.78	0.95	6.0	58.3	79	24.4	3.2
Li et al. (2017)	Electro-ionic robotic fish	0.135	0.093	1.5	5.0	0.024	0.18	0.0425	4.18
Ahmad Mazlan (2015)	RoboSalmon	0.143	0.90	0.16	1.0	5.4	37.8	4.3	8.8
Mazlan (2015)	Robosalmon	0.143	0.90	0.16	1.0	5.4	37.8	4.30	8.8
Villanueva et al. (2013)	Cyro	0.0847	0.316	0.268	0.12	70.0	826	76.0	11
Sfakiotakis et al. (2015)	Robotic octopus	0.0986	0.38	0.26	0.9	3.83	38.8	2.68	14.5
Zhong et al. (2017)	Wire-driven robotic fish	0.67	0.31	2.2	3.0	5.6	8.3	0.5	17
Cianchetti et al. (2015)	OCTOPUS	0.05	0.17	0.3	0.75	2.6	53	3.0	18
Nguyen & Ho (2022)	Pneumatic eel robot	0.105	0.530	0.198	1.25	13.74	131	6.81	19.21
Yang et al. (2021)	Origami cephalopod robot	0.067	0.335	0.20	0.18	0.82	12.2	0.620	19.6
Paschal et al. (2017)	Reconfigurable armed robot	0.1	0.6	0.2	2.0	4.51	45	2.1	21
Fujiwara & Yamaguchi (2017)	Single-motor-actuated fish	0.58	0.345	1.7	16.0	20.4	35	0.597	59.0
Shintake et al. (2020)	Tensegrity trout robot	0.23	0.400	0.58	3.0	1.9	8.3	0.102	81.0
Chen et al. (2021)	Leaping fish robot	1.88	0.264	7.12	15.04	89	47	0.350	135
Berlinger et al. (2021)	Finbot	0.122	0.160	0.763	4.25	3.3	27	0.160	169
Wang et al. (2021)	Robotic larval zebrafish	0.133	0.0043	31	83	4.8E-05	3.6E-04	1.535E-06	235
Kwak & Bae (2017)	Robotic water beetle	0.117	0.095	1.2	1.3	0.66	5.7	0.02265	250
Christianson et al. (2019)	DEA robotic jellyfish	0.0032	0.163	0.020	0.2	0.25	78	0.23	340
Christianson et al. (2018)	DEA robotic leptocephali	0.0019	0.22	0.0086	0.33	0.020	10.5	0.0251	419
Villanueva et al. (2011)	Robojelly	0.0542	0.6	0.1	0.5	17.0	314	0.242	1296
Chen et al. (2015)	IPMC robotic cownose ray	0.007	0.21	0.034	0.157	2.0	280	0.119	2354
Shintake et al. (2018)	DEA robotic fish	0.0372	0.15	0.25	0.75	0.92	25	0.0044	5621
Erturk (2015)	MFC piezoelectric fish	0.075	0.243	0.31	5.0	1.4	19	n/a	n/a
Kumph (2000)	Robopike	0.09	0.82	0.1	1.0	8.5	94	n/a	n/a
Liu & Curet (2018)	KnifeBot	0.325	0.462	0.703	3.0	2.55	7.85	n/a	n/a
Mehdi Saadat et al. (2021)	Finbot with foil	0.091	0.209	0.44	1.75	2.15	23.6	n/a	n/a
Wang et al. (2010)	SPC-3 UUV	1.87	1.6	1.2	2.5	194.0	104	n/a	n/a
Yu et al. (2016a)	Single-motor-actuated fish	1.14	0.37	3.1	8.0	25.6	22.5	n/a	n/a

Chapter 2

Tunabots V1–V3: Proofs of Concept and Prototypes

2.1 Overview

In Chapter 2, we design and test our first three generations of tuna-inspired robots: Tunabot V1, Tunabot V2, and Tunabot V3. Through these generations, we develop the fundamental design that enables us to access and subsequently explore the high-performance space of fish. We also develop the experimental setups and testing protocols for using these research platforms. We then quantify performance using metrics of fish performance to directly compare our results with those of fish, especially tuna. By doing so, we create the foundational design and methodology that enables us to improve our understanding of high-performance fish swimming.

First, we describe the actuation mechanism that converts the rotary motion of a single motor into flapping motion of the tail. Next, we detail our development of Tunabot V1 and its bio-inspired design based on the morphology and kinematics of yellowfin tuna. We then test Tunabot V1's free-swimming performance in a stationary water tank. Tunabot V1 achieves the

high tail-beat frequency required to access the high-performance space of fish, but its ineffective waterproofing motivates our development of the second generation.

Tunabot V2 freely swims in the stationary water tank without leaks. We quantify its performance in terms of tail-beat frequency, swimming speed, stride length, swimming kinematics, head amplitude, tail-beat amplitude, midline curvature, and Strouhal number. Tunabot V2's flapping tail generates a wake pattern that is emblematic of fish swimming. We also demonstrate Tunabot V2's ultimate purpose as a research platform by using its modular design to explore the impact of peduncle stiffness on performance.

To enhance Tunabot V2's capabilities as a research platform, we redesign the system for testing in a flow tank as opposed to the stationary water tank. We do this by adding tethers and external power cables to Tunabot V2. The power cables connect to an external system we develop that measures electrical power consumption and thus energy efficiency. The same external system also controls the swimming speed via tail-beat frequency. Together, the flow tank and external system enable greater experimental control. We then test Tunabot V2 and quantify its performance using new metrics: power, cost of transport, work per meter, and self-propelled swimming speed.

Finally, we design Tunabot V3 to access even higher tail-beat frequencies and speeds. To achieve this, we use a larger motor and stiffer peduncle joint compared to Tunabots V1 and V2. Additionally, we strengthen aspects of the design to withstand the high-cycle fatigue of high-frequency swimming. We also explore different waterproofing techniques.

2.2 Tunabot V1

2.2.1 *Actuation Mechanism Theory*

The mechanism for actuating the body back and forth was the initial design consideration of the first Tunabot prototype. Bio-inspired underwater robots have addressed this core design problem with an impressive diversity of solutions. The most common solution utilizes varying numbers of direct current (DC) servomotors [6], [8], [23], [28], [29], [32], [36], [37], [40], [41], [43], [56], [58], [60], [61], [64], [88]–[91]. A popular subset of servomotor-based designs involves cables and pulleys [3], [22], [26], [30], [34], [38], [44], [52], [62], [68]–[70], [92] and tensegrity structures [9], [20], [50], [93] to generate more natural tail curvatures than would be possible with servomotors alone. Another common design-scheme for creating propulsion uses a single [19], [21], [27], [45], [53], [66], [94] or multiple [16], [17], [35], [55], [65], [67], [95] DC motors. A more classic approach to underwater propulsion is the application of hydraulics [2], [25] or pneumatics [7], [24]. Others applied magnetism to generate underwater propulsion through the use of magnetic fields [59] or electromagnetism [4], [96]. The use of smart materials in underwater propulsion is another active area of research, especially actuators made from an electroactive polymer (EAP). There are several types of EAP actuators implemented by bio-inspired underwater robots: piezoelectric actuators composed of piezoelectric fiber composite (PFC) [95] and macro-fiber composite (MFC) [18], [48]; dielectric elastomer actuators (DEAs) [13], [14], [31], [49], [57]; polypyrrole (PPy) actuators [39]; ionic polymer-metal composite (IPMC) actuators [10], [11], [51]; and hydrogel actuators [97]. In addition to EAPs, shape memory alloy (SMA) actuators are another subset of smart material actuators used to propel bio-inspired swimmers [15], [54], [98]. Researchers have also modified living cells through tissue engineering to create artificial swimmers [99]–[101]. Others enhanced the performance of living

organisms such as jellyfish through implanted microelectronics [102], [103]. Finally, some bio-inspired systems rely on a combination of these actuation mechanisms as opposed to just a single one [11], [15], [31], [60]. There is neither a single solution nor a lack of imagination when it comes to the actuation mechanisms of bio-inspired swimmers.

Out of all these demonstrated types of actuation mechanisms, this dissertation focuses on several generations of tuna-inspired research platforms all centered around one novel actuation mechanism powered by a single DC motor. Our platforms had to be capable of accessing the high-performance space of swimming fishes (see Figure 1-1(A)) in order to explore it. As such, our initial design consideration when creating the first Tunabot prototype's actuation mechanism was how to develop a robust system capable of producing high tail-beat frequencies with a high degree of energy efficiency. We also devoted extensive efforts towards producing the simplest design possible without sacrificing performance. Multiple motors, gears, shafts, springs, cables, pulleys, and other components introduce complexities and inefficiencies while reducing reliability with each added part. Previous fish robots demonstrated the high-frequency capabilities of single-motor-actuated designs [21], [66], [104]. Additionally, DC motors are typically more energy efficient compared to other AUV actuator types and even muscle fibers of certain fish species [105]. For these reasons, we focused on creating an actuation mechanism powered by a single DC motor.

The Tunabots were actuated by a single motor coupled to an oscillatory slot mechanism (Figure 2-1) that converted motor rotation into 2D sweeping motion of the tail. We developed this mechanism during the three design iterations of Tunabot V1 and improved it with each Tunabot generation through Tunabot V5 (see Figure 1-3). We present the dynamic equations characterizing this mechanism next. As an additional resource, we solved and animated these

equations elsewhere (please see Video S1 [106]) using MATLAB (MathWorks Inc., Natick, MA, USA). Spherical coordinates and 2D components are convenient for posing the mechanism's dynamics. The shaft is bent with angle θ , and the motor rotates the root of this shaft with angular displacement φ . When $\varphi = 0^\circ$ and 180° , the midline of the body is straight. The bent portion of

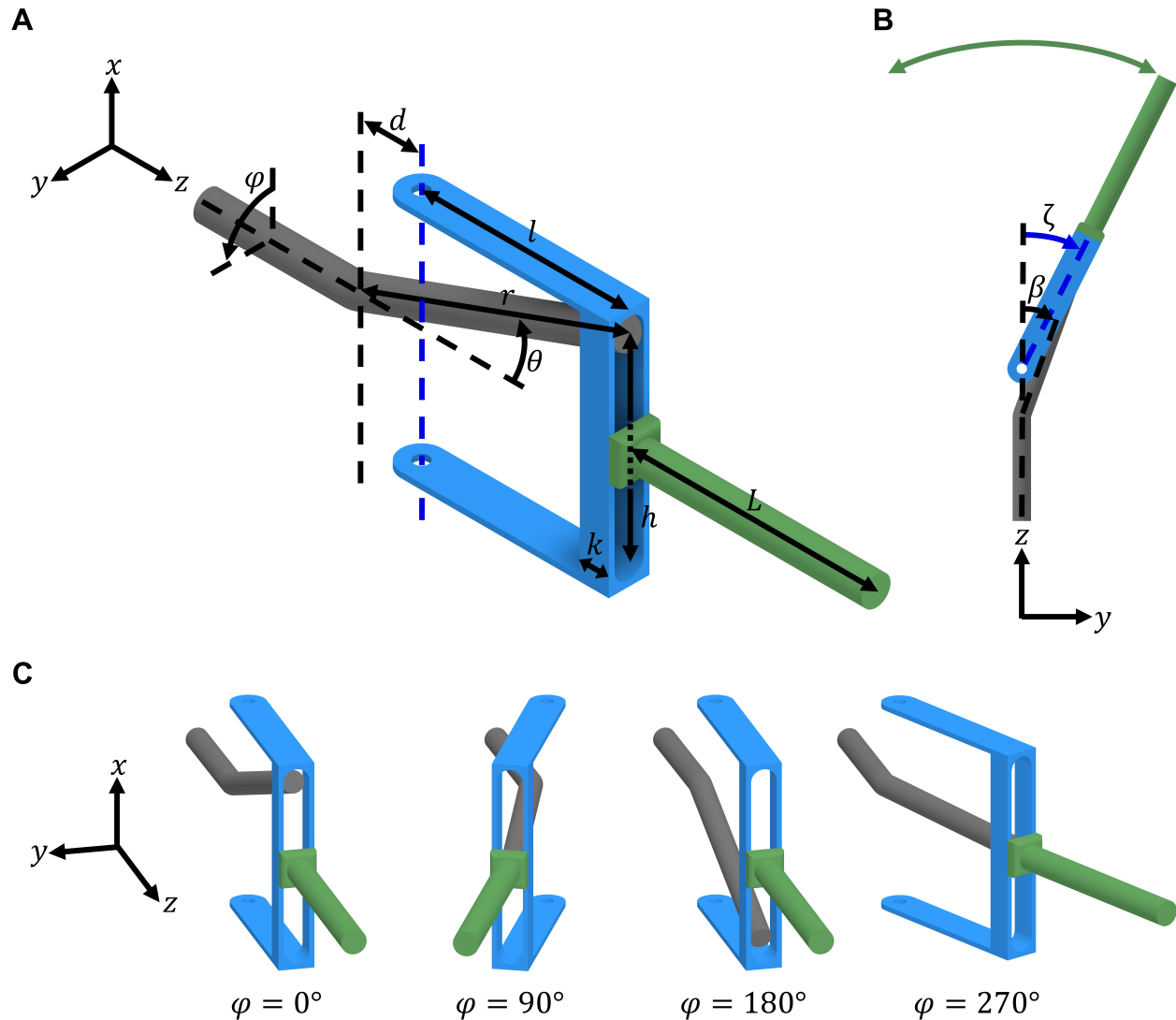


Figure 2-1: Actuation mechanism diagram. Rotational motion of a single motor is converted into oscillatory tail motion to propel the Tunabots. Isometric (A) and planform (B) views of the diagram are illustrated. The actuation mechanism is composed of three components: a bent shaft (gray), flapper (blue), and spar (green). Color shading is provided to visually differentiate components. As the shaft's tip slides within the flapper's slot, the flapper sweeps back and forth about two pinned joints. The spar fixed to the flapper transfers and amplifies this sweeping motion (green arc) to the peduncle of the Tunabots. (C) One rotational period of the bent shaft is shown for four different angles of φ .

the shaft has length r . The following set of parametric equations describes the circle traced by the spinning shaft's tip in Cartesian coordinates:

$$x_{\text{shaft}} = r \sin \theta \cos \varphi \quad (1)$$

$$y_{\text{shaft}} = r \sin \theta \sin \varphi \quad (2)$$

$$z_{\text{shaft}} = r \cos \theta \quad (3)$$

The shaft's tip resides within the slot of the flapper throughout its circular motion. The slot is connected by two arms to pinned joints that permit rotation about a parallel x-axis. This axis is a set distance d from the shaft's bend location. The arm length l must be carefully selected to prevent the shaft's tip from binding, especially at the extreme y-displacements when $\varphi = 90^\circ$ and 270° . We calculate the minimum length l as follows:

$$l = \sqrt{(r \sin \theta)^2 + (r \cos \theta - d)^2} = \sqrt{r^2 - 2dr \cos \theta + d^2} \quad (4)$$

In addition to l , the slot height h must also be considered to prevent binding at the extreme x-displacements of the shaft's tip, which occur when $\varphi = 0^\circ$ and 180° :

$$h = 2r \sin \theta \quad (5)$$

The shaft's tip moves in two dimensions within the slot plane (x-z plane for $\varphi = 0^\circ$) and not just vertically, as is the case for similar mechanisms such as the Scotch yoke. Consequently, the depth of the slot in the z-direction, k , must be chosen with care so that the shaft's tip does not slip out of the slot. The following three equations describe k and the 2D trace of the shaft's tip within the slot projected onto the x-z plane:

$$k = l + d - z_{\text{shaft}} \quad (6)$$

$$x_{\text{trace}} = x_{\text{shaft}} \quad (7)$$

$$z_{\text{trace}} = z_{\text{shaft}} + k|\sin \varphi| \quad (8)$$

When viewed from above (Figure 2-1(B)), two important angles are apparent: β and ζ . We calculate the angle β between the z-axis and bent portion of the shaft as follows:

$$\beta = \tan^{-1} \left(\frac{y_{\text{shaft}}}{z_{\text{shaft}}} \right) = \tan^{-1}(\tan \theta \sin \varphi) \quad (9)$$

We similarly find the angle ζ between the z-axis and flapper centerline:

$$\zeta = \tan^{-1} \left(\frac{y_{\text{shaft}}}{z_{\text{shaft}} - d} \right) = \tan^{-1} \left(\frac{r \sin \theta \sin \varphi}{r \cos \theta - d} \right) \quad (10)$$

Next, we define the parametric curve of the flapper at the point of spar attachment:

$$y_{\text{slot}} = l \sin \zeta \quad (11)$$

$$z_{\text{slot}} = l \cos \zeta + d \quad (12)$$

This parametric curve demonstrates that the rotational motion of the motor is converted into a 2D flapping motion. With the correct value of l , the shaft's tip intersects the flapper's curve at $\varphi = 90^\circ$ and 270° (please see Video S1 [106]).

Since the spar is a fixed extension of the flapper, the angle between the z-axis and spar is also ζ . For fish, the narrow region between the base of the caudal fin and posterior ends of the dorsal and anal fins is termed the 'caudal peduncle' or simply the 'peduncle'. The spar of length L transfers the flapping motion posteriorly to the peduncle and increases the side-to-side amplitude. The peduncle is synonymous with the leading edge of the caudal fin since the two are joined by a pinned joint for all Tunabot designs. Therefore, the parametric curve of the peduncle's displacement is finally calculable:

$$y_{\text{peduncle}} = (l + L) \sin \zeta \quad (13)$$

$$z_{\text{peduncle}} = (l + L) \cos \zeta + d \quad (14)$$

A special condition occurs when the flapper's rotational axis intersects the shaft bend

location (i.e., $d = 0$), as is the case for Tunabots V1–V5. When this condition is met, we see from Equations (4) and (10) that $l = r$ and $\zeta = \beta$, respectively. These results are expected since the flapper arms precisely overlay the bent portion of the shaft when $\varphi = 90^\circ$ and 270° for $d = 0$. With this in mind, we simplify Equations (13) and (14):

$$y_{\text{peduncle}} = \frac{(r + L) \tan \theta \sin \varphi}{\sqrt{\tan^2 \theta \sin^2 \varphi + 1}} \quad (15)$$

$$z_{\text{peduncle}} = \frac{(r + L)}{\sqrt{\tan^2 \theta \sin^2 \varphi + 1}} \quad (16)$$

Equations (15) and (16) reveal several important points concerning the tail kinematics generated by the actuation mechanism's motion. First, the swept position of the peduncle joint is a function of the motor's angle of rotation. These equations combined with a motor encoder would enable precise tail control for variable swimming gaits and turns based on observed yellowfin tuna performance [107]. Furthermore, this would be achieved through a single motor rather than the multiple DC or servo motors that often actuate fish robots. Second, the swept curve is a combined, periodic motion of pitching and heaving that is emblematic of fish caudal kinematics [108], [109]. Third, the curve traced by the actuation mechanism is highly customizable based on simple design parameters such as r , θ , d , and L . The tail-beat amplitude is readily tuned this way, as we demonstrate later in Section 4.5.1. Fourth, the periodicity of tail beats is tailored by modifying the slot geometry, such that tail velocity or mechanical advantage may be heightened during specific portions of the tail-beat cycle.

By differentiating Equation (15) with respect to φ while assuming constant angular velocity of the motor spinning the bent shaft, we find the y-component (i.e., side-to-side or heaving component) of the peduncle's velocity:

$$v_{y_{\text{peduncle}}} = \frac{\partial y_{\text{peduncle}}}{\partial \varphi} = \frac{(r + L) \tan \theta \cos \varphi}{(\tan^2 \theta \sin^2 \varphi + 1)^{3/2}} \quad (17)$$

By differentiating Equation (17) once more with respect to φ , we get the following expression for the y-component of the peduncle's acceleration:

$$a_{y_{\text{peduncle}}} = \frac{\partial^2 y_{\text{peduncle}}}{\partial \varphi^2} = \frac{-(r + L) \tan \theta \sin \varphi (\tan^2 \theta (\cos 2\varphi + 2) + 1)}{(\tan^2 \theta \sin^2 \varphi + 1)^{5/2}} \quad (18)$$

Equations (15), (17), and (18) form the equations of motion of the peduncle's displacement, velocity, and acceleration in the side-to-side direction and are illustrated in Figure 2-2.

Through further investigation of Equations (15), (17), and (18), we derive maximum and minimum values:

$$(y_{\text{peduncle}})_{\text{global extrema}} = \frac{(-1)^{n+1}(r + L) \tan \theta}{\sqrt{\tan^2 \theta + 1}} \quad \text{for } \varphi = \pi \left(n - \frac{1}{2} \right) \quad \text{where } n = 1, 2, \dots \quad (19)$$

$$(v_{y_{\text{peduncle}}})_{\text{global extrema}} = (-1)^{n+1}(r + L) \tan \theta \quad \text{for } \varphi = \pi(n - 1) \quad \text{where } n = 1, 2, \dots \quad (20)$$

$$(a_{y_{\text{peduncle}}})_{\text{local extrema}} = \frac{(-1)^n(r + L) \tan \theta}{|\sec \theta|^3} \quad \text{for } \varphi = \pi \left(n - \frac{1}{2} \right) \quad \text{where } n = 1, 2, \dots \quad (21)$$

These extrema are highlighted in Figure 2-2 alongside their corresponding plotted equations of motion. Equation (20) shows that maximum velocity of the peduncle occurs mid-stroke when the leading edge of the caudal fin passes the body's straight midline (i.e., $\varphi = 0^\circ$ and 180°). The peduncle's acceleration is zero at these points but peaks when $\varphi \approx 90^\circ$ and 270° during the transition period as the tail switches directions (Equation (21)).

The side-to-side displacement of the peduncle resembles a sinusoidal waveform that is almost indistinguishably stretched in the direction of having a square shape. The displacement curve (Figure 2-2(A)) overlaps the sine wave plotted for reference (dotted-dashed line) nearly completely. The velocity of the peduncle resembles a cosinusoidal waveform that is slightly

narrowed, giving it a triangle-like appearance. The reference sine wave's first derivative is visible in Figure 2-2(B), albeit slightly, indicating that the displacement of the peduncle from which the velocity is derived is not a pure sine wave. This is confirmed by the three equations of motion (Equations (15), (17), and (18)) and is most obvious when viewing the acceleration (Figure 2-2(C)). The acceleration of the peduncle has periods of roughly constant acceleration with an overall waveform resembling a combination of a sine and square waveform. Upon closer inspection (Figure 2-2(C)), the periods of roughly constant acceleration call to mind the Gibbs phenomenon present in the three-term Fourier series approximation of a square waveform.

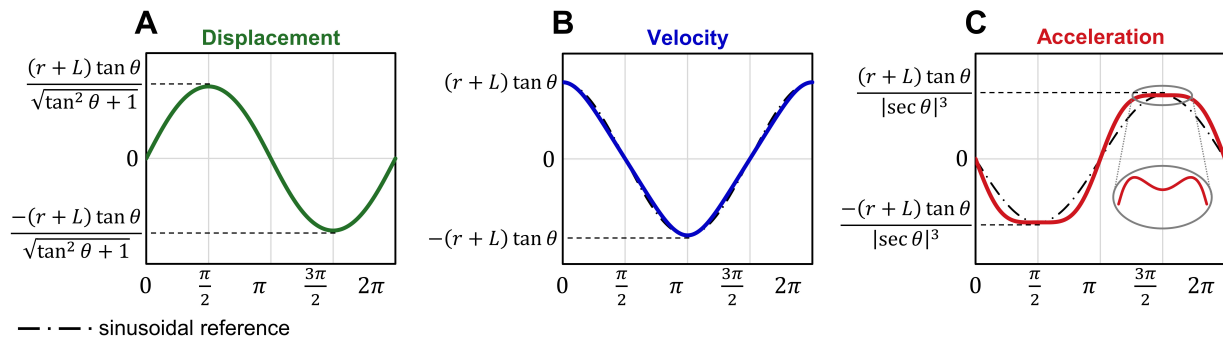


Figure 2-2: Plotted equations of motion of the peduncle's horizontal component. As the shaft turns one complete revolution ($0 \leq \varphi \leq 2\pi$, Figure 2-1(A)), the actuation mechanism sweeps the peduncle back and forth (see green arc in Figure 2-1(B)). The y-component (i.e., horizontal component) of this two-dimensional motion is plotted here in terms of the **(A)** displacement from Equations (15) and (19), **(B)** velocity from Equations (17) and (20), and **(C)** acceleration from Equations (18) and (21). Extrema values are indicated on the y-axes from Equations (19), (20), and (21). For reference, a sine wave is plotted in all three plots (dotted-dashed, black line). The nonsinusoidal nature of the waveform is slightly apparent when viewing the velocity **(B)** and obvious when viewing the acceleration **(C)**, especially for the provided zoomed-in view.

The sinusoidal displacement of the actuation mechanism is comparable to swimming fishes, which are observed as having sinusoidal, undulatory motion [72], [110]–[112]. In addition to direct observation, sinusoidal motion has long been a central element of the mathematical models describing fish swimming. In his seminal 1933 work, Gray quantitatively analyzed the kinematics of eels in great detail and noted that waves traveled backward sinusoidally along the

body faster than the forward swimming speed [113], [114]. Influenced in 1952 by Gray's analysis, Taylor formulated an undulatory propulsion model for long, narrow fish where viscous forces dominate, which is referred to as the 'resistive model' [115], [116]. Lighthill in 1960 mathematically modeled the kinematics of swimming fish as a traveling wave that moves down the fish's body [117]–[120]. Independently during the same year, Wu derived the basic mechanism of fish propulsion by combining thin, flexible plate theory with chordwise traveling waves [121]. Conversely to Taylor's resistive model, the 'reactive models' of Lighthill and Wu described propulsion dominated by inertial effects in inviscid flow and were named after the reaction forces due to added mass [116]. We discuss the role of added mass in propulsion later in Section 3.3.6. Both well-established biological observations and mathematical theories of fish locomotion center around sinusoidal motion; therefore, the sinusoidal-like motion generated by our actuation mechanism is representative of fish kinematics.

Many fish roboticists have applied sinusoidal motion to their designs. Basic sine waves are commonly used for the input signals that oscillate the tails of robotic fish [4], [60], [88]–[90], [122], [123]. Despite the prevalence of sinusoidal waveforms, the consideration of nonsinusoidal waveforms is an active area of research. Different waveform shapes are compared using swimming robotic systems [70], numerical simulations [124], and foils in a flow tank [125]. For a fish robot, sinusoidal signals produce the largest average static thrust and steady swimming speed, whereas triangular signals provide superior yaw stability when comparing sinusoidal, over-cambered sinusoidal, and triangular input signals [70]. For a numerically simulated 2D pitching-heaving plate, the gait that optimizes thrust combines a sinusoidal-like pitching component and a triangular-like heaving component [124]. For a foil in a flow tank, sinusoidal motion maximizes efficiency, whereas square-like motion maximizes speed when comparing

sinusoidal, square-like, and triangular-like waveforms generated from Jacobi elliptic functions [125]. These three examples highlight how sinusoidal motion is not necessarily optimal depending on the desired performance metric.

The findings that nonsinusoidal motions may be optimal seem to contradict the longstanding biological observations of sinusoidal fish locomotion, but they are likely complementary. Objectives of fish swimming include survival and reproduction and not simply the optimization of single metrics such as thrust or efficiency. The swimming performance requirements of fish are shaped by evolutionary pressures and constrained by biological material properties. To satisfy these requirements, a sinusoidal gait may, in fact, be optimal for fish. However, the design requirements of a fish robot are entirely the choice of the engineer and constrained by available technology. This introduces the interesting possibility that fish robots may outperform real fish with unnatural, nonsinusoidal motions.

2.2.2 *Design and Fabrication*

Tunabot V1 (Figure 2-3) was the first-generation Tunabot and completed in July 2017. The swimming system of Tunabot V1 consisted of an active part and a passive part to model the kinematics of swimming tuna. At the start of the design process, we studied dorsal-view footage of steadily swimming yellowfin tuna (see Section 3.3.3) recorded by Lauder Laboratory (Harvard University's Museum of Comparative Zoology, Cambridge, MA, USA). We studied this footage to determine how the tuna's oscillatory kinematics could be closely approximated by a mechanical system that still managed to be relatively simple, capable of high tail-beat frequencies, and durable. Based on this reference footage, we determined that an actively driven body joint coupled to a passively rotating caudal fin would effectively model the tuna's

kinematics. We also determined that both joints would only rotate laterally based on the anatomical joint structure of tunas. The intervertebral joints of tunas are structured and connected in such a way that prevents dorso-ventral flexion, limiting bending to just the lateral plane [126]. The motions of Tunabot V1's joints were similarly constrained but without the complexity of vertebrae.

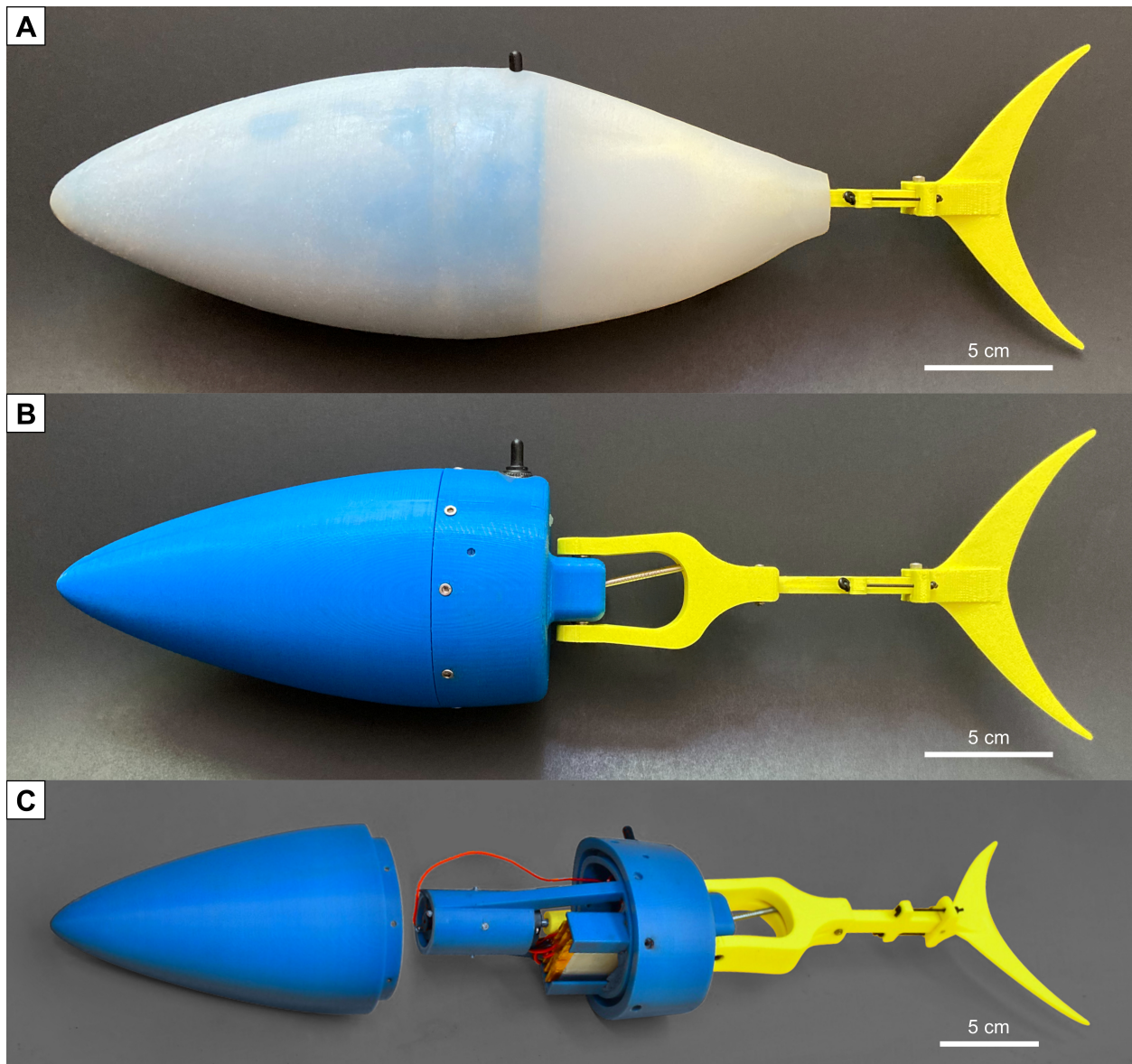


Figure 2-3: Design of Tunabot V1. (A) Tunabot V1 fully assembled, (B) with the skin removed, and (C) with the head segment removed to reveal the internal components.

We then traced the tuna’s midline on individual video frames to measure the foundational design parameters of Tunabot V1. For our two-joint model, the body joint would be located at 0.50 BL and actively rotate about symmetric limits of 16°, and the peduncle joint would be located at 0.83 BL and passively rotate about symmetric limits of 16° (Table 2-1). These joint positions and rotation angles encapsulated the tuna’s range of motion that we traced including the 0.18 BL tail-beat amplitude. The position of Tunabot V1’s mid-body joint (0.50 BL) was based on our observations of tuna kinematics, specifically where the most mid-body flexure occurred. The mid-body joint’s positioning had anatomical justification as well; the bulk of yellowfin tuna’s red (i.e., aerobic) muscle is positioned around 0.50 BL and found in the region of maximum body flexure [127]–[129]. The yellowfin tuna we studied measured ~1 m in body length, but we selected a wieldier 40.6 cm body length for Tunabot V1. This shorter body length was emblematic of moderately sized yellowfin tuna [128]. Substantially larger tuna-inspired systems have existed, such as Barrett’s Robotuna which measured 1.25 m in length [3], but would have outgrown our stationary water tank for testing.

Table 2-1: Design parameters of Tunabots V1–V5. Key design parameters for the five generations of Tunabots included body length, unsubmerged (i.e., dry) body mass, the mid-body and peduncle joints’ angles of rotation (symmetrically away from a straight midline) and positions along the body’s length (as measured from the snout), and the model number of the 12 V DC motor (Actobotics, RobotZone LLC). Each generation built upon the last as evidenced by the similar values and often subtle modifications of these parameters. We varied Tunabot V5’s mid-body joint in addition to adding a third and fourth joint, so we provide those joint parameters separately in Table 4-1 and Table 4-3.

Generation	Body Length (cm)	Mass (kg)	Mid-Body Joint		Peduncle Joint		Motor Model No.
			Angle (°)	Position (BL)	Angle (°)	Position (BL)	
Tunabot V1	40.6	0.90	16	0.50	16	0.83	638260
Tunabot V2	40.6	0.90	16	0.50	16	0.83	638260
Tunabot V3	36.1	0.93	16	0.50	16	0.82	638286
Tunabot V4	25.5	0.306	16	0.49	18	0.84	638358
Tunabot V5	25.5	0.190	10, 16, 25	0.47	18	0.84	638358

After planning the joints and body length, we started creating the 3D model of Tunabot V1 (Figure 2-4) beginning with the design of the swimming system's actively driven body joint. For the 3D modeling, we used computer-aided design (CAD) software (Inventor Professional, Autodesk Inc., San Rafael, CA, USA). As explained previously in Section 2.2.1, the foundational design consideration of the first Tunabot prototype, Tunabot V1, was how it would be mechanically driven. We developed the actuation mechanism pictured in Figure 2-1 over three design iterations of Tunabot V1. Multiple redesigns were required as we determined the proper shapes and tolerances of the mechanism's three core components (i.e., bent shaft, flapper, and spar). The end result was a working, physical prototype based on our concept of Tunabot V1 sketched one month prior in June 2017. The mechanism actively rotated the mid-body joint about two pinned joints (see Figure 2-1) between symmetric limits of 16° , thereby sweeping the caudal fin back and forth. We precisely aligned the rotational axis of the mid-body joint with the bend location of the actuation mechanism's bent shaft (see Section 2.2.1).

After designing the actively driven body joint, we determined the second aspect of Tunabot V1's swimming system: a passively rotating caudal fin. To enable the caudal fin to freely rotate behind the actively driven tail, we designed a single peduncle joint connecting the caudal fin to the body. Tunabot V1's peduncle joint was a simplification of yellowfin tuna anatomy. A tuna's peduncle consists of a complex structure of uniquely shaped vertebrae with tendons that insert directly into the caudal fin rays [82], [126], [130]–[132]. Having only a single joint, our peduncle design did not capture the smooth curvature of a tuna peduncle's multiple intervertebral joints. Instead, we prioritized modeling the peduncle's overall angle of lateral flexion based on the dorsal-view reference footage of yellowfin tuna. As such, Tunabot V1's peduncle joint rotated between symmetric limits of 16° . We also prioritized the function of

peduncle tendons by stiffening Tunabot V1's peduncle joint with two elastic bands. Resembling a tuna's peduncle tendons, these elastic bands ran longitudinally along each side of Tunabot V1's peduncle and attached directly to the caudal fin's base, providing rotational stiffness to the joint.

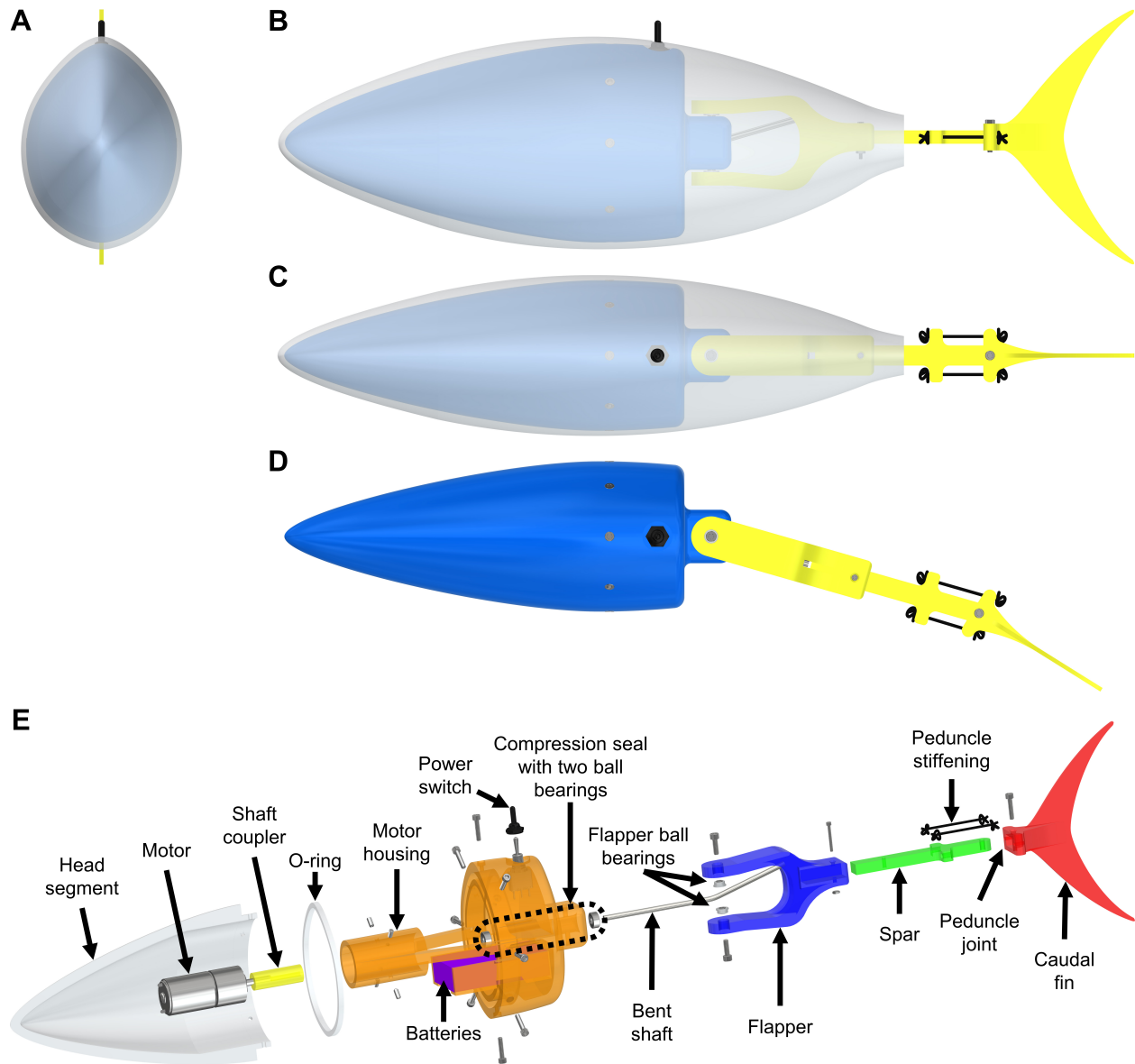


Figure 2-4. CAD model of Tunabot V1. (A) Anterior, (B) lateral, and (C) dorsal views of Tunabot V1's CAD model. (D) Dorsal view of the body with maximum tail deflection. The prescribed rotation angles of the mid-body and peduncle joints are provided in Table 2-1. The skin is removed for visualization purposes. (E) Exploded view with the names of components indicated. Color shading is provided to differentiate components and emphasize their design evolution from Tunabot V1 through Tunabot V5 (see Figure 1-3). The bent shaft (gray), flapper (blue), and spar (green) compose the actuation mechanism and are synonymous with the color-coded components of Figure 2-1.

In effect, the two elastic bands functioned as a torsional spring that returned the joint to the neutral position of 0° . This concept of a passively rotating peduncle joint with tendon-like stiffness was inspired by the previous work of Gregory Lewis [132], who investigated the influence of peduncle stiffness on swimming performance using a tuna-inspired platform. That platform's peduncle joint was based on dissections of yellowfin tuna performed at Lauder Laboratory in 2015.

We then determined the lateral profile of Tunabot V1 by tracing a true-to-life reference image of yellowfin tuna (Figure 2-5). This image was an important part of Tunabot V1's bio-inspired design process and chosen for its accurate portrayal of tuna morphology. As a result, Tunabot V1 incorporated key morphological features of yellowfin tuna: a fusiform, streamlined body; narrow peduncle; and lunate caudal fin. We omitted all fins from the model except for the caudal fin for a simplified version of tuna morphology since our focus was on the propulsive contributions of the body and tail.

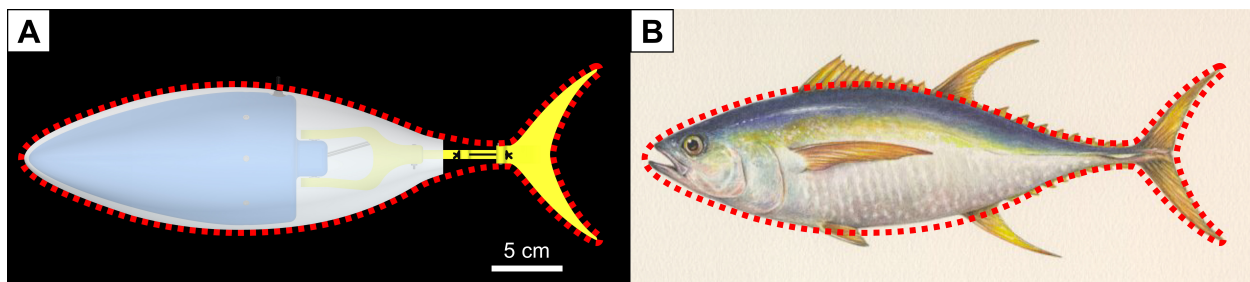


Figure 2-5: Tunabot V1's design inspired by yellowfin tuna. We designed the morphology of Tunabot V1 using reference images of yellowfin tuna (*Thunnus albacares*). For instance, (A) the lateral profile and proportions of Tunabot V1's CAD model (red, dashed outline) were derived directly from (B) this true-to-life image of yellowfin tuna [133].

As with Tunabot V1's lateral profile, we incorporated reference images from dissections of yellowfin tuna [126], [134] to determine the cross-sectional profile of Tunabot V1's body. Together, the 2D lateral profile and 2D cross-sectional shape traced from reference images of

yellowfin tuna formed the 3D framework of Tunabot V1's bio-inspired design. We developed this CAD technique of creating 3D models from 2D cross-sectional images of swimming animals as an undergraduate student. Tasked by Dr. Trevor Kemp, we processed raw magnetic resonance imaging (MRI) scan data of marine mammals' flukes into 3D-printed models for experimental testing (Figure 2-6). The MRI scans were provided by Professor Frank Fish of West Chester University (West Chester, PA, USA).

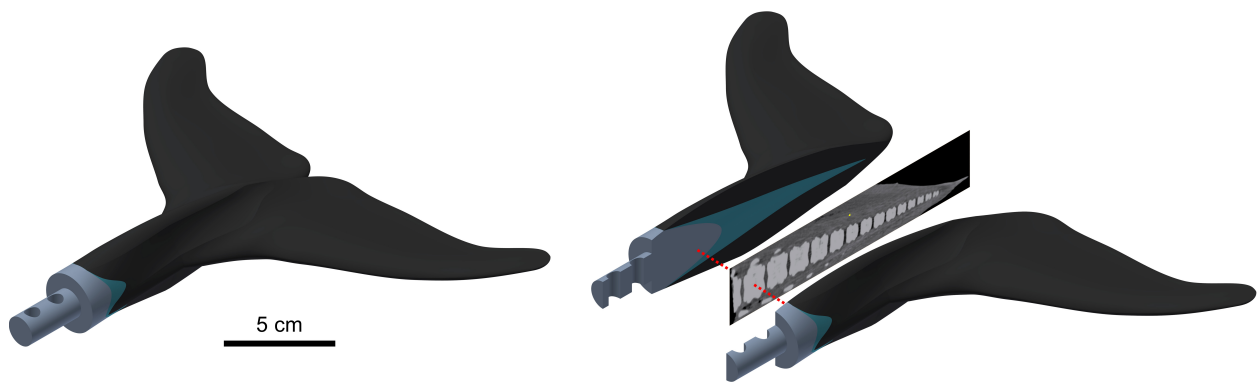


Figure 2-6: 3D-printed whale fluke with nonhomogeneous stiffness. We designed the 3D shape of Tunabot V1 using 2D reference images of yellowfin tuna. We developed this approach previously when creating 3D models of whales and dolphins from 2D MRI images. **(Left)** We created a biologically realistic CAD model of the fluke of a dwarf sperm whale (*Kogia sima*) from a spanwise series of 225 MRI images. The 1:2 scale of our model was based on the 0.41 m span of the specimen's fluke. The model was then 3D printed by a Stratasys Connex500 and connected to a flapping rig for experimental testing, hence the cylindrical adapter attached to the fluke's anterior end. **(Right)** This bisectonal view of the model reveals the internal structure composed of three different materials distinguished by color. These materials (PolyJet resins) were 3D printed simultaneously and selected for their different stiffnesses: VeroWhite (white, highly rigid), a blend of VeroWhite and TangoBlack (turquoise, moderately flexible), and TangoBlack (black, highly flexible). An MRI slice is shown to illustrate how the model's moderately flexible core aligns with the specimen's vertebral column. The end result was a physical model with morphology and nonhomogeneous stiffness resembling the biological specimen. We created similar models of flukes from MRI scans of a spinner dolphin (*Stenella longirostris*) and narwhal (*Monodon monoceros*). MRI scans were provided by Professor Frank Fish.

Tunabot V1 featured a flexible, external skin that matched the lateral and cross-sectional reference images of yellowfin tuna. The main function of the skin was to provide streamlining capable of bending with the mid-body joint. We made the elastomer skin by injecting liquid silicone (Dragon Skin Ecoflex 10 NV; Smooth-On Inc., Macungie, PA, USA) into a 3D-printed

mold using 60 ml plastic syringes. The 3D printer we used (Dimension SST 1200es, Stratasys Ltd., Eden Prairie, MN, USA) extruded acrylonitrile butadiene styrene (ABS) plastic. A nearly identical mold is pictured in Figure 2-11 for Tunabot V2. Our material selection of the silicone was influenced by previous work [132], [135]. The skin had 5 mm thickness around the head but nonuniformly, which Tunabot V2's skin addressed. The skin's removability enabled disassembly of Tunabot V1 (Figure 2-3). Including the skin, Tunabot V1 measured 40.6 cm in length, 7.6 cm in width, and 10.1 cm in height with an unsubmerged (i.e., dry) mass of 0.90 kg.

Tunabot V1 consisted of three main sections: a head assembly, a central actuating region, and a peduncle-caudal fin assembly. The parts composing these three sections are labeled in Figure 2-4(E) and detailed here next beginning with the head assembly. The head assembly consisted of the head segment and motor housing. We fabricated both components in ABS plastic using a 3D printer (Stratasys Dimension SST 1200es) and waterproofed them using a silicone injection technique (see Section 2.2.3). The interface of the head segment and motor housing was a circumferential, tongue-and-groove joint; the anterior lip of the head segment (i.e., tongue) fit into the posterior groove of the motor housing and was secured by eight longitudinal screws. A custom silicone O-ring, which was positioned inside this groove, sealed the interface. The DC motor was secured inside the motor housing by four set screws. These set screws together with the stilt-like structures of the motor housing prevented the motor's outer casing from rotating relative to the body. The DC motor we selected (Actobotics model 638260, RobotZone LLC, Winfield, KS, USA) had a high rotational speed (730 rpm) to achieve high tail-beat frequencies with a nominal voltage of 12 V. The DC motor was sealed inside the head assembly and wired to an external power switch located on the dorsal side of Tunabot V1's body. The motor was powered by three rechargeable lithium polymer batteries (3.7 V, 1200

mAh, model LP503562, PKCell Battery Co. Ltd., Shenzhen, CHN), which were wired in series to a protection circuit module (model PCM-L03S04-559, Quawin Technology Co. Ltd., Shenzhen, CHN). This resulted in a single, rechargeable battery pack with an output voltage of 11.1 V.

The central actuating region consisted of the actuation mechanism's components. The 3D-printed shaft coupler transmitted the rotational motion of the motor's shaft directly to the bent shaft of the actuation mechanism. We handmade the bent shaft from a pre-fabricated, stainless-steel shaft (3.18 mm diameter) using life-size, 2D printouts of the CAD model's bent shaft as a guide. The bent shaft was centered in the motor housing by two ball bearings that maintained the bent shaft's alignment with the motor's longitudinal axis. This alignment prevented the actuation mechanism from binding due to the bent shaft's natural tendency to rotate off-axis in response to reactionary forces from the flapper. The bent shaft passed through a silicone compression seal that waterproofed the rotating shaft (see Section 2.2.3) and was located between the two ball bearings. The posterior tip of the bent shaft slid inside the 3D-printed flapper's slot forcing the flapper from side to side. The flapper rotated laterally about a single vertical axis through two pinned joints (see Figure 2-1) that attached the flapper to the motor housing. Both joints incorporated ball bearings to reduce friction of the flapper's motion. The mid-body joint's symmetrical angle of rotation (16°) was mainly determined by the bent shaft's bend angle (θ from Section 2.2.1). The 3D-printed spar inserted into the posterior end of the flapper and was fixed in place by a nut and bolt. The spar's function was to magnify the arched path of the flapper and transmit this motion posteriorly to the peduncle joint. Together the bent shaft, flapper, and spar comprised the core elements of the actuation mechanism, hence their combined appearance in Figure 2-1.

The peduncle-caudal fin assembly consisted of the stiffened peduncle joint and caudal fin. As mentioned above, two elastic bands bilaterally stiffened the peduncle joint and were based on the longitudinal peduncle tendons of yellowfin tuna. The bands connected the spar to the caudal fin, which was 3D printed in ABS plastic and thus rigid. A single screw attached the caudal fin to the spar's posterior end creating a pinned joint. By design, the joint's symmetrical angle of rotation (16°) was physically limited by the internal structure of the caudal fin. The peduncle-caudal fin assembly inserted into the posterior end of the flapper and was held in place by a nut and bolt.

We balanced Tunabot V1's buoyancy by positioning the internals and by adding ballast. We designed the heaviest components (i.e., the motor and batteries) to be located inside the head to counteract the anticipated buoyancy of the hollow head. This was not enough to prevent the head's buoyancy from pitching Tunabot V1 upwards, so we also carefully added ballast inside the head. As a result, Tunabot V1 rested level underwater and was slightly buoyant to aid in its retrieval. We positioned the batteries and ballast ventrally to lower Tunabot V1's center of gravity. This caused Tunabot V1's orientation in water to be upright and quickly self-stabilizing. To this end, we also ensured that all design aspects were symmetrical about the sagittal plane. We created the ballast by mixing metallic powder (nickel-based brazing filler: Microbraz 31; Wall Colmonoy Corp., Madison Heights, MI, USA) into liquid silicone (Dragon Skin Ecoflex 10 NV) which we then cast into the head and motor housing (Figure 2-7). We used molds while casting that preserved space for the internal parts, such as the motor and batteries. Pure liquid silicone efficiently filled the limited internal spaces of Tunabot V1 but was insufficiently dense without the metallic powder to properly balance Tunabot V1. Standard brass masses were not practical despite their significantly higher density because of their rigid, cylindrical shape. The dense metal-silicone mixture effectively balanced Tunabot V1's buoyancy in addition to its pitch and roll stabilities.

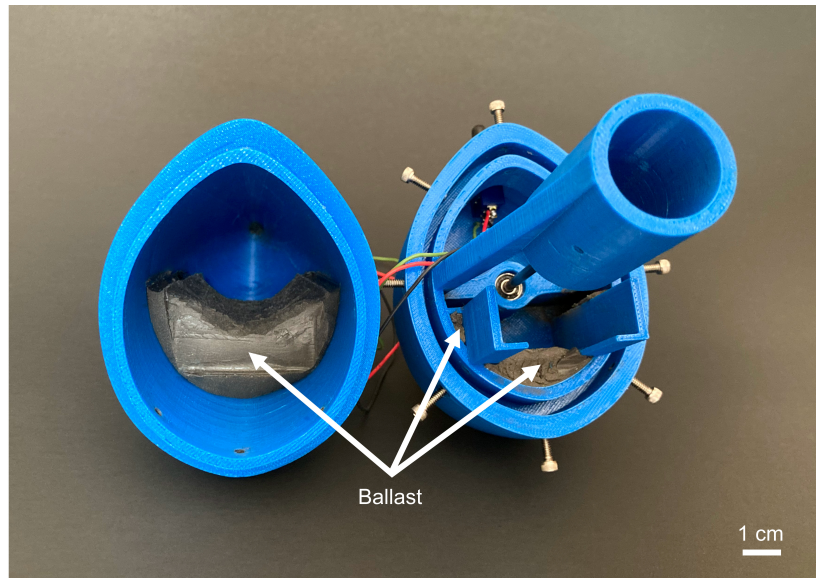


Figure 2-7: Internal ballast of Tunabot V1. (Left) The head of Tunabot V1 and (Right) motor housing contained ballast to achieve an overall slightly positive buoyancy with neutral pitch. The ballast consisted of liquid silicone mixed with metallic powder to increase its density, which was necessary given the internal volume constraints. The head and motor housing are shown with the motor and batteries removed for visualization purposes.

2.2.3 *Waterproofing Methods*

Waterproofing was an essential design aspect of Tunabot V1, as is typical for underwater robots. Electronics and other sensitive components contained within a submersible vehicle must be shielded from water to prevent service-ending damage such as electrical shorting and corrosion. As such, waterproofing was a foundational and persistent design consideration for each Tunabot generation. The waterproofing had to work symbiotically with the tuna-related features, which were also core parameters of the Tunabots. As we modified and refined the Tunabot designs with each new version, so too did the waterproofing methods evolve. Despite this advancement, the main objective remained constant across all Tunabot versions: to prevent water from reaching the DC motor. This meant creating a waterproof barrier around the motor and the rotating bent shaft. Sealing the motor and shaft required two distinct but complementary solutions. We detail the waterproofing methods of the motor and shaft for each Tunabot version beginning

here with Tunabot V1 (Figure 2-8).

3D-printed parts injected with silicone and a custom silicone O-ring waterproofed Tunabot V1's motor. A custom silicone compression seal waterproofed the rotating bent shaft. Tunabot V1 also featured a power toggle switch whose rubber cover was sealed to the motor housing with epoxy. First, we will explain the motor's waterproofing. The motor was encased by the head segment and motor housing, which are the two blue parts in Figure 2-3(C) and are labeled in Figure 2-4(E). These two parts needed to be waterproof both individually and at their attachment interface. For the individual waterproofing, we applied a method of injecting silicone into 3D-printed parts that was used by Dr. Jianzhong Zhu for other projects. Parts that are 3D printed by means of fused deposition modeling (FDM) technology are inherently porous and therefore not waterproof, hence the need for an internal layer of silicone. FDM 3D printing is a type of additive manufacturing in which a material (most commonly a thermoplastic) is extruded through a high-temperature nozzle and deposited layer-by-layer in a pattern, fusing to itself.

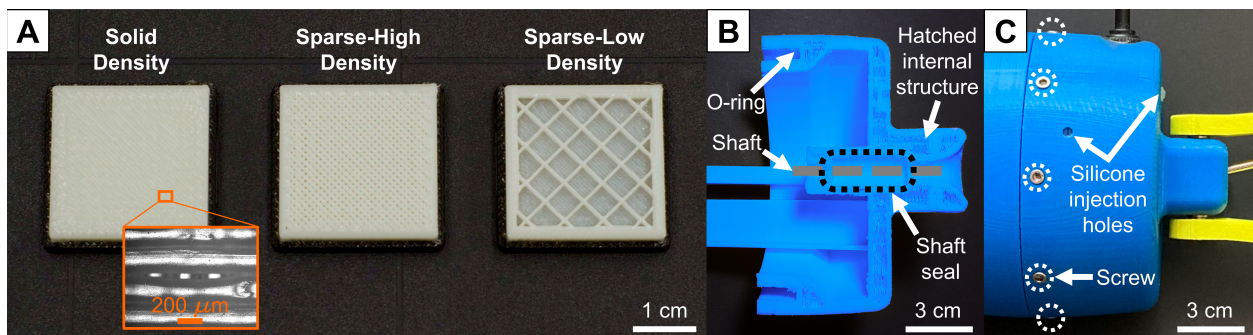


Figure 2-8: Waterproofing methods of Tunabot V1. (A) 3D-printed samples demonstrating the three options of infill densities: solid, sparse-high, and sparse-low. Orange, zoomed-in view depicts porosity of the solid density square, motivating the need for waterproofing. Samples are white ABS plastic with 1 in² areas. (B) Cutaway lateral view of the motor housing reveals the hatched internal structure from 3D printing in sparse-low density that we injected with silicone to waterproof. A custom silicone O-ring (not shown) rests within the motor housing's groove. We cast a custom silicone compression seal inside the cylindrical volume (black, dashed oval) to waterproof the actuation mechanism's rotating shaft (gray, dashed line). (C) Exterior lateral view of the motor housing highlights the silicone injection holes in addition to the circumferential screws (white, dashed circles) that attach the head and motor housing together.

3D printing for Tunabots V1–V4 (with the exception of Tunabot V4’s caudal fin) was performed by a Stratasys Dimension SST 1200es 3D printer extruding ABS plastic. This printer offered three infill densities (also referred to as ‘fill styles’): solid density, sparse-high density, and sparse-low density. Figure 2-8(A) shows three sample pieces that demonstrate these different infill densities. The solid density may appear impermeable, but gaps in the printed layers are evident upon closer inspection (orange, zoomed-in view of Figure 2-8(A)). Water inevitably passes through these gaps once submerged, resulting in leaks. The sparse-high density has a hatched or latticed internal structure that is visible to the naked eye, and the sparse-low density’s internal structure has even greater spacing (Figure 2-8(A)). Lower infill densities are commonly utilized to expend less printing material, expedite printing time, and decrease part weight although at the cost of part strength. This decrease in strength was not detrimental to the head and motor housing of Tunabot V1, so we selected the sparse-low density to intentionally create hatched internal structures (Figure 2-8(B)). We cast liquid silicone (Dragon Skin Ecoflex 10 NV) into these structures through hand-drilled injection holes (Figure 2-8(C)) using 60 ml plastic syringes. The minimum wall thickness of the head and motor housing (6 mm) formed hatched structures large enough to inject the silicone by hand without requiring difficult pressure. Once cured, the silicone solidified to form a waterproof, internal barrier. Due to its efficacy, the silicone-injection method was used again for Tunabots V2 and V4 (see Sections 2.3.2 and 3.2.2, respectively) but retired for the advanced design of Tunabot V5 (see Section 4.2.2). We explored alternative waterproofing methods for Tunabot V3 that proved to be less convenient than the silicone-injection method (see Section 2.5.2).

After individually waterproofing the head and motor housing by injecting silicone, we waterproofed their attachment interface. This round interface was a tongue-and-groove joint

wherein the head's tongue fit into the motor housing's groove (see Figure 2-3(B)–(C)). We cast a custom O-ring made of liquid silicone using a 3D-printed mold in the shape of the groove. The placement of the O-ring is indicated in Figure 2-8(B). The head's tongue compressed the O-ring in the motor housing's groove to form a waterproof seal when attaching the two parts together. The head and motor housing were held together by eight circumferential screws, five of which are indicated in Figure 2-8(C). Although the O-ring had to be compressed in order to insert the screws, the screw orientation did not adequately compress the O-ring enough to form a waterproof seal. The circumferential screw design of Tunabot V1 precipitated the development of Tunabot V2, which corrected the leaky O-ring with a longitudinal screw orientation (see Section 2.3.2).

A silicone compression seal waterproofed the rotating bent shaft. The design of our seal was inspired by industrial seals used for waterproofing rotating shafts. The rotating bent shaft of Tunabot V1's actuation mechanism had to be waterproof because it bridged the motor housing's dry interior and wet exterior. We designed a cylindrical volume inside the motor housing that separated these dry and wet regions. We filled this volume with liquid silicone leaving a hole for the shaft to pass through. To shape the silicone, we plugged the cylindrical volume at both ends with a temporary stainless-steel shaft that was centered inside and spanned both ends. The diameter of this temporary shaft (0.0625 inch) was less than that of the actuation mechanism's bent shaft (0.125 inch). This resulted in a snug fit around the bent shaft's larger diameter created by the cured silicone's elasticity. Figure 2-8(B) indicates where the straight portion of the bent shaft (gray, dashed line) passed through the motor housing's cylindrical volume (black, dashed oval) which contained the silicone compression seal. Two ball bearings bookended the volume to center the straight portion of the bent shaft within the seal. The cylindrical

compression seal with two ball bearings prevented leaks effectively, so Tunabots V2–V4 utilized the same design (see Sections 2.3.2, 2.5.2, and 3.2.2). Although effective, the waterproofing afforded by the compression seal’s snug fit came at the cost of significant frictional losses. Tunabot V5 implemented a stuffing tube design to waterproof the shaft with less friction (see Section 4.2.2).

2.2.4 *Free-Swimming Results*

Tunabot V1 successfully applied the theorized actuation mechanism detailed in Section 2.2.1 to swim underwater. Testing took place in a custom stationary water tank with wetted dimensions of $4.65 \times 1.45 \times 0.65$ m (length \times width \times height). This tank was located inside the Bio-Inspired Engineering Research Laboratory at the University of Virginia (Charlottesville, VA, USA) and was used for previous research [86], [93], [136], [137]. We held Tunabot V1 by hand underwater, powered it on, and then released it from rest to swim the length of the stationary tank. Since Tunabot V1 did not feature autonomous controls, we had to sprint to the far end of the tank to catch it. After repeating this process several times back and forth, we found that the straight swimming path and general performance were consistent. Out of water, the tail-beat frequency was 10.7 Hz and decreased by about 2 Hz when submerged due to the greater hydrodynamic forces. Tail-beat frequency is a measure of how rapidly the tail beats back and forth and is a common metric for quantifying fish swimming. We measured the tail-beat frequency using a digital stroboscope (model DS-303, The Pioneer Electric & Research Corp., Wood Dale, IL, USA). Tunabot V1 demonstrated that the applied actuation mechanism generated flapping propulsion and was robust at high frequencies. However, it became apparent during testing that Tunabot V1 was affected by water leaks and required a redesign. This

prevented thorough experiments using Tunabot V1 and prompted the creation of Tunabot V2. The cause of these leaks and associated solution are detailed in Section 2.2.3.

2.3 Tunabot V2: Free-Swimming Experiments

2.3.1 *Design and Fabrication*

Tunabot V2 (Figure 2-9) was the second-generation Tunabot and based largely upon the design of its predecessor, Tunabot V1 (see Section 2.2.2). As before, Tunabot V2's two-joint swimming system consisted of an actively driven mid-body joint and a passively rotating, stiffened peduncle joint. The positions and rotation angles of these two joints were unchanged from Tunabot V1 (see Table 2-1). The two-joint swimming system modeled the swimming kinematics of yellowfin tuna that we previously traced from dorsal-view footage recorded by Lauder Laboratory. Tunabot V2's lateral and cross-sectional profiles were based on the same reference images of yellowfin tuna as Tunabot V1. Thus, the morphologies and dimensions of Tunabots V1 and V2 were identical (40.6 cm in length, 7.6 cm in width, and 10.1 cm in height). As with Tunabot V1, we balanced Tunabot V2's buoyancy using internal ballast composed of a suspension of metallic powder in cast silicone. We created the 3D model of Tunabot V2 (Figure 2-10) closely following the design of Tunabot V1. The majority of Tunabot V2's individual parts (Figure 2-10(E)) were slightly modified versions of Tunabot V1's corresponding parts, which are itemized and described in Section 2.2.2. The notable modifications that advanced the design of Tunabot V2 are detailed next.

Tunabot V2 improved upon the design of Tunabot V1 which enhanced its utility as a research platform for conducting experiments. Three notable areas of improvement were the waterproofing, skin, and stiffened peduncle joint. Tunabot V1's ineffective waterproofing gave

impetus to the design of Tunabot V2. The attachment interface between Tunabot V1's head segment and motor housing did not properly seal, resulting in leaks (see Section 2.2.3). To address this issue, we redesigned the head segment, motor housing, and O-ring for Tunabot V2. The particulars of the corrected waterproofing are detailed in Section 2.3.2. When redesigning the motor housing, we moved the power toggle switch from the dorsal surface to the anterior end.

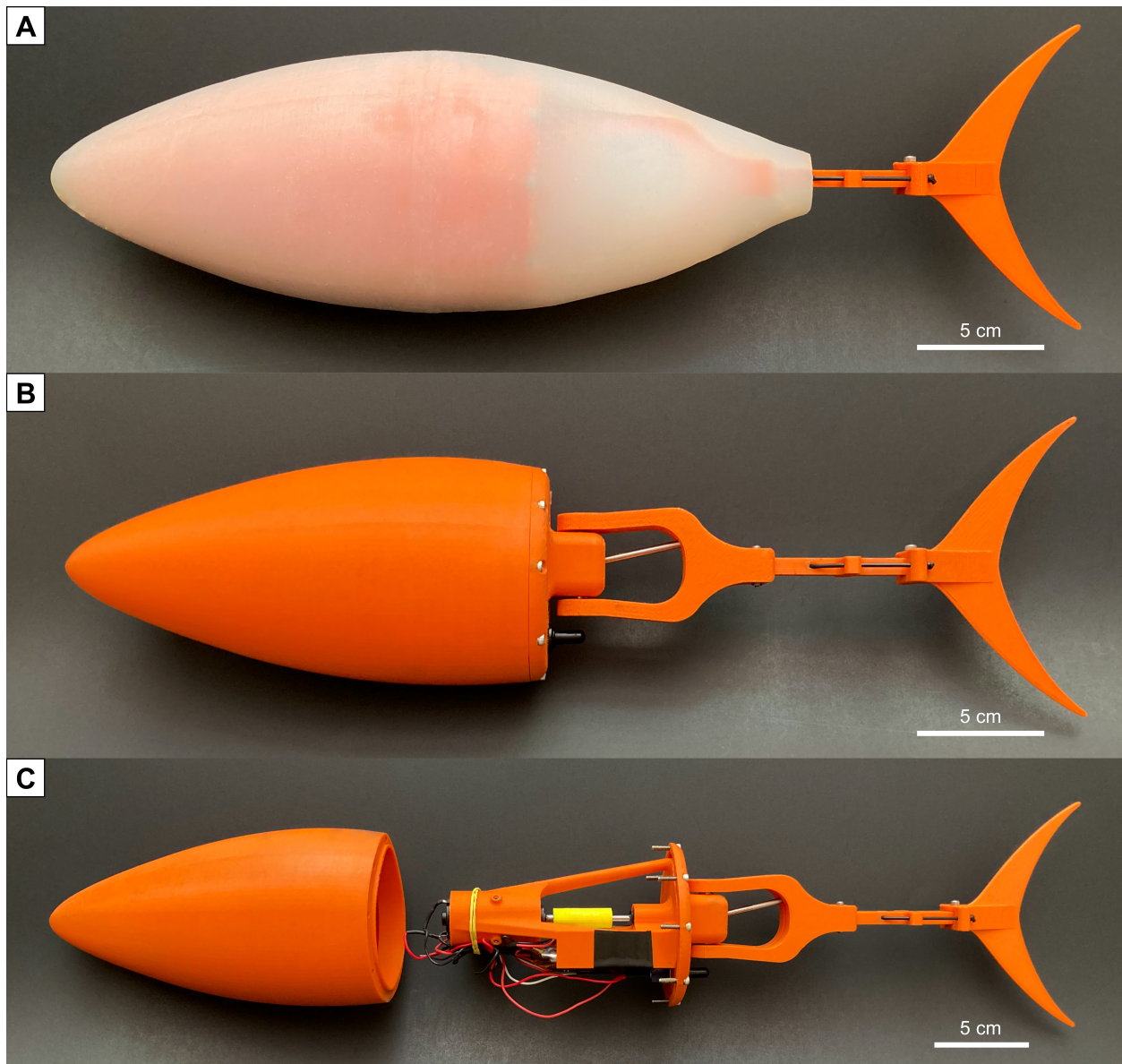


Figure 2-9: Design of Tunabot V2. (A) Tunabot V2 fully assembled, (B) with the skin removed, and (C) with the head segment removed to reveal the internal components.

Doing so slightly streamlined Tunabot V2 by placing the switch beneath the skin's surface. The skin's flexibility enabled us to activate the switch through the skin. For waterproofing, we sealed the switch's rubber cover to the motor housing with epoxy as with Tunabot V1.

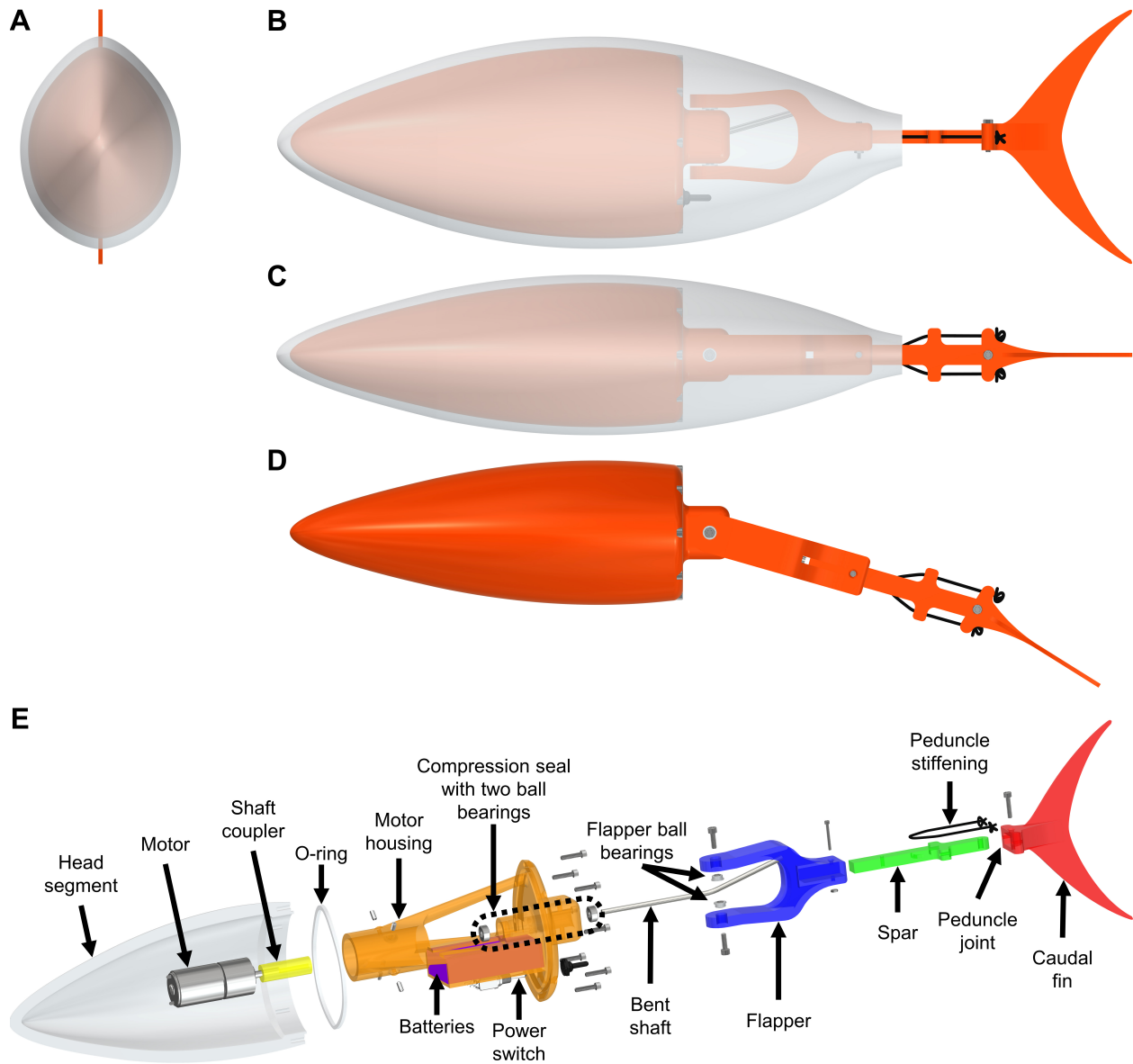


Figure 2-10: CAD model of Tunabot V2. (A) Anterior, (B) lateral, and (C) dorsal views of Tunabot V2's CAD model. (D) Dorsal view of the body with maximum tail deflection. The prescribed rotation angles of the mid-body and peduncle joints are provided in Table 2-1. The skin is removed for visualization purposes. (E) Exploded view with the names of components indicated. Color shading is provided to differentiate components and emphasize their design evolution from Tunabot V1 through Tunabot V5 (see Figure 1-3). The bent shaft (gray), flapper (blue), and spar (green) compose the actuation mechanism and are synonymous with the color-coded components of Figure 2-1.

We also improved the silicone skin design for Tunabot V2. The skin of Tunabot V1 had nonuniform thickness around the anterior half of the body (see Figure 2-4(B)–(C)). Thinner areas of the skin were needlessly at risk for tearing, so we improved the uniformity of the skin’s 5 mm thickness while maintaining the same external dimensions and morphology (Figure 2-10(A)–(C)). We accomplished this by reshaping the head segment and modifying the skin mold accordingly. We 3D printed the skin mold (Figure 2-11(A)) using a Stratasys Dimension SST 1200es printer extruding ABS plastic. We coated the inner surfaces of the mold with a thin layer of petroleum jelly to prevent the skin from adhering to the surfaces while curing. The two outer halves of the mold were screwed together with the inner piece centered inside. The inner piece was minimally suspended by three points of contact located dorsally, ventrally, and posteriorly.

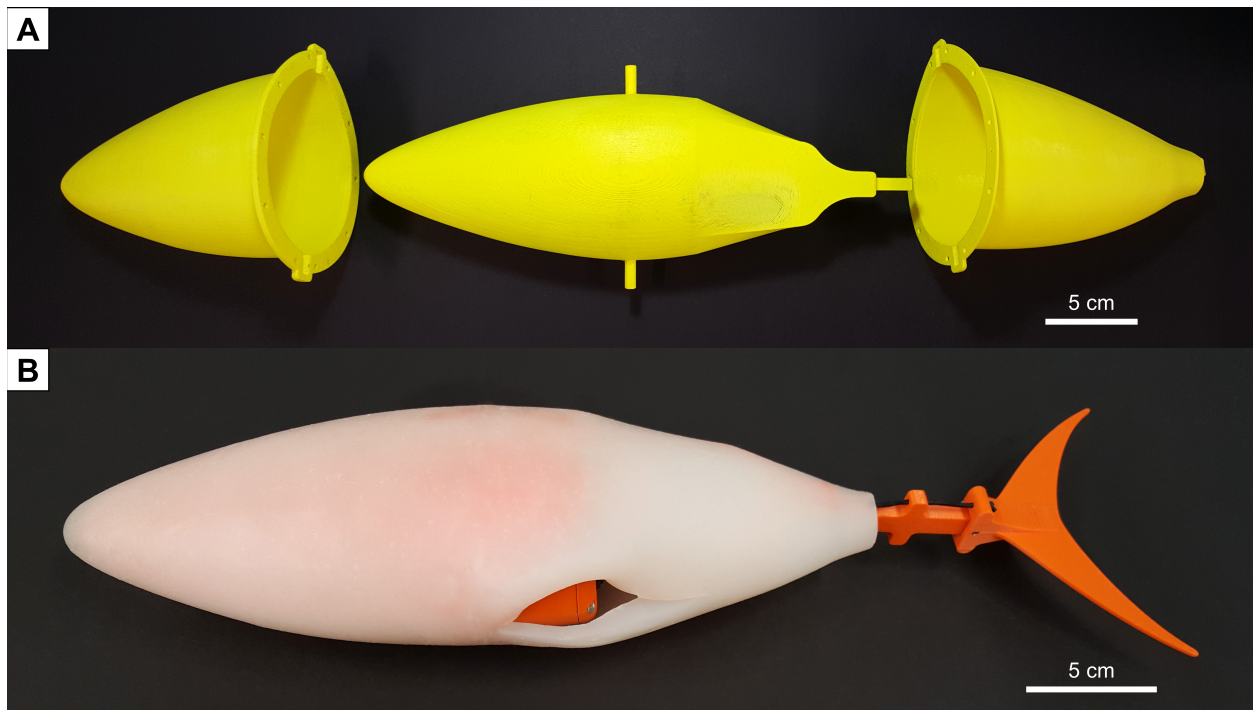


Figure 2-11: Design and fabrication of Tunabot V2’s skin. (A) We fabricated the skin of Tunabot V2 by injecting liquid silicone into the 3D-printed mold shown here. The mold consisted of an inner piece enclosed by two exterior halves that were sealed together as the silicone cured. (B) We slit the skin’s ventral surface to create an incision through which we removed the mold’s inner piece. We then inserted Tunabot V2’s body through this incision before attaching the peduncle-caudal fin assembly. Finally, we closed the incision with removable silicone tape.

We injected liquid silicone (Dragon Skin Ecoflex 10 NV) into the mold using 60 ml plastic syringes. After the silicone cured, we disassembled the mold. To remove the mold's inner piece from inside the skin, we first made an incision using a razor blade along the length of the skin's ventral surface, somewhat like gutting a fish. We then stretched the incision wider and removed the inner piece. To install the skin around Tunabot V2 (Figure 2-11(B)), we inserted the body through the stretched incision before attaching the peduncle-caudal fin assembly. Finally, we closed the incision with a strip of self-fusing silicone tape, which adhered to the silicone skin and was easily removable. This molding process and skin installation for Tunabot V2 were the same for Tunabot V1.

We improved the design of the stiffened peduncle joint for Tunabot V2. Tunabot V2's redesigned peduncle joint modeled the longitudinal peduncle tendons of yellowfin tuna as with Tunabot V1. Previously, two separate elastic bands stiffened the peduncle joint of Tunabot V1 (see Figure 2-4(E)). During assembly of the peduncle-caudal fin assembly, we tied each elastic band one at a time. When the length of the two bands differed even slightly, they would apply bilateral tension asymmetrically to the caudal fin. Consequently, Tunabot V1 would experience a directional bias towards the left or right when swimming. This was not conducive to straight swimming experiments, hence our redesign of the joint. For Tunabot V2, we replaced the two elastic bands with a single elastic band (Figure 2-10(E)) which simplified the adjustment of symmetrical tension. We modified the actuation mechanism's spar with a hole through which we forcibly threaded the single band. We gently pulled the band on either side of the spar to fine-tune its length and subsequent stiffness applied to either side of the caudal fin. The band's two attachment points to the caudal fin's base were the same as before.

To investigate the impact of peduncle stiffness on swimming performance, we created

two modular tail sections (Figure 2-12). The first tail section had moderate stiffness. This was the default peduncle-caudal fin assembly of Tunabot V2 with the single elastic band described above. The second tail section had rigid stiffness. For this, we removed the peduncle joint entirely by fixing the actuation mechanism's spar directly to the base of the caudal fin. Both the moderately stiff and rigid tail sections inserted into the posterior end of the actuation mechanism's flapper. A nut and bolt secured them to the flapper. We tested two different conditions of peduncle stiffness by swapping out the two modular tail sections.

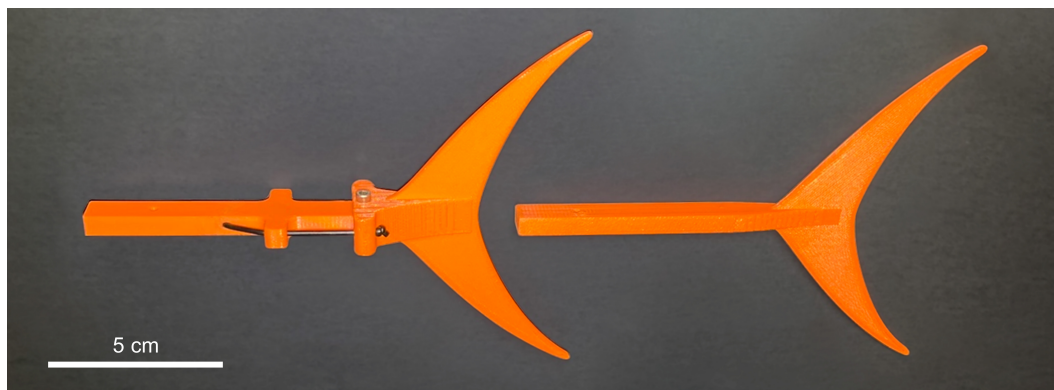


Figure 2-12: Modular peduncle stiffness of Tunabot V2. We investigated the impact of peduncle stiffness on Tunabot V2's swimming performance using two different tail sections, demonstrating Tunabot V2's purpose as an experimental platform. We varied the peduncle stiffness by swapping out these two modular tail sections. **(Left)** A black elastic band moderately stiffened the peduncle joint of Tunabot V2's peduncle-caudal fin assembly. **(Right)** Eliminating the peduncle joint produced a tail section with rigid peduncle stiffness.

2.3.2 *Waterproofing Methods*

We waterproofed Tunabot V2's motor using the same methods as Tunabot V1 (see Section 2.2.3) except for one necessary difference: we corrected Tunabot V1's leaky O-ring design for Tunabot V2. As with Tunabot V1, the head segment and motor housing were both 3D printed in ABS plastic with sparse-low density. We injected liquid silicone into the hatched internal structures of the two parts through hand-drilled holes using 60 ml syringes. After curing, the silicone solidified to form an embedded waterproof barrier. As with Tunabot V1, we sealed

the rubber cover of Tunabot V2's power toggle switch to the motor housing with epoxy. As before, we also waterproofed the actuation mechanism's rotating shaft using a silicone compression seal and two ball bearings (black, dashed oval in Figure 2-10(E)). We cast this seal inside the motor housing, and the ball bearings centered the shaft. Despite all these similarities, the design of Tunabot V2's silicone O-ring crucially differed from that of Tunabot V1.

The attachment interface of Tunabot V2's head segment and motor housing consisted of a tongue-and-groove joint wherein the head's tongue fit into the motor housing's groove (see Figure 2-9(C)). The oblong-shaped groove is most apparent in Figure 2-13 at the base of the motor housing. We cast a custom O-ring (see Figure 2-10(E)) made of liquid silicone into a 3D-printed mold. Once cured, we placed the O-ring inside the groove. When we assembled the head and motor housing, the head's tongue compressed the O-ring in the motor housing's groove to form a waterproof seal. Eight longitudinal screws held the head and motor housing together, six of which are visible in Figure 2-9(D). The O-ring compressed as the screws tightened due to their orientation, which sufficiently deformed the elastic O-ring to form a waterproof seal. This

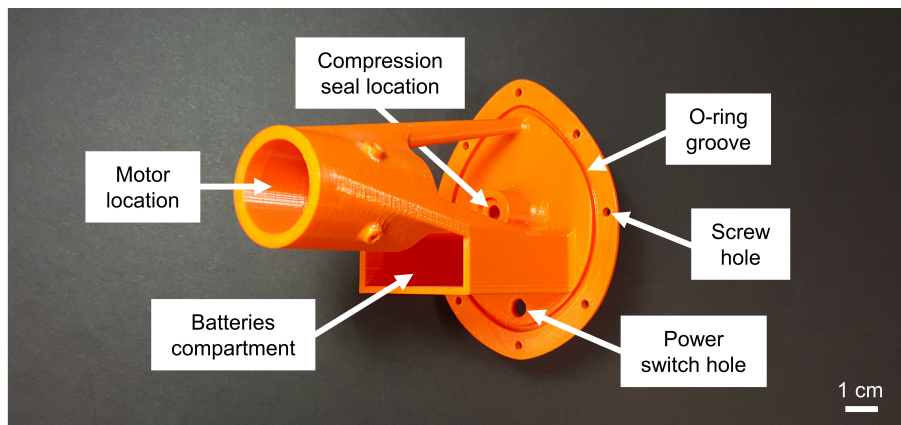


Figure 2-13: Motor housing of Tunabot V2. The 3D-printed motor housing of Tunabot V2 served many purposes through its compact and efficient design. Key features of the motor housing are labeled above. The motor housing of Tunabot V2 amended the leaky design of Tunabot V1's O-ring.

corrected the circumferential screw design of Tunabot V1 that resulted in leaks (see Section 2.2.3). Due to its success, we used the silicone O-ring design with eight longitudinal screws again for Tunabot V4 (see Section 3.2.2). Tunabot V5 featured a similar design, except the O-ring was rubber and purchased off-the-shelf as opposed to hand-cast silicone (see Section 4.2.2). Tunabot V3 omitted the O-ring entirely by permanently sealing the head and motor housing together (see Section 2.5.2).

2.3.3 Methodology for Free-Swimming Experiments

We investigated the free-swimming performance of Tunabot V2 in August 2017 over three separate experiments: flow visualization of the wake, steady swimming with midline kinematics, and variable peduncle stiffness. We quantified Tunabot V2's free-swimming performance in terms of important metrics used for analyzing fish performance: speed normalized by body length, stride length, swimming kinematics, head amplitude, tail-beat amplitude, and midline curvature. Later, we apply additional fish performance metrics, especially the cost of transport, for Tunabot V2's tethered experiment in Section 2.4.3. Until Tunabot V2, the only fish performance metric that we measured was tail-beat frequency. The testing of Tunabot V2 introduced the foundational metrics that later quantified the performances of Tunabots V4 and V5. Furthermore, by expanding the number of metrics and exploring their feasibility now, we were able to make future comparisons directly between tunas and Tunabots (e.g., see Section 4.4).

The first experiment visualized the vortices and wake generated by Tunabot V2's flapping tail. Testing occurred in the same stationary water tank as Tunabot V1 (see Section 2.2.4). We held Tunabot V2 powered off just below the water's surface such that only the tip of the caudal fin's dorsal side was unsubmerged. This was the starting position. We then turned the

power switch on and released Tunabot V2 from rest. Tunabot V2 swam the length of the water tank and had to be caught at the far end since it lacked autonomous controls, as with Tunabot V1. The starting position caused the flapping caudal fin to entrain air from the water's surface. This air entrainment formed bubbles that were drawn down around the caudal fin as it swept back and forth. We used these bubbles to qualitatively observe the generated vortices and wake patterns. Others have utilized sophisticated bubble particle image velocimetry (PIV) systems for visualizing flows surrounding sea lion foreflippers [138] and dolphin flukes [139]. We recorded a video of Tunabot V2's lateral side at a frame rate of 240 fps through the transparent side wall of the water tank. We show every other frame from this video in Figure 2-14 to visualize a single tail-beat period. We calculated the tail-beat frequency from the video by dividing the frame rate by the number of video frames per tail-beat period. We also calculated the speed from the video by dividing the body length by the time between frames. For fish and Tunabots alike, body length (BL) is the distance between the snout's tip and the end of the caudal fin's two lobes (i.e., the most anterior and posterior points of the body, respectively). We normalized speed by body length, yielding the unit body lengths per second (BL/s). Normalizing by body length is commonplace in fish research (e.g., [77]) and is important later when we draw comparisons between Tunabots and fishes of different sizes (see Section 4.7.1). Water temperature during testing was 22.1°C , corresponding to a density ρ of 997.74 kg/m^3 and a dynamic viscosity μ of $0.9510\text{ mPa}\cdot\text{s}$. We used these values to calculate the Reynolds number (Re), which is the dimensionless ratio of inertial forces to viscous forces in a flow [140]:

$$Re = \frac{\rho \cdot U \cdot BL}{\mu} \quad (22)$$

where U is the swimming speed and BL is the body length (i.e., characteristic length) of Tunabot V2 (40.6 cm).

The second experiment investigated Tunabot V2's linear, steady swimming performance. As before, testing occurred in the stationary water tank. For the starting position, we held Tunabot V2 underwater halfway between the water's surface and the tank's floor. We then turned the power switch on and released Tunabot V2 from rest. Tunabot V2 accelerated straight down the center of the tank to the far end where it achieved maximum velocity before we caught it by hand. At the tank's far end, a dorsal-view camera recorded video at a frame rate of 30 fps. As in the first experiment, we calculated both swimming speed and tail-beat frequency from the video, and we calculated the Reynolds number using Equation (22). The stride length (SL) expresses the distance traveled per single, complete tail-beat period, and is calculated with the following expression:

$$SL = \frac{U}{f} \quad (23)$$

where U is swimming speed and f is tail-beat frequency. We scaled both swimming speed and stride length by body length.

We digitized the midlines from the video footage by using MATLAB scripts to manually track the midline, resembling previous work [85], [141]. Additional scripts used these digitized sequences to calculate head amplitude, tail-beat amplitude, and midline curvature. Head and tail-beat amplitudes are defined as the distances between the lateral extremes of the snout and caudal fin's trailing edge, respectively. We scaled midlines, amplitudes, and curvatures by body length. With the tail-beat amplitude known, the Strouhal number was then calculable. In general, the Strouhal number (St) is a dimensionless value useful for characterizing oscillatory flow. In the context of tail kinematics of swimming fishes or robots, the Strouhal number relates the frequency of vortex shedding, amplitude of oscillation, and flow velocity. We calculated the Strouhal number with the following expression:

$$St = \frac{f \cdot A_{tb}}{U} \quad (24)$$

were f is tail-beat frequency, A_{tb} is tail-beat amplitude, and U is swimming speed [142]. Our calculations of curvature from the midline sequence resembled previous work [85], [143]. After interpolating 200 points per midline, we calculated the curvature, $\kappa(x)$, using the following equation [144]:

$$\kappa(x) = \frac{|c''(x)|}{(1 + [c'(x)^2])^{\frac{3}{2}}} \quad (25)$$

where $c(x)$ defines the midline curve and x is the position along the body's length from snout to tail tip.

The third experiment was a preliminary investigation of the role of peduncle stiffness on swimming performance. This research area was the Master's thesis topic of Gregory Lewis [132], who graduated from the same lab one month prior to the beginning of this dissertation's work. We tested two stiffness conditions of Tunabot V2's peduncle: moderately stiff and rigid. The moderately stiff condition was the default design of Tunabot V2's peduncle-caudal fin assembly; an elastic band stiffened the peduncle joint bilaterally based on the peduncle tendons of yellowfin tuna. For the rigid condition, we removed the peduncle joint entirely by fixing the caudal fin in a straight position. We swapped out two modular tail sections (see Figure 2-12) to reconfigure Tunabot V2 during testing. For each condition, Tunabot V2 swam the length of the water tank several times as in the second experiment.

2.3.4 *Free-Swimming Wake Visualization Results*

Tunabot V2 swam untethered in the stationary water tank (Figure 2-14) near the surface

with a speed of 0.58 m/s (1.43 BL/s) and a tail-beat frequency of 8.0 Hz. The Reynolds number at this speed was 2.5×10^5 . This speed was not constant since Tunabot V2 was accelerating from rest; we provide steady swimming results later in Section 2.3.5. For reference, the tail-beat frequency was 9.3 Hz out of water and with the silicone skin removed. By swimming near the surface, bubbles were drawn down around the caudal fin. These bubbles visualized the formation and shedding of a vortex on the leading edge of the caudal fin and showed the subsequent wake pattern (Figure 2-14). These vortices on the caudal fin are termed ‘leading-edge vortices’, which we will explain next.

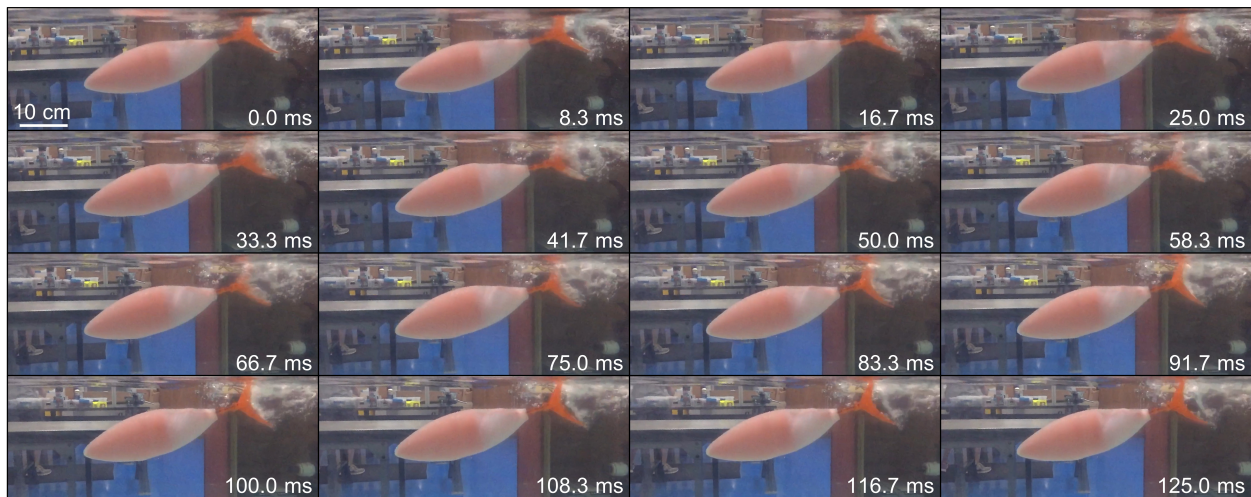


Figure 2-14: Flow visualization of free-swimming Tunabot V2. A single tail-beat period of Tunabot V2 swimming untethered in the stationary water tank at the University of Virginia with a speed of 1.43 BL/s and a tail-beat frequency of 8.0 Hz. The flow is visualized here frame-by-frame (lateral view) using air bubbles entrained from the water’s surface by the tail’s flapping motion. The formation and shedding of a leading-edge vortex on the caudal fin are visible as well as the resulting periodic wake structure.

A leading-edge vortex is traditionally an aerodynamic event and is, as the name suggests, a vortex that forms on the leading-edge region of a surface. This surface is typically an airfoil in the context of aerodynamics but can also be a flat plate. The caudal fins of Tunabots V1–V3 were lunately shaped flat plates with 2 mm thickness, and Tunabots V4 and V5 featured caudal

fins with an airfoil (NACA 0016) cross-section. Immediately preceding the formation of a leading-edge vortex, a thin layer of flow reverses at the bottom of the boundary layer at a point just downstream of the suction peak [145]. This flow reversal along the surface is triggered by the strong adverse pressure gradient [146] produced by moving the airfoil in pure pitch [147]–[152], pure heave (or ‘plunge’ as its often called in the context of aerodynamics) [152], [153], or combined pitch-heave motions [153]. For Tunabot V2 (and all other Tunabots), the combined pitching and heaving motion of the caudal fin generated leading-edge vortices. The motion of fish caudal fins was shown through numerical simulations to form attached leading-edge vortices [154]. Vorticity strengthens locally as the reversed flow interacts with the downstream-facing flow before being abruptly released into the outer flow from unsteady boundary layer separation [150]. The released vorticity remains near the airfoil surface and recirculates within a separation bubble [155], which is the region between flow separation and reattachment to the airfoil surface [156]. At this point, a leading-edge vortex has been created.

A leading-edge vortex formed on the caudal fin of Tunabot V2 as the tail beat towards the midline. Two separate vortices formed at each tip of the caudal fin when the tail began to sweep away from its maximum lateral position. As the tail continued to move towards the midline, the peduncle joint rotated to its maximum angle. This, in turn, increased the angle of the caudal fin relative to the oncoming flow. Simultaneously, the two vortices at the tips grew symmetrically towards one other. Just after passing the midline, these two vortices combined into a single, lunately shaped vortex spanning the caudal fin’s entire planform area. The leading-edge vortex was then shed as the tail transitioned beat directions.

The leading-edge vortex of Tunabot V2’s caudal fin behaved similarly to the leading-edge vortex of an aircraft’s wing. The leading-edge vortex on a swept wing was shown to

increase in size as the angle of attack increased [157]. A similar trend was apparent for Tunabot V2; its leading-edge vortex increased in size as the caudal fin's angle relative to the oncoming flow (i.e., angle of attack) increased. In this example, the Reynolds numbers of the swept wing and Tunabot V2 were also similar ($1.6\text{--}9.7\times 10^6$ and 2.5×10^5 , respectively). The angles of attack of the swept wing and caudal fin are not directly comparable because the swept wing was stationary during wind tunnel testing, whereas the caudal fin was flapping. Instead, we must use the caudal fin's effective angle of attack when comparing. We show later in Section 3.3.6 (see Figure 3-7) how flapping motion results in an effective angle of attack that differs from the angle of attack. This effective angle of attack increases as the tail beats from side to side (see Figure 3-13). The effective angle of attack is directly comparable to the swept wing's angle of attack; just as the leading-edge vortex on a swept wing increases with the angle of attack, so does the leading-edge vortex on Tunabot V2's caudal fin increase with the effective angle of attack.

Dynamic stall is the process that describes leading-edge vortices from formation to shedding. Leading-edge vortices and dynamic stall (also known as 'delayed stall') are traditionally aircraft-related concepts. But they have been increasingly found throughout nature from swimming fish [155], [158] to flying insects, birds, and bats [159]–[165]. Dynamic stall is an involved variation of static stall. As with leading-edge vortices, both static and dynamic stall originate from the field of aerodynamics. Static stall is the condition of separated flow from a static airfoil when a certain critical angle of attack is exceeded. Once this stall angle is reached, the lift force created by the airfoil begins to decrease [166]. Dynamic stall involves oscillating airfoils and delays complete flow separation to angles of attack much greater than the static stall angle [145]. Notable interest in dynamic stall began when helicopter blades were observed as

experiencing torsional stress and consequently fatigue far exceeding static airfoil predictions [148], [149]. During the dynamic stall process, the leading-edge vortex moves rearward while growing in size. As this occurs, the magnitudes of lift, drag, and aerodynamic moment increase until reaching maximum values at the airfoil's trailing edge. These three values significantly surpass those produced by a static airfoil [145]. The leading-edge vortex is then shed into the wake, causing the lift, drag, and moment to decrease precipitously.

In the wake of Tunabot V2's caudal fin, a complex vortex structure formed from the shed vortices interacting with one another. Once the leading-edge vortex shed completely, its lunate shape narrowed to a slender column spanning the caudal fin's two tips. From there, this column moved backward in the wake and linked to a complex, repeating vortex structure from previously shed vortices. Depending on the tail-beat direction, the direction of the vortex's rotation alternated between clockwise and counter-clockwise when viewed from the water's surface. Each beat of the tail generated and shed a new, alternately rotating leading-edge vortex which resulted in a rhythmic wake structure.

The vortex wake of Tunabot V2 was similar to the wake generated by swimming fish. The wake produced by a fish's caudal fin features counter-rotating, linked ring vortices, each with a central jet directed downstream [75], [167]. This fluid wake pattern is termed a 'reverse von Kármán street'. A von Kármán street is the characteristic wake pattern behind a stationary cylinder composed of counter-rotating vortices wherein the jet flow between vortices is oriented upstream [76], [168]. A reverse von Kármán street is similar except the rotation direction of the counter-rotating vortices is opposite, causing the interspersed jet flow to be oriented downstream. When oriented downstream, the jet exerts a reactionary thrust force upstream, propelling the fish

forward [169]. The rhythmic wake structure of Tunabot V2 was a reverse von Kármán street, indicating that the caudal fin's propulsive behavior was emblematic of fish swimming.

In summary, Tunabot V2 swam untethered with bubbles that visualized the caudal fin's vortices and wake. Both the leading-edge vortex and the reverse von Kármán street wake were similar to those of fish. In Section 3.4.10, we visualize the leading-edge vortex and thrust-producing wake structure again for Tunabot V4 steadily swimming. We also show the same for Tunabot V5 linearly accelerating from rest in addition to full-body flow visualizations [170]. The traditionally aerodynamic phenomena of leading-edge vortices and dynamic stall are applicable to undulatory swimming; we describe and derive the concept of lift-based, aquatic propulsion in Section 3.3.6.

2.3.5 *Free-Swimming Performance and Kinematic Results*

The following results describe the maximum performance of untethered Tunabot V2 steadily swimming in the stationary water tank. Tunabot V2 swam with a constant speed of 0.79 m/s (1.9 BL/s), corresponding to a Reynolds number of 3.4×10^5 and a tail-beat frequency of 7.5 Hz. This steady-state speed was 0.21 m/s faster than the results of untethered Tunabot V2 accelerating from rest (see Section 2.3.4). Also, the tail-beat frequency was 0.5 Hz lower than before (see Section 2.3.4). This was because the body was fully submerged unlike before when the caudal fin breached the water's surface (see Figure 2-14). The hydrodynamic load was less for the partially submerged caudal fin which resulted in its 0.5 Hz higher tail-beat frequency. The stride length was 0.26 BL, which we calculated from the speed and frequency. We present the swimming kinematics in Figure 2-15. The overall midlines (Figure 2-15(A)) appear wave-like along the length of the body, but abrupt displacement changes are apparent and caused by body

joint movements. These abrupt changes result in two local peaks of the midline curvature (Figure 2-15(B)) which correspond to the positions of Tunabot V2's two joints (see Table 2-1). From the midlines, the tail-beat amplitude was 0.055 m (0.14 BL), and the head amplitude was 0.016 m (0.04 BL). The Strouhal number was 0.53.

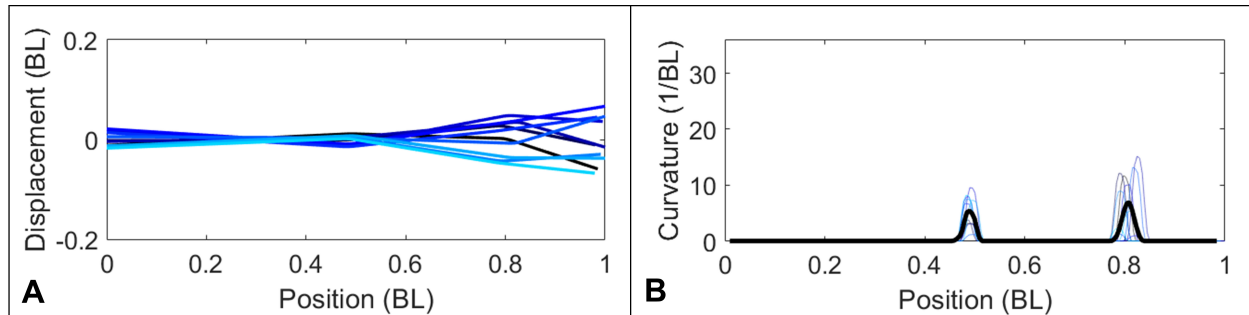


Figure 2-15: Swimming kinematics of free-swimming Tunabot V2. Kinematic data of untethered Tunabot V2 steadily swimming in the stationary water tank with a speed of 1.9 BL/s and a tail-beat frequency of 7.5 Hz. A dorsal-view camera positioned above the tank captured Tunabot V2 swimming past for 2.5 tail-beat periods. From this footage, we extracted (A) the midline kinematics of 10 midlines. (B) Calculated curvatures along the body corresponding to the 10 midlines with the mean indicated by the thicker, black line.

One area of improvement became apparent during testing. Tunabot V2 would eventually pitch up due to its imperfectly balanced ballast. This did not affect our results but would be unsuitable for experiments requiring greater control, namely autonomous swimming. Neutral buoyancy and neutral pitch would be difficult to achieve perfectly with ballast alone, so active pitch control would be necessary. Bio-inspired pectoral fins with a closed-loop controller for pitch and depth are readily achievable but not pursued in this study. After Tunabot V2, ballast was no longer a concern because Tunabots V3–V5 were tethered instead.

A second area of improvement became apparent when analyzing data. We were unable to extract 10 midlines equally spaced throughout a single tail-beat period because the video's frame rate was only 30 fps. The 10 midlines of Figure 2-15(A) correspond to all 10 video frames in which Tunabot V2 was swimming past the camera's field of view. This encompassed 2.5

tail-beat periods rather than a single one. Later, we were able to extract 10 equally spaced midlines from a single tail-beat period for Tunabot V4 by recording video at a much higher frame rate (1000 fps). The equally spaced midlines better visualized the wave-like kinematic pattern of Tunabot V4's two joints (see Section 3.4.2). We carried this improvement forward to Tunabot V5, which incorporated up to four joints (see Section 4.4.3).

2.3.6 *Free-Swimming Peduncle Stiffness Results*

Tunabot V2 demonstrated that peduncle stiffness impacted swimming performance. We tested two modular tail sections that featured either a moderately flexible or fully rigid peduncle joint (see Figure 2-12). The rigid peduncle appeared to increase swimming speed and slightly reduce the tail-beat frequency compared to the moderately flexible peduncle. Hydrodynamic forces on the caudal fin were greater for the rigid condition resulting in its lower tail-beat frequency. Greater forces on the caudal fin meant higher loads on the motor, so we expected the power consumption to be higher for the rigid peduncle. However, we were unable to measure power until we designed Tunabot V2's tethered configuration (see Section 2.4.2). The rigid peduncle's faster speed suggested that higher stiffness is desirable for high-frequency swimming but likely at the cost of higher power consumption. Thus, a tradeoff exists between efficiency and speed depending on peduncle stiffness and tail-beat frequency. These results supported the previous findings of Gregory Lewis [132], who inspired this experiment. As a side experiment, we also tested Tunabot V2 without installing either tail section. Without a caudal fin, Tunabot V2's mid-body and skin rapidly flapped but did not generate thrust in any direction. This suggested that the caudal fin was the primary contributor of propulsion. We confirm this finding again for Tunabot V4 in Section 3.4.9.

Our preliminary investigation of stiffness also demonstrated Tunabot V2's purpose as an experimental platform. We varied the peduncle stiffness (i.e., independent variable) by simply swapping out modular tail sections (see Figure 2-12). A more advanced Tunabot would benefit from the ability to vary peduncle stiffness without swapping or manually adjusting parts. From the free-swimming experiments of Tunabots V1 and V2, we found that symmetrical, bilateral stiffness of the peduncle joint was crucial for straight swimming. Unequal tension of the elastic bands on either side of their caudal fins would skew the swimming direction to the left or right. In other words, asymmetrical tension of a peduncle joint changes swimming direction. This concept could be applied to swimming systems. A swimming robot could intentionally turn by actively tuning the symmetry of its peduncle's bilateral stiffness. For example, increasing right-side stiffness or decreasing left-side stiffness would result in a left turn. A larger magnitude change of an individual side would result in a sharper turn, as would adjusting both sides simultaneously. In either case, the turning radius is a function of the stiffness differential between both sides. Furthermore, the overall stiffness of the peduncle joint could be varied by tuning the bilateral stiffness symmetrically (i.e., zero differential). For example, increasing the stiffness of both the left and right sides together would increase the peduncle's overall stiffness. Doing so was advantageous for Tunabot V2's high-speed swimming, as mentioned above. The ability to actively tune peduncle stiffness both symmetrically and asymmetrically would be extraordinarily beneficial for an autonomous Tunabot. However, such functionality would come at the cost of greater design complexity, which would entail more time, expense, and parts that might fail. If not prudently designed, the power requirements of such a stiffness mechanism might also negate or even detract from the gained performance benefit.

2.4 Tunabot V2: Tethered Experiment

2.4.1 Design and Fabrication

We reconfigured Tunabot V2 with a system of external tethers for testing in the University of Virginia’s flow tank. A flow tank is a channel that recirculates water, like an aquatic treadmill of sorts. Flow tanks were developed in the early 1960s to study the respiratory metabolism of swimming fish [171]–[173]. Figure 2-16 shows Tunabot V2 suspended in air from a display rig to picture the tethered design. Tethers were necessary because Tunabot V2 lacked the ability to self-regulate its swimming direction and orientation. This was not a concern during the free-swimming experiments of untethered Tunabot V2 (see Section 2.3) because its heading needed to remain straight only briefly while swimming the length (4.65 m) of the stationary water tank. For flow tank testing, however, Tunabot V2 needed to indefinitely sustain straight,

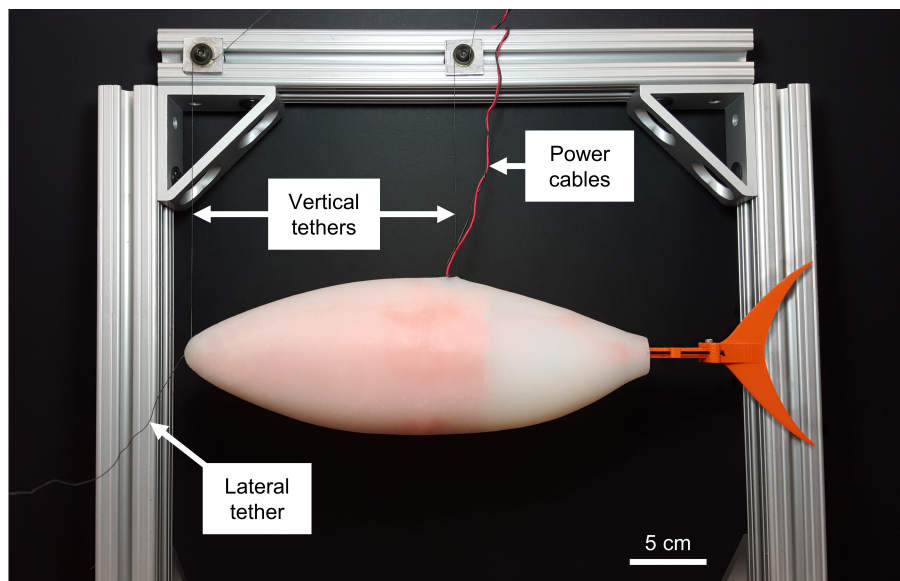


Figure 2-16: Tethered configuration of Tunabot V2. We added external tethers and power cables to the previously free-swimming Tunabot V2. This enabled us to test Tunabot V2’s swimming performance in the flow tank (see Figure 2-18). For illustrative purposes, Tunabot V2 is pictured here suspended in air. Three thin, flexible threads (two vertical and one lateral) tethered Tunabot V2 in the flow tank during testing. The two power cables connected to the external system that controlled swimming speed and measured power consumption (see Figure 2-17(A)). This tethered configuration enhanced Tunabot V2’s capabilities as a research platform by providing greater experimental control and performance quantification.

steady swimming in the center of the flow tank's test section. Tunabot V2 required tethers to achieve this.

In order to investigate sustained swimming, we transitioned away from the stationary tank and into the flow tank. The flow tank facility provided exceptional experimental control which greatly improved Tunabot V2's functionality as a research platform. The flow tank enabled us to continuously observe Tunabot V2 steadily swimming at high speeds, whereas this was possible for only a few seconds in the stationary tank. This expedited experiments and improved Tunabot V2's convenience as a research tool by eliminating the need to release, catch, and reset Tunabot V2 for every trial. Continuous swimming in the flow tank also enabled us to test the durability of Tunabot V2, especially in regard to its actuation mechanism and peduncle joint. High-cycle fatigue was a concern due to the intentionally high tail-beat frequencies of Tunabot V2, which were necessary to explore the high-performance space of fish. Anticipating this potential cause of mechanical failure, we designed the actuation mechanism and peduncle joint to be robust, beginning with Tunabot V1. Tunabot V2 swam tethered in the flow tank for extended periods of time without issue, proving its durability.

The tethered configuration of Tunabot V2 consisted of three tethers and two power cables (Figure 2-16). With the exception of streamwise drag, the tethers and power cables did not hinder streamwise, lateral, or yaw motion of any part of Tunabot V2. As such, the tethered configuration of Tunabot V2 was representative of its prior free-swimming design. For waterproofing, we sealed the two new holes where the tethers and power cables exited the body using a bead of epoxy.

The three tethers positioned Tunabot V2 in the flow tank's test section. These tethers were thin, flexible threads (Spectra Power Pro fishing line, Innovative Textiles Inc., Grand

Junction, CO, USA) with 0.25 mm thickness. Their stretch was negligible having a high Young's modulus of 108.3 GPa, which we measured using a tensile testing machine (MicroTester 5848, Instron Corp., Norwood, MA, USA). Two of the three threads vertically exited the body of Tunabot V2 near the snout and mid-body. These vertical threads suspended the negatively buoyant body in the flow tank. We adjusted the vertical threads' lengths such that Tunabot V2 was centered and level in the flow tank's test section. The vertical threads attached to an overhead rig positioned above the test section's center. The third thread exited the snout and loosely attached to the test section's side wall. This lateral snout tether prevented Tunabot V2 from straying from the test section's center but was only necessary at higher swimming speeds. Interestingly, Tunabot V2's symmetrical swimming motion appeared to self-correct its centered position, so we did not add the lateral tether until we began testing higher speeds.

We controlled Tunabot V2 through its two power cables. Both power cables vertically exited Tunabot V2's mid-body. We wired the power cables to the external system that controlled swimming speed and measured power consumption (see Section 2.4.2). The new abilities to vary speed and calculate energy efficiency vastly improved the overall effectiveness of Tunabot V2 as a research platform. We loosely attached the power cables to the same overhead rig as the vertical tethers to stay clear of the flapping tail. Unlike the vertical tethers, the power cables did not support any weight. We did not remove Tunabot V2's batteries or power switch even though the power cables supplanted them. Doing so was not only simpler, but also the batteries still functioned as ballast. Furthermore, this ensured that the mass of tethered Tunabot V2 remained the same as its prior free-swimming design, enabling us to directly compare their performance.

2.4.2 *Speed Control and Power Measurement*

Tunabot V2 introduced the abilities to vary swimming speed and measure electrical power consumption. These new capabilities improved the overall effectiveness of Tunabot V2 as an experimental platform by providing greater experimental control and more detailed results. Previously, the free-swimming Tunabot V2 was limited to a single speed, and the length of the stationary water tank restricted its swimming distance. By tethering Tunabot V2 in the flow tank and adding external control, Tunabot V2 could now swim indefinitely at adjustable speeds while measuring power consumption. The ability to measure power was extremely valuable because it enabled us to quantify energy efficiency. The cost of transport was the primary metric of energy efficiency that we utilized because it made direct comparisons possible between tunas and Tunabots (see Section 4.3.4). Two power cables (see Figure 2-16) connected Tunabot V2's motor to an external system of electronics and equipment (Figure 2-17(A)) that we stationed next to the flow tank during testing. We use this exact setup again including all equipment for Tunabot V4 (see Section 3.3.2) because of its success with Tunabot V2.

We varied the swimming speed of Tunabot V2 by changing the tail-beat frequency. We based this approach on others' observations that the speed of fishes is mainly determined by tail-beat frequency [77], [174]. Fishes also vary tail-beat amplitude at lower speeds, but tail-beat amplitude is generally constant across the higher speed range [174], [175]. With this in mind, the tail-beat amplitude of Tunabot V2 (and all other generations) was constant by design. We changed the tail-beat frequency using a pulse-width modulation (PWM) controller (model CCM6DS-K, Unique Goods International Supply Store, Guangzhou, CHN) that we wired to Tunabot V2's motor. The PWM controller generated a voltage signal that cycled between 'on' and 'off' states, creating a square waveform (blue in Figure 2-17(B)). The percentage of time

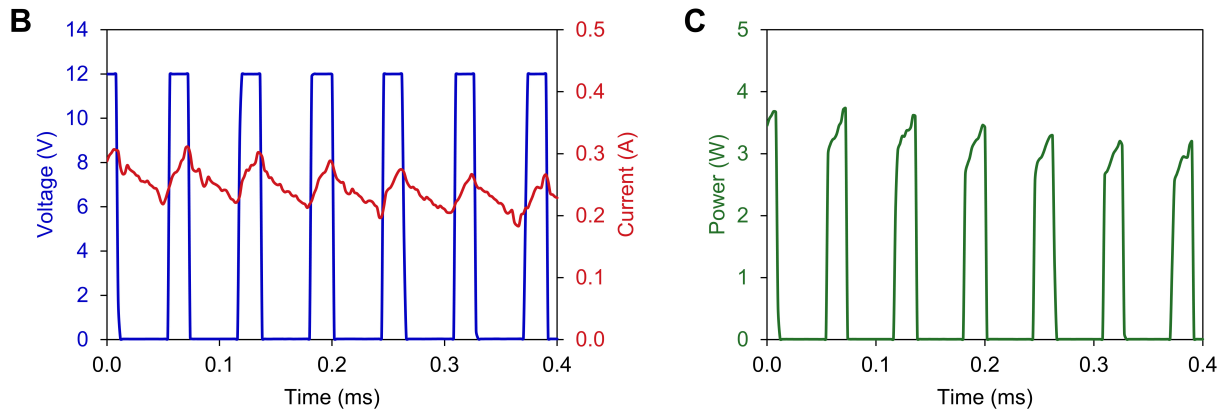
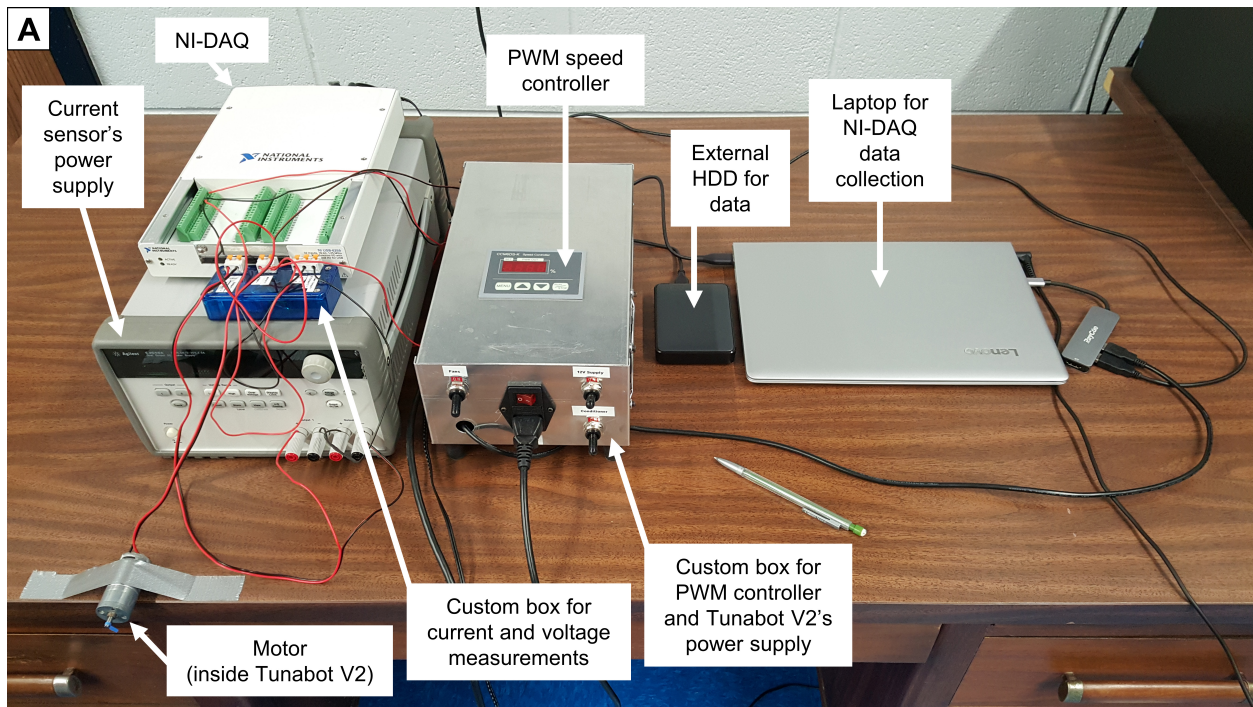


Figure 2-17: Speed control and power measurement system of Tunabot V2. (A) Complete system that controlled the swimming speed of Tunabot V2 and measured electrical power consumption. We used the same system again for Tunabots V3 and V4. Everything shown above was positioned adjacent to the flow tank during experiments. The two power cables of Tunabot V2 (see Figure 2-16) connected its internal motor (included above) to this system. We varied Tunabot V2's tail-beat frequency and, therefore, speed in real time by pressing the 'up' and 'down' arrows on the pulse-width modulation (PWM) controller. We recorded the voltage and current signals using custom electronics (blue box) and the National Instruments data acquisition device (NI-DAQ). The separate power supply was dedicated to a current transducer inside the blue box. LabVIEW software on the laptop controlled the NI-DAQ, and the hard disk drive (HDD) saved all data. The custom-built, aluminum box contained additional power supplies, featured cooling fans, and also held electronics for Tunabot V4's thrust and drag experiments in Chapter 3. (B) Actual data that we collected for illustrative purposes using the pictured setup. The PWM controller generated a square voltage signal with a duty cycle of 30% for this example. The voltage (blue) and current (red) signals are time-synchronized. (C) The instantaneous power curve (green) is the product of the time-synchronized voltage and current signals. We averaged the instantaneous power for a single value of mean power.

spent ‘on’ to ‘off’ is termed the ‘duty cycle’. For a duty cycle of 100%, the voltage signal is continuously ‘on’, which means the full voltage is supplied to the motor. We changed the tail-beat frequency by modulating the duty cycle of the PWM signal sent to the motor. We did so in real time by pushing the ‘up’ and ‘down’ arrows on the controller’s panel, which had a digital display showing the duty cycle percentage. During the flow tank testing of Tunabot V2, we found that the tail-beat frequency was linearly related to the duty cycle (see Section 2.4.4), confirming the effectiveness of varying the tail-beat frequency via the duty cycle as a highly predictable, controlled method.

We calculated power by multiplying the voltage and current waveforms at each time instant. We found that doing so was more accurate than time-averaging the two waveforms individually before multiplying them together. We recorded the voltage and current signals at a sampling rate of 500 kHz using LabVIEW software and the National Instruments data acquisition device (NI-DAQ) shown in Figure 2-17(A). This rate sufficiently resolved the 15.09 kHz frequency of the PWM voltage signal and therefore the associated current signal as well. The square PWM waveform ranged from 0 to 12.22 V due to the PWM controller’s 12.22 V power supply. We measured the frequency and range of the PWM signal using an oscilloscope (model TDS3014B, Tektronix Inc., Beaverton, OR, USA). The NI-DAQ (model USB-6259, National Instruments Corp., Austin, TX, USA) was capable of receiving analog inputs up to 10 V, so a voltage divider composed of two resistors ($5.1 \text{ k}\Omega \pm 5\%$) was necessary to halve the 12.22 V, PWM signal for data collection. We built an electronics enclosure (blue box in Figure 2-17(A)) to house the voltage divider and current transducer.

A current transducer (model LAH 25-NP, LEM Electronics Co. Ltd., Meyrin, CHE) converted the current signal to a proportional voltage signal, which the NI-DAQ then recorded.

We wired this transducer between the positive terminals of the motor and PWM controller. The specific transducer that we selected was a closed-loop, single-channel Hall effect transducer with a frequency bandwidth of 200 kHz. The transducer's 8 A wiring configuration encompassed the maximum current drawn by the motor and provided excellent sensitivity with a turns ratio of 3:1000. We dedicated a separate, high-quality power supply (model E3648A, Agilent Technologies Inc., Santa Clara, CA, USA) outputting two 12 V channels to the transducer for the best current measurements possible (Figure 2-17(A)).

We simultaneously recorded the voltage and current signals for 5 seconds. Using MATLAB, we then filtered and corrected the raw voltage and current data before calculating the 5-second power average. For the voltage data, we applied a median filter to isolate the square PWM waveform. Next, we rescaled the voltage data to range from 0 to 12.22 V to correct for the voltage divider. For the current data, we applied a cubic-weighted Savitzky-Golay filter with the smallest frame length possible (i.e., five points) to eliminate noise with minimal smoothing of meaningful data. After filtering the voltage and current, we multiplied the two waveforms together to calculate the power with respect to time. Lastly, we averaged this power over the entire 5-second collection window to arrive at the mean power. The 5-second collection window ensured that the power was averaged over 27 to 40 complete tail-beat periods of Tunabot V2 depending on the tail-beat frequency.

We time-synchronized the voltage and current signals during recording. Synchronization was essential for multiplying their waveforms together at each time point to calculate power. To illustrate this, we plot a sample of actual recorded data in Figure 2-17(B). For visualization purposes, we set the duty cycle of the PWM voltage signal to 30% and plot only 0.4 milliseconds of data from the 5-second measurement. When viewing Figure 2-17(B), the square shape of the

voltage (blue) is apparent along with the time-alignment of the current (red). Unlike the square voltage waveform, the current does not alternate between ‘on’ and ‘off’ states; rather, the current is smoother and always nonzero (i.e., continuous). The rising and falling shape of the current waveform is due to the armature inductance of the DC motor [176]. The instantaneous power curve (green in Figure 2-17(C)) is the product of Figure 2-17(B)’s voltage and current. For actual experiments, we averaged all 5 seconds of similar power curves to calculate single values of mean power.

2.4.3 Methodology for Tethered Testing

We tested the swimming performance of Tunabot V2 tethered in a flow tank in September 2017. This flow tank (model 1520, Rolling Hills Research Corp., El Segundo, CA, USA) was part of the University of Virginia’s Bio-Inspired Engineering Research Laboratory and was used for previous research [132], [135], [177]. The flow tank’s test section had wetted dimensions of $152.4 \times 38.2 \times 45.6$ cm (length \times width \times height). Flow speeds ranged from 0 to 0.94 m/s and were measured using the tank’s built-in flowmeter. The maximum flow speed corresponded to 900 rpm of the tank’s motor.

Three thin, flexible threads with negligible stretch tethered Tunabot V2 in the flow tank’s test section (Figure 2-18). Two of the three threads vertically exited the body of Tunabot V2 near the snout and mid-body. Together, both threads suspended the negatively buoyant Tunabot V2 from a rig overhead while ensuring that the body was centered and level in the test section. The projected area of Tunabot V2 (5830 mm^2) occupied 3.0% of the test section’s cross-sectional area, meaning wall and blockage effects were negligible. The third thread loosely connected the snout laterally to the test section’s side wall in order to prevent extreme lateral deviations from

the test section's center. This lateral thread attached near the bottom of an aluminum bar with 2 mm thickness clamped vertically to the test section wall (Figure 2-18). The two power cables of Tunabot V2 loosely attached to the overhead rig and did not support weight. With the exception of streamwise drag, this tethered arrangement did not hinder streamwise, lateral, or yaw motion of any part of Tunabot V2 and was, therefore, representative of free swimming.

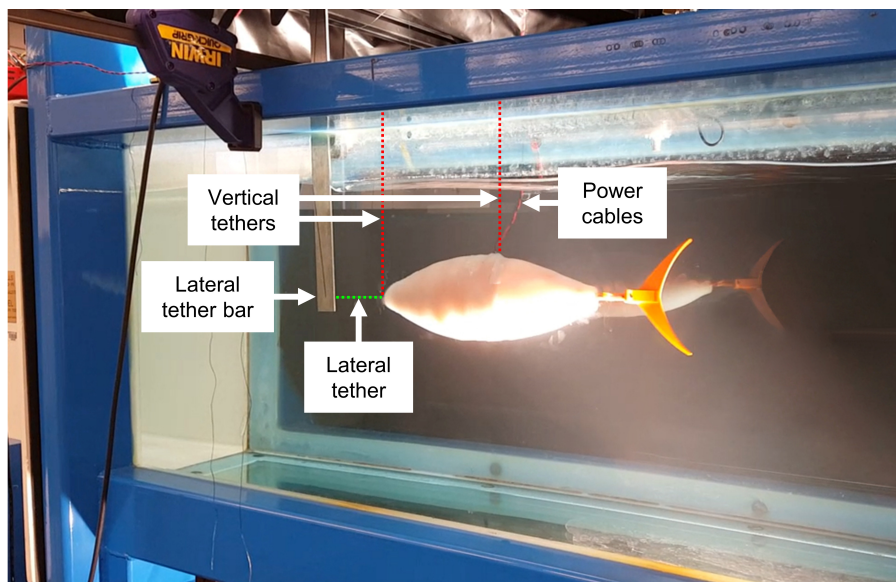


Figure 2-18: Experimental setup for Tunabot V2's tethered performance testing. We quantified Tunabot V2's self-propelled swimming performance in the flow tank at the University of Virginia. Two vertical tethers (red, dashed lines) suspended Tunabot V2 in the flow tank's test section from an overhead rig. The two power cables loosely attached to the same overhead rig and plugged into an external system that controlled swimming speed and measured power consumption (see Figure 2-17(A)). The lateral tether (green, dashed line) loosely connected Tunabot V2's snout to the thin aluminum bar clamped vertically to the test section's side wall.

We tested five tail-beat frequencies of Tunabot V2. We varied the tail-beat frequency by increasing the duty cycle of the PWM voltage signal powering the motor (see Section 2.4.2) from 70% to 100%. We only tested higher duty cycles in order to confirm the robustness of the flow tank setup and of Tunabot V2 continuously swimming at its fastest speeds. We later tested the entire performance range by sweeping through the full range of tail-beat frequencies for Tunabots V4 and V5 (e.g., see Section 3.3.1).

At each tail-beat frequency of Tunabot V2, we measured the ‘self-propelled’ swimming speed [178]. A self-propelled vehicle generates its own movement. For example, a ship under sail is self-propelled, whereas a ship being towed is not. The Tunabots were self-propelled systems. The self-propelled speed of Tunabot V2 swimming in the stationary water tank was simply the traveled distance divided by the elapsed time. In the flow tank, however, the self-propelled speed was the speed of the oncoming flow generated by the flow tank that matched Tunabot V2’s upstream swimming speed. Under these conditions, Tunabot V2 appeared to swim in place within the flow tank’s test section from a laboratory reference frame.

To measure self-propelled speed, we marked the position of Tunabot V2’s snout on both walls of the transparent test section under conditions of zero flow. Marking both walls was necessary to prevent measurement inconsistencies due to parallax; the near mark, snout, and far mark all intersected a single line of sight when viewing the lateral side of Tunabot V2. We later improved this aspect of the experimental setup by using a fixed video camera for Tunabots V4 and V5. Both Tunabot V2 and the flow tank ran continuously throughout the experiment, even as we incrementally increased the tail-beat frequency. At each tested tail-beat frequency, we adjusted the flow speed until Tunabot V2’s snout settled at the zero position, indicating that the net thrust and drag of the body were equal. At this point, we monitored the body’s position for at least 10 seconds to ensure stability. Then we recorded the flow speed as Tunabot V2’s self-propelled swimming speed and measured the electrical power consumption (see Section 2.4.2). Finally, we measured the tail-beat frequency using a digital stroboscope (model DS-303) before moving on to the next tail-beat frequency.

We further quantified Tunabot V2’s performance using a variety of metrics. We calculated the Reynolds number, stride length, and Strouhal number as before using Equations

(22), (23), and (24), respectively. We quantified energy efficiency in terms of the cost of transport (COT), which describes the energy required to move a unit mass over a unit distance.

We calculated COT for Tunabot V2 using the following expression:

$$COT = \frac{P}{U \cdot m_u} \quad (26)$$

where P is the total electrical power drawn by the motor, U is self-propelled swimming speed, and m_u is unsubmerged mass (0.900 kg). A secondary metric of energy efficiency is the work per meter (WPM), which describes the work required to move a unit distance. Unlike COT, this quantity is not mass-specific and thus does not account for mass differences (see Section 4.3.4).

We calculated WPM as follows:

$$WPM = \frac{P}{U} \quad (27)$$

where P is the total electrical power drawn by the motor and U is self-propelled swimming speed.

The COT is an extremely valuable performance metric because it enables the energy efficiencies of fishes and Tunabots to be directly compared while accounting for mass differences. COT is calculable for fishes since their active metabolic rate is analogous to the total electrical power consumption of the Tunabots (see Section 4.3.4). The sophistication of data analysis grew with each passing generation of Tunabot, so we do not make rigorous comparisons between tunas and Tunabots until Chapter 4 (e.g., see Figure 4-13).

2.4.4 Tethered Performance Results

Tunabot V2 swam tethered in the flow tank with a maximum tail-beat frequency of 8.0 Hz and a corresponding speed of 1.6 BL/s, demonstrating that accessing the high-performance

space of fish was possible in a flow tank setup. The tail-beat frequency ranged from 5.5 to 8.0 Hz. This corresponded to swimming speeds of 0.47–0.64 m/s or 1.2–1.6 BL/s when normalized by body length. At these speeds, the Reynolds number was $2.0\text{--}2.7\times 10^5$. Tail-beat frequency was linearly related to the duty cycle of the PWM voltage input with a coefficient of determination (R^2) equaling 0.999, confirming the effectiveness of varying tail-beat frequency via duty cycle. This high correlation indicated that specific tail-beat frequencies could be targeted by entering predicted duty cycle values into the speed controller.

For the maximum tail-beat frequency of 8.0 Hz, the duty cycle of the PWM voltage input was 100%. This corresponded to an equivalent input to the motor of 12.22 V, which was the measured output of the PWM controller's power supply. The tethered frequency of 8.0 Hz with 12.22 V was expected when recalling the free-swimming frequency of 7.5 Hz with 11.1 V (see Section 2.3.5) because the tail-beat frequency increased with the input voltage.

The swimming speed of tethered Tunabot V2 was 1.5 BL/s with a tail-beat frequency of 7.5 Hz. However, free-swimming Tunabot V2 swam 0.4 BL/s faster with the same frequency (see Section 2.3.5). Drag incurred by the tethers and power cables caused this loss in speed. We later quantified these drag forces for Tunabots V4 and V5 (see Sections 3.4.1 and 4.4.2, respectively) and found that tethered drag did, indeed, significantly hinder performance.

Tunabot V2's swimming speed was a linear function of tail-beat frequency ($R^2 = 0.998$). Such a linear trend (Figure 2-19(A)) is a classic feature of fish swimming [179]. Bainbridge found that speed and frequency were linearly related for a variety of fish species in his seminal paper published in 1958 [77]. He modeled this linear relationship through the following expression, which is now called 'Bainbridge's Equation':

$$U = \frac{1}{4}\{BL(3f - 4)\} \quad (28)$$

where U is the speed in meters per second, BL is the body length of the specimen in meters, and f is the frequency in beats per second. Bainbridge's Equation was remarkable because it described multiple species with varying body sizes through only a single expression. Specifically, Bainbridge observed three species: common dace (*Leuciscus leuciscus*), goldfish (*Carassius auratus*), and rainbow trout (*Salmo irideus*). Bainbridge's Equation applied to these three species for frequencies greater than 5 Hz. Below 5 Hz, Bainbridge noted that a linear trend was no longer appropriate because the tail-beat amplitude varied with the tail-beat frequency. As a result, his equation did not necessarily pass through the origin. Slow swimming speeds pose challenging stability issues for fish [180], so low-speed performance is often unclear [179]. For Tunabot V2 (Figure 2-19(A)), the linear fit passed near the origin if extrapolated because the tail-beat amplitude was constant by design, and we only modulated the tail-beat frequency.

The average stride length of Tunabot V2 was 0.20 ± 0.01 BL ($n = 3$). Since stride length is the ratio of swimming speed to tail-beat frequency (see Equation (23)), we calculated the stride length from each data point in Figure 2-19(A). The slope of the linear fit through these data points similarly equaled 0.20 BL but differed from the average stride length. The reason for this was related to the nature of trendlines as opposed to the collected data itself. The least-squares method of finding trendlines minimizes the sum of squared residuals, which are the errors between the linear regression model (i.e., linear fit) and data points. This method is inherently different from calculating the overall mean of a data set. As such, the slope of the linear fit of Figure 2-19(A) is a predictive stride length that does not necessarily equal the average stride length.

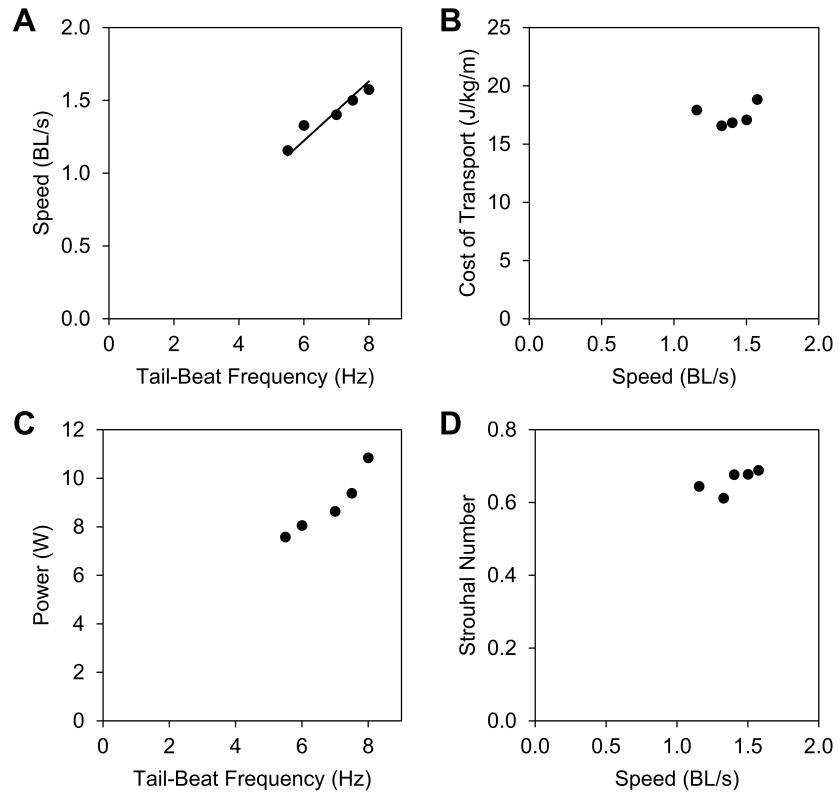


Figure 2-19: Performance results of Tunabot V2. We quantified the performance of tethered Tunabot V2 steadily swimming in the flow tank using metrics of fish performance. We normalized speed by body length (BL). **(A)** Swimming speed increased linearly ($R^2 = 0.998$) with the tail-beat frequency. **(B)** Cost of transport (COT), which is a metric of energy efficiency, varied with the swimming speed. **(C)** Total electrical power consumption of the motor increased nonlinearly with the tail-beat frequency and was analogous to the active metabolic rate of fish (see Section 4.3.4). **(D)** Strouhal number related the frequency of vortex shedding, amplitude of oscillation, and flow velocity (i.e., the tail-beat frequency, tail-beat amplitude, and swimming speed, respectively) and depended on the swimming speed.

The COT of Tunabot V2 was 16.6–18.8 J/kg/m (Figure 2-19(B)). The WPM, which is the COT unscaled by mass (0.900 kg for Tunabot V2), was 14.9–16.9 J/m. The 18.8 J/kg/m COT and 16.9 J/m WPM of Tunabot V2 corresponded to its maximum swimming speed of 1.6 BL/s; we compare this data point against Tunabots V4 and V5 in Chapter 4 (see Figure 4-13(B)–(C)) to encapsulate the significant progress made by future designs in terms of both speed and energy efficiency. The electrical power consumption varied between 7.6 and 10.8 W and increased nonlinearly with tail-beat frequency (Figure 2-19(C)).

The Strouhal number ranged from 0.61 to 0.69 (Figure 2-19(D)). We used the 0.14 BL tail-beat amplitude from free-swimming Tunabot V2's midline kinematics (see Section 2.3.5) to calculate the Strouhal number for tethered Tunabot V2. Doing so was necessary because collecting kinematic data was not a part of the tethered experiment's testing protocol, which we changed for Tunabots V4 and V5 (see Sections 3.3.3 and 4.3.3, respectively). Using the free-swimming tail-beat amplitude to calculate the tethered Strouhal number was reasonable in two ways. First, Tunabot V2's tail-beat amplitude was inherently constant due to the design of the flapping mechanism (see Section 2.2.1). Second, the flow tank setup was representative of free swimming (see Section 2.4.1). Therefore, we expected the tethered and untethered tail-beat amplitudes to be equal.

The tethered setup did not hinder the natural yawing motion of Tunabot V2. In air, Tunabot V2 yawed freely while flapping when we loosely held the body about its center of mass. The tethered setup in the flow tank similarly enabled Tunabot V2's natural yawing motion. Conversely, firmly holding Tunabot V2 by its head in air prevented the body's natural rotation about its center of mass as the tail flapped. This underscored the importance of selecting tethered setups that do not constrain natural body kinematics when studying bio-inspired systems; otherwise, the results would not be representative of untethered conditions. The tethered setup of Tunabot V2 was representative of free swimming, and we used this foundational setup again for Tunabots V3, V4, and V5.

We also observed that eliminating Tunabot V2's yawing motion in air increased the electrical power consumption. We attributed the stationary head's increased power consumption to the larger tail-beat amplitude in the lab reference frame. Tunabot V2's tail-beat amplitude was constant by design, so irrespective of yawing motion, the tail traveled the same distance back and

forth relative to the head. However, in the lab reference frame, the tail swept a greater lateral distance when we prevented the body from yawing. The load on the motor was audibly louder as the tail flapped when holding Tunabot V2 by its head. By extension, this provided insight into how the natural yawing motion of fish kinematics may reduce energy consumption.

2.5 Tunabot V3

2.5.1 *Design and Fabrication*

We designed Tunabot V3 (Figure 2-20(A)) to test the feasibility of extremely high tail-beat frequencies. Up until this point, the tethered configuration of Tunabot V2 achieved the highest tail-beat frequency of 8.0 Hz. To surpass this performance, Tunabot V3's design centered around a faster motor. The DC motor we selected (Actobotics model 638286) had a rotational speed of 1621 rpm (27.0 Hz unloaded). For comparison, the motor of Tunabots V1 and V2 (Actobotics model 638260) had a rotational speed of 730 rpm (12.2 Hz unloaded). To generate the necessary power for such speeds, the new motor's dimensions (32 mm diameter) and mass (0.30 kg) were considerably larger than those of the previous motor (22 mm diameter, 0.08 kg). Consequently, most of Tunabot V3's unique design aspects served to accommodate the new motor's greater speed, size, and mass.

We stiffened Tunabot V3's peduncle joint to improve swimming performance at the higher tail-beat frequencies generated by the larger motor. We expected the speed of Tunabot V3 to increase with the tail-beat frequency as with Tunabot V2 (see Figure 2-19(A)), and a stiffer peduncle joint was found to be desirable for energy efficiency at high swimming speeds [132]. Consequently, we replaced the bilateral elastics of Tunabots V1 and V2 with stiffer springs for Tunabot V3 (Figure 2-21(E)). The stiffened peduncle joint of Tunabot V3 modeled the

longitudinal tendons of tuna as before (see Section 2.2.2). We predicted that the performance benefit of the springs would outweigh the drag penalty of their protruding profile. The design of Tunabot V3's passively rotating peduncle joint stiffened by two springs closely resembled previous work [132].

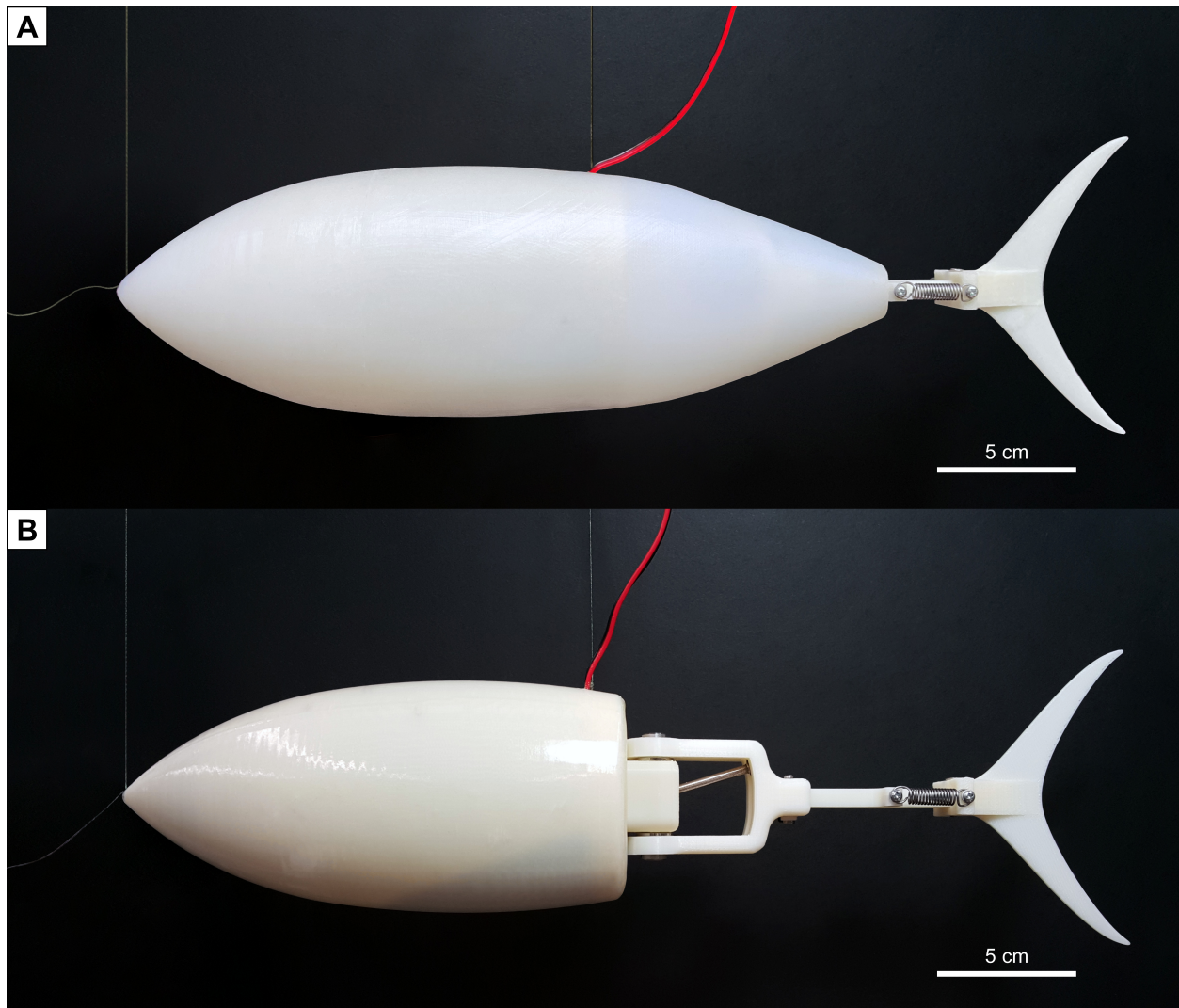


Figure 2-20: Design of Tunabot V3. (A) Tunabot V3 fully assembled and (B) with its skin removed. Tunabot V3 is shown suspended in air for illustrative purposes. The three thin threads (one lateral from the snout and two vertical) tethered Tunabot V3 in the flow tank, as was the case for Tunabot V2 (see Figure 2-16). The two power cables (red and black) connected to an external system that controlled swimming speed and measured power consumption (see Figure 2-17(A)).

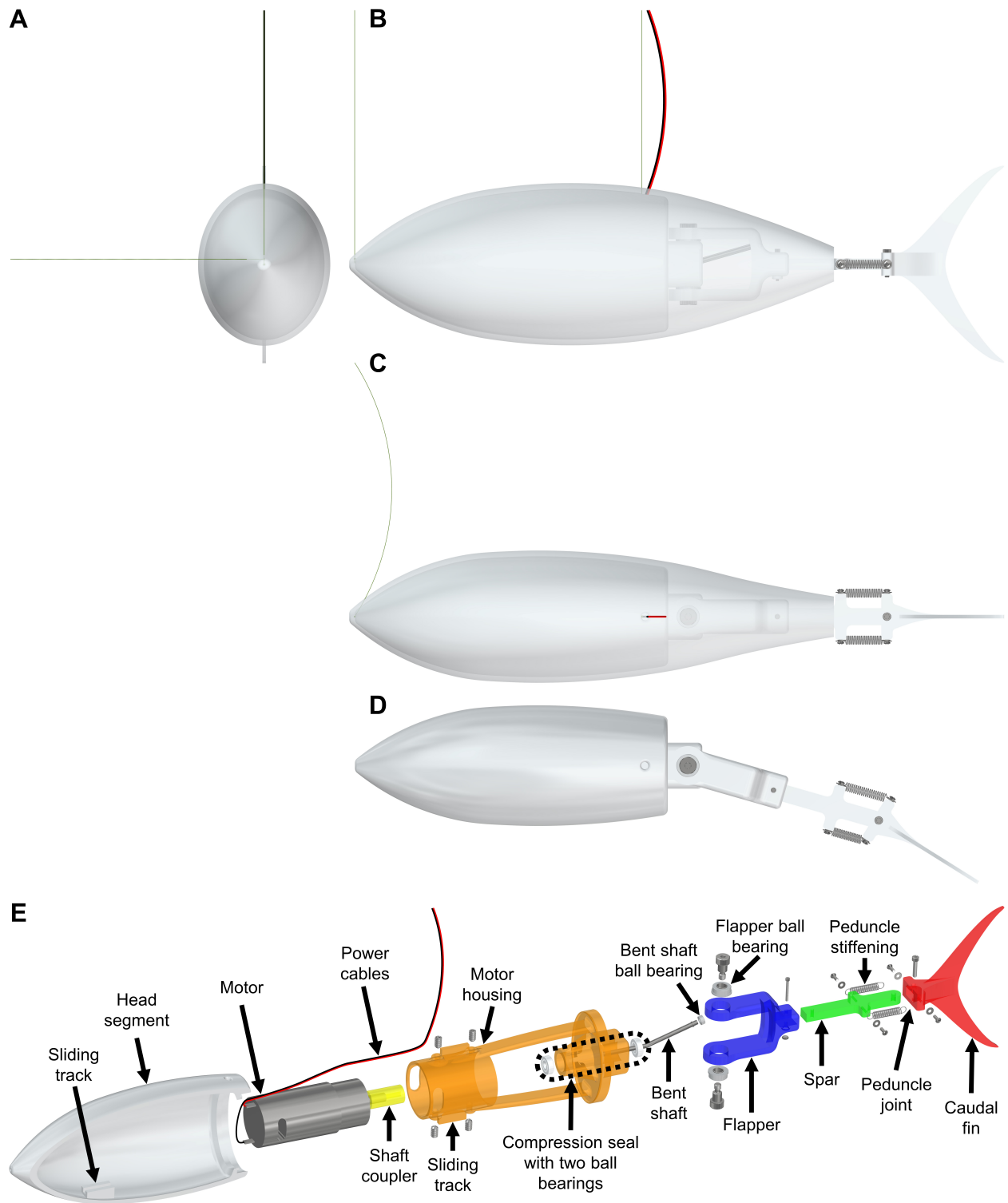


Figure 2-21: CAD model of Tunabot V3. (A) Anterior, (B) lateral, and (C) dorsal views of Tunabot V3's CAD model. The submerged lengths of the three tethers and two power cables are shown to scale for Tunabot V3 centered in the flow tank's test section. (D) Dorsal view of the body with maximum tail deflection. The prescribed rotation angles of the mid-body and peduncle joints are provided in Table 2-1. The skin is removed for visualization purposes. (E) Exploded view with the names of components indicated. Color shading is provided to differentiate components and emphasize their design evolution from Tunabot V1 through Tunabot V5 (see Figure 1-3). The bent shaft (gray), flapper (blue), and spar (green) compose the actuation mechanism and are synonymous with the color-coded components of Figure 2-1.

The morphology of Tunabot V3's body differed from that of Tunabot V2. The head segment of Tunabot V3 was less narrow to fit the larger motor. Tunabot V3 measured 36.1 cm in length, 7.3 cm in width, and 8.9 cm in height. Previously, we used reference images of tuna to directly create the biological proportions of Tunabot V2's body (see Section 2.3.1). For Tunabot V3, however, deviation from these images was necessary to create sufficient internal volume for the larger motor. Consequently, Tunabot V3's body shape was slightly less grounded in biology but still reasonable given the diversity of shapes present within any one particular tuna species. The body width and height of similarly sized yellowfin tuna ($n = 6$) were 0.17 BL and 0.28 BL, respectively [134], [181]. Similarly, Tunabot V3's respective width and height were 0.20 BL and 0.25 BL, but their aspect ratio demonstrated how the large, circular motor caused Tunabot V3's body to be rounder than tuna. Additionally, Tunabot V3's position of maximum cross-sectional thickness was located 0.34 BL from the snout, whereas this position was located more posteriorly at 0.41 BL for yellowfin tuna [134], [181]. The less natural thickness distribution of Tunabot V3's body was necessary to accommodate its larger motor.

We made Tunabot V3's silicone skin thinner than Tunabot V2's skin. Doing so slimmed down the body's overall dimensions after expanding them for the larger motor. The thickness of Tunabot V3's skin around the head was 3 mm, which was 2 mm thinner than Tunabot V2's skin. Creating such a thin skin with uniform thickness was challenging due to its large surface area. We refined the previous mold design of Tunabot V2's skin (see Figure 2-11(A)) to create a new mold design for Tunabot V3's thinner skin (Figure 2-22(A)–(B)).

We strengthened the actuation mechanism in anticipation of the new motor's greater power output. We placed larger diameter ball bearings between the flapper and motor housing, which improved stability of the mid-body joint by mitigating rotation about Tunabot V3's

anteroposterior axis. We also strengthened both flapper arms to withstand the forces of higher tail-beat frequencies. The ring of material that surrounded the dorsal flapper arm's bearing failed during preliminary testing, so we thickened the circumference of both flapper arms' rings.

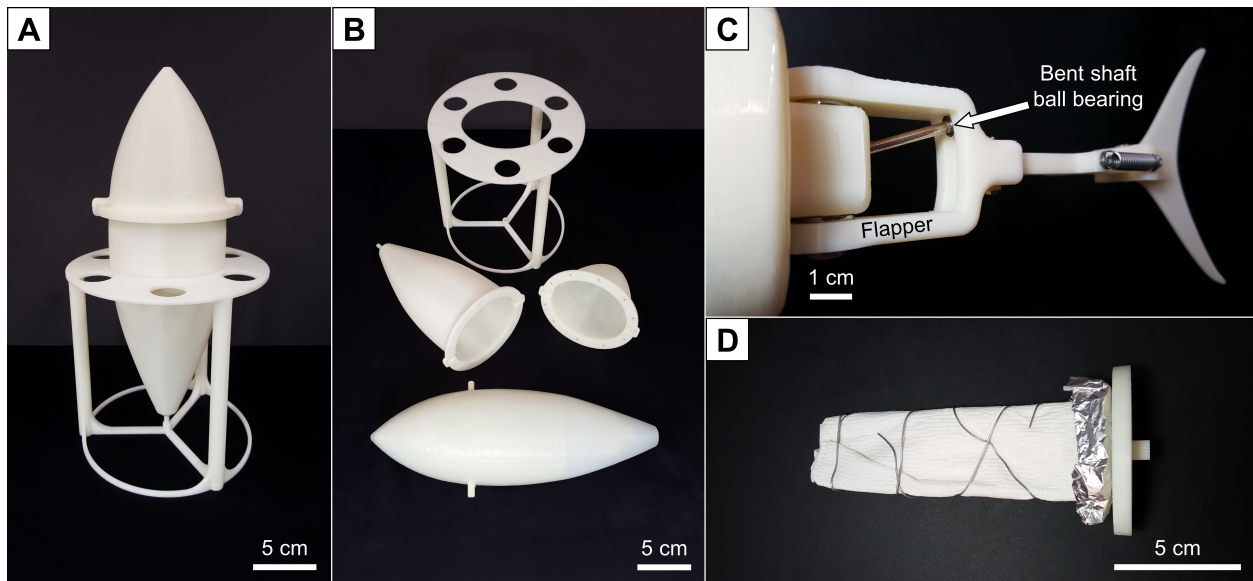


Figure 2-22: Design and fabrication of Tunabot V3. (A) We fabricated the skin of Tunabot V3 by injecting liquid silicone into the 3D-printed mold shown here. We designed the mold specifically for Tunabot V3's unique body shape. The mold's vertical stand aided us during the molding process and improved the skin's quality. Tunabot V3's mold improved upon the previous mold for Tunabot V2 (see Figure 2-11(A)). (B) Tunabot V3's mold consisted of an inner piece enclosed by two exterior halves that we sealed together. The cured skin is shown here with the exterior halves opened and before we removed the inner piece. (C) We added a ball bearing onto the tip of the actuation mechanism's bent shaft that reduced friction inside the flapper's slot. (D) We used acetone vapors to chemically smooth and thus waterproof the interior surface of Tunabot V3's plastic head segment. To do so, we soaked the absorbent, popsicle-like device shown here in acetone before inserting it into the head for 10 minutes. This device ensured that only acetone vapors contacted the head's interior surface and not liquid acetone, which would have rapidly melted the plastic nonuniformly.

We also reduced the actuation mechanism's friction to generate the highest tail-beat frequency possible with the faster motor. At the posterior tip of the bent shaft, we added a deep-groove ball bearing (6.35 mm diameter) to reduce friction as the shaft slid within the flapper's slot (Figure 2-22(C)). The orientation of this bearing caused it to roll against the slot's inner surface as the bent shaft rotated. In other words, this bearing added a degree of radial rotation

relative to the bent shaft's tip. However, there was a relatively insignificant component of motion (k from Section 2.2.1) that did not coincide with the bearing's rotational axis and thus did not benefit from the bearing's presence. A linear ball bearing coupled with the existing deep-groove ball bearing would have added the absent second degree of motion axially along the length of the bent shaft's tip, but this was unfeasible due to size constraints. To position the deep-groove ball bearing, we added a circumferential ledge to the bent shaft. This custom shaft was 3D printed in stainless steel using direct metal laser sintering (DMLS) technology by Xometry Inc. (Gaithersburg, MD, USA). In the interest of compactness, Tunabot V3 would be the only Tunabot whose bent shaft featured a posterior bearing and was 3D-printed rather than handmade.

We managed to decrease the overall size of Tunabot V3 by utilizing different waterproofing methods than before, which we fully describe in Section 2.5.2. Despite its larger motor, the body length of Tunabot V3 (36.1 cm) was smaller than that of Tunabots V1 and V2 by 4.5 cm. We waterproofed Tunabot V3's head and motor housing using acetone vapor, an applied coating, and epoxy (see Section 2.5.2) instead of the previous silicone-injection method (see Section 2.2.3). One aspect of Tunabot V3's waterproofing involved inserting a popsicle-like device soaked in acetone (Figure 2-22(D)) into the head for 10 minutes to chemically smooth the head's interior surface. Our desire to reduce unnecessary bulk motivated this space-efficient approach. The silicone-injection method required the outer wall thickness of the head and motor housing to be at least 6 mm to create the necessary internal volume for the liquid silicone. Forgoing this method, the wall thickness of Tunabot V3 was 3 mm and could likely have been thinner if optimized. As before, the ballast of Tunabot V3 was a mixture of liquid silicone and metallic powder (see Section 2.2.2). This time, however, we injected the mixture into the head cavity. Injection was necessary because we permanently sealed the head shut using epoxy in leu

of an O-ring for waterproofing (see Section 2.5.2). We injected the ballast inside the head's posterior to achieve neutral body pitch by counterbalancing the mass of the anteriorly positioned motor.

Three additional aspects of Tunabot V3's design were notable. First, we decreased the overall size of Tunabot V3 by improving the actuation mechanism's compactness, especially the flapper and bent shaft. This complemented the different waterproofing methods that also served to reduce Tunabot V3's size. Second, the two ball bearings of Tunabot V3's compression seal (Figure 2-21(E)) were made of glass instead of stainless steel to prevent corrosion more effectively. Previously, the stainless-steel bearings of Tunabot V2 rusted after months of use and subsequently impeded the bent shaft's rotation. Third, we ensured that the new DC motor's nominal voltage was 12 V so that we could reuse the speed control and power measurement system of tethered Tunabot V2 (see Figure 2-17). These three points and the various modifications related to the larger motor distinguished Tunabot V3's design from the tethered configuration of Tunabot V2.

2.5.2 *Waterproofing Methods*

We explored new methods for waterproofing Tunabot V3's head segment and motor housing (see Figure 2-21(E)) to reduce the body's size. We were unsatisfied with the bulkiness of our previous waterproofing methods despite carefully refining them to save space. The silicone-injection method that we used for waterproofing Tunabots V1 and V2 (see Sections 2.2.3 and 2.3.2, respectively) added size to the head and motor housing because of the requisite 6 mm wall thickness. Also, the O-ring design of Tunabots V1 and V2 required additional space for the tongue-and-groove joint that attached the head and motor housing together. Instead, we

waterproofed Tunabot V3's head and motor housing using three new approaches to reduce the body's size: acetone vapor, an applied coating, and epoxy.

We initially attempted to only use acetone vapor to waterproof Tunabot V3's head and motor housing. Both parts were porous despite being 3D printed in ABS plastic with solid infill density (see Section 2.2.3), and acetone vapor seals such pores. Acetone smoothing is a type of chemical post-processing for parts 3D printed in ABS. Acetone is a dissolvent of ABS filament, so ABS melts in the presence of acetone. We applied acetone vapor rather than liquid to slow this reaction. Doing so provided greater control and enhanced the uniformity of the final, smoothed surface. We suspended the head and motor housing for 20 minutes inside a sealed bucket with acetone-soaked paper towels covering its bottom. Afterwards, the exteriors of the head and motor housing were less porous but still not watertight. Furthermore, the head's interior was largely unaffected despite its cavity facing down towards the acetone-soaked towels. Additional time in the bucket only resulted in the parts softening to the point of deformation. Circulating the acetone vapor within the bucket using fans would have yielded better results, but the innermost surfaces of the head would still have likely remained porous after other areas had already deformed. Acetone vapor alone was insufficient for waterproofing the head and motor housing.

We reprinted the head and motor housing and waterproofed their exterior surfaces by brushing on a liquid coating. This coating (model XTC-3D, Smooth-On Inc., Macungie, PA, USA) filled striations before hardening with a high-gloss finish (see Figure 2-20(B)). Unlike acetone, XTC-3D did not melt plastic. A single coat of XTC-3D sealed nearly all of the head's pores. To seal the remaining leaks, we chemically smoothed the head's interior using acetone vapor. We accomplished this by soaking a popsicle-like device that consisted of paper towels

wrapped around a metal wire frame (see Figure 2-22(D)). We carefully poured acetone onto the absorbent towels before inserting the popsicle into the head for 10 minutes. We trapped the acetone vapors inside the head by designing the popsicle's 3D-printed base to tightly match the shape of the head's opening. A tray made of aluminum foil shielded the ABS base from excess acetone dripping from the towels. The towels reached far into the head without touching the interior surface, ensuring that the vapors uniformly smoothed all areas. Our hybrid approach of XTC-3D on the outside and acetone smoothing on the inside effectively sealed Tunabot V3's head. For waterproofing Tunabot V3's motor housing, XTC-3D was sufficient by itself and did not require acetone. The XTC-3D coating and acetone smoothing did not reappear in Tunabots V4 and V5. Although effective, these two methods were less convenient than silicone-injection, which Tunabot V4 revisited (see Section 3.2.2), and 3D-printed nylon, which was unique to Tunabot V5 (see Section 4.2.2).

After individually waterproofing Tunabot V3's head and motor housing, we sealed them together using clear Devcon epoxy (ITW Global Brands Inc., Solon, OH, USA). While waterproof, this attachment was permanent and consequently prevented disassembly. We were unable to access Tunabot V3's internal components for maintenance or modifications, so we did not use this epoxy waterproofing method again after Tunabot V3. Instead, we resumed using an O-ring for Tunabots V4 and V5 like Tunabots V1 and V2.

We completed Tunabot V3's waterproofing using our previous methods. First, we sealed the two holes where the external tethers and power cables exited the body using a bead of epoxy as with tethered Tunabot V2. Second, we waterproofed the actuation mechanism's rotating bent shaft using a silicone compression seal. As with Tunabots V1 and V2, we cast this seal inside the motor housing alongside ball bearings at each end to center the shaft (black, dashed oval in

Figure 2-21(E)). Except for these two points, the waterproofing methods of Tunabot V3 differed from those of all other Tunabots.

In summary, Tunabot V3 explored three different waterproofing methods: acetone smoothing, XTC-3D coating, and epoxy sealing. Even though we did not reuse any of these methods, this exploration was an important part of the prototyping process, which frequently involved an element of trial and error. Our findings directly informed the waterproofing of future Tunabots, especially Tunabot V4.

2.5.3 Tethered Results

Tunabot V3 achieved the highest tail-beat frequency of any Tunabot in February 2018. Out of water and without the silicone skin, the tail-beat frequency of Tunabot V3 was 22.4 Hz, which we measured using a digital stroboscope (model DS-303). This more than doubled the in-air tail-beat frequencies of Tunabots V1 and V2 (10.7 Hz and 9.3 Hz, respectively). Our design improvements of the actuation mechanism and the significantly faster motor enabled Tunabot V3 to generate such an extreme tail-beat frequency. However, we never tested the swimming performance of Tunabot V3 tethered in the flow tank; Tunabot V4 was completed at this point in time and became our priority to test.

We expected Tunabot V3's in-water tail-beat frequency to be about 18 Hz based on its 22.4 Hz in-air frequency. A tail-beat frequency of 18 Hz would have produced a swimming speed of 3.7 BL/s based on the linear fit of tethered Tunabot V2 (see Figure 2-19(A)). Extrapolating this linear fit was reasonable for three reasons. First, we expected the swimming kinematics of Tunabots V2 and V3 to be similar due to their nearly identical joint parameters (see Table 2-1). Second, the caudal fins of Tunabots V2 and V3 were similar in size and shape.

Third, swimming speeds of the linear extrapolation were length-specific and thus accounted for the slight difference in size between Tunabots V2 and V3.

Initially, the flapper of Tunabot V3 was not resilient enough to withstand the high-cycle fatigue and large forces generated by the extraordinarily high tail-beat frequencies. The flapper (see Figure 2-21(E)) fractured where its two arms encircled the ball bearings. Material failure occurred along the seams between the deposited layers from 3D printing. The flapper no longer broke after we strengthened it by thickening its material around the ball bearings.

Besides Tunabot V3, the structural integrity of the flapper was an important design consideration for future Tunabots with smaller dimensions. To decrease the body's overall dimensions, the flapper would need to be miniaturized accordingly. However, there would be less internal space for a thickened flapper in a smaller Tunabot. Moreover, the 3D-printed flapper would scale down poorly in terms of strength, which was already insufficient at its current size before we modified the design. For these reasons, the 3D-printed flapper was reinforced with stainless-steel eyelets for Tunabots V4 and V5 (see Sections 3.2.1 and 4.2.1, respectively).

We required a Tunabot with significantly smaller dimensions than Tunabot V3 to explore its full range of tail-beat frequencies. Our prediction of Tunabot V3's maximum speed was 3.7 BL/s, which equated to 1.3 m/s based on its 36.1 cm body length. As such, Tunabot V3 would have outswum the flow tank's maximum speed (0.94 m/s). Since the swimming speed of fish for a given frequency is directly related to specimen length [77], a Tunabot with shorter body length would have a slower absolute speed. This would reduce the flow speed necessary for testing equally high tail-beat frequencies rather than needing to find a faster flow tank. Reducing the absolute speed would also not detract from our objective of exploring high-speed swimming because we were interested in normalized speed; speed relative to body length (BL/s) rather than

absolute speed (m/s) enabled us to fairly compare fishes, robots, and Tunabots by accounting for size differences. In effect, a smaller Tunabot would enable the advancement and exploration of high-speed, high-frequency swimming without the limitation of the flow tank's speed. The desire for a Tunabot with smaller dimensions directly motivated the development of Tunabot V4.

Chapter 3

Tunabot V4: Exploring the Performance Space of Fish Swimming

3.1 Overview

In Chapter 3, we present Tunabot V4 [182] which is the fourth generation of tuna-inspired robots. Tunabot V4's compact dimensions and additional biological features improve upon the designs of Tunabots V1–V3. We test Tunabot V4's swimming performance in a flow tank over its full range of tail-beat frequencies using the methodology and equipment developed in Chapter 2. We also design new experiments and data analysis techniques to more thoroughly quantify Tunabot V4's performance. Doing so enables us to measure the dead-drag, static thrust, caudal fin's effective angle of attack, and wake flow via PIV. We compare our results with yellowfin tuna (*Thunnus albacares*) and Atlantic mackerel (*Scomber scombrus*), demonstrating Tunabot V4's fish-like, high-performance capabilities.

3.2 Tunabot V4

3.2.1 *Design and Fabrication*

Tunabot V4 (Figure 3-1(A)) applied the designs of Tunabots V1–V3 into a more compact system and was designed by Dr. Jianzhong Zhu independently from us. Previously, Tunabot V3 demonstrated that we needed a Tunabot with significantly smaller dimensions to test the high tail-beat frequencies we were achieving; a shorter Tunabot could reach its maximum, relative swimming speed (i.e., normalized by body length) without outswimming the flow tank's maximum, absolute speed (see Section 2.5.3). Tunabot V4 measured 25.5 cm in length, 4.9 cm in width, and 6.8 cm in height with an unsubmerged mass of 0.306 kg. This marked a 10.6 cm reduction in body length from Tunabot V3. Tunabot V4's size was comparable to juvenile tuna [183] and adult Atlantic mackerel [184].

All aspects of Tunabot V4's design and fabrication were similar or identical to Tunabots V1–V3. Such aspects included the biological model of yellowfin tuna which excluded all fins except for the caudal fin (see Figure 2-5), the two-joint swimming system with an actively driven body joint coupled to a passively rotating caudal fin (see Section 2.2.2), the positions and rotation angles of these two joints (see Table 2-1), the actuation mechanism driving the mid-body joint (see Figure 2-1), the peduncle joint bilaterally stiffened by elastics (see Section 2.2.2), the individual components and their functions (see Figure 1-3 and Section 2.2.2), the three tethers and two power cables for testing in a flow tank (see Figure 2-16), the silicone skin (see Section 2.2.2), the multiple waterproofing techniques (see Section 3.2.2), and even finer points such as how we handmade the bent shaft using life-size, 2D printouts of its CAD model as a reference (see Section 2.2.2).

Tunabot V4 improved upon the bio-inspired designs of Tunabots V1–V3 by

incorporating additional biological features of yellowfin tuna. This was possible thanks to a wealth of high-quality reference material provided generously by Lauder Laboratory, which they later published [82]. Tunabot V4's spar incorporated lateral keels based on the keeled peduncle of yellowfin tuna (Figure 3-1(B)–(E)). The lateral and cross-sectional profiles of Tunabot V4's

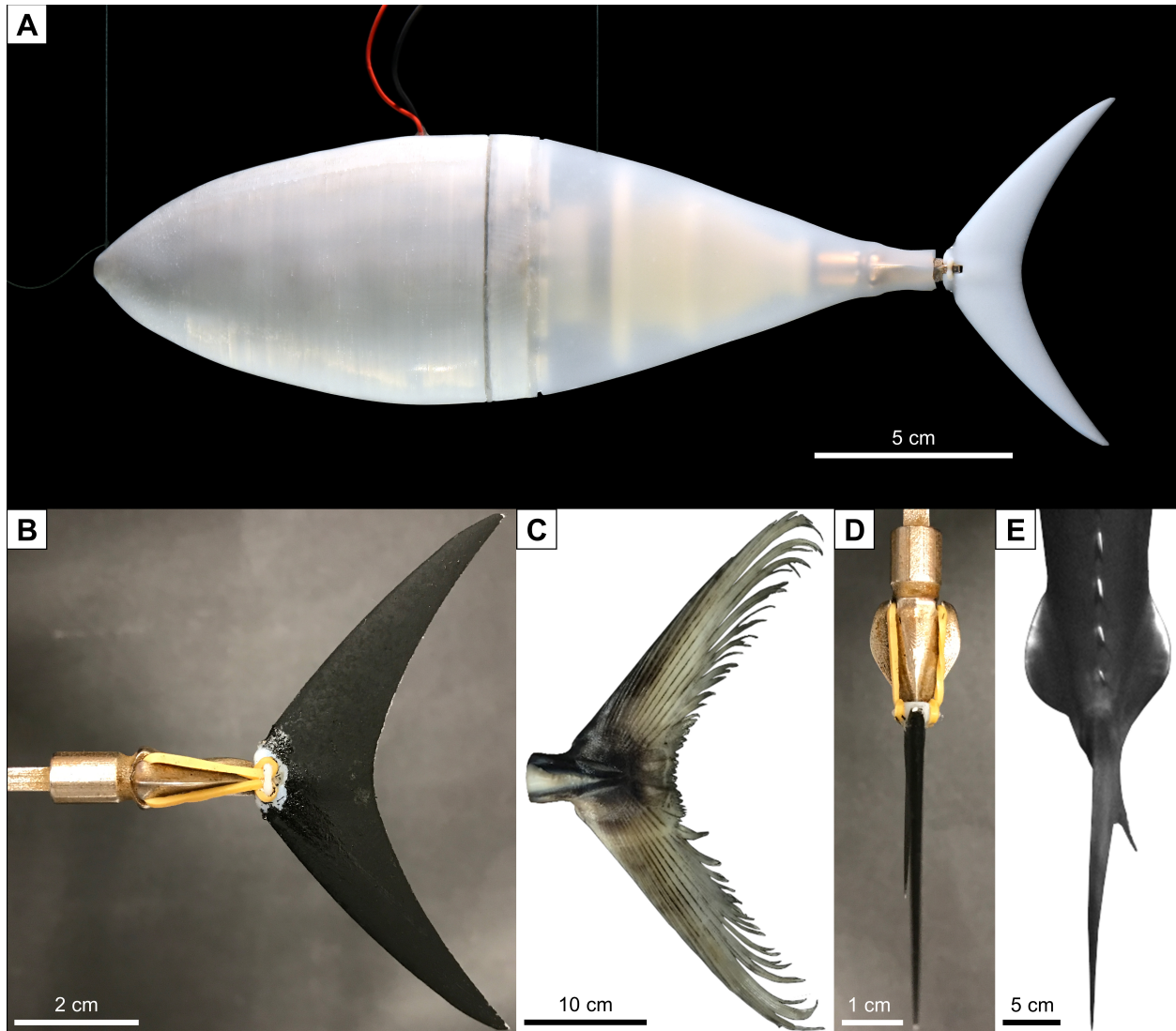


Figure 3-1: Design of Tunabot V4. (A) Tunabot V4 fully assembled including its three tethers (one lateral snout tether plus two vertical tethers) and two power cables. (B) The lateral profile of Tunabot V4's peduncle-caudal fin assembly was based on (C) the lateral profile of a yellowfin tuna's caudal fin from dissections performed by Gregory Lewis and Lauder Laboratory [132]. (D) A dorsal view of Tunabot V4's peduncle-caudal fin assembly highlights the peduncle's lateral keels and caudal fin's tapered cross-section. For comparison, these bio-inspired features are apparent in (E) a zoomed-in, dorsal view of a swimming yellowfin tuna's tail from high-speed video provided by Lauder Laboratory.

caudal fin modeled the caudal fin of a yellowfin tuna dissected by Gregory Lewis and Lauder Laboratory [132]. Specifically, the caudal fin's chordwise, cross-sectional profile was shaped like an airfoil (NACA 0016) along the caudal fin's entire span. The caudal fin was 3D printed by a Stratasys Connex500 in VeroWhite resin, which was smoother and stronger than 3D-printed ABS plastic. The technique used to create the caudal fin's CAD model and subsequent 3D printing in VeroWhite material resembled previous work (see Figure 2-6). These features improved the accuracy of Tunabot V4's bio-inspired design.

The compact design of Tunabot V4 was accomplished in part by using a different motor than before (see Table 2-1). The motor (Actobotics model 638358) had a nominal voltage of 12 V, diameter of 25 mm, mass of 0.08 kg, and rotational speed of 970 rpm (16.2 Hz unloaded). This was slightly larger and faster than the motor of Tunabots V1 and V2 (22 mm diameter, 730 rpm) but significantly smaller and slower than Tunabot V3's motor (32 mm diameter, 1621 rpm). To select Tunabot V4's motor, we tested Tunabot V4 in the flow tank at the University of Virginia with two different motors: the same motor as Tunabots V1 and V2 (730 rpm) and the new motor (970 rpm). The 730-rpm motor generated a maximum tail-beat frequency of 9.3 Hz with a power consumption of 5.5 W. However, the 970-rpm motor required 0.2 W less power for a tail-beat frequency that was faster by 2.9 Hz. Furthermore, the maximum tail-beat frequency of the 970-rpm motor was even higher at 15.3 Hz (7.7 W). We concluded that the 970-rpm motor was faster and more energy efficient for Tunabot V4's application.

Tunabot V4's compact design came at the cost of accessibility to the motor and balanced buoyancy. The head segment (Figure 3-2(E)) had just enough interior space to fit the motor, so the motor was glued in place to prevent its outer casing from rotating. This differed from the designs of Tunabots V1 and V2 whose motors were removable for servicing and secured without

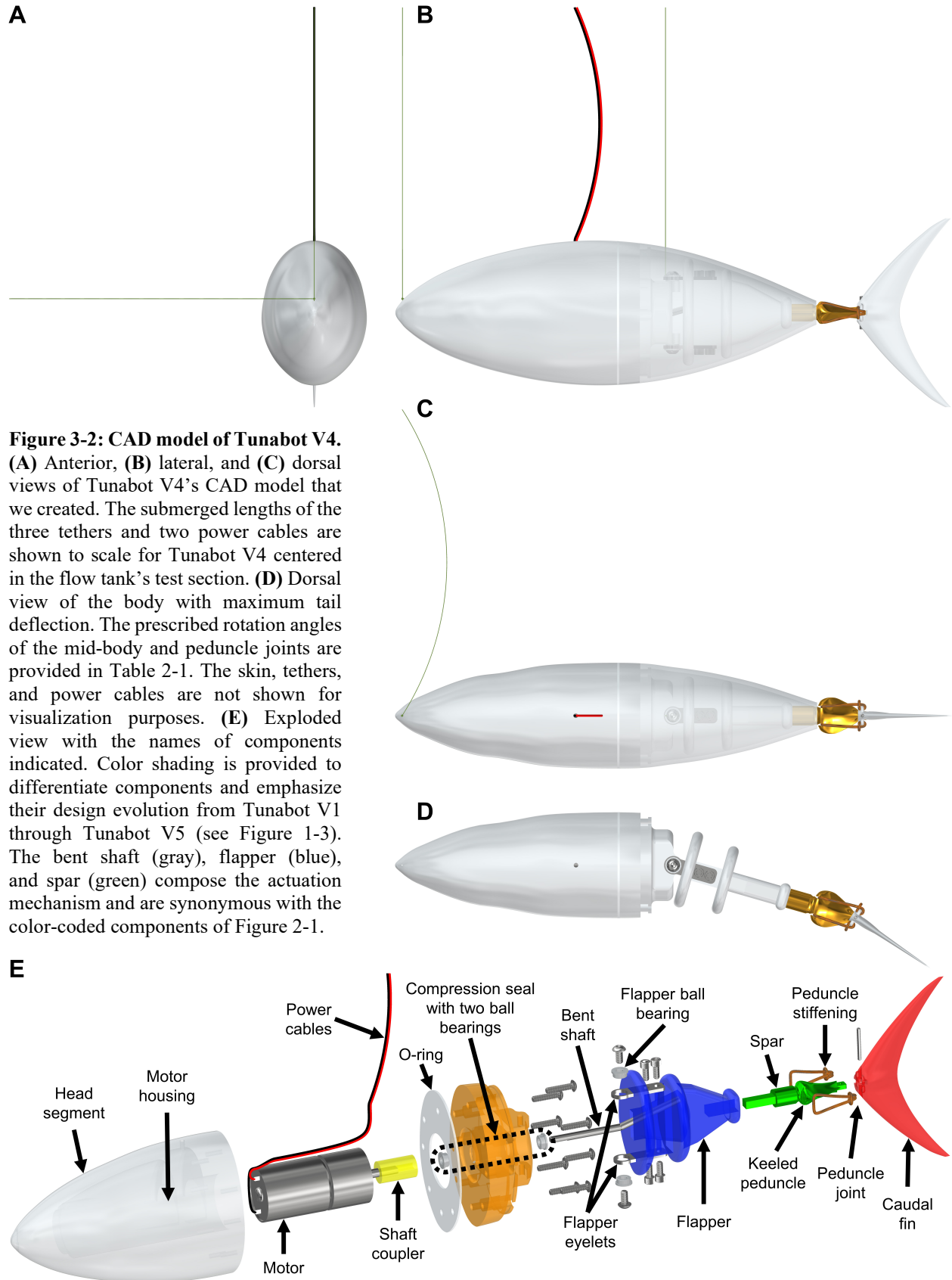


Figure 3-2: CAD model of Tunabot V4. (A) Anterior, (B) lateral, and (C) dorsal views of Tunabot V4's CAD model that we created. The submerged lengths of the three tethers and two power cables are shown to scale for Tunabot V4 centered in the flow tank's test section. (D) Dorsal view of the body with maximum tail deflection. The prescribed rotation angles of the mid-body and peduncle joints are provided in Table 2-1. The skin, tethers, and power cables are not shown for visualization purposes. (E) Exploded view with the names of components indicated. Color shading is provided to differentiate components and emphasize their design evolution from Tunabot V1 through Tunabot V5 (see Figure 1-3). The bent shaft (gray), flapper (blue), and spar (green) compose the actuation mechanism and are synonymous with the color-coded components of Figure 2-1.

glue. Silicone occupied the majority of Tunabot V4's head segment for waterproofing purposes (see Section 3.2.2). The solid volume of silicone resulted in negative buoyancy of the overall body with significant nose-down pitch. Conversely, the head segments of Tunabots V1–V3 were hollow shells that provided sufficient internal space for us to balance their buoyancies via carefully positioned ballast (see Figure 2-7).

Tunabot V4's flapper and spar (Figure 3-2(E)) incorporated stainless steel to miniaturize their designs. Previously, the rings of Tunabot V3's flapper arms were fragile until we increased their strength by thickening them (see Section 2.5.1). However, this solution was impractical for Tunabot V4's smaller flapper. The plastic rings of Tunabot V4's flapper arms were replaced by stainless-steel eyelets with superior material strength. Four screws connected these flapper eyelets to the flapper (Figure 3-2(E)), which was fabricated in ABS plastic using a 3D printer (Stratasys F370) as with Tunabots V1–V3. The eyelets were milled using a computer numerical control (CNC) machine (model MDX-540, Roland DGA Corp., Irvine, CA, USA). The spar's material was similarly changed from ABS plastic to stainless steel due to concerns over the posterior tip's strength where the caudal fin attached. The spar was 3D printed in stainless steel using DMLS technology by Xometry Inc. much like Tunabot V3's bent shaft (see Section 2.5.1) and was plated with gold as per Dr. Jianzhong Zhu's preference.

The skin of Tunabot V4 covered the body's posterior from mid-body to caudal fin (Figure 3-2). This differed from the skins of Tunabots V1–V3, which encased the entire body. Cyanoacrylate adhesive secured Tunabot V4's skin to the motor housing's posterior circumference. As with Tunabots V1–V3, the elastomer skin was created by injecting liquid silicone (Dragon Skin Ecoflex 10 NV, Smooth-On Inc.) into a 3D-printed mold using plastic syringes. This mold resembled the posterior halves of the skin molds that we used for Tunabots

V1–V3 (see Figure 2-11(A) and Figure 2-22(A)–(B)). However, Tunabot V4’s skin mold was simpler because it corresponded to a smaller body and because it excluded the body’s anterior half. As a result, producing thinner skins was an easier task than before. Tunabot V4’s skin (1.5 mm) was half the thickness of Tunabot V3’s skin (3 mm). Tunabot V4’s thin skin was unable to maintain its shape due to its design, so two circumferential ribs were added to the flapper that internally supported the skin’s shape (Figure 3-2(E)). We later discuss in Section 3.5.1 how the skin continued to deform despite the flapper’s ribs and other modifications.

3.2.2 *Waterproofing Methods*

The same three waterproofing methods of Tunabots V1 and V2 sealed Tunabot V4’s motor: the silicone-injection method for the head and motor housing (see Section 2.2.3), a silicone O-ring compressed by eight longitudinal screws where the head and motor housing attached together (see Section 2.3.2), and a silicone compression seal with two ball bearings for the actuation mechanism’s rotating shaft (see Section 2.2.3).

The silicone-injection method waterproofed the head segment and motor housing of Tunabot V4, as was the case with Tunabots V1 and V2. The head segment and motor housing of Tunabot V4 (see Figure 3-2(E)) were 3D printed in white ABS plastic with sparse-low density to produce hatched, internal structures. Liquid silicone was injected into these structures through hand-drilled holes using 60 ml syringes. Once cured, the cast silicone solidified to form an internal, waterproof barrier. Tunabot V4’s head segment was designed with internal space for essentially just the motor, so the injected silicone occupied the majority of the head segment’s volume. This solid design differed from the head segments of Tunabots V1–V3 which maximized internal space with their shell-like design. Tunabot V4’s bulky waterproofing sealed

the hole where the vertical snout tether exited the head. Previously, Tunabots V2 and V3 required a bead of epoxy to prevent water from passing through this hole into their hollow head cavities. As before, a bead of epoxy sealed the hole where the mid-body tether and two power cables exited the body.

A silicone compression seal waterproofed the actuation mechanism's rotating shaft of Tunabot V4, exactly like Tunabots V1–V3. An internal volume was designed into the motor housing that contained the silicone seal with a ball bearing at each end to center the shaft (black, dashed oval in Figure 3-2(E)). During casting, a smaller diameter shaft was centered through the silicone in place of the actuation mechanism's larger diameter shaft. This resulted in the elastic silicone compressing the larger shaft to create a waterproof seal.

A silicone O-ring waterproofed the attachment interface of Tunabot V4's head and motor housing, as with Tunabots V1 and V2. Liquid silicone was cast into a 3D-printed mold to form a custom O-ring. Eight longitudinal screws compressed this O-ring between the two flat surfaces of the head and motor housing (see Figure 3-2(E)) to create a waterproof seal. Tunabot V4's flat mating surfaces differed from the tongue-and-groove joints of Tunabots V1 and V2. This change increased the design simplicity of the head and motor housing but at the cost of significantly less accessibility to the motor. Besides this modification, the waterproofing methods of Tunabot V4 were the same as those previously demonstrated by Tunabots V1 and V2.

3.3 Materials and Methods

3.3.1 *Performance Testing Protocol*

We tested Tunabot V4's swimming performance in May 2018 at Harvard University. The facility we used was Lauder Laboratory's custom-built flow tank from previous research on fish

locomotion [185]–[188]. The flow tank’s test section had wetted dimensions of $90 \times 28 \times 28$ cm (length \times width \times height). Flow speeds ranged from 0 to 1.25 m/s and were measured using past PIV calibrations. The maximum speed corresponded to 900 rpm of the tank’s motor. Lauder Laboratory’s flow tank was faster than the one we had utilized up until this point at the University of Virginia.

We tethered Tunabot V4 in the flow tank’s test section (Figure 3-3) using the same setup as Tunabot V2 (see Section 2.4.3). Two vertical tethers suspended the negatively buoyant Tunabot V4 in the test section’s center from an overhead rig. The projected area of Tunabot V4 (2570 mm^2) occupied 3.3% of the test section’s cross-sectional area, thus minimizing wall and blockage effects. A third tether loosely connected the snout to the test section’s side wall in order to prevent extreme lateral deviations from the center. This lateral tether attached near the bottom of a transparent, plexiglass bar with 6 mm thickness clamped vertically to the test section’s wall. All three tethers were thin, flexible threads (Spectra Power Pro fishing line) with negligible stretch (see Section 2.4.1). We loosely attached the two power cables to the same overhead rig as the vertical tethers to stay clear of the flapping tail. Unlike the vertical tethers, the power cables did not support any weight. To control swimming speed and measure electrical power consumption, we wired the two power cables to an external system that we positioned adjacent to the flow tank (see Section 3.3.2). This tethered arrangement did not hinder streamwise, lateral, or yaw motion of any part of Tunabot V4 except for streamwise drag (see Section 3.4.1) and was, therefore, representative of free swimming.

We tested nine tail-beat frequencies of Tunabot V4 with three trials per tail-beat frequency. We varied the tail-beat frequency by setting the duty cycle of the PWM voltage signal powering the motor from 20% to 100% by 10% increments. We did not test duty cycles less than

20% because 14% was the minimum input capable of turning over the motor. In effect, we tested the entire performance range of Tunabot V4 by sweeping through the full range of tail-beat frequencies. At each tail-beat frequency, we recorded the swimming kinematics (see Section 3.3.3) and the self-propelled speed. We normalized the self-propelled speed by body length.

We measured Tunabot V4's self-propelled swimming speed by effectively adding a high-speed camera to Tunabot V2's similar methodology (see Section 2.4.3). To measure Tunabot V4's self-propelled speed, we marked the snout's position on the outside of the flow tank under conditions of zero flow. We laterally positioned a FASTCAM Mini AX100 high-speed camera (Photron USA Inc., San Jose, CA, USA) that recorded the relative position between the snout

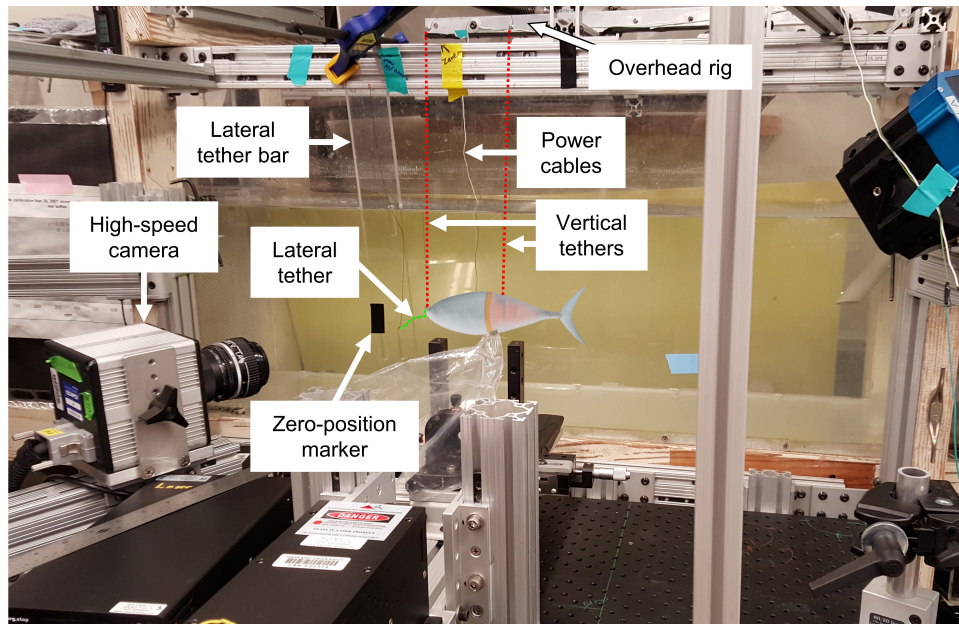


Figure 3-3: Experimental setup for Tunabot V4's performance testing. We quantified Tunabot V4's self-propelled swimming performance in the flow tank at Harvard University. Two vertical tethers (red, dashed lines) suspended Tunabot V4 in the flow tank's test section from the overhead rig. The two power cables loosely attached to the overhead rig and plugged into an external system that controlled swimming speed and measured power consumption (see Section 3.3.2). The lateral tether (green, dashed line) loosely connected the snout to the plexiglass bar clamped vertically to the test section's side wall. This tethered arrangement was the same as Tunabot V2's setup (see Figure 2-18). The zero-position marker corresponded to the snout's position when both Tunabot V4 and the flow tank's water were stationary. The lateral-view, high-speed camera tracked the relative position between the snout and zero-position marker. While Tunabot V4 swam at a particular tail-beat frequency, we adjusted the flow speed until the snout re-aligned with the marker. At this point, the net thrust and drag of Tunabot V4 were equal, and we recorded the self-propelled swimming speed.

and zero-position marker in real time. We indicate this marker and the high-speed camera in Figure 3-3. Photron FASTCAM Viewer software displaying the camera's image with a calibrated length scale enabled zero-position detection within 3 mm. We incrementally tested the full range of tail-beat frequencies from low to high for every trial. Both Tunabot V4 and the flow tank started from a standstill between trials and ran continuously during each frequency sweep. At each tested tail-beat frequency, we adjusted the flow speed until the snout settled at the zero position. This indicated that the net thrust and drag of Tunabot V4 were equal. At this point, we monitored the body's position for at least 10 seconds to ensure stability. Then we recorded the flow speed as Tunabot V4's self-propelled swimming speed and measured the electrical power consumption.

3.3.2 *Speed Control and Power Measurement*

We reused the speed control and data acquisition system from Tunabot V2's tethered flow tank experiment. The methodology (see Section 2.4.2) and physical equipment (see Figure 2-17) were identical. As with Tunabot V2, the performance metric that we used to quantify Tunabot V4's energy efficiency was the COT, which we calculated using Equation (26) after measuring the electrical power consumption. However, applying the same methodology to Tunabot V4 caused a subtle difference; the single values of mean power encompassed a wider range of tail-beat periods for Tunabot V4 compared to Tunabot V2. This was because Tunabot V4's maximum tail-beat frequency was higher and because we tested more than just the higher tail-beat frequencies. Over 5 seconds of data collection, Tunabot V4's mean power included 12 to 73 complete tail-beat periods (depending on the tail-beat frequency) versus 27 to 40 tail-beat periods for Tunabot V2.

Portability was a core design feature of the speed control and data acquisition system. Originally, this was for transporting the system to and from the flow tank when testing Tunabot V2. The portability was also convenient for testing Tunabot V4 because we had to transport the system from our lab at the University of Virginia to Lauder Laboratory at Harvard University. This first trip to Lauder Laboratory later motivated our development of Tunabot V5's more compact, streamlined system for future collaborations (see Figure 4-5).

3.3.3 *Swimming Kinematics of Tuna, Mackerel, and Tunabot V4*

The swimming kinematics of yellowfin tuna, mackerel, and Tunabot V4 were derived from high-speed video data. Lauder Laboratory recorded video footage of yellowfin tuna at the Greenfins Aquaculture Center of Excellence (Greenfins Inc., Narragansett, RI, USA) with special thanks to Professor Terry Bradley of the University of Rhode Island and to Peter Mottur, the director of Greenfins. The tuna at Greenfins swam inside the facility's circular seawater tank (12.2-meter diameter, 3-meter water depth, 473.2-kiloliter maximum volume). This tank was large enough for tuna averaging 1.0 m in body length to freely swim and maneuver unconstrained. Dorsal and lateral-view video sequences of the tuna were recorded using a portable, color camera (HERO4, GoPro Inc., San Mateo, CA, USA) at frame rates of 120 fps (1920 × 1080 resolution) and 240 fps in addition to a FASTCAM Mini AX100 camera (Photron USA Inc.) at 250 and 500 fps. Routine, steady swimming was recorded (Figure 3-4) along with high-speed swimming and maneuvering during feeding. The average ($n = 20$) steady swimming speed was 1.0 ± 0.1 BL/s with a tail-beat frequency of 2.4 ± 0.2 Hz. Feeding sequences provided kinematic data over a range of tail-beat frequencies up to 10 Hz when locomotion was especially active. Speeds during feeding were unmeasurable due to the rapid, 3D motions. Lauder

Laboratory recorded video footage of mackerel in the flow tank at Harvard University under animal care protocol 20-03 to Professor George Lauder. A high-speed camera (Photron FASTCAM PCI-1024) placed beneath the transparent bottom of the tank's test section captured ventral-view footage (500 fps, 1024×1024 resolution) of mackerel steadily swimming at speeds of 1.0–2.0 BL/s. The average ($n = 20$) speed of mackerel was 1.21 ± 0.05 BL/s with a tail-beat frequency of 3.7 ± 0.4 Hz. We similarly recorded video footage of Tunabot V4 in the same flow tank as the mackerel using a Photron FASTCAM Mini UX100 camera (1000 fps, 1280×1024 resolution). During Tunabot V4's performance testing, we recorded the self-propelled swimming speeds of all nine tail-beat frequencies across all three trials.

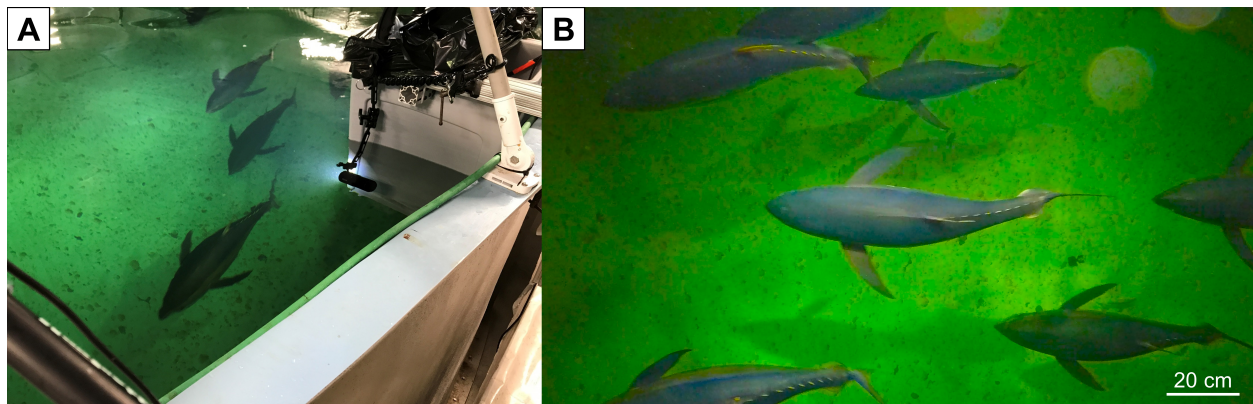


Figure 3-4: Video capture of freely swimming yellowfin tuna. High-speed video was recorded of yellowfin tuna steadily swimming in the large seawater tank at the Greenfins Aquaculture Center of Excellence. **(A)** The high-speed camera was enclosed in a waterproof container (top right) and suspended above the tuna. **(B)** Swimming kinematics were extracted from the dorsal-view footage which captured body deformation during swimming. High-speed videos and the images above were provided by Lauder Laboratory.

We extracted the swimming kinematics of the yellowfin tuna, mackerel, and Tunabot V4 from their respective high-speed video data using custom MATLAB scripts. We manually tracked and digitized the midlines of 10 video frames spaced evenly across a full tail-beat period, resembling previous work [85], [141]. In total, we created 20 midline sequences each for the tuna

and mackerel, and Tunabot V4's 3 trials of 9 tail-beat frequencies produced 27 midline sequences. Individual video frames from the recorded footage of Tunabot V4, yellowfin tuna, and mackerel are pictured later in Figure 3-10(A)–(C).

We created additional MATLAB scripts that calculated the tail-beat frequency, head amplitude, tail-beat amplitude, and midline curvature from the digitized midline sequences. We calculated the tail-beat frequency by dividing the frame rate by the number of video frames per tail-beat period. We defined the head and tail-beat amplitudes as the distances between the lateral extremes of the snout and caudal fin's trailing edge, respectively. We calculated the curvature using Equation (25). We then plugged these kinematic metrics into Equations (23) and (24) to calculate the stride length and Strouhal number, respectively. We scaled the midlines, amplitudes, curvature, and stride length by body length.

Our methodology for extracting the swimming kinematics of Tunabot V4 was identical to the free-swimming experiment of Tunabot V2 (see Section 2.3.3) except for one improvement: we recorded video at a much higher frame rate for Tunabot V4 compared to Tunabot V2 (1000 vs. 30 fps, respectively). This important difference provided the sampling rate necessary to evenly divide a single tail-beat period (as opposed to 2.5 periods) into 10 frames, which was crucial for higher tail-beat frequencies. Doing so also matched the presentation format of fish midlines, enabling us to directly compare fishes and Tunabot V4 side-by-side (see Figure 3-10).

3.3.4 *Drag Forces and Coefficients*

We quantified the dead-drag (i.e., towed resistance) of Tunabot V4's body centered in the flow tank at the University of Virginia. Drag coefficients of fish are usually based on the drag of stiff bodies (typically dead or anesthetized) that are stretched straight, hence the term 'dead-drag'

[189]. We emulated this practice when designing Tunabot V4's drag experiment to enable reasonable comparisons between fish and Tunabot V4. We fixed all of Tunabot V4's body joints such that the midline was straight and rigid. Tunabot V4's placement and tethering inside the flow tank's test section (Figure 3-5) were identical to self-propelled conditions (see Figure 3-3). This included the snout's lateral tether and corresponding aluminum bar clamped vertically to the test section's side wall, which we reused from Tunabot V2 (see Figure 2-18), despite neither appearing in Figure 3-5. The flow tank (model 1520) had a flow speed range of 0–0.94 m/s, and we measured the flow speed using an ultrasonic flow meter (Dynasonics TFX Ultra model DTFXB-ZN-AKNN-NN, Badger Meter Inc., Milwaukee, WI, USA).

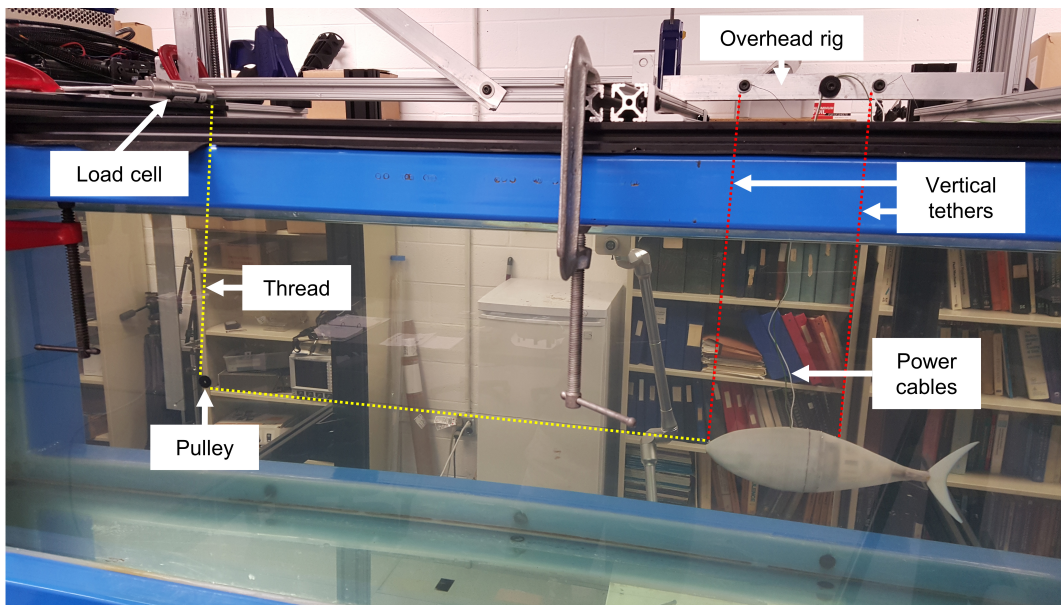


Figure 3-5: Experimental setup for Tunabot V4's drag measurement. We quantified Tunabot V4's drag forces and coefficients in the flow tank at the University of Virginia. We fixed the mid-body and peduncle joints such that the body's midline was straight and rigid. The two vertical tethers (red, dashed lines) suspended Tunabot V4 in the flow tank's test section from the overhead rig. We loosely attached the two power cables to the overhead rig to reproduce swimming conditions (see Figure 3-3), but we did not supply power to Tunabot V4's motor. The thin, flexible thread (yellow, dashed line) connected the load cell to Tunabot V4's snout through the pulley. The thread and pulley transferred downstream dead-drag (i.e., towed resistance) of the body to a downward force on the load cell. We wired the load cell to the control and data measurement system pictured previously in Figure 2-17(A).

We measured Tunabot V4's dead-drag force using a constant moment beam load cell (model LC601-1, serial 278001, Omega Engineering Inc., Norwalk, CT, USA). We attached an additional thread (Spectra Power Pro fishing line) to Tunabot V4's snout that ran horizontally upstream, around a black pulley, and vertically to the load cell (yellow, dashed line in Figure 3-5). A loop of thread loosely attached the pulley to a vertical aluminum bar at the same depth (22.8 cm) as the snout. The thread permitted the pulley to move in three dimensions. Wake effects of the bar were negligible due to its 3 mm thickness and the 50 cm downstream distance to Tunabot V4. In the presence of flow, the load cell registered the corresponding drag force of the body, lateral snout tether, two vertical tethers, and two power cables. We separately calibrated the load cell by hanging a series of 16 masses ranging from 0 to 460 g directly from the load cell and measuring their corresponding voltage outputs, which yielded a linear calibration curve ($R^2 = 0.999$).

We performed four trials at eight of the nine average flow speeds from performance testing (see Figure 3-11). The ninth and fastest speed (1.02 m/s) was untestable since the maximum speed of the flow tank was 0.94 m/s; the flow tank at Harvard University that we used for performance testing was faster with speeds up to 1.25 m/s. Before each trial, we applied non-zero tension (approximately 5 g) to the load cell thread to remove slack, which we subtracted from subsequent load cell measurements. The output voltage of the load cell passed through a signal conditioner (model DMD4059, Omega Engineering Inc.) before being recorded by a National Instruments data acquisition device (model USB-6008, National Instruments Corp., Austin, TX, USA) with LabVIEW software at a sampling rate of 10 kHz for 10 seconds.

We calculated the wetted and projected drag coefficients C_D of Tunabot V4 using the following equation [140]:

$$C_D = \frac{2F_D}{\rho U^2 A} \quad (29)$$

where F_D is the drag force that we obtained experimentally (which included the body, tethers, and power cables), ρ is the water density in the flow tank, U is the input flow speed, and A is the reference area (wetted or projected, see Table 4-4) of Tunabot V4's body that we found from the CAD model. Water temperature during testing was 22.1°C, corresponding to a density of 997.74 kg/m³ and a dynamic viscosity of 0.9510 mPa·s. We calculated the Reynolds number using these values, Tunabot V4's 25.5 cm body length, and Equation (22).

Up until this point, the drag force and coefficients that we measured experimentally pertained collectively to the body, tethers, and power cables. To estimate the dead-drag of the body alone, we estimated the significant hydrodynamic drag generated by the lateral tether, two vertical tethers, and two power cables as follows. We simply modeled the tethers and power cables as straight, round cylinders in uniform flow and assumed no wake interactions. For such a cylindrical model, the hydrodynamic drag force F_D is given by the following equation [140]:

$$F_D = \frac{1}{2} \rho U^2 C_D A \quad (30)$$

where ρ is the water density, U is the flow speed, C_D is the drag coefficient, and A is the cylinder's frontal area. Flow speed U ranged from 0 to 0.94 m/s corresponding to the flow tank's full range of operation. The drag coefficient C_D of a circular cylinder is a function of Reynolds number, which we calculated using Equation (22) wherein the characteristic length was the cylinder's diameter. The diameters of a tether and a power cable were 0.25 mm and 1.10 mm, respectively, which we measured using electronic calipers (model CD-6"ASX, Mitutoyo Corp., Kanagawa, JPN). Values of C_D depended on the Reynolds number and were obtained experimentally [140]. The frontal area A of the tethers and power cables was the product of their

diameters and submerged lengths. To be centered in the flow tank’s test section, the submerged lengths of the lateral tether, fore and aft vertical tethers, and power cables were 19.1, 22.7, 19.8, and 19.5 cm respectively. Next, we subtracted our estimate of the combined drag due to all tethers and power cables from our measured drag force. This difference yielded our final estimate of the dead-drag of the isolated body. We then plugged this final estimate of dead-body drag into Equation (29) as F_D to estimate the dead-body drag coefficients (wetted and projected).

3.3.5 Static Thrust Measurement

We measured Tunabot V4’s static thrust using a custom-built rig in the stationary water tank (Figure 3-6). This was the same tank that we previously used for the free-swimming experiments of Tunabots V1 and V2 (see Chapter 2). Tunabot V4’s static thrust experiment utilized the full capabilities of the control and data collection system that we originally designed

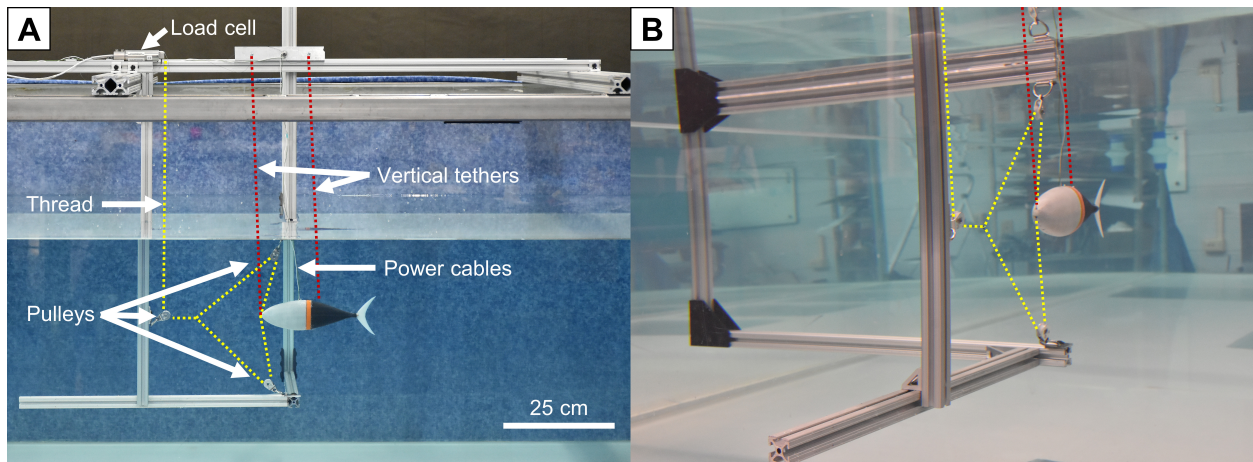


Figure 3-6: Experimental setup for Tunabot V4’s static thrust measurement. We quantified Tunabot V4’s static thrust in the stationary water tank at the University of Virginia. **(A)** Lateral and **(B)** anterior views of the experimental setup. The two vertical tethers (red, dashed line) suspended Tunabot V4 in the custom-built rig centered in the tank. The two power cables loosely attached to the rig overhead. The thin, flexible thread (yellow, dashed line) connected the load cell to Tunabot V4’s snout through a system of three pulleys. The thread and pulleys transferred the forward swimming thrust to a downward force on the load cell. We wired the load cell and power cables to the control and data measurement system pictured previously in Figure 2-17(A).

for Tunabot V2 (see Figure 2-17(A)); this would be the only experiment that required simultaneous use of every feature. We suspended Tunabot V4 in the rig at mid-depth in the tank's center. The tethered arrangement was the same as flow tank testing (see Section 3.3.1) with one difference: we omitted the lateral snout tether because it did not serve a purpose in stationary water. We measured the thrust using a constant moment beam load cell (model LC601-1), which we also used to measure the dead-drag (see Section 3.3.4). A thin, flexible thread with negligible stretch (same as the tethers, see Section 2.4.3) connected the load cell to the snout of Tunabot V4 through a system of three pulleys. The triangular arrangement of these pulleys transferred the forward, underwater thrust during swimming to a downward force on the load cell above the water's surface. By design, this force transfer was one-to-one, and the load cell registered only the forward component of thrust. The attachments of the pulleys to the rig had three degrees of freedom and thus did not restrict Tunabot V4's swimming motion; the body kinematics of flow tank testing were present in the stationary thrust rig, especially the oscillatory, transverse motion of the head and tail. The output voltage of the load cell passed through a signal conditioner (model DMD4059) before being recorded by a National Instruments data acquisition device (model USB-6008) with LabVIEW software at a sampling rate of 10 kHz. The custom-built, aluminum box (see Figure 2-17(A)) contained the signal conditioner and USB-6008 device. We separately calibrated the load cell by hanging a series of 18 masses ranging from 0 to 450 g directly from the load cell and measuring their corresponding voltage outputs, which yielded a linear calibration curve ($R^2 = 0.999$).

We measured Tunabot V4's thrust across a range of tail-beat frequencies with three trials per tail-beat frequency. We set the duty cycle of the PWM controller from 20% to 100% by 10% increments, matching the protocol of flow tank testing (see Section 3.3.1). At the beginning of

each trial, we recorded the force on the load cell when Tunabot V4 was still (i.e., 0% duty cycle) and the water had calmed. We subtracted this value from the following force measurements to zero the thrust data. We recorded the thrust and power consumption simultaneously for 5 seconds for every tail-beat frequency. We collected the power data as before (see Section 3.3.2). We averaged the 5-second thrust signals to obtain single values of mean thrust. Between each trial, we removed and then reattached the caudal fin and skin of Tunabot V4 to account for experimental errors associated with reassembly and skin tension. We extracted the tail-beat frequencies directly from the thrust data in the time domain using Fourier transforms; the sweeping motion of the tail back and forth consistently generated two thrust peaks per tail-beat period, enabling a robust frequency calculation from the 5-second thrust signal.

The peduncle's equations of motion (see Figure 2-2) were useful when analyzing the variation of static thrust throughout a single tail-beat period (see Figure 3-13(A)). Note that the x-axis of Figure 2-2 is the rotation angle φ of the actuation mechanism and not the tail-beat period, as is the case for Figure 3-13(A). However, the two figures were directly comparable after shifting the phase angle; both the rotation angle of Figure 2-2 and the tail-beat period of Figure 3-13(A) corresponded to the same moment when the rotation angle equaled zero ($\varphi = 0$) and the tail-beat period equaled 0.7. At this moment, the peduncle crossed the body's centerline (i.e., mid-stroke) as the tail beat from right to left.

3.3.6 *Added Mass, Lift-Based Propulsion, and Effective Angle of Attack*

A fish and its surrounding water are constantly interacting with each other, and these interactions are ultimately what provide the mechanisms necessary for propulsion. Swimming animals employ four main types of propulsion: drag-based, lift-based, added mass, and

momentum jet [190]. Added mass and lift-based mechanisms primarily generate the thrust for tuna locomotion, so we focused on these two propulsive methods. Due to the tuna-like swimming kinematics of the Tunabots, these two methods also apply to Tunabot locomotion by extension. The effective angle of attack of a caudal fin is a defining metric of lift-based propulsion, so we experimentally measured this metric for both fish and Tunabot V4 (see Section 3.4.8). In this section, we summarize the mechanisms of added mass and lift-based underwater propulsion, and we define the effective angle of attack as it pertains to lift-based fish locomotion.

Added mass (also referred to as ‘virtual mass’ or ‘effective mass’) is one propulsive mechanism that generates thrust for swimming fish. An object moving through a fluid is dynamically equivalent to the same object having a greater mass while moving through a vacuum [191], [192]. The difference in the object’s mass between the fluid and vacuum is termed the ‘added mass’, which can be thought of as the change in inertia resulting from the fluid acceleration required for the object to pass through it. This general concept is present in fish swimming. As a fish flaps its body, water near the body’s surface displaces throughout the motion. During displacement, some of this water is deflected backward along the body’s surface [113], [120]. In effect, a volume of water with a particular mass is accelerated away from the fish’s body, generating an added mass force. The forward thrust component of this reactionary force propels the fish forward. The added mass force F_{am} is formulated by Newton’s Second Law:

$$F_{am} = m_f \frac{\partial U}{\partial t} \quad (31)$$

where m_f is the added fluid mass, and $\frac{\partial U}{\partial t}$ is the fluid acceleration [190], [193]. The reactive models of Lighthill [117] and Wu [121] describe fish propulsion in inviscid flow where inertial

effects dominate. According to their models, added mass is the basic mechanism of energy transfer to the fluid and is required to produce thrust and its associated vortex wake [116]. Added mass is a significant propulsive mechanism for anguilliform fish such as eels [113], [194] because their slender body shape and undulatory kinematics lend themselves to this method of thrust generation [120], [195].

We do not further investigate added mass besides discussing its importance here for two reasons. First, added mass thrust forces are typically small [190]. Conversely, the generated vortices and subsequent propulsion due to lift-based mechanisms are more evident. Second, calculating the added mass force is not readily feasible because doing so would require an accurate estimation of the accelerated fluid volume. The fluid surrounding the body theoretically extends to infinity where its velocity is zero [193]. In other words, there is no finite volume of accelerated fluid; all the fluid is accelerated to some extent and not simply the near-body fluid [196]. As a result, accurately estimating the accelerated fluid volume in order to calculate the added mass force is difficult beyond simple motions and shapes [190], [193].

Besides added mass, lift-based propulsion is the second mechanism of tuna locomotion and our main focus. In this section, we explain the general concept of lift-based propulsion followed by its mathematical theory. In 1933, Gray modeled the body of an eel as a series of distinct flat plates that each had their own velocity and cyclically changing angle of attack relative to the flow [113]. Gray's approach suggested that airfoil theory could be applied to the eel's body segments [114]. More generally, this demonstrated how airfoil theory could be applied to swimming fish to understand the propulsive contribution of a particular body part. Because caudal fins produce thrust, they are commonly isolated from the rest of the body and modeled as an airfoil [190], [197], [198]. By modeling the caudal fin as an airfoil and applying aerodynamic

concepts, the mechanism of lift-based propulsion naturally follows. Some researchers considered the caudal fin as an isolated body part quite literally by amputating it and studying the impacted swimming performance [199], [200]. We similarly investigated Tunabot V4 with its caudal fin removed (see Section 3.4.9). As a fish flaps its tail, the caudal fin's combined pitching and heaving motion generates lift with a forward thrust component. Tuna caudal fins have an airfoil-like cross-section [82], and Tunabot V4's bio-inspired caudal fin had an airfoil cross-section that was intentionally similar (see Section 3.2.1). The aerodynamic effects of pitching and heaving airfoils are foundational to the lift-based propulsion of swimming fish.

One noteworthy topic related to the thrust of pitching and heaving airfoils is their resulting wake. Pitching and heaving airfoils generate the characteristic wake pattern known as the 'reverse von Kármán street'. This vortex street is indicative of thrust production as opposed to the drag-producing von Kármán street behind a stationary cylinder [169], [190], [201], [202]. The difference between thrust and drag production is the orientation of the jet flow (downstream vs. upstream, respectively), resulting from the rotation direction of the counter-rotating vortices. The reverse von Kármán street is a hallmark of fish swimming [75], [167], [169], [203] and is also apparent for Tunabots V2 and V4 (see Sections 2.3.4 and 3.4.10, respectively).

A second noteworthy topic related to the thrust of pitching and heaving airfoils is their kinematics. The topology of the vortex wake is highly sensitive to relatively small changes in the kinematics of a pitching and heaving foil [204]. The pitching and heaving motions can be considered separately. For a purely pitching airfoil, the thrust is entirely due to added mass forces; however, the thrust is entirely due to lift-based forces for a purely heaving airfoil [205], [206]. The phenomenon of a heaving airfoil producing thrust is known as the 'Knoller-Betz effect' [201], which was independently described by Knoller [207] and Betz [208] in 1909 and

1912, respectively. The Knoller-Betz effect is also referred to as the ‘Katzmayr effect’ after Katzmayr, who first validated the Knoller-Betz effect experimentally in 1922 [201], [209]. The combined pitching and heaving motion of an airfoil is emblematic of fish kinematics when the two motions occur simultaneously. The mean input power and efficiency for a pitching and heaving airfoil depend on both added mass and lift-based forces [206]. The phase difference of this combined motion is an important kinematic variable that governs to what extent the trailing edge of the airfoil lags behind the leading edge. A phase difference of 270° maximizes the propulsive efficiency [125], [190], [210], [211] and visually appears fish-like compared to other values [206]. At an angle of 270° , the peak angles of attack are also minimized throughout the motion, reducing the likelihood of flow separation [190], [206]. The phase angle can be varied depending on the desired performance. For example, a phase difference around 330° maximizes thrust [206]. We have highlighted kinematic aspects here such as pitching, heaving, and phase difference, but kinematics alone do not determine performance; the shape of an airfoil works in tandem with the kinematics to maximize performance [212]. Next, we mathematically present how the pitching and heaving caudal fins of the Tunabots produced thrust.

The following set of equations demonstrates how we calculated the effective angle of attack of Tunabot V4’s caudal fin in addition to the lift-generated force that propelled Tunabot V4 (Figure 3-7(A)). The two data sources that we used for these calculations were the midline kinematics and their corresponding self-propelled swimming speeds. First, we linearly fit the caudal fin from the midline kinematics scaled to meters using MATLAB. This linear model was a reasonable simplification due to the caudal fin’s rigid design, which caused any curvature along its length to be negligible. A single, linear fit was not appropriate for a mackerel’s flexible caudal fin, which we discretized into multiple lines instead (see Section 3.4.8). The linear model

of Tunabot V4's caudal fin (green lines in Figure 3-7(B)) was synonymous with the foil's chord line and was defined by two points: one at the peduncle joint (point a) and a second at the trailing edge (point b). We calculated the chord's slope m from the linear fit moving from point b to point a . We then used this slope to calculate the foil's angle of attack α :

$$\alpha = \tan^{-1} m \quad (32)$$

The angle of attack is defined as the angle between a foil's chord and the oncoming freestream flow. In our case, the flow tank generated the freestream flow. The flow's freestream velocity v_∞ can be thought of as Tunabot V4's swimming velocity since both velocities were equal during self-propelled conditions. However, v_∞ was not the incoming velocity in the foil's frame of reference due to the foil's pitching and heaving motion through the fluid. In order to find the relative, incoming velocity seen by the foil (U_{rel}), we had to find the average velocity of the caudal fin itself (\bar{v}_{caudal}). We calculated \bar{v}_{caudal} using two consecutive snapshots in time

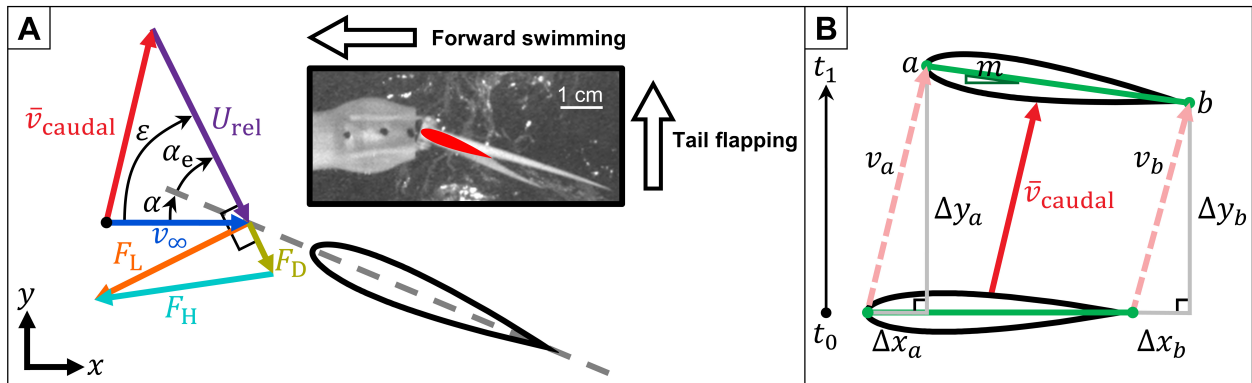


Figure 3-7: Theory of lift-based propulsion generated by caudal fin. Besides added mass, the propulsive mechanisms of swimming fish and the Tunabots are lift-based. The combined pitching and heaving motion of a flapping caudal fin generates thrust, which Equations (32)–(53) demonstrate. **(A)** Vector diagram of velocities and forces for a pitching-heaving airfoil. For this example, the vectors and airfoil shown correspond to the snapshot of Tunabot V4's caudal fin (black box) from actual experimental data. Tunabot V4's caudal fin had an airfoil cross-section (highlighted in red) based on the airfoil-like cross-section of tuna caudal fins [82]. The airfoil's motion results in an effective angle of attack (α_e) and forward hydrodynamic force (F_H). **(B)** Vector diagram visualizing how we calculated the caudal fin's average velocity (\bar{v}_{caudal}). A single airfoil chord (green line) rotates and translates between two consecutive time instants (t_0 and t_1). For both diagrams, vectors are not drawn to scale for illustrative purposes but are accurately orientated.

(t_0 and t_1) of the linearly modeled caudal fin from the midline kinematics (Figure 3-7(B)). As the caudal fin moved, its leading and trailing edges changed positions, which we designated as Δx_a , Δx_b , Δy_a , and Δy_b . We knew the amount of time dt over which this movement occurred, so we were able to calculate the component velocities of the leading and trailing edges (v_{a_x} , v_{a_y} , v_{b_x} , and v_{b_y}) as follows:

$$dt = t_1 - t_0 \quad (33)$$

$$v_{a_x} = \frac{\Delta x_a}{dt} \quad (34)$$

$$v_{a_y} = \frac{\Delta y_a}{dt} \quad (35)$$

$$v_{b_x} = \frac{\Delta x_b}{dt} \quad (36)$$

$$v_{b_y} = \frac{\Delta y_b}{dt} \quad (37)$$

Due to the combined pitching and heaving motion of the caudal fin about its leading edge, the velocities of the leading and trailing edges (v_a and v_b , respectively) were not equal. As such, we needed both v_a and v_b to find \bar{v}_{caudal} . We averaged the velocity components of v_a and v_b to find the average velocity components of the overall caudal fin ($\bar{v}_{\text{caudal}_x}$ and $\bar{v}_{\text{caudal}_y}$) and then \bar{v}_{caudal} :

$$\bar{v}_{\text{caudal}_x} = \frac{1}{2}(v_{a_x} + v_{b_x}) \quad (38)$$

$$\bar{v}_{\text{caudal}_y} = \frac{1}{2}(v_{a_y} + v_{b_y}) \quad (39)$$

$$\bar{v}_{\text{caudal}} = \sqrt{(\bar{v}_{\text{caudal}_x})^2 + (\bar{v}_{\text{caudal}_y})^2} \quad (40)$$

After calculating \bar{v}_{caudal} and v_∞ , we were able to find the magnitude U_{rel} and direction ε

of the relative incoming velocity seen by the foil (Figure 3-7(A)):

$$U_{rel_x} = v_{\infty_x} - \bar{v}_{caudal_x} \quad (41)$$

$$U_{rel_y} = v_{\infty_y} - \bar{v}_{caudal_y} \quad (42)$$

$$U_{rel} = \sqrt{(U_{rel_x})^2 + (U_{rel_y})^2} \quad (43)$$

$$\varepsilon = \tan^{-1}\left(\frac{U_{rel_y}}{U_{rel_x}}\right) \quad (44)$$

The freestream velocity's y-component v_{∞_y} was zero because the flow tank's current was unidirectional. We ensured that the borders of the ventral-view, high-speed footage aligned exactly with the flow's downstream direction; otherwise, v_{∞_y} would have been nonzero which would have erroneously affected our results.

Finally, we calculated the effective angle of attack α_e using the following expression:

$$\alpha_e = \varepsilon + \alpha \quad (45)$$

The effective angle of attack is defined as the angle between a foil's chord and the relative oncoming flow velocity seen by the foil. In the example that Figure 3-7 depicts, ε is negative and α is positive. The signs of ε and α reverse when the flapping tail transitions towards the opposite direction during the second half of a tail-beat period. These periodic sign changes result in α_e alternating between positive and negative values as well (see Figure 3-13(B)). The effective angle of attack determines the amount of thrust produced.

Next, we calculated the lift-generated force that propelled Tunabot V4. We began by using the following lift equation to calculate the lift force F_L , which is perpendicular to U_{rel} :

$$F_L = \frac{1}{2} \rho (U_{rel})^2 S C_L \quad (46)$$

where ρ is the water density, S is the planform area of the caudal fin when viewed laterally, and C_L is the foil's lift coefficient. The effective angle of attack determines the lift coefficient and, consequently, the magnitude of lift. We used the similar drag equation to calculate the drag force F_D , which is parallel to U_{rel} :

$$F_D = \frac{1}{2} \rho (U_{rel})^2 S C_D \quad (47)$$

where C_D is the foil's drag coefficient. We then split F_L and F_D into their components:

$$F_{L_x} = F_L \cos\left(\frac{\pi}{2} - \varepsilon\right) = F_L \sin(\varepsilon) \quad (48)$$

$$F_{L_y} = F_L \sin\left(\frac{\pi}{2} - \varepsilon\right) = F_L \cos(\varepsilon) \quad (49)$$

$$F_{D_x} = F_D \cos(\varepsilon) \quad (50)$$

$$F_{D_y} = F_D \sin(\varepsilon) \quad (51)$$

Finally, we used these components to calculate Tunabot V4's propelling force. The hydrodynamic force F_H (Figure 3-7(A)) was the resultant of the lift and drag vectors:

$$F_{H_x} = F_{L_x} - F_{D_x} \quad (52)$$

$$F_{H_y} = F_{L_y} - F_{D_y} \quad (53)$$

This hydrodynamic force is referred to as the 'aerodynamic force' in the context of aircraft theory. The x-component of the hydrodynamic force F_{H_x} was the forward thrust force generated by Tunabot V4's pitching and heaving caudal fin.

In summary, these equations detailed our methodology for calculating the effective angle of attack of the caudal fin. We also demonstrated through lift theory how the pitching and heaving motion of the foil-shaped caudal fin generated a propelling thrust force.

3.3.7 Flow Visualization

We visualized the flow surrounding Tunabot V4 using a PIV setup resembling previous research [75], [85], [188], [213], [214]. The flow tank's water was seeded with near-neutrally buoyant, reflective particles measuring 50 μm in mean size. These particles were illuminated by a horizontal laser sheet created by a 5 W argon ion laser (Opto Engine LLC, Midvale, UT, USA) in conjunction with a Powell lens. The green laser sheet bisected Tunabot V4 at the half-span (i.e., midspan) and quarter-span of the caudal fin (Figure 3-8). We collected PIV data at the half-span for duty cycles ranging from 30% to 60% by 10% increments. We also collected PIV data at the quarter-span for duty cycles ranging from 30% to 70% by 10% increments. By doing so, the PIV data we collected corresponded to performance testing (i.e., the points in Figure 3-11).

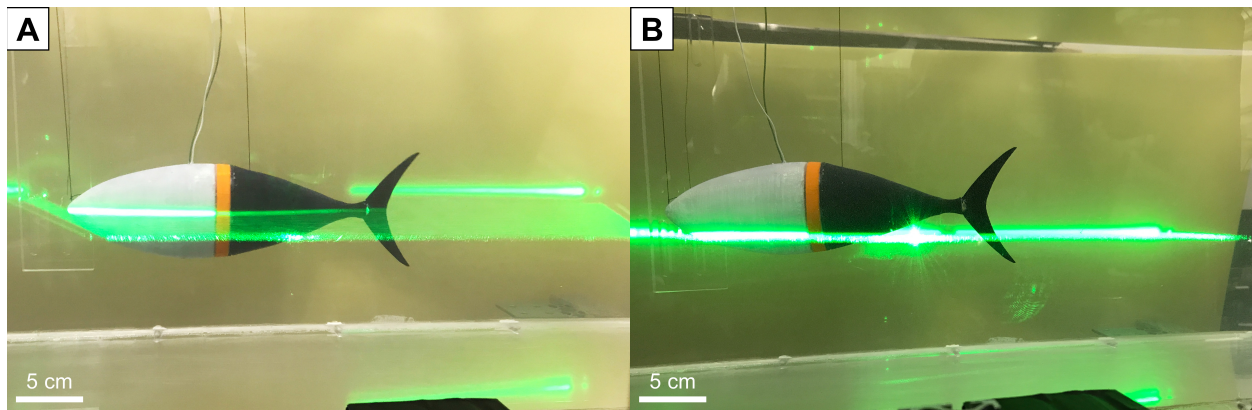


Figure 3-8: Experimental setup for visualizing the flow field around Tunabot V4. A green laser sheet illuminated reflective particles in the water at the caudal fin's (A) half-span (i.e., midspan) and (B) quarter-span. A ventral-view, high-speed camera recorded the particles through the transparent bottom of the flow tank at Harvard University while Tunabot V4 steadily swam. The flow field was then visualized from this footage using PIV software.

A ventral-view, high-speed camera (Photron FASTCAM Mini UX100, 1000 fps, 1280×1024 resolution) recorded the motion of the illuminated particles through the transparent bottom of the flow tank's test section while Tunabot V4 steadily swam. Pairs of sequential video frames were processed by Lauder Laboratory using DaVis 8.4 software (LaVision Inc., Ypsilanti, MI,

USA) to generate a time series of velocity vector fields throughout the tail-beat period. The tethered setup of Tunabot V4 in the flow tank's test section was identical to that of performance testing (see Figure 3-3) except for three minor alterations: we painted the caudal fin black; we replaced the white, translucent tail skin with a black, opaque skin made of the same silicone material; and we covered the metal, overhead rig that suspended Tunabot V4 with thin strips of black foam. Doing so prevented reflections of the laser sheet from over-brightening the PIV video image.

3.3.8 Statistical Analysis

Error propagation mostly involved the averaging of values over multiple trials and the associated uncertainty. When multiplying or dividing values, we evaluated the propagation of uncertainties using the following approach [215]:

$$\text{For some } Q = \frac{ab \dots c}{xy \dots z},$$

$$\delta Q = \pm |Q| \sqrt{\left(\frac{\delta a}{a}\right)^2 + \left(\frac{\delta b}{b}\right)^2 + \dots + \left(\frac{\delta c}{c}\right)^2 + \left(\frac{\delta x}{x}\right)^2 + \left(\frac{\delta y}{y}\right)^2 + \dots + \left(\frac{\delta z}{z}\right)^2} \quad (54)$$

where $Q \pm \delta Q$ is the final result calculated from the input values ($a \dots z$), which each have their own uncertainty ($\delta a \dots \delta z$). We quantified uncertainty in terms of the 95% confidence interval (CI). In order to find the 95% CI, we first found the sample standard deviation σ_x [216]:

$$\sigma_x = \sqrt{\frac{1}{n-1} \sum_{i=1}^n (x_i - \bar{x})^2} \quad (55)$$

where n is the sample size, x_i is the i^{th} value of the data set, and \bar{x} is the sample mean. Next, we calculated the standard error of the mean (SEM) $\sigma_{\bar{x}}$ using the following expression [216]:

$$\sigma_{\bar{x}} = \frac{\sigma_x}{\sqrt{n}} \quad (56)$$

where σ_x is the sample standard deviation and n is the sample size. Other common names for SEM are ‘standard error’ and ‘standard deviation of the mean’. After finding SEM, the 95% CI was finally calculable [216]:

$$CI = \pm t\sigma_{\bar{x}} \quad (57)$$

where t is the ‘t-statistic’, which equals 1.96 for a CI of 95%, and $\sigma_{\bar{x}}$ is the SEM. In text and plotted error bars, we reported average values with uncertainty as the mean \pm 95% CI.

3.4 Results

3.4.1 Drag Forces and Coefficients

Tunabot V4’s dead-drag (Figure 3-9(A)) fit a quadratic polynomial ($R^2 = 0.98$), as is often the case for drag forces. The maximum average dead-drag was 0.50 ± 0.03 N ($n = 4$) at the highest speed of the University of Virginia’s flow tank (0.94 m/s). The lateral snout tether, two vertical tethers, and two power cables were significant sources of drag (Figure 3-9(B)). At 0.94 m/s, the estimated drag force of all tethers and power cables (0.23 N) was 46% of the measured dead-drag. This significant percentage increased to 87% as the speed decreased to 0.20 m/s. The two power cables contributed the majority of drag to the estimate due to their larger diameters compared to the thin tethers; at 0.94 m/s, the power cables comprised 37% of the measured dead-drag and 79% of the estimated drag force of all tethers and power cables. For an estimate of the dead-drag of Tunabot V4’s body alone, we subtracted the estimated drag of all tethers and power cables from the measured dead-drag. The body-only estimate of dead-drag at 0.94 m/s was 0.27 N, which was nearly half of the measured dead-drag. Because the estimated drag of the tethers

and power cables was a substantial component of the measured dead-drag across all speeds, we would expect a free-swimming Tunabot V4 to achieve significantly faster speeds.

The drag coefficients of Tunabot V4 (Figure 3-9(C)–(D)) ranged from 0.031 to 0.078 (wetted) and from 0.35 to 0.88 (projected) depending on the reference area of the body (see Table 4-4). We calculated these values using the measured dead-drag. To estimate the drag coefficients of the body alone, we re-calculated the coefficients using the body-only estimate of

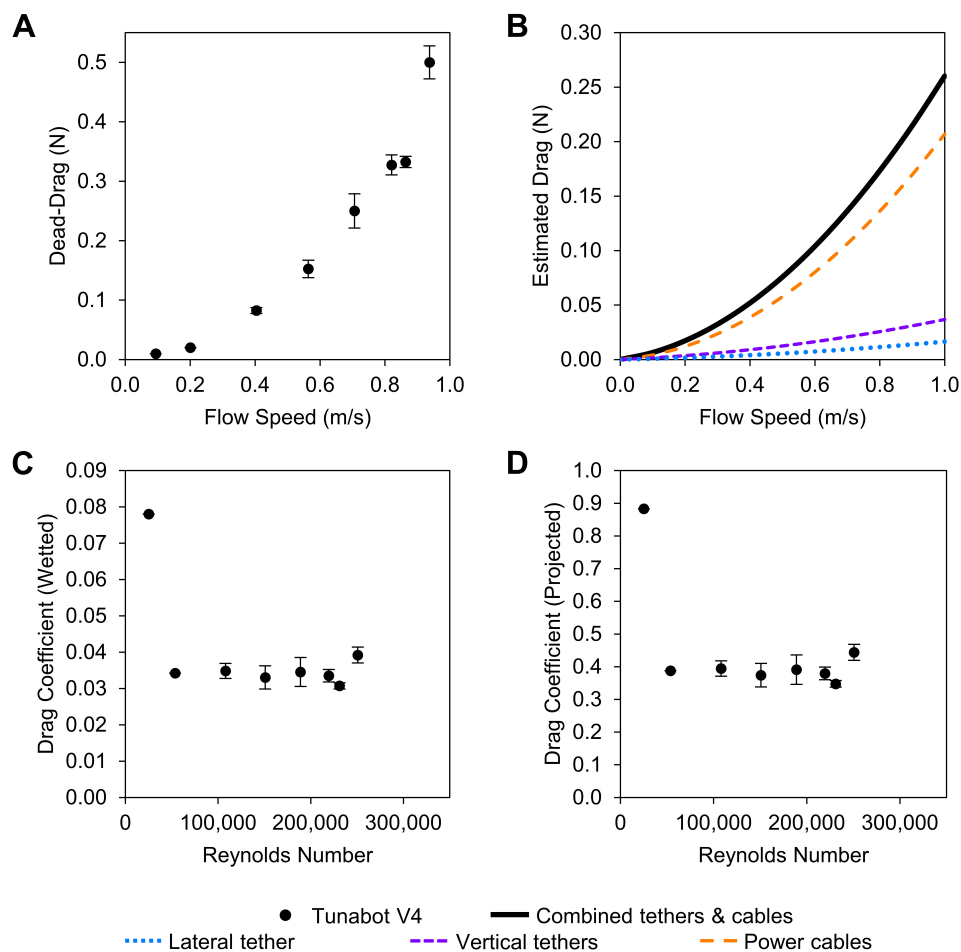


Figure 3-9: Drag forces and coefficients of Tunabot V4. (A) We measured the dead-drag (i.e., towed resistance) of Tunabot V4 with a straight, immobile midline in oncoming flow. The flow tank’s speed settings matched Tunabot V4’s self-propelled speeds from performance testing (see Figure 3-11). (B) We estimated the drag forces of the lateral tether (dotted, blue line), two vertical tethers (dashed, purple line), and two power cables (dashed, orange line). Their sum determined the combined drag of all tethers and power cables (solid, black line). We calculated the drag coefficients using Tunabot V4’s (C) wetted area and (D) projected area (see Table 4-4). Data points represent the mean \pm 95% CI ($n = 4$).

the dead-drag and then averaged them together ($n = 8$). The mean, body-only estimates of the drag coefficients were 0.016 ± 0.005 (wetted) and 0.18 ± 0.06 (projected). In Section 4.7.3, we compare Tunabot V5's wetted drag coefficients against tunas and other relevant fish species, and we discuss the general limitations of dead-drag measurements.

3.4.2 *Swimming Kinematics*

We compared the swimming kinematics of Tunabot V4, yellowfin tuna, and mackerel (Figure 3-10) steadily swimming at similar speeds (2.20 BL/s, 1.0 BL/s, 2.0 BL/s, respectively). We provided a single frame from the high-speed video data for each swimmer at similar points throughout their tail-beat periods (Figure 3-10(A)–(C)). The midlines of all three demonstrated a wave-like kinematic pattern (Figure 3-10(D)–(F)). However, abrupt displacement changes were visible in Tunabot V4's midlines, unlike the gradual midlines of the yellowfin tuna and mackerel. The motion of Tunabot V4's mid-body and peduncle joints caused these changes. Consequently, Tunabot V4's midline curvature exhibited local peaks (Figure 3-10(G)) corresponding to the positions of the two joints (see Table 2-1). This curvature profile differed from those of the yellowfin tuna and mackerel, whose curvature smoothly increased from head to tail (Figure 3-10(H)–(I)). The curvature of Tunabot V4 was highest at the positions of its two joints and effectively zero elsewhere due to the rigidity of its manufactured body components. Conversely, the highest curvatures of the yellowfin tuna and mackerel occurred in their posterior regions due to the flexibility of their caudal fins. We further discuss caudal fin flexibility in Section 3.5.3.

We extracted the lateral amplitudes of the head and caudal fin from all midline sequences, including the three sequences of Figure 3-10(D)–(F). We averaged the amplitudes across all trials and speeds. The average head amplitudes were 0.05 ± 0.01 BL (Tunabot V4,

$n = 27$), 0.05 ± 0.01 BL (yellowfin tuna, $n = 20$), and 0.02 ± 0.01 BL (mackerel, $n = 20$). The head amplitudes of Tunabot V4 and the yellowfin tuna were the same, but both were greater than the mackerel's head amplitude. The average tail-beat amplitudes were 0.15 ± 0.01 BL (Tunabot V4, $n = 27$), 0.19 ± 0.01 BL (yellowfin tuna, $n = 20$), and 0.16 ± 0.01 BL (mackerel, $n = 20$). The tail-beat amplitudes of Tunabot V4 and the mackerel were similar but slightly less than that of the yellowfin tuna. Tunabot V4's tail-beat amplitude fell short of tuna due to the prescribed angles of its body joints and because of its limited body flexibility. We improved both the angles and flexibility with the following Tunabot generation (Tunabot V5) for a more biomimetic, tuna-inspired research platform (see Section 4.2.1).

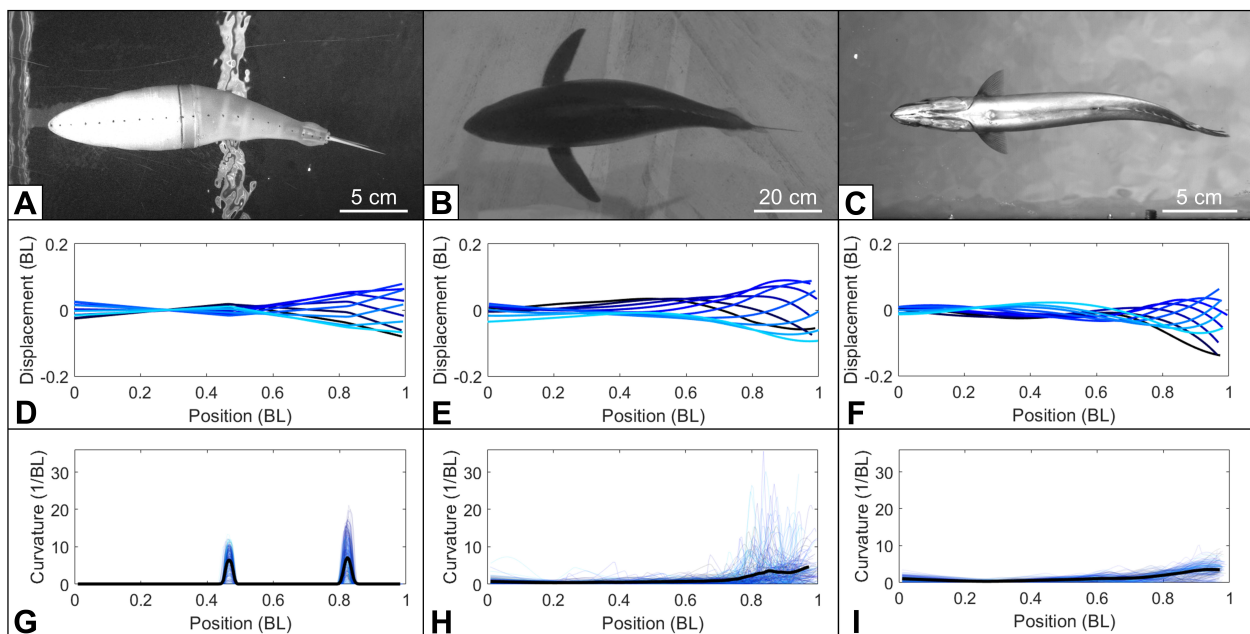


Figure 3-10: Swimming kinematics of Tunabot V4, yellowfin tuna, and mackerel. We compared the swimming kinematics of Tunabot V4, yellowfin tuna, and mackerel side-by-side. **(A)** Ventral view of Tunabot V4 steadily swimming at 50% duty cycle of the PWM voltage input. **(B)** Dorsal view of a yellowfin tuna steadily swimming (see Figure 3-4). **(C)** Ventral view of a mackerel steadily swimming. **(D–F)** Corresponding midline kinematics of a single tail-beat period divided into 10 equally spaced time intervals. The provided views and kinematics are representative of the average and selected for their similar swimming speeds: 2.20, 1.0, and 2.0 BL/s, respectively. **(G–I)** Calculated curvatures along the body for $n = 270$, 200, and 200 midlines from all trials and swimming speeds, corresponding to 27, 20, and 20 tail-beat periods, with the means indicated by thicker, black lines. High-speed videos of the yellowfin tuna and mackerel were provided by Lauder Laboratory.

3.4.3 *Swimming Speed and Tail-Beat Frequency*

Tunabot V4's swimming speed increased with the tail-beat frequency (Figure 3-11(A)). The range in swimming speed was 0.37–4.00 BL/s which corresponded to tail-beat frequencies from 2.5 to 14.8 Hz. Swimming speed was linearly proportional to the tail-beat frequency ($R^2 = 0.996$) up to 10.2 Hz. Similarly, a linear relationship with positive slope between swimming speed and tail-beat frequency is a well-documented feature of fish performance [77], [78], [128], [134], [183], [184], [217]–[220].

We attribute the swimming speed's gradient change beyond 10.2 Hz to the reduced tail-beat amplitude of the caudal fin at higher tail-beat frequencies (see Section 3.4.6). Despite this gradient change, the swimming speed continued to increase with the tail-beat frequency. This suggested that a faster motor would further increase speed. The full range of tail-beat frequencies was linearly related ($R^2 = 0.999$) to the duty cycle of the PWM voltage input, confirming that varying the duty cycle was an effective methodology (see Section 3.3.2) for controlling swimming speed.

Lauder Laboratory measured the swimming speeds and tail-beat frequencies of steadily swimming yellowfin tuna and mackerel (see Section 3.3.3). Tunabot V4's range of swimming speeds (0.37–4.00 BL/s) encompassed the observed speeds of yellowfin tuna (1.0 BL/s) and mackerel (1.0–1.4 BL/s). Tunabot V4's tail-beat frequencies (2.5–14.8 Hz) were similar as well to those of yellowfin tuna (0.9–2.9 Hz) and mackerel (2.9–5.8 Hz). Lauder Laboratory also measured the tail-beat frequencies of yellowfin tuna during feeding when locomotion was especially active. Tunabot V4's maximum tail-beat frequency (14.8 Hz) exceeded the 10 Hz maximum that was recorded for larger (1 m long) yellowfin tuna during these feeding bouts.

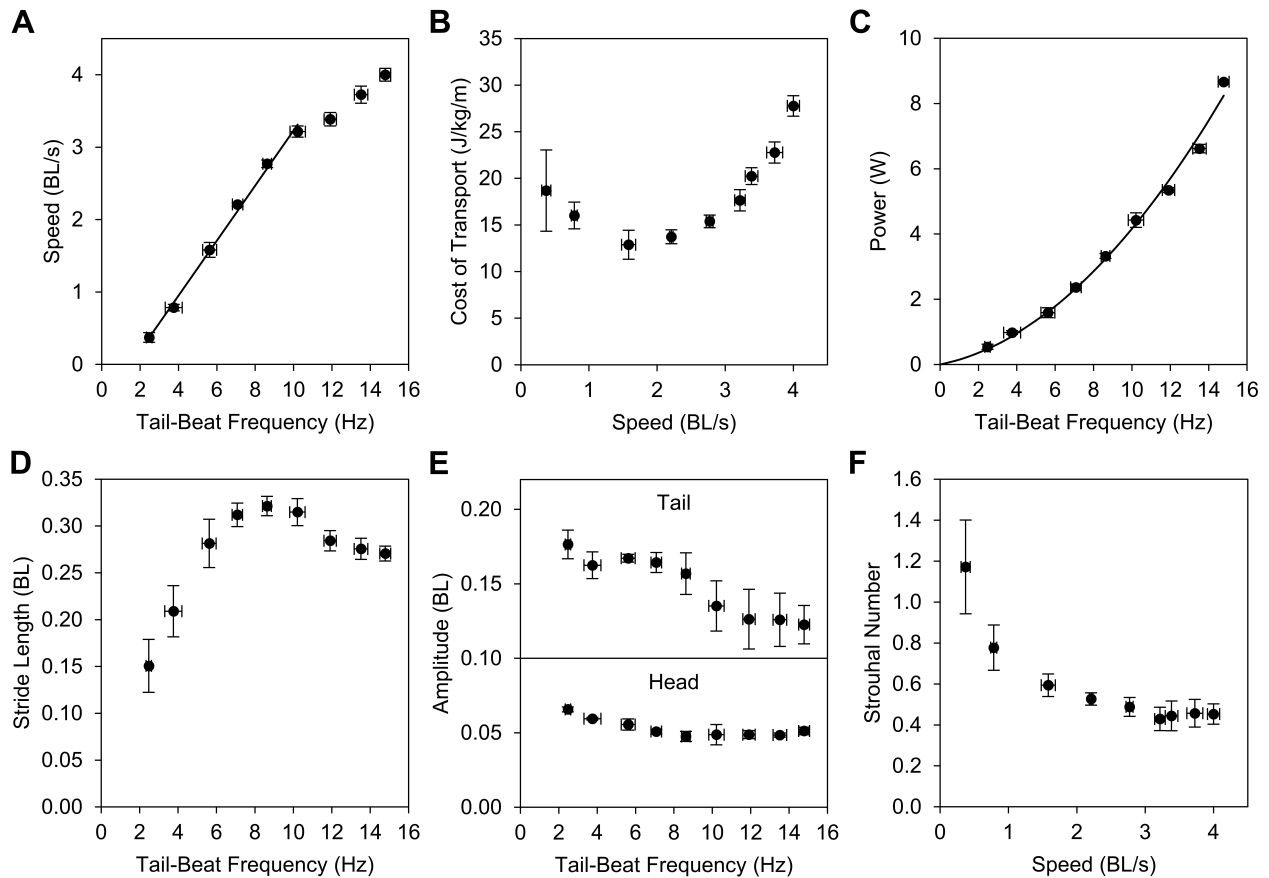


Figure 3-11: Performance results of Tunabot V4. We quantified the performance of Tunabot V4 steadily swimming using metrics of fish performance. Testing occurred in the flow tank at Harvard University. We normalized speed, stride length, and amplitudes by body length (BL). Data points represent the mean \pm 95% CI ($n = 3$).

3.4.4 Cost of Transport

The relationship between Tunabot V4's COT and swimming speed had a U-shaped curve (Figure 3-11(B)). The COT was higher at both low and high speeds compared to intermediate speeds. At Tunabot V4's maximum swimming speed (4.00 ± 0.09 BL/s), the COT was 27.8 ± 1.1 J/kg/m ($n = 3$). At 1.58 BL/s, Tunabot V4 reached its minimum COT of 12.9 ± 1.6 J/kg/m ($n = 3$). Total electrical power consumption of Tunabot V4's motor was analogous to the active metabolic rate of fish (see Section 4.3.4). Many fishes exhibited similarly U-shaped relationships between COT and swimming speed [189], [221]–[223]. As is the case for fish, Tunabot V4's energetic costs increased with swimming speed. Tunabot V4's COT increased at higher tail-beat

frequencies as its electrical power consumption quadratically increased ($R^2 = 0.992$) with tail-beat frequency (Figure 3-11(C)). However, the minimum COT of yellowfin tuna (1.10 J/kg/m) [79] was 25 times lower than that of Tunabot V4 (12.9 J/kg/m) and occurred at a slower swimming speed (1.15 vs. 1.58 BL/s).

At Tunabot V4's minimum tail-beat frequency, the body oddly rolled from side to side. This rolling motion negatively impacted the swimming kinematics and caused the body to unsteadily bounce on the two vertical tethers. These stability issues contributed to the COT's increase and large error bars (95% CI) at the lowest tested tail-beat frequency. Similarly, fish expend more energy at lower speeds to maintain stability [222]–[224].

3.4.5 *Stride Length*

Stride length is an important indicator of propulsive efficiency for undulatory locomotion and is the ratio of swimming speed to tail-beat frequency (see Equation (23)). Tunabot V4's stride length (Figure 3-11(D)) was less than the stride lengths of the observed yellowfin tuna and mackerel (see Section 3.3.3). Tunabot V4's swimming speeds and tail-beat frequencies were similar to those of the yellowfin tuna and mackerel; however, Tunabot V4 swam more slowly for a given tail-beat frequency. Tunabot V4's stride length ranged from 0.15 to 0.32 BL with the maximum corresponding to a tail-beat frequency of 8.6 Hz. The decline in stride length beyond this maximum indicated decreasing performance. The average ($n = 20$) stride length of the yellowfin tuna was 0.41 ± 0.05 BL corresponding to a tail-beat frequency of 2.4 ± 0.2 Hz. This was nearly three times greater than Tunabot V4's average ($n = 3$) stride length of 0.15 ± 0.03 BL at a similar tail-beat frequency (2.5 ± 0.1 Hz). As a result, the tuna swam nearly three times faster than Tunabot V4 (1.0 ± 0.1 vs. 0.37 ± 0.07 BL/s) for essentially the same tail-beat

frequency. This was true for the mackerel as well. The average ($n = 20$) stride length of the mackerel was 0.33 ± 0.04 BL corresponding to a tail-beat frequency of 3.7 ± 0.4 Hz. This was greater than Tunabot V4's average ($n = 3$) stride length of 0.21 ± 0.03 BL at a similar tail-beat frequency (3.8 ± 0.4 Hz). Consequently, the mackerel swam 0.43 BL/s faster than Tunabot V4 (1.21 ± 0.05 vs. 0.78 ± 0.04 BL/s) for nearly the same tail-beat frequency. The larger stride lengths of the yellowfin tuna and mackerel meant that they swam a further distance for each beat of their tail compared to Tunabot V4, indicating greater overall thrust output per tail-beat period.

3.4.6 *Head and Tail-Beat Amplitudes*

We extracted the head and tail-beat amplitudes of Tunabot V4 (Figure 3-11(E)), yellowfin tuna, and mackerel from their swimming kinematics (see Figure 3-10). Tunabot V4's head and tail-beat amplitudes were inversely related to the tail-beat frequency. As the tail-beat frequency increased, the average ($n = 3$) head amplitude decreased from 0.07 ± 0.01 BL to 0.05 ± 0.01 BL. Similarly, the average ($n = 3$) tail-beat amplitude decreased from 0.18 ± 0.01 BL to 0.12 ± 0.01 BL. We did not expect this result since the tail-beat amplitude was fixed by design. We attributed the tail-beat amplitude's non-zero slope to the peduncle's stiffness, which we discuss in Section 3.5.2. The average ($n = 20$) head and tail-beat amplitudes of the yellowfin tuna were 0.05 ± 0.01 BL and 0.19 ± 0.01 BL, respectively. The average ($n = 20$) head and tail-beat amplitudes of the mackerel were slightly less than this (0.02 ± 0.01 BL and 0.16 ± 0.01 BL, respectively). Tunabot V4's head and tail-beat amplitudes agreed well with our measured values of the yellowfin tuna and mackerel.

3.4.7 *Strouhal Number*

The Strouhal number (St) is a useful metric for characterizing the oscillatory flow in the wake of a fish [225] and relates the tail-beat frequency, tail-beat amplitude, and swimming speed (see Equation (24)). Tunabot V4's St (Figure 3-11(F)) decreased as swimming speed increased. Fishes demonstrated a similar trend [225]. Tunabot V4 reached its minimum St of 0.43 ± 0.06 at a swimming speed of 3.22 ± 0.08 BL/s. At higher speeds, Tunabot V4's St settled near 0.45. For comparison purposes, we calculated the St of steadily swimming yellowfin tuna and mackerel using data provided by Lauder Laboratory (see Section 3.3.3). The average ($n = 20$) St s of the yellowfin tuna and mackerel were 0.45 ± 0.06 and 0.50 ± 0.06 , respectively. Tunabot V4's St s were similar to these values, demonstrating fish-like performance.

However, our St values for Tunabot V4, yellowfin tuna, and mackerel were slightly above the 0.2–0.4 St range that optimizes the propulsive efficiency of flying and swimming animals [142], [226]. Others found that a 0.25–0.35 St range optimized the propulsive efficiency of a flapping foil [202], [227]–[229]. Tunabot V4's St s were slightly greater than the range considered typical for undulatory fish swimming, suggesting that Tunabot V4 did not optimally generate thrust. A lower St could be achieved by increasing Tunabot V4's tail-beat amplitude (see Equation (24)), by adding flexibility to the caudal fin (see Section 3.5.3), and by lowering the caudal fin's effective angle of attack (see Section 3.5.4).

3.4.8 *Static Thrust and the Effective Angle of Attack*

We quantified Tunabot V4's static thrust and the associated electrical power consumption over the full performance range (Figure 3-12). The static thrust linearly increased ($R^2 = 0.997$) with tail-beat frequencies above ~ 3 Hz (Figure 3-12(A)). We excluded the lowest tail-beat

frequency (2.2 ± 0.1 Hz, $n = 3$) from the linear fit because the body oddly rolled from side to side. This rolling motion also occurred during self-propelled performance testing at the lowest tail-beat frequency (see Section 3.4.4). The maximum static thrust was 3.28 ± 0.08 N ($n = 3$). For a given duty cycle of the PWM voltage input, tail-beat frequencies were about 0.5 Hz lower when measuring the static thrust compared to the self-propelled conditions (Figure 3-12 vs. Figure 3-11, respectively). This slight decrease indicated that hydrodynamic loads on Tunabot V4 were greater when flapping in place in the stationary water tank compared to self-propelled swimming in the flow tank. As a result, the electrical power consumption of static thrust was higher by ~ 2 W compared to self-propelled conditions at the highest tail-beat frequencies (Figure 3-12(B) vs Figure 3-11(C), respectively). Power quadratically increased ($R^2 = 0.998$) with the tail-beat frequency as before (see Figure 3-11(C)).

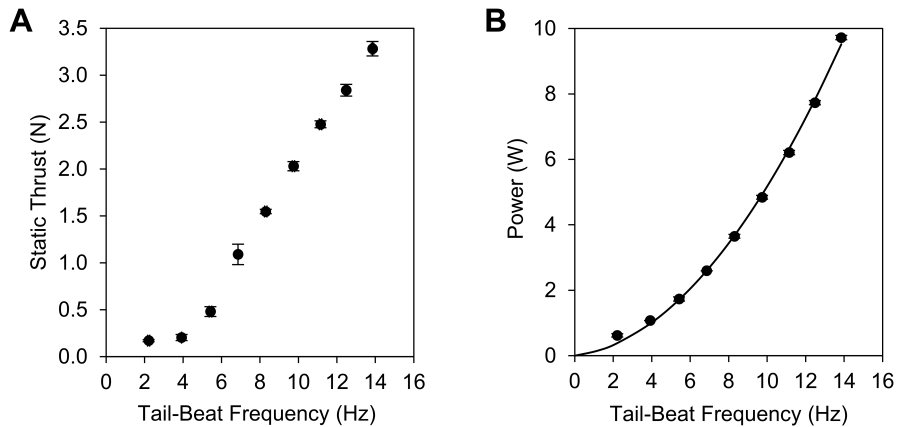


Figure 3-12: Static thrust and the associated electrical power consumption of Tunabot V4. We simultaneously measured Tunabot V4’s static thrust and the total electrical power consumption of Tunabot V4’s motor. **(A)** The static thrust linearly increased with the tail-beat frequency ($R^2 = 0.997$) above ~ 3 Hz. **(B)** The power quadratically increased with the tail-beat frequency ($R^2 = 0.998$). Data points represent the mean \pm 95% CI ($n = 3$).

The static thrust of Tunabot V4 varied throughout a single tail-beat period (Figure 3-13(A)). Static thrust sharply increased as the peduncle accelerated away from its leftmost position towards the body’s centerline. When the caudal fin swept past the body’s centerline (i.e.,

mid-stroke), static thrust briefly peaked. At mid-stroke, the peduncle velocity was at a maximum (see Figure 2-2(B)). Static thrust then dramatically diminished throughout the second half of the tail-beat period as the peduncle decelerated. A transition phase occurred before the tail swept back in the opposite direction. During this transition, the static thrust slightly increased twice while the caudal fin's direction reversed. Also, the static thrust's magnitude was low due to the

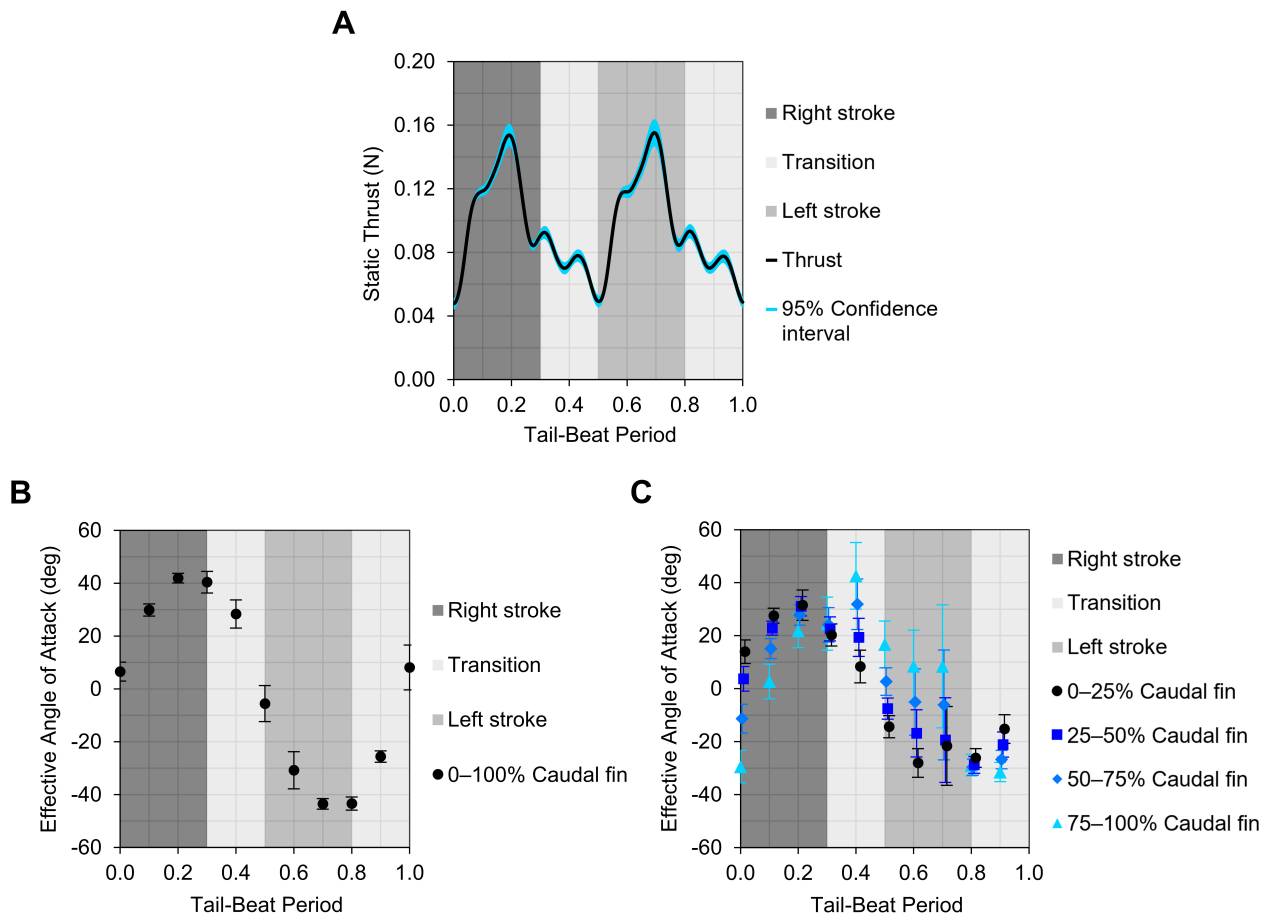


Figure 3-13: Static thrust and the effective angle of attack of Tunabot V4 and mackerel. (A) Tunabot V4's static thrust cyclically varied as its tail swept back and forth. Two thrust peaks occurred per tail-beat period when the caudal fin swept past the body's centerline (i.e., mid-stroke). We generated the plot above by averaging consecutive tail-beat periods ($n = 9$) that all had 3.9 Hz tail-beat frequencies (i.e., 30% duty cycle of the PWM voltage input). The blue-shaded region represents the 95% CI. (B) The effective angle of attack of Tunabot V4's caudal fin varied approximately sinusoidally throughout each tail-beat period. We modeled Tunabot V4's rigid caudal fin as a single flat panel. The plot above corresponds to a tail-beat frequency of 3.8 ± 0.4 Hz (i.e., 30% duty cycle of the PWM voltage input) and a speed of 0.78 ± 0.04 BL/s (0.20 m/s). Data points represent the mean \pm 95% CI ($n = 3$). (C) We modeled the mackerel's flexible caudal fin as four flat panels spaced equally along its length. The effective angle of attack of each quarter panel also varied approximately sinusoidally but over a smaller range compared to Tunabot V4. The plot above corresponds to a similar tail-beat frequency of 3.7 ± 0.4 Hz and a speed of 1.21 ± 0.05 BL/s (0.28 m/s). Data points represent the mean \pm 95% CI ($n = 20$).

low relative velocity between the caudal fin and fluid. The overall process then repeated itself as the tail beat from right to left, completing one tail-beat period back and forth.

The static thrust curve was highly consistent across tail-beat periods as indicated by the narrow 95% CI (blue-shaded region in Figure 3-13(A)). We used the periodicity of the recorded, 5-second thrust signal to calculate Tunabot V4's 3.9 Hz tail-beat frequency, which corresponded to 30% duty cycle of the PWM voltage input. Static thrust was nonzero at all times which indicated that Tunabot V4's flapping motion continuously generated thrust, including the transition phases. However, static thrust is not the same as self-propelled thrust (see Section 3.5.4), so our results were not wholly applicable to the self-propelled results (see Figure 3-11).

The average thrust coefficient across the tested range was 0.23 ± 0.03 ($n = 24$). We found this coefficient by using the static thrust (Figure 3-12(A)) and corresponding self-propelled velocities (see Figure 3-11(A)). We excluded the lowest tail-beat frequency from the average due to Tunabot V4's body oddly rolling at that frequency. Throughout a single tail-beat period, the thrust coefficient oscillated between 0.08 and 0.27. We calculated this range by using the static thrust of Figure 3-13(A) and the self-propelled velocity at the same 30% duty cycle input (0.20 m/s).

We analyzed the caudal fin's effective angle of attack as it varied throughout a single tail-beat period for both Tunabot V4 and the mackerel (Figure 3-13(B)–(C)). For comparison purposes, we selected similar tail-beat frequencies: 3.8 ± 0.4 Hz ($n = 3$) for Tunabot V4 and 3.7 ± 0.4 Hz ($n = 20$) for the mackerel. The swimming speeds associated with these frequencies were 0.78 ± 0.04 BL/s ($n = 3$) for Tunabot V4 (25.5 cm BL) and 1.21 ± 0.05 BL/s ($n = 20$) for the similarly sized mackerel (23 cm BL). For completeness, we also examined Tunabot V4's static thrust (Figure 3-13(A)) at a similar tail-beat frequency (3.9 Hz). We modeled Tunabot V4's rigid

caudal fin as a flat panel. Each data point in Figure 3-13(B) represents the panel's effective angle of attack (see α_e in Figure 3-7). We discretized the mackerel's flexible caudal fin into four flat panels to determine how the effective angle of attack varied along its length. Each of the four sets of data points in Figure 3-13(C) corresponds to one of these panels, where '0–25%' is the panel nearest to the peduncle joint and '75–100%' is the trailing-edge panel.

The effective angle of attack of Tunabot V4's caudal fin followed a sinusoidal-like profile throughout the tail-beat period (Figure 3-13(B)). The profile's magnitude repeated twice per tail-beat period, resembling the static thrust. We expected this due to the tail's symmetrical motion back and forth. The maximum amplitude of the caudal fin's tip occurred at 0.4 and 0.9 of the tail-beat period. At 0.2 and 0.7 of the tail-beat period, the caudal fin passed the body's centerline with maximum absolute values of its effective angle of attack ($\pm \sim 43^\circ$). For a sense of the velocity vectors and angles at this instant, Figure 3-7 illustrates Tunabot V4's tail flapping leftward near mid-stroke (i.e., ~ 0.2 of the tail-beat period). The mackerel's mid-stroke and maximum values also coincided with 0.2 and 0.7 of the tail-beat period (Figure 3-13(C)). In contrast to Tunabot V4, the mackerel's effective angle of attack oscillated over a smaller range ($\pm \sim 32^\circ$) except during the transition phase when the angle of the trailing edge reached 43° . For the mackerel, the range in values of the effective angle of attack cyclically increased towards mid-stroke and decreased towards transition. At the end of the stroke (i.e., beginning of the transition phase), the angles of all four caudal fin segments converged to $\pm \sim 26^\circ$. In other words, the angles were uniform over the entire length of the flexible caudal fin. Such uniformity was remarkable considering the considerable curvature of the mackerel's caudal fin (see Figure 3-10(I)). At all other times, the four segments' effective angles of attack appeared to be stacked sequentially from the flexible caudal fin's leading edge to its trailing edge (Figure 3-13(C)).

3.4.9 Thrust after Caudal Fin Removal

We performed a simple experiment to determine the propulsive contribution of Tunabot V4's caudal fin (Figure 3-14). We tested the swimming performance of Tunabot V4 after removing its peduncle-caudal fin assembly (see Figure 3-1(B)). Previously, we found that Tunabot V2 was unable to generate thrust without its caudal fin (see Section 2.3.6), so we were interested in revisiting this experiment with Tunabot V4 to see if its higher tail-beat frequencies (15 vs. 8 Hz, approximately) would make a difference. We tethered Tunabot V4 without its peduncle-caudal fin assembly in the University of Virginia's flow tank. We tested Tunabot V4's full range of tail-beat frequencies as before (see Section 3.3.1). Turning on the flow tank proved unnecessary because Tunabot V4's swimming velocity was zero for all tested frequencies; in stationary water, Tunabot V4 did not progress in any direction with its caudal fin removed. As such, the caudal fin alone generated the propulsive thrust of Tunabot V4. This result confirmed our previous findings regarding Tunabot V2. This result also supported the simple model in which a fish's caudal fin was thrust-producing, and all other body parts were drag-producing [190], [197], [198], [230]. This model was convenient for demonstrating the lift-based

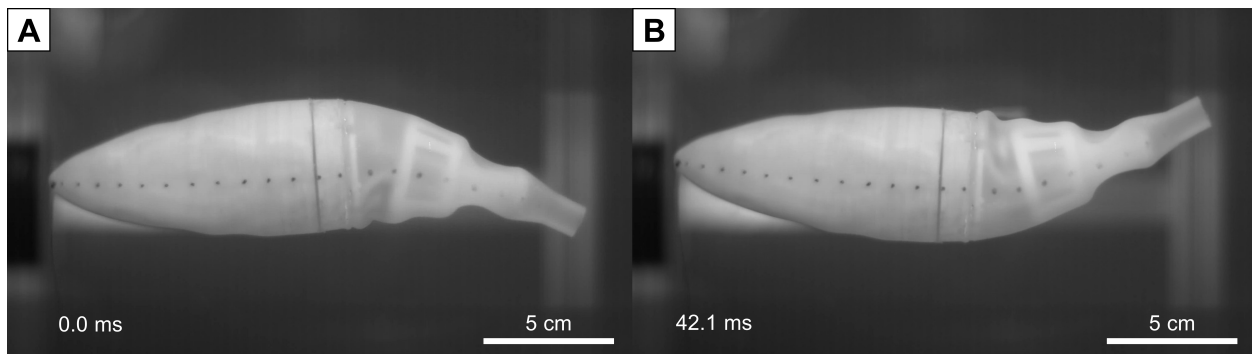


Figure 3-14: No propulsion without the caudal fin of Tunabot V4. Tunabot V4 was unable to swim forward without its peduncle-caudal fin assembly (see Figure 3-1(B)). Testing occurred in the University of Virginia's flow tank with zero flow velocity. (A), (B) Two frames from ventral-view, high-speed video showing both lateral extremes of Tunabot V4's tail flapping at a tail-beat frequency of 11.9 Hz (i.e., 80% duty cycle of the PWM voltage input).

propulsion of a caudal fin (see Section 3.3.6) and explained Tunabot V4's lack of thrust after we removed its caudal fin. However, the reality is that fish are able to swim with a severely lacerated tail [200] or without a caudal fin entirely [199], [200].

Breder [199] and Gray [200] amputated the caudal fins of fishes to determine the consequent impact on swimming ability. Breder found that amputating the caudal fin of a rudd (*Scardinius erythrophthalmus*) did not affect its top speed over a distance of 2.4 m, but the tail-beat frequency and amplitude increased. He further observed that the rudd required more effort to swim and concluded correctly that the caudal fin must be associated with the efficiency of locomotion. Based on this, Breder predicted that the rudd amputee would fall short over a greater distance compared to an intact companion. Gray amputated the caudal fin of a whiting (*Gadus merlangus*) and observed that its cruising speed was nearly unaffected although with markedly different body kinematics. Gray also estimated that the whiting's caudal fin contributed about 40% of the total thrust produced. Beal et al. took these sorts of experiments to their conclusion when they discovered that a dead fish can passively 'swim' upstream; the flexible body of a lifeless fish extracts energy from oncoming flow when resonating with Kármán street vortices [231].

Both Breder and Gray observed that fishes automatically compensated for a compromised caudal fin by modifying their swimming kinematics and by generating thrust with their bodies. Conversely, Tunabot V4 was incapable of adaptation because of its prescribed kinematics, and its body did not produce thrust regardless of the tail-beat frequency. This differed from the next Tunabot generation (Tunabot V5) and its more flexible body, whose caudal fin was not the only thrust-producing surface; Tunabot V5's posterior body and caudal fin both generated thrust during linear accelerations from rest [170].

3.4.10 *Caudal Fin Wake Flow Patterns*

Tunabot V4 produced a reverse von Kármán street wake (Figure 3-15(A)). Leading-edge vortices were also evident on Tunabot V4's caudal fin for all tested swimming speeds (Figure 3-15(B)–(C)). A leading-edge vortex began to form on the caudal fin after the tail transitioned between beat directions (i.e., the tail-beat period's beginning). As the caudal fin swept towards the midline, the vorticity grew until maximized just past the midline. Then the vortex traveled posteriorly along the caudal fins' surface and shed from the surface entirely before the tail began to transition between beat directions. Each beat of the tail generated and shed a new, alternately rotating leading-edge vortex, producing a classic reverse von Kármán street in the wake.

Tunabot V4's leading-edge vortex and vortex wake were emblematic of fish swimming. Numerical simulations showed that attached leading-edge vortices formed on the caudal fins of fish [154]. Furthermore, the reverse von Kármán street is a hallmark of fish swimming [75], [167], [169], [203]. Tunabot V4's PIV results visualized both phenomena, suggesting that Tunabot V4's kinematics and morphology resulted in fish-like propulsion. These results also agreed with those of free-swimming Tunabot V2's wake-visualization experiment (see Section 2.3.4).

We expected that the leading-edge vortex contributed to thrust for three reasons. First, the shed vortices formed a reverse von Kármán street in the wake, which is indicative of thrust production [169], [190], [201], [202]. Second, the flapping direction of the tail in Figure 3-15(B)–(C) corresponds to Figure 3-7. This shows that the leading-edge vortex was present while the caudal fin had a thrust-producing effective angle of attack. Third, the vorticity of the leading-edge vortex grew during the portion of the tail-beat period wherein the static thrust increased to a maximum (see Figure 3-13(A)). These three reasons provided insight into the propulsive fluid mechanisms of Tunabot V4 and, therefore, fish swimming.

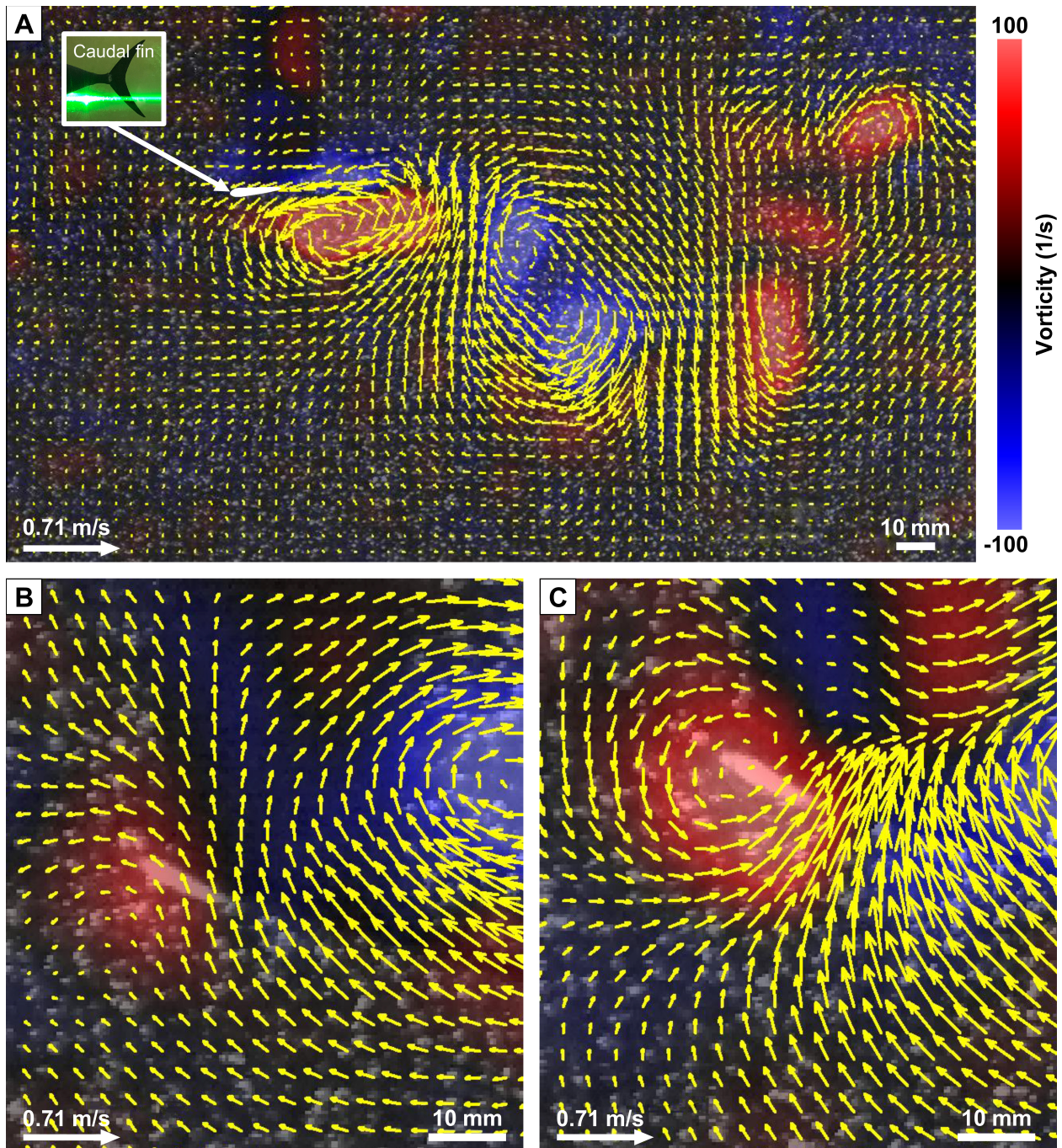


Figure 3-15: Visualized flow field in the wake and around the tail of Tunabot V4. PIV data at the quarter-span of Tunabot V4's caudal fin revealed the velocity field (yellow arrows) and vorticity (red/blue regions) of the flow. Tunabot V4 steadily swam at 0.71 m/s (i.e., 60% duty cycle of the PWM voltage input) in the flow tank at Harvard University. The vorticity scale (top right) applies to all three images, and mean free-stream flow was subtracted. **(A)** A reverse von Kármán street was visible in the generated wake with counter-rotating vortices and high-velocity thrust jets between shed vortex centers. For visualization purposes, we highlighted the caudal fin in white and included a picture of the experimental setup (top left, from Figure 3-8(B)). **(B)** After the tail transitioned between beat directions, a trailing vortex had just been shed (blue vorticity), and a leading-edge vortex began to develop (red vorticity). **(C)** A strong leading-edge vortex was apparent (red vorticity) 13 ms later during the second half of the tail-beat period. PIV data processing was performed by Lauder Laboratory.

3.5 Discussions

3.5.1 *Complications of the Elastomer Skin*

Tunabot V4's thin skin was unable to maintain its shape. Two circumferential ribs were added to the flapper that internally supported the skin's shape (see Figure 3-2(E)). The ribs were ineffective in preventing the skin from buckling as the tail flapped (see Figure 3-14), so the elastomer skin was tightened by stretching its posterior end over the peduncle keels (see Figure 3-1(A)). Removing slack from the skin somewhat reduced the severity of deformation. However, the tighter skin's elastic force resisted the actuation mechanism's motion and increased power consumption. Removing slack from the skin also ensured that the peduncle-caudal fin assembly stayed inserted into the flapper; the assembly was not secured into the flapper by a nut and bolt as with Tunabots V1–V3. In a final attempt to maintain the skin's shape, the skin was inflated like a balloon with water using a hypodermic needle. However, this introduced new deformations as the volume of water inside the skin sloshed about with each beat of the tail (see Figure 3-10(A)). The sloshing worsened at higher tail-beat frequencies (see Figure 4-18(A)). The rippling bulges and depressions along the skin's surface disrupted the surrounding flow; when analyzing the wake flow pattern of Tunabot V4 using PIV (see Section 3.4.10), we noticed that flow would circulate within the skin's depressions creating drag-inducing vortices.

Tunabots V1–V3 did not experience these issues because we designed their skins to completely fill the internal volume on either side of the flapper (see Figure 2-11). This approach maintained the skin's shape without the need for ribs, elasticity, or inflation. Foreseeing that the skin would resist the actuation mechanism's motion, we also designed the skins of Tunabots V1–V3 with just enough space surrounding the mid-body joint to provide unrestricted range of

motion with minimal resistance. The skin designs of Tunabots V1–V3 could have been modified to include only their posterior half as with Tunabot V4’s skin.

3.5.2 *Peduncle Stiffness*

The average head and tail-beat amplitudes varied depending on the tail-beat frequency (see Figure 3-11(E)). As the frequency increased, the head and tail-beat amplitudes decreased at different rates. We did not expect the tail-beat amplitude to vary since it was supposedly constant by design. The actuation mechanism directly oscillated the mid-body joint and peduncle back and forth with a prescribed, fixed motion (see Figure 2-1). The peduncle joint’s physical limit of rotation (18°) and torsional stiffness were also constant (see Section 3.2.1). However, the peduncle joint’s stiffness affected its rotational behavior before the physical limit was reached at a tail-beat frequency of approximately 10 Hz. Below ~ 10 Hz, the peduncle joint’s range of rotation increased with the tail-beat frequency as hydrodynamic loads on the caudal fin overcame the joint’s stiffness. As a result, the tail-beat amplitude decreased, as did the head amplitude slightly (see Figure 3-11(E)). Greater rotation of the caudal fin meant that the extremes of its lateral displacement were less, which denoted a smaller tail-beat amplitude by definition. Consequently, the body yawed less, resulting in the smaller head amplitude. At tail-beat frequencies above ~ 10 Hz, hydrodynamic forces exceeded the peduncle joint’s stiffness and reached the joint’s physical limit. This was reflected by the steadier head and tail-beat amplitudes (see Figure 3-11(E)). We further discuss the complex interactions between head amplitude, tail-beat amplitude, tail-beat frequency, body yaw, and peduncle stiffness in Sections 4.4.3 and 4.7.4 as they relate to Tunabot V5’s swimming kinematics.

3.5.3 *Caudal Fin Flexibility*

The structure and kinematics of Tunabot V4's rigid caudal fin differed from the flexible caudal fins of yellowfin tuna and mackerel. The caudal fin structure of fishes consists of bilaminar, tapered fin rays separated by a thin membrane [82], [175], [178]. This arrangement produces anisotropic flexibility with both stiff and compliant bending axes. Conversely, the manufactured caudal fin of Tunabot V4 consisted of a single piece of rigid material and thus did not replicate such biological flexibility. This difference in flexibility was apparent in the swimming kinematics; the curvature of Tunabot V4 was effectively zero in the region of its caudal fin, whereas the highest curvatures of the yellowfin tuna and mackerel occurred in that very region (see Figure 3-10(G)–(I)).

Caudal fin kinematics of fishes are a function of both active neuromuscular control and passive mechanisms. Fishes actively control their caudal fins through side-to-side flapping motion, angular rotation, and modification of surface curvature [175], [178], [217], [232], [233]. Passive mechanisms include the fluid interactions between the body and its various fins ('body-fin') and between the fins themselves ('fin-fin'). Such interactions occur between the body and the caudal fin [234], between other median fins (i.e., dorsal and anal fins) and the caudal fin [235], and between the finlets and the caudal fin [236]. A passive peduncle joint connected Tunabot V4's caudal fin to the body, so no active control was possible besides the tail's prescribed flapping motion. In regard to passive mechanisms, Tunabot V4 did not feature any fins besides the caudal fin, so fin-fin interactions were not applicable. Body-fin interactions were beyond the scope of this study. The proper addition of median fins would enhance Tunabot V4's performance by enabling fin-fin and body-fin interactions while advancing insight into the nature of such interactions.

Caudal fin flexibility is another passive mechanism that affects the caudal fin kinematics of fishes [178]. Anisotropic flexibility of the caudal fin was numerically shown to yield a higher propulsive efficiency and reduce lateral forces compared to a rigid fin with the same geometry [237]. Furthermore, for a robot fish based on bluegill sunfish (*Lepomis macrochirus*), increasing the stiffness of the caudal fin's rays produced more thrust [238] but likely at the cost of greater power consumption. Tunabot V4's caudal fin was unable to benefit from flexibility due to its rigidity. We would expect a flexible caudal fin to reduce the COT and body yaw (i.e., head amplitude) of Tunabot V4 at slower swimming speeds but require stiffening to access higher speeds. We also would expect a flexible caudal fin to produce more fish-like swimming kinematics, especially in the caudal fin region. The caudal fins of Tunabots V1–V5 were all rigid, so this discussion applies to the other Tunabot generations as well.

3.5.4 *Static Thrust and the Effective Angle of Attack*

The effective angle of attack was an important performance metric because it determined the amount of thrust produced. Specifically, the effective angle of attack provided valuable insight into the lift-based thrust generated by the pitching and heaving caudal fins of Tunabot V4 and the mackerel. However, the angle of attack, which we used to calculate the effective angle of attack (see Section 3.3.6), would have been insufficient for our thrust analyses. Nevertheless, the angle of attack is informative of fish kinematics. The angle of attack was calculated for the tails of a largemouth bass (*Micropterus salmoides*) [219] and an aquatic salamander (*Siren intermedia*) [239]. Others designed a sensor inspired by passive weathervanes to measure the angle of attack of a robotic fish's caudal fin [240]. In these three examples, the angle of attack provided valuable kinematic data concerning tail orientation relative to the body. However, to

examine tail orientation relative to oncoming flow, the effective angle of attack must be calculated. The effective angle of attack accounts for both the tail's angle of attack in addition to the relative flow velocity seen by the tail.

The effective angle of attack of Tunabot V4's caudal fin affected thrust production. Static thrust (see Figure 3-13(A)) rose and fell with the effective angle of attack (see Figure 3-13(B)). At mid-stroke, both the peduncle's velocity and the caudal fin's rotation about the peduncle joint were greatest. Together, the high velocity and extreme orientation generated the maximum effective angles of attack at mid-stroke. The two peaks of static thrust coincided with the mid-stroke as well, indicating that the effective angle of attack was related to thrust. In Section 3.3.6, we mathematically showed how the effective angle of attack determined the amount of lift-based propulsion generated by a pitching and heaving caudal fin. Our experimental findings with Tunabot V4 supported this relationship.

Our comparisons between static thrust and the effective angle of attack were imperfect, however, because static thrust is not the same as self-propelled thrust. We calculated the effective angle of attack of Tunabot V4 swimming self-propelled, whereas we measured the static thrust of Tunabot V4 flapping in place. A closer comparison would have been between self-propelled thrust and the calculated effective angle of attack. But measuring the self-propelled thrust of swimming, undulatory bodies is challenging, much like the drag (see Section 4.7.3). We carefully preserved the swimming kinematics and tethered setup of Tunabot V4's self-propelled conditions when designing the static thrust rig (see Figure 3-6). The rig did not constrain finer motions such as the body's natural yawing motion, which included the side-to-side oscillation of the head. As such, our experimental results of static thrust were representative

of self-propelled thrust. The experimental setup we developed may offer new ideas to fish roboticists and biologists alike for measuring the static thrust of undulatory, yawing bodies.

Advanced applications of computational fluid dynamics (CFD) and PIV techniques may estimate the self-propelled thrust more accurately than our static thrust rig. Using CFD, Tunabot V4 was simulated flapping in oncoming flow [230], [241]. The thrust coefficient from this simulation oscillated between approximately -0.02 and 0.12 throughout a tail-beat period. The range of our experimentally obtained coefficients of static thrust (0.08–0.27) was about twice as large and always positive. The profile of the CFD thrust coefficient was more sinusoidal in appearance than our own, but both featured two thrust peaks per period at mid-stroke of the caudal fin. The next Tunabot generation (Tunabot V5) was analyzed using PIV techniques to estimate the thrust force during acceleration from rest [170]. This thrust varied sinusoidally with positive values only and with two thrust peaks at mid-stroke, resembling our static thrust measurements of Tunabot V4. Regardless of the technique employed, three trends were evident. First, the cyclical variation of thrust throughout the tail-beat period was sinusoidal-like. Second, the thrust curve was symmetric about both halves of the tail-beat period. Third, the phase of the thrust curve was aligned such that the two maxima coincided with the caudal fin's mid-stroke. The exact values and precise waveform shape were less clear with the available data.

We would expect Tunabot V4 to swim substantially faster as a free-swimming system without tethers or external power cables. In Section 3.4.1, we concluded this by examining how the estimated tethered drag comprised 46–87% of the measured dead-drag. Here, we compare the estimated tethered drag with the measured static thrust force. A significant percentage of thrust was consumed to overcome the tethered drag. On average ($n = 9$), tethered drag was $8.2 \pm 1.3\%$ of the static thrust and ranged from 3.5% to 11%. For example, 100% duty cycle corresponded to

a self-propelled speed of 4.00 BL/s (see Figure 3-11(A)). At this speed, the estimated drag due to tethers and power cables was 0.27 N (see Figure 3-9(B)). The same 100% duty cycle generated 3.28 N of static thrust (see Figure 3-12(A)), meaning that the tethered drag was 8.2% of static thrust in this instance. This type of comparison is not absolute since self-propelled and static conditions are not perfectly equivalent (as previously discussed) and because our model for estimating drag was basic (see Section 3.3.4). Although this type of comparison is imperfect, there is no doubt that the tethers and power cables considerably impeded Tunabot V4's swimming speed.

The effective angle of attack of Tunabot V4's caudal fin affected thrust generation via leading-edge vortices. The formation and shedding of leading-edge vortices are described by the process called 'dynamic stall' (see Section 2.3.4). The leading-edge vortex on Tunabot V4's caudal fin (see Figure 3-15) was shed prematurely sometime after mid-stroke but before the tail reached its maximum lateral displacement. Two factors contributed to the early shedding of the leading-edge vortex. First, the range of the effective angle of attack ($\pm \sim 43^\circ$) was high. This range exceeded that of the mackerel by $\sim 10^\circ$. The effective angle of attack determines the behavior of leading-edge vortices during dynamic stall. This includes vortex detachment from the lift surface after a sufficiently high angle is reached (i.e., the 'critical' angle). A smaller range of effective angles of attack would have prolonged the attachment of the leading-edge vortex. This could be accomplished by decreasing the peduncle joint's rotation limit. Second, Tunabot V4's caudal fin was rigid and thus had one overall effective angle of attack. For mackerel, however, the effective angle of attack varied along the length of its flexible caudal fin. The curvature of a flexible caudal fin also produces a leading-edge vortex but delays its shedding, enhancing thrust and propulsive efficiency. Vortex shedding is delayed by prolonging the

duration of vortex attachment to the caudal fin. Doing so is advantageous because thrust was shown to generate only during the time of vortex attachment for a simulated pitching-heaving airfoil [242], and thrust decreases precipitously once the vortex is shed into the wake.

Consequently, the mackerel produced more thrust than Tunabot V4 as indicated by its greater stride length (0.33 vs. 0.21 BL) despite their similar tail-beat frequencies (3.7 vs. 3.8 Hz). Tuning the flexibility of a yellowfin tuna's caudal fin was shown to directly affect the behavior of leading-edge vortices [243], so a flexible caudal fin could enhance Tunabot V4's thrust.

Furthermore, an actively stiffened peduncle joint could optimize the effective angle of attack throughout the tail-beat period; modifying the peduncle joint's stiffness to cyclically vary throughout the tail-beat period could potentially sustain higher thrust by maintaining a higher, more level thrust curve compared to Figure 3-13(A). Our thrust analysis focused primarily on the caudal fin, but other aspects of Tunabot V4's body could be modified to enhance thrust as well.

The anterior body of carangiform fishes produced thrust in a manner resembling the leading-edge suction mechanics on airfoils [244]. After Tunabot V4, we found that Tunabot V5's posterior body and caudal fin both generated thrust during linear accelerations from rest [170].

There are several approaches to enhancing thrust production that take inspiration from biology.

Chapter 4

Tunabot V5: Body Flexibility Improves High-Performance Swimming

4.1 Overview

In Chapter 4, we present two studies [106]. In our first study, we design and test Tunabot V5 (‘Tunabot Flex’) to investigate the impact of body flexibility on swimming performance. The two-jointed designs of Tunabots V1–V4 produced midline kinematics that lacked the smooth curvature exhibited by yellowfin tuna, so we hypothesize that modeling such curvature in a tuna-inspired system would improve its swimming performance. For our approach, we compare the swimming performance of three different body flexibility configurations using the Tunabot V5 experimental platform. We quantify Tunabot V5’s performance in terms of metrics used for fish swimming, enabling us to directly compare our results with data for tunas and other fishes. In our second study, we compare the swimming performance of Tunabot V5 against its predecessor, Tunabot V4. To do so, we design and test a specialized configuration of Tunabot V5 that does not benefit from increased body flexibility and has the same tail-beat amplitude as Tunabot V4. This ensures that the comparisons we make are reasonable and that performance differences are

due to mechanical design rather than kinematics. These two studies demonstrate how we enhance both bio-inspired and mechanical designs together to further close the performance gap between high-performance fish and fish-like robotic systems.

4.2 Tunabot V5: ‘Tunabot Flex’

4.2.1 *Design and Fabrication*

We designed Tunabot V5 (Figure 4-1(A)) to investigate the impact of body flexibility on swimming performance, hence the name ‘Tunabot Flex’ [106]. The two-jointed designs of Tunabots V1–V4 produced midline kinematics that lacked the smooth curvature exhibited by yellowfin tuna (e.g., Figure 2-15 and Figure 3-10), so we hypothesized that modeling such curvature in a tuna-inspired system would improve its swimming performance. We created the Tunabot V5 experimental platform to test our hypothesis with three different body flexibility conditions. We varied Tunabot V5’s degree of body flexibility by incorporating two, three, and four body joints in total. In other words, we varied Tunabot V5’s degrees of freedom (DOF) by modifying its number of joints to produce three body flexibility configurations: 2 DOF Flex, 3 DOF Flex, and 4 DOF Flex (Figure 4-1(B)). In conjunction with the number of joints, we also varied the joints’ angles of rotation and positions. We determined Tunabot V5’s joint parameters (Table 4-1) by modeling the midline kinematics of steadily swimming yellowfin tuna from video footage recorded by Lauder Laboratory (see Section 3.3.3). Tunas have numerous intervertebral joints that permit lateral bending along the body’s midline [82], [126], [130], [245]. Tunabot V5’s multi-joint design with lateral rotation provided a simple model for investigating the complex internal anatomy and flexibility of tunas. The multi-joint design also caused the lateral deflection of Tunabot V5’s tail to increase posteriorly as with fish [219], which was previously

accomplished using servo-driven tensegrity structures [132], [246], [247]. To isolate the effects of variable body flexibility, we carefully selected Tunabot V5's joint parameters such that the tail-beat amplitude was constant. The caudal fin's trailing edge measured 69 mm (i.e., 0.27 BL) laterally from the neutral midline for all three body flexibility configurations (Figure 4-1(B)).

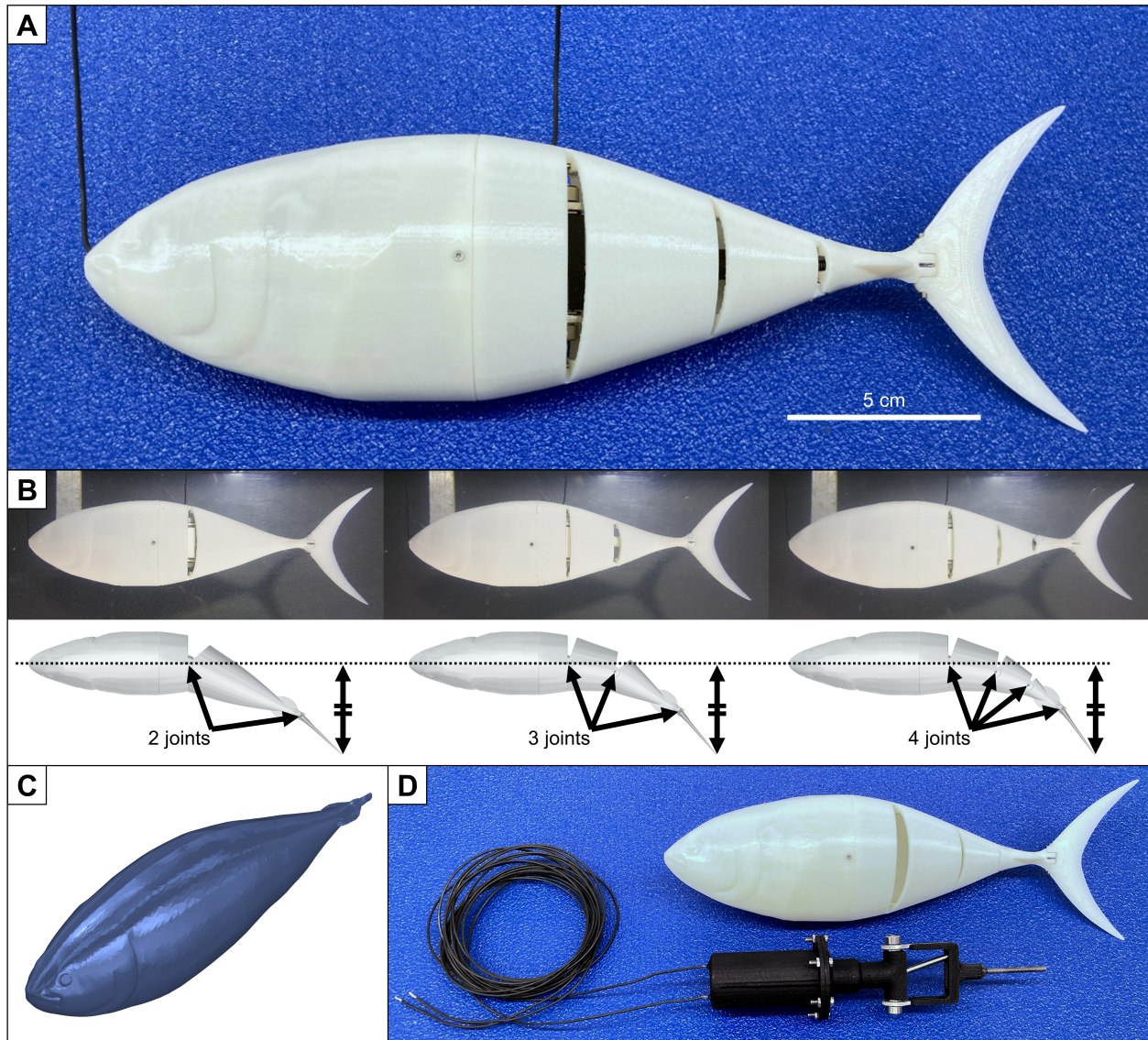


Figure 4-1: Design of Tunabot V5. (A) We created Tunabot V5 ('Tunabot Flex') to investigate the impact of body flexibility on swimming performance. (B) Tunabot V5's three body flexibility configurations differed by the number and rotation angles of their joints (Table 4-1). Tail-beat amplitude was constant by design. (C) We incorporated this μ CT scan of yellowfin tuna directly into Tunabot V5's body to preserve biological morphology and features. The scan was provided by Lauder Laboratory. (D) Tunabot V5's powertrain was removable from the exterior body, and all parts were accessible for servicing.

To effectively test body flexibility, Tunabot V5’s exterior consisted of rigid segments connected by joints. Physical gaps were necessary between body segments for the joints to rotate, and the size of these gaps determined the rotation angles of the joints (Table 4-1). These gaps did not significantly affect our results (see Section 4.4.2). To isolate the performance differences due to body flexibility, we did not create a flexible skin for Tunabot V5. Flexible skins are commonplace in the designs of robotic fish, including Tunabots V1–V4, but Tunabot V5’s results demonstrated that soft materials are not required for high performance (see Section 4.7.10) and may even be detrimental (see Section 4.7.11).

Table 4-1: Joint parameters of Tunabot V5’s three body flexibility configurations. The design parameters of Tunabot V5’s joints defined the three body flexibility configurations. These parameters were the total number of joints, the joints’ angles of rotation (symmetrically away from a straight midline), and the joints’ positions along the length of the body (as measured from the snout).

Configuration	Joint 1 (Mid-Body)		Joint 2		Joint 3		Joint 4 (Peduncle)	
	Angle (°)	Position (BL)	Angle (°)	Position (BL)	Angle (°)	Position (BL)	Angle (°)	Position (BL)
2 DOF Flex	25	0.47	-	-	-	-	18	0.84
3 DOF Flex	10	0.47	21.5	0.61	-	-	18	0.84
4 DOF Flex	10	0.47	12	0.61	14	0.72	18	0.84

In addition to body flexibility, we advanced the bio-inspired design of Tunabot V5 by improving the biological accuracy of its body morphology. We determined the anatomical dimensions of Tunabot V5’s body using a 3D reconstruction of yellowfin tuna (Figure 4-1(C)). Specifically, Lauder Laboratory utilized a micro-computed tomography (μ CT) scanner (SkyScan 1173, Bruker Corp., Billerica, MA, USA) and software (Mimics 17.0, Materialise NV, Leuven, BEL) to reconstruct a 3D model of yellowfin tuna (6–30 μ m voxel size, 30–80 kV, 120–200 mA). Tunabot V5’s head segment incorporated this reconstruction without alteration, so physical features of the scanned yellowfin tuna were evident including its eyes, gills, and mouth. We

divided the reconstruction's posterior half into segments to vary Tunabot V5's body flexibility, and we incorporated the keeled peduncle [82] into our design as well. The end result was a system that thoroughly modeled the morphology and kinematics of yellowfin tuna.

Tunabot V5 measured 25.5 cm in length, 4.8 cm in width, and 6.8 cm in height (8.8 cm including the caudal fin) with an unsubmerged mass of 0.190 kg. This size was comparable to juvenile tuna [183]. We intentionally selected lightweight materials to minimize the rotational inertia of the actuation mechanism and tail. We fabricated the head segment, body segments, flapper, and caudal fin in ABS plastic using a 3D printer (Stratasys F370) with 0.0100-inch slice height. We machined the flapper eyelets from aluminum with the help of Sebring Smith using a waterjet cutter (Maxiem 1515, Omax Co., Kent, WA, USA) at the University of Virginia. All parts were accessible and replaceable (Figure 4-1(D)) including the motor (Actobotics model 638358), although no parts needed replacing throughout testing. The high-aspect ratio and the airfoil-shaped (NACA 0016) chordwise cross-section of Tunabot V5's caudal fin closely matched the geometry of a tuna's caudal fin [82]. Many of the anisotropic properties and degrees of freedom that are present in tuna were beyond the scope of this study including caudal fin flexibility (see Section 3.5.3), active neuromuscular control of the caudal fin [217], details of internal caudal fin structure and fin rays [82], [175], and adjustable body stiffness [248]–[251].

We designed Tunabot V5's three body joints and one peduncle joint to be extremely compact in order to fit them all while leaving enough internal space for the actuation mechanism. We also designed the joints to be robust in order to withstand the forces and fatigue associated with high tail-beat frequencies. Tunabot V5's body joints consisted of pairs of thin, stainless-steel joint tabs embedded into the body segments that rotated about set screws. For example, 4 DOF Flex had three body segments and six joint tabs in total (Figure 4-2(E)). We machined the

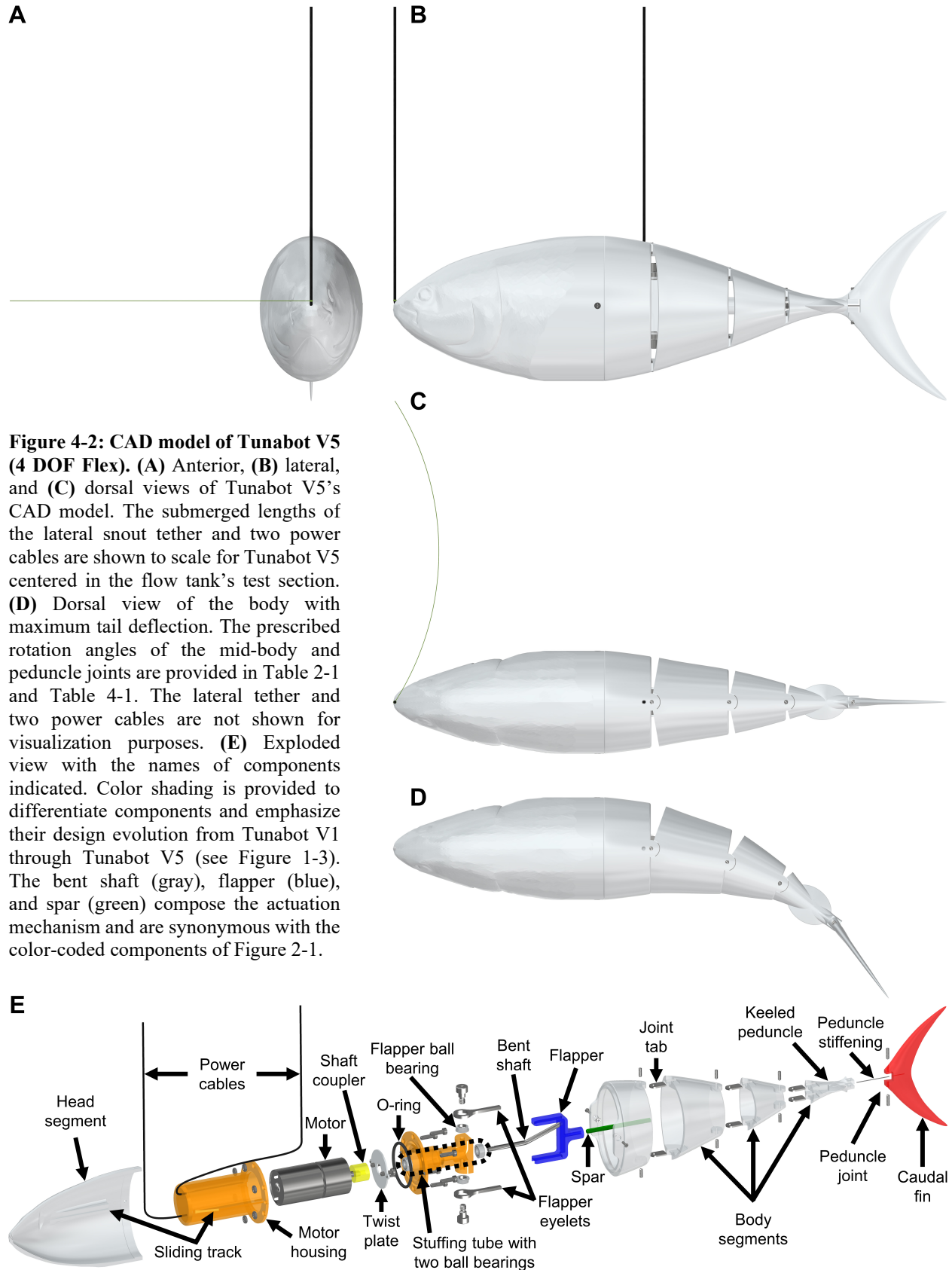


Figure 4-2: CAD model of Tunabot V5 (4 DOF Flex). (A) Anterior, (B) lateral, and (C) dorsal views of Tunabot V5's CAD model. The submerged lengths of the lateral snout tether and two power cables are shown to scale for Tunabot V5 centered in the flow tank's test section. (D) Dorsal view of the body with maximum tail deflection. The prescribed rotation angles of the mid-body and peduncle joints are provided in Table 2-1 and Table 4-1. The lateral tether and two power cables are not shown for visualization purposes. (E) Exploded view with the names of components indicated. Color shading is provided to differentiate components and emphasize their design evolution from Tunabot V1 through Tunabot V5 (see Figure 1-3). The bent shaft (gray), flapper (blue), and spar (green) compose the actuation mechanism and are synonymous with the color-coded components of Figure 2-1.

joint tabs with the help of Sebring Smith using a waterjet cutter (Maxiem 1515). The peduncle joint connected the keeled body segment and caudal fin together through pinned rotation about a pair of set screws. A single, internal spring wire provided torsional stiffness to the peduncle joint and a passive restoring force that returned the caudal fin to its neutral (0°) position. Like the bilateral elastic bands of Tunabots V1–V4, this new design imitated the function of lateral tuna tendons [126], [131], [252].

We applied the actuation mechanism (see Section 2.2.1) in a new way that enabled its single-motor design to drive multiple joints with wave-like motion down the body. This was necessary for creating the different body flexibility conditions. The actuation mechanism only flapped a single mid-body joint previously (Tunabots V1–V4). However, Tunabot V5 featured up to three body joints depending on the configuration. These joints were actuated posteriorly by the keeled peduncle body segment, which was directly driven by the actuation mechanism's spar. The spar's tip slid laterally inside a slot within the peduncle segment, permitting the body's full range of lateral flexion; directly fixing the spar tip to the peduncle segment would have restricted bending motion due to the body's increasing curvature towards the tail. The peduncle joint, which was part of the peduncle segment, passively rotated behind the actively driven body joints. This differed from all the previous Tunabot designs in which the peduncle joint was part of the spar rather than a separate segment. The peduncle segment added a mediating degree of freedom between the spar and peduncle joint.

Our novel design made it possible for the actuation mechanism to laterally oscillate a variable number of joints using just a single rotary motor. Furthermore, the design replicated the propulsive wave of bending that passes posteriorly along a fish's body [110]–[112], [253]. By design, Tunabot V5's joints rotated in succession with wave-like motion down the body. We

achieved this by transmitting the spar's motion posteriorly to the freely rotating body joints. While driving the tail from its rear may seem counterintuitive, we utilized the hydrodynamic forces during swimming to sequentially rotate the body segments from head to tail, creating a traveling kinematic wave resembling fish undulation. Without these forces (e.g., in air), the traveling wave was nonexistent. The passive peduncle joint followed suit to complete the wave-like motion through the caudal fin. Together, the joints and actuation mechanism modeled the kinematics of yellowfin tuna.

We tethered Tunabot V5 in Lauder Laboratory's flow tank for testing. A thin, flexible thread (Spectra Power Pro fishing line) loosely connected Tunabot V5's snout laterally to the test section's side wall. Tunabot V5's two flexible power cables suspended its body in the test section's center from an overhead rig. These two power cables exited the head segment at the snout and 116 mm aft of the snout. To control speed and measure power consumption, we wired the power cables to a new controller and data acquisition system (see Section 4.3.2). Tunabot V5's power cables doubled as vertical tethers, which differed from Tunabots V2–V4. The tethered configuration of Tunabot V5 was simpler than before having two fewer tethers, which reduced drag and improved the experimental setup's likeness to untethered swimming.

4.2.2 *Waterproofing Methods*

The waterproofing methods of Tunabot V5 substantially differed from those of Tunabots V1–V4, significantly advancing the design. Tunabot V5 was a complete redesign that included new waterproofing methods. These methods were necessary to achieve Tunabot V5's compact dimensions and modularity. Waterproofing resided at the core of Tunabot V5's design, as with Tunabots V1–V4. However, unlike its predecessors, we waterproofed only the motor housing of

Tunabot V5 and not the head segment (see Figure 4-2(E)). This was possible because the drivetrain, which included the motor housing, became a distinct and fully removable entity (see Figure 4-1(D)). Conversely, the actuation mechanisms of Tunabots V1–V4 were incorporated into their bodies. Tunabot V5's entire body, including the head segment, flooded with water around the waterproof motor housing. We waterproofed the motor housing using three methods: 3D-printed nylon, a rubber O-ring, a 'stuffing tube' with two ball bearings, and epoxy.

The motor housing was composed of two halves of selective laser sintering (SLS) 3D-printed nylon PA12 with 60 μ resolution and 2 mm wall thickness. With these parameters, this material was sufficiently waterproof and thus incredibly convenient compared to the silicone-injection method (see Section 2.2.3), XTC-3D coating (see Section 2.5.2), and acetone smoothing (see Section 2.5.2). We designed the motor housing to accommodate an off-the-shelf rubber O-ring. Doing so avoided the need to cast a custom silicone O-ring (Tunabots V1, V2, and V4) or create a permanent seal with epoxy (Tunabot V3). Six longitudinal screws compressed the rubber O-ring between the motor housing's two halves (Figure 4-2(E)). An additional two longitudinal screws on both lateral sides secured the motor housing to the head segment and did not meaningfully compress the O-ring. A stuffing tube and two ball bearings (black, dashed oval in Figure 4-2(E)) waterproofed the actuation mechanism's rotating bent shaft, which protruded from inside the motor housing. The stuffing tube consisted of a cylindrical volume packed with petroleum jelly inside the posterior half of the motor housing. A ball bearing at each end of the volume centered the rotating shaft and held the jelly in place. Waterproofing techniques used to seal the driveshafts of motorboats inspired our stuffing tube design. Tunabots V1–V4 utilized silicone compression seals to waterproof the rotating shaft (see Section 2.2.3), which experienced significant frictional losses due to the snug fit of the elastic

silicone around the shaft. Tunabot V5's stuffing tube traded silicone for petroleum jelly with a marked improvement in efficiency without compromising waterproofness. We sealed the two holes where the motor's power cables exited the anterior side of the motor housing using beads of epoxy. Altogether, the 3D-printed nylon, rubber O-ring, stuffing tube, and epoxy waterproofed Tunabot V5's motor.

4.3 Body Flexibility Experiment: Materials and Methods

4.3.1 Performance Testing Protocol

We investigated the impact of body flexibility on high-performance fish swimming using the Tunabot V5 experimental platform. We conducted this experiment at Harvard University in September 2019. We tested three body flexibility configurations of Tunabot V5, which we compare in Figure 4-3. To create these three configurations, we simply swapped out the modular

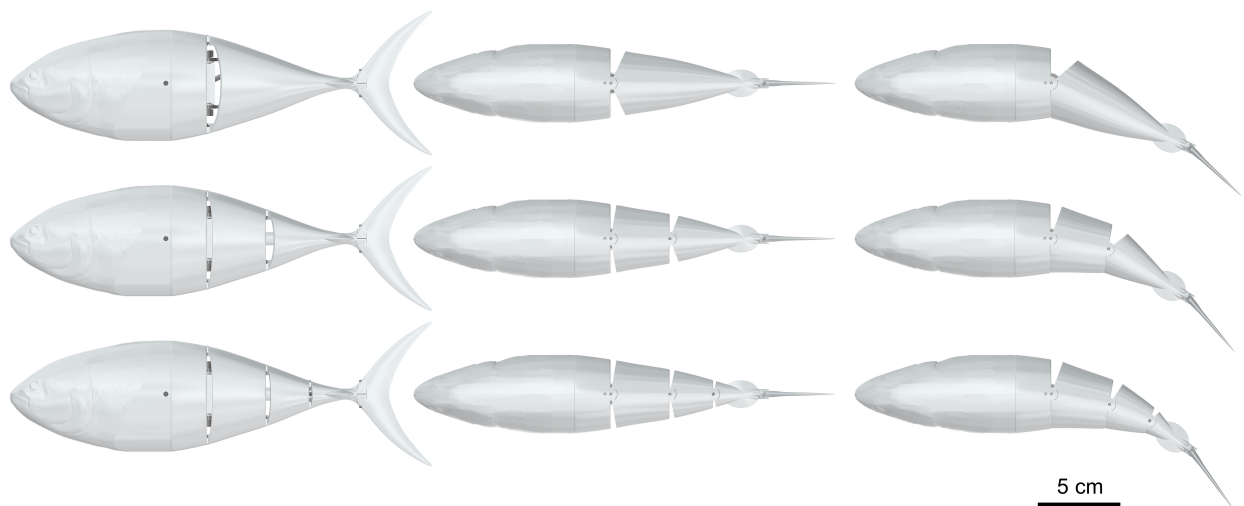


Figure 4-3: Design comparisons of Tunabot V5's three body flexibility configurations. Here we compare the designs of Tunabot V5's three body flexibility configurations: **(from Top to Bottom)** 2 DOF, 3 DOF, and 4 DOF Flex. For visual comparisons, we show three different views of their CAD models: **(from Left to Right)** lateral views, dorsal views with straight midlines, and dorsal views with maximum tail deflections. Tunabot V5's three body flexibility configurations differed by the number and rotation angles of their joints (Table 4-1). The lateral tether and two power cables are not shown for visualization purposes.

body segments to vary the number and rotation angles of the body joints (see Table 4-1). We previously used modular parts to research aspects of fish swimming, specifically peduncle stiffness, with Tunabot V2 (see Section 2.3.3). We distinguished between Tunabot V5's three body flexibility configurations by their number of joints, or degrees of freedom (DOF): 2 DOF Flex, 3 DOF Flex, and 4 DOF Flex. Across these three configurations, their dimensions, mass, and all other components such as the drivetrain and motor were constant.

The testing facility we used was Lauder Laboratory's flow tank from previous fish research [185]–[188] and our performance study of Tunabot V4 (see Section 3.3.1). The flow tank's test section had wetted dimensions of $90 \times 28 \times 28$ cm (length \times width \times height) and a flow speed range of 0–1.25 m/s. Two flexible power cables suspended the negatively buoyant Tunabot V5 in the test section's center from an overhead rig (Figure 4-4). The projected area of Tunabot V5 (2570 mm^2) occupied 3.3% of the test section's cross-sectional area, thus minimizing wall and blockage effects. To control swimming speed and measure electrical power consumption, we wired the two power cables to a new, external system that we positioned adjacent to the flow tank (see Section 4.3.2). A thin, flexible thread (Spectra Power Pro fishing line) loosely connected the snout to the test section's side wall in order to prevent extreme lateral deviations from the center. This lateral tether attached near the bottom of an aluminum bar with 2 mm thickness clamped vertically to the test section wall. This tethered arrangement did not hinder streamwise, lateral, or yaw motion of any part of Tunabot V5 except for streamwise drag (see Section 4.4.2) and was, therefore, representative of free swimming. This tethered arrangement was also simpler than the previous setups of Tunabots V2–V4 (see Sections 2.4.3, 2.5.1, and 3.3.1, respectively); Tunabot V5's setup required two fewer tethers because its two power cables doubled as vertical tethers.

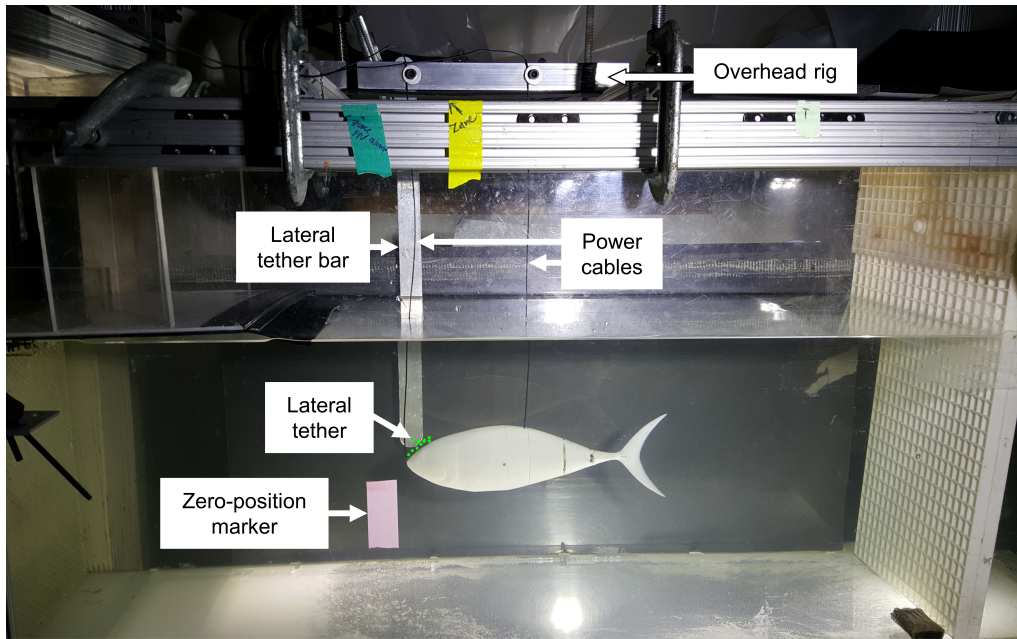


Figure 4-4: Experimental setup for Tunabot V5's performance testing. We incrementally increased Tunabot V5's body flexibility by adding joints, or degrees of freedom (DOF), along the body. We quantified the self-propelled swimming performances of three flexibility configurations (2 DOF, 3 DOF, and 4 DOF Flex) in the flow tank at Harvard University (4 DOF Flex pictured here). Two power cables suspended Tunabot V5 in the flow tank's test section from the overhead rig. The two power cables also plugged into the new, external system that controlled swimming speed and measured power consumption (see Figure 4-5). The lateral tether (green, dashed line) loosely connected the snout to the thin aluminum bar clamped vertically to the test section's side wall. This tethered arrangement simplified previous setups (e.g., see Figure 3-3). The zero-position marker corresponded to the snout's position when both Tunabot V5 and the flow tank's water were stationary. A lateral-view, high-speed camera tracked the relative position between the snout and zero-position marker. While Tunabot V5 swam at a particular tail-beat frequency, we adjusted the flow speed until the snout re-aligned with the marker. At this point, the net thrust and drag of Tunabot V5 were equal, and we recorded the self-propelled swimming speed.

For each of Tunabot V5's 3 body flexibility configurations, we tested 10 tail-beat frequencies with 3 trials per tail-beat frequency. We varied the tail-beat frequency by setting the duty cycle of the PWM voltage signal powering the motor from 15% to 60% by 5% increments. We did not test duty cycles less than 15% because that was the minimum input capable of turning over the motor. Testing duty cycles above 60% was not possible because the self-propelled swimming speed of Tunabot V5 exceeded the maximum flow speed (1.25 m/s) of the flow tank. The 5% increments characterized performance over the testable range of tail-beat frequencies and did so with twice the resolution of Tunabot V4's 10% increments (see Section

3.3.1). In effect, we thoroughly tested the entire performance range of Tunabot V5 by sweeping through the full range of tail-beat frequencies for all three body flexibility configurations. At each tail-beat frequency, we recorded the swimming kinematics (see Section 4.3.3) and the self-propelled speed. We normalized the self-propelled speed by body length (see Section 4.7.1). The methodology and experimental setup for measuring the self-propelled speed of Tunabot V5 were identical to those of Tunabot V4 (see Section 3.3.1), which improved upon those of Tunabot V2 (see Section 2.4.3).

4.3.2 *Speed Control and Power Measurement*

We developed a new system for externally controlling Tunabot V5's swimming speed and measuring the electrical power consumption (Figure 4-5). This system improved upon the previous one that we used for the flow tank experiments of Tunabots V2 and V4 (see Sections

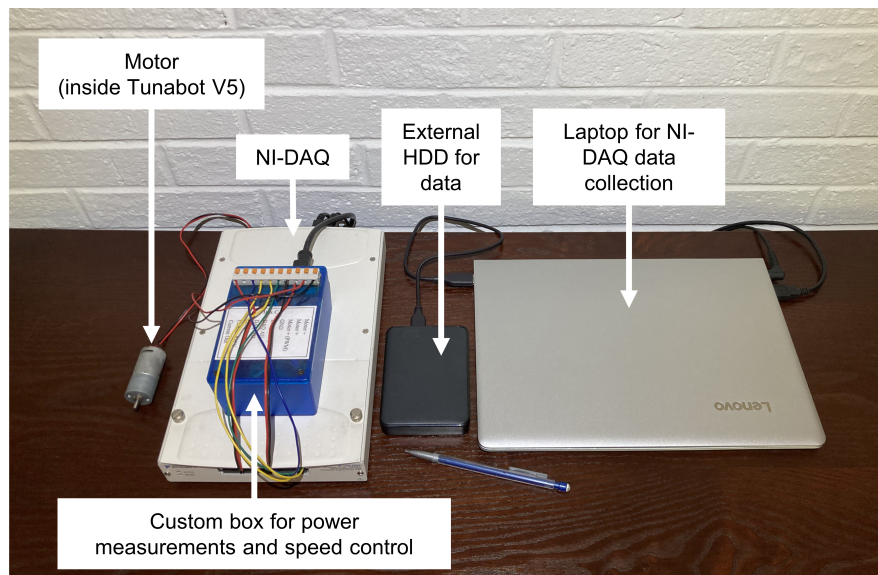


Figure 4-5: Speed control and power measurement system of Tunabot V5. We created a new speed control and power measurement system for Tunabot V5 to enhance its capabilities as a platform for conducting experiments. This external system improved upon our previous one (see Figure 2-17). The LabVIEW software that we developed for this system is shown in Figure 4-6.

2.4.2 and 3.3.2, respectively). The new system consisted of a National Instruments data acquisition device (model USB-6259), custom software developed in LabVIEW, and a custom-built circuitry box. We rebuilt the LabVIEW software and user-interface from scratch for a more capable, efficient, and user-friendly program (Figure 4-6). The new circuitry box combined the previous functions of the electronics boxes (i.e., the blue and aluminum boxes) and the dedicated power supply (see Figure 2-17) into a single, compact package. The new system measured power more precisely than the original system, so filtering the recorded voltage and current signals was no longer necessary. Altogether, these improvements enhanced Tunabot V5's capabilities as a research platform and streamlined the experimental process, including travel to Harvard University, setup, testing, and data analysis.

We wired Tunabot V5's power cables to the new circuitry box (Figure 4-5), which contained three main components: a motor driver, a current transducer, and a voltage divider. The motor driver (model TB6612FNG, SparkFun Electronics Inc., Niwot, CO, USA) supplied the motor with a 12 V, PWM signal (square waveform with 10 kHz frequency). Tunabot V5's tail-beat frequency and thus swimming speed were user-defined in real time by varying the PWM signal's duty cycle within our LabVIEW software (Figure 4-6). The NI-DAQ received analog inputs up to 10 V, so a voltage divider composed of two $1\text{ k}\Omega \pm 1\%$ resistors halved the 12 V, PWM signal to enable recording. To measure the electrical current of Tunabot V5's motor, we used a closed-loop, Hall effect transducer (model LTSR 6-NP, LEM USA Inc., Milwaukee, WI, USA) with single-channel, 2 A wiring. We simultaneously recorded the voltage and current whenever we measured the self-propelled swimming speed.

We calculated the electrical power consumption by recording the voltage and current signals and multiplying them together. We sampled the voltage and current signals at 200 kHz

them to ensure instantaneous power was calculable. We calculated the instantaneous power waveform by multiplying the voltage and current waveforms together at each time point. We time-averaged the 5-second instantaneous power waveform for a single mean value of power. This technique yields more accurate power averages compared to individually averaging the voltage and current before multiplication. Furthermore, instantaneous power waveforms enable advanced analyses of energetic costs, such as how the power of Tunabot V5 cyclically varied throughout a single tail-beat period [170].

4.3.3 *Swimming Kinematics of Tuna and Tunabot V5*

We used high-speed video data of yellowfin tuna and Tunabot V5 to compare their swimming kinematics. High-quality data sets of yellowfin tuna kinematics were scarce, so we re-analyzed the same data set that we previously compared against Tunabot V4. The complete methodology for obtaining this yellowfin tuna data is detailed in Section 3.3.3. To summarize, Lauder Laboratory recorded dorsal-view video sequences of yellowfin tuna averaging 1.0 m in body length for both steady swimming (see Figure 3-4) and high-speed maneuvering during feeding. The average ($n = 20$) steady swimming speed was 1.0 ± 0.1 BL/s with a tail-beat frequency of 2.4 ± 0.2 Hz. Feeding sequences provided kinematic data over a range of tail-beat frequencies up to 10 Hz, but speeds were unmeasurable due to the rapid, 3D motions of the feeding tuna.

We recorded high-speed video footage of Tunabot V5 swimming self-propelled in the flow tank at Harvard University. This footage captured Tunabot V5's performance testing, which encompassed 10 tail-beat frequencies for each of the 3 body flexibility configurations with 3 trials per tail-beat frequency. A high-speed camera (Photron FASTCAM Mini UX100) placed

beneath the transparent bottom of the flow tank’s test section captured ventral-view footage (500 fps, 1024×1024 resolution). Individual video frames from this footage of Tunabot V5 and from the dorsal-view footage of yellowfin tuna are pictured in Figure 4-10(A)–(D).

We extracted the swimming kinematics of yellowfin tuna and Tunabot V5 from their respective high-speed video data. We manually tracked and digitized the midlines for 10 evenly spaced frames across a full tail-beat period using custom MATLAB scripts, resembling previous work [85], [141]. In total, we created 20 midline sequences for the tuna. For Tunabot V5, the 10 tail-beat frequencies tested over 3 trials for all 3 body flexibility configurations produced 90 midline sequences. Our methodology for extracting Tunabot V5’s swimming kinematics was similar to that of Tunabot V4 (see Section 3.3.3). Figure 4-7 depicts the midline tracking process for one of these 10-framed sequences of a single tail-beat period.

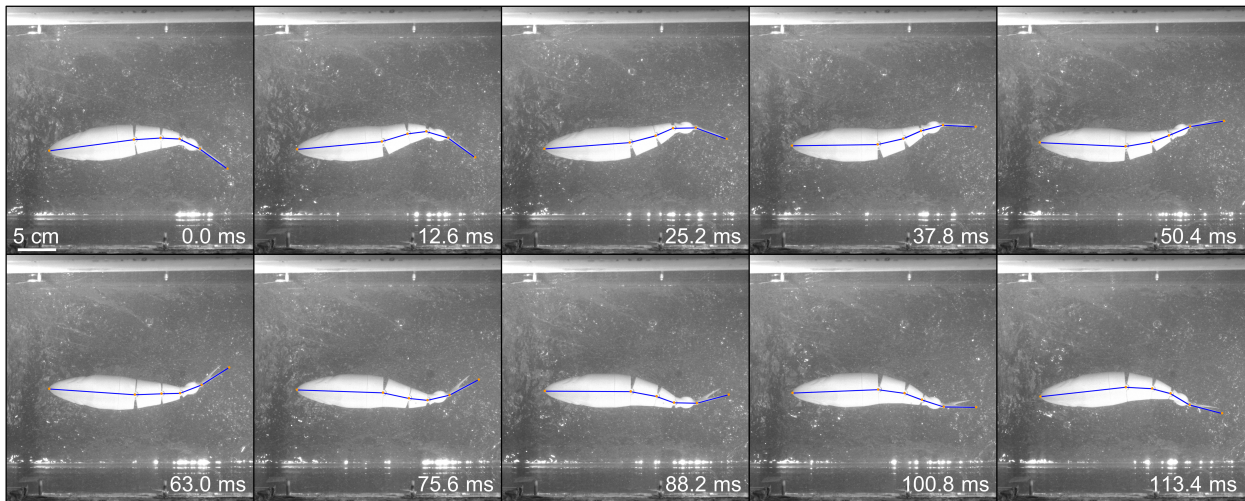


Figure 4-7: Midline tracking of Tunabot V5 to determine swimming kinematics. High-speed video footage (ventral-view, 500 fps) of Tunabot V5’s midline captured body deformation during steady swimming. We divided a single tail-beat period into 10 evenly spaced frames for each tested tail-beat frequency of the different body flexibility configurations. We traced the midline (blue line) by tracking the locations of the snout, joints, and caudal fin’s trailing edge (orange nodes). Using the digitized midline sequences, we calculated the swimming kinematics, which included the tail-beat frequency, head amplitude, tail-beat amplitude, and midline curvature. Pictured here is 4 DOF Flex swimming during its second trial with a tail-beat frequency of 7.94 Hz (i.e., 60% duty cycle of the PWM voltage input) and a speed of 4.66 BL/s (1.19 m/s). The exact midline sequence shown here produced the kinematics in Figure 4-7(G) and 10 of the 300 curvatures in Figure 4-7(K).

Using additional MATLAB scripts, we calculated the tail-beat frequency, head amplitude, tail-beat amplitude, and midline curvature of yellowfin tuna and Tunabot V5 from their digitized midline sequences. We calculated the tail-beat frequency by dividing the video's frame rate by the number of video frames per tail-beat period. We defined the head and tail-beat amplitudes as the distances between the lateral extremes of the snout and caudal fin's trailing edge, respectively. We calculated the midline's curvature using Equation (25). Using these kinematic metrics, we then calculated the stride length and Strouhal number using Equations (23) and (24), respectively. We scaled the midlines, amplitudes, curvatures, and stride lengths by body length (see Section 4.7.1).

4.3.4 *Biological Comparison of Energy Efficiency: Cost of Transport*

We quantified the energy efficiency of Tunabot V5 in terms of the COT. This metric of performance enabled direct comparisons between tunas and Tunabot V5. In general, the COT describes the energy required to move a unit mass over a unit distance. We calculated Tunabot V5's COT using Equation (26) wherein the unsubmerged mass m_u was 0.190 kg. For fishes, the various methods used to quantify the COT depend on the metabolic rate used during calculations. There are three metabolic rate levels in fishes: basal (minimum level required to sustain life), standard (background level for increased activity), and active (level for swimming at a particular speed) [111]. The standard metabolic rate (SMR or $S\dot{V}O_2$) is equivalent to the resting power or 'hotel power' of robotic swimmers. For example, the SMR of tuna [254] would be compared against the resting power of a fully autonomous Tunabot. The active metabolic rate (AMR or $\dot{V}O_2$) is analogous to the total electrical power consumption of man-made systems such as Tunabot V5. As such, it is important to ensure that the COT of a fish robot is compared

against a fish's COT that is calculated with the AMR and includes the SMR [255]. COT calculated with the AMR is sometimes referred to as the 'gross cost of transport (GCOT)' [256], but simply 'cost of transport' is more common. A less accurate robot-biology comparison is made when using the 'net cost of transport (COT_{net})' of fishes, which subtracts the SMR from the AMR [257]. COT_{net} is the total amount of aerobic energy available to an animal and thus also referred to as the 'absolute aerobic scope (AAS)' [258]. Overall, the 'cost of transport (COT)' of fish calculated with the AMR is the appropriate metric when comparing against the energy efficiencies of fish robots.

The units of COT must also be considered when comparing fish robots against biological systems. The total electrical power consumption of Tunabot V5 (and other robots) is analogous to the metabolic rate of an animal. The metabolic rate of fish is measured in terms of the oxygen consumption rate ($\dot{M}O_2$). This rate is comparable to electrical power after converting its units ($mg \cdot O_2/min$) to energy (kcal or joule) using an oxycalorific coefficient [111], [259]. The rate is then scaled by the fish's speed and unsubmerged mass to finally arrive at the COT [260]. Scaling by body mass enabled us to compare a multitude of fishes and robots while accounting for mass differences. Unlike the COT, the work per meter (WPM) is not mass-specific having the unit J/m and is calculated using Equation (27). Two units of COT are typically used: J/kg/m (e.g., [261]) and J/N/m (e.g., [222]). The dimensionless unit J/N/m describes the power required to transport a unit weight at a particular velocity and is calculated by dividing J/kg/m by gravitational acceleration g . In 1950, Gabrielli and von Kármán proposed this dimensionless metric ϵ for comparing efficiencies of locomotion [236]. They demonstrated its wide applicability by directly comparing sensationally different vehicles, such as a racehorse and battleship. They also plotted efficiency as a function of maximum velocity as we did (see Figure 1-1(B), Figure 4-13(B)). The

units J/kg/m and J/N/m are both appropriate, although the latter is less common. We recommend using the unit J/kg/m when comparing the COT of fish robots against biological systems.

We compare the COT of Tunabot V5 against three sources of live tuna data [79]–[81] in Figure 4-13. For consistency, we ensured that all values of COT were in terms of the unit J/kg/m. We also ensured that the tuna data’s COT was calculated with the AMR and included the SMR for the reasons discussed above. Blank et al. [79] and Dewar & Graham [80] included the SMR in their COT calculations unlike Sepulveda & Dickson [81]. For Sepulveda & Dickson, we calculated the COT (6.6 J/kg/m) by summing the reported COT_{net} (3.1247 J/kg/m) and the SMR (1.385 mg·O₂/min, which we converted to 3.5 J/kg/m using the provided oxycaloric coefficient, mass, and speed). In this instance, the value of COT was more than double the value of COT_{net} , illustrating the importance of including the SMR when making uniform comparisons of COT. This difference between COT and COT_{net} was significant for other fish as well [222].

4.3.5 Drag Forces and Coefficients

We quantified the dead-drag (i.e., towed resistance) of Tunabot V5’s three body flexibility configurations. Doing so enabled us to compare the drag coefficients of Tunabot V5 with biological data. Quantifying the dead-drag also demonstrated that the joint gaps in Tunabot V5’s body did not significantly affect our results. The methodology for measuring Tunabot V5’s dead-drag closely resembled Tunabot V4’s dead-drag experiment and thus studies of fish drag (see Section 3.3.4). We fixed Tunabot V5’s joints for each body flexibility configuration such that the midlines were straight and rigid. The placement and tethering of Tunabot V5 in Lauder Laboratory’s flow tank (Figure 4-8) were identical to the setup that we used to test Tunabot V5’s swimming performance (see Figure 4-4).

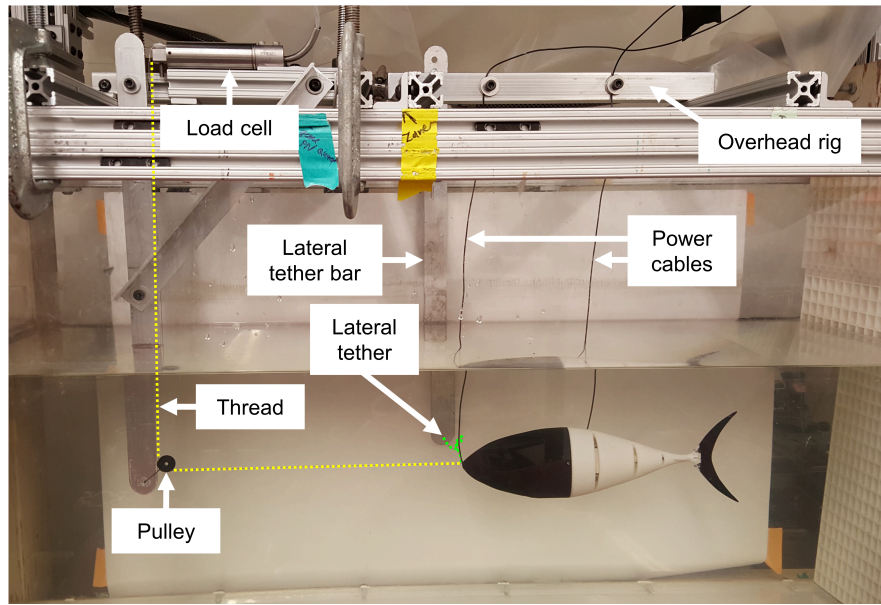


Figure 4-8: Experimental setup for Tunabot V5's drag measurement. We quantified the drag forces and coefficients of Tunabot V5's three body flexibility configurations (4 DOF Flex pictured here). We fixed every joint such that the body's midline was straight and rigid in the flow tank at Harvard University. The two power cables suspended Tunabot V5 in the flow tank's test section from the overhead rig, but we did not supply power to Tunabot V5's motor. The lateral tether (green, dashed line) loosely connected the snout to the thin aluminum bar clamped vertically to the test section's side wall. This was the same tethered arrangement as performance testing (see Figure 4-4). The thin, flexible thread (yellow, dashed line) connected the load cell to Tunabot V5's snout through the pulley. The thread and pulley transferred downstream dead-drag (i.e., towed resistance) of the body to a downward force on the load cell. This setup was a slightly modified version of Tunabot V4's drag experiment (see Figure 3-5).

We measured Tunabot V5's dead-drag force using a constant moment beam load cell (model LC601-1). We attached an additional thread (Spectra Power Pro fishing line) to Tunabot V5's snout that ran horizontally upstream, around a black pulley, and vertically to the load cell (yellow, dashed line in Figure 4-8). A loop of thread loosely attached the pulley to a vertical aluminum bar at the same depth (14.0 cm) as the snout. The thread permitted the pulley to move in three dimensions. Wake effects of the bar were negligible due to its 3 mm thickness and the 30 cm distance downstream to Tunabot V5. In the presence of flow, the load cell registered the corresponding drag force of the body, lateral snout tether, and two power cables. We separately calibrated the load cell by hanging a series of 18 masses ranging from 0 to 450 g directly from the load cell and measuring their corresponding voltage outputs, which yielded a linear

calibration curve ($R^2 = 0.999$).

We performed 3 trials at 10 flow speed settings for each of Tunabot V5's 3 body flexibility configurations. The flow speeds matched the 10 average self-propelled swimming speeds of each body flexibility configuration from performance testing (see Figure 4-13). Before each trial, we applied non-zero tension (approximately 5 g) to the load cell thread to remove slack, which we subtracted from subsequent load cell measurements. The output voltage of the load cell passed through a signal conditioner (model DMD4059) before being recorded by a National Instruments data acquisition device (model USB-6008) with LabVIEW software at a sampling rate of 10 kHz for 10 seconds. The signal conditioner and USB-6008 device were previously housed inside the custom-built aluminum box for Tunabot V4 (see Figure 2-17(A)). Tunabot V5's improved speed control and power measurement system replaced this box (see Figure 4-5), so we removed and transported both items separately from this box to Lauder Laboratory.

We calculated the wetted and projected drag coefficients of Tunabot V5 using Equation (29) where F_D is the drag force that we obtained experimentally (which included the body, lateral tether, and two power cables), ρ is the water density in the flow tank, U is the input flow speed, and A is the reference area (wetted or projected, Table 4-2) of Tunabot V5's body that we found from the CAD model. Water temperature during testing was 22.8°C, corresponding to a density of 997.59 kg/m³ and dynamic viscosity of 0.9354 mPa·s. We calculated the Reynolds number using these values, Tunabot V5's 25.5 cm body length, and Equation (22).

Up until this point, the drag force and coefficients that we measured experimentally pertained collectively to the body, lateral tether, and two power cables. To estimate the dead-drag of the body alone, we estimated the significant hydrodynamic drag generated by the tether

Table 4-2: Wetted and projected areas of Tunabot V5. We calculated the drag coefficients of Tunabot V5’s three body flexibility configurations using their respective wetted and projected areas. The wetted area slightly increased with the degree of body flexibility as the collective area of the body gaps decreased. The projected area was identical for all three configurations. We calculated the wetted and projected areas from the CAD models.

Configuration	Wetted Area (mm ²)	Projected Area (mm ²)
2 DOF Flex	27642	2570
3 DOF Flex	27822	2570
4 DOF Flex	27941	2570

and power cables as follows. We simply modeled the tether and power cables as straight, round cylinders in uniform flow and assumed no wake interactions. For such a cylindrical model, the hydrodynamic drag force F_D is given by Equation (30) where ρ is water density, U is flow speed, C_D is the drag coefficient, and A is the cylinder’s frontal area. Flow speed U ranged from 0 to 1.2 m/s corresponding to Tunabot V5’s range of self-propelled speeds. The drag coefficient C_D of a circular cylinder is a function of Reynolds number, which we calculated using Equation (22) wherein the characteristic length was the cylinder’s diameter. The diameters of a tether and a power cable were 0.25 mm and 1.27 mm, respectively, which we measured using electronic calipers (model CD-6”ASX). Values of C_D depended on the Reynolds number and were obtained experimentally [140]. The frontal area A of the tether and power cables was the product of their diameters and submerged lengths. To be centered in the flow tank’s test section, the submerged lengths of the lateral tether and of the fore and aft power cables were 14.0, 11.0, and 14.0 cm respectively. Next, we subtracted our estimate of the combined drag due to the tether and power cables from our measured drag force. This difference yielded our final estimate of the dead-drag of the isolated body. We then plugged this final estimate of dead-body drag into Equation (29) as F_D to estimate the dead-body drag coefficients (wetted and projected).

The methodology for measuring Tunabot V5’s dead-drag closely resembled Tunabot V4’s dead-drag experiment (see Section 3.3.4) with one improvement: we used the same flow

tank for drag measurements as performance testing. For Tunabot V4, we tested its swimming performance at Harvard University but measured its dead-drag at the University of Virginia. We centered Tunabot V4 in the test sections of both flow tanks, but the test section at the University of Virginia had larger dimensions. This difference caused the submerged lengths of Tunabot V4's three tethers and two power cables to be longer at the University of Virginia, incurring greater drag compared to the performance testing at Harvard University. We rectified this discrepancy with Tunabot V5 by using the flow tank at Harvard University for both the performance and dead-drag experiments. We were unable to directly compare the dead-drag of Tunabots V4 and V5 because of their difference in flow tank facilities.

4.3.6 *Motor Efficiency*

We experimentally measured the efficiency of Tunabot V5's DC motor (Actobotics model 638358) to quantify how severely the motor's inefficiencies negatively impacted the COT. In general, the efficiency of a motor describes how well it converts electrical energy input to mechanical power output, and motor efficiency is diminished by several sources, such as frictional and iron losses [176]. To measure the efficiency of Tunabot V5's motor, we completely removed it from inside Tunabot V5 without disconnecting the two power cables. We did so after quantifying Tunabot V5's swimming performance (see Figure 4-13). By using the exact same motor and power cables as before, we ensured that the measured motor efficiency was as authentic as possible.

The measurement of motor efficiency consisted of having the motor lift a series of increasing masses while we recorded its rpm and power consumption. We 3D printed a spool and fixed it to the motor's shaft before securing the motor horizontally 2 m above the ground. We

then suspended a 1 L water bottle from the spool by a thin, flexible thread (Spectra Power Pro fishing line) such that the motor raised the bottle as the spool wound up the thread. The spool's diameter was 7.9 mm before raising the bottle and increased to 8.5 mm as the wound thread overlapped itself on the spool. At the beginning of each trial, the bottle rested on the ground before accelerating upwards. We then waited for 2 s before collecting data to ensure that the bottle was no longer accelerating. At this point, we measured the motor's total electrical power consumption via the voltage and current for 1–2 s depending on how quickly the motor raised the bottle before running out of thread. We controlled the motor and measured its power consumption using the same system as Tunabot V5's performance testing (see Section 4.3.2). We measured the motor's rpm as the motor lifted the mass using a stroboscope (model DS-303) aimed at the spinning spool. To vary the lifted mass, we incrementally added water to the bottle at rest, which we measured using a digital scale (Model ZK14-S, Ozeri Inc., San Diego, CA, USA).

With our experimentally obtained values in hand, we calculated the motor's efficiency using the following approach. First, we calculated the torque τ of the motor:

$$\tau = m_{\text{load}} \cdot r_{\text{spool}} \cdot g \quad (58)$$

where m_{load} was the mass of the lifted bottle, r_{spool} was the radius of the spool, and g was gravitational acceleration. Next, we found the rotational mechanical power P_{rot} of the motor:

$$P_{\text{rot}} = \omega \cdot \tau \quad (59)$$

where ω was the angular velocity (rad/s), which we calculated from the measured rpm. Finally, we calculated the efficiency η of the motor:

$$\eta = \frac{P_{\text{rot}}}{P} \quad (60)$$

where P_{rot} was the rotational mechanical power (output), and P was the measured total electrical power consumption (input).

Using this approach, we measured the motor's characteristics for two conditions: swimming conditions and maximum performance. For swimming conditions, we replicated the hydrodynamic load on 4 DOF Flex's motor during performance testing in the flow tank. The purpose was to quantify the motor's efficiency to understand the extent of its impact on swimming performance, especially the COT. To replicate the hydrodynamic load, we adjusted the amount of lifted mass until the motor's rotational speed exactly matched a targeted tail-beat frequency from flow tank testing for a given duty cycle of the PWM voltage input. For example, 4 DOF Flex swam with a tail-beat frequency of 2.0 Hz given a voltage input of 15% duty cycle. To measure the motor's efficiency for this particular swimming condition, we input 15% duty cycle and adjusted the lifted mass until the motor's speed was 121 rpm (i.e., 2.0 Hz). We adjusted the mass through trial and error by presetting the stroboscope to 121 rpm and adding or subtracting water from the bottle until the motor's speed matched the stroboscope. We tested 10 duty cycles ranging from 15% to 60% by 5% increments, exactly matching the 10 duty cycles of flow tank testing. This meant that we tested 10 different masses, which replicated the 10 tail-beat frequencies (2.0–8.0 Hz) of flow tank testing. We performed three trials per mass. Overall, the 10 data points of motor efficiency (see Figure 4-15) corresponded to the 10 data points of performance testing (see Figure 4-13).

The second condition we measured was the maximum performance of the motor. To do so, we held the duty cycle constant at 100% and methodically increased the lifted mass from 0.000 to 0.600 kg by 0.100 kg increments. We also tested 0.920 kg for a larger value; we did not test masses between 0.600 and 0.920 kg since the data trends were apparent for those

intermediate masses. We performed three trials per mass. We calculated the stall current I_{stall} and stall torque τ_{stall} by linearly extrapolating the data.

4.3.7 *Statistical Analysis*

We took great care to minimize sources of error through careful methodology, high-quality instrumentation, and proven experimental facilities. We rigorously documented and calculated error as it propagated through calculations. Doing so was especially crucial when comparing and contrasting the three body flexibility configurations of Tunabot V5. Most error propagation involved values averaged over multiple trials and their associated uncertainties. When multiplying or dividing averages, we evaluated the propagation of uncertainties as before using Equation (54). We quantified uncertainty in terms of the 95% CI to clearly communicate our results [262] as opposed to the standard deviation or other error statistics. In text and plotted error bars, we reported average values with uncertainty as the mean \pm 95% CI unless otherwise specified.

We compared and contrasted the three different body flexibility configurations of Tunabot V5 using the standard error of the mean (SEM) and 95% CI. We calculated the SEM and the 95% CI using Equations (55)–(57). Overlapping SEM indicated that sample means were statistically similar ($p > 0.05$). Non-overlapping 95% CI meant that sample means were statistically different ($p < 0.05$). Overlapping CI error bars do not indicate statistical similarities; conversely, overlapping SEM error bars do not indicate statistical differences [263]. Hence, we required both the SEM and the 95% CI to evaluate the statistical significance of similarities and differences, respectively.

4.4 Body Flexibility Experiment: Results

4.4.1 *Center of Mass*

We analytically estimated the COM of Tunabot V5's three body flexibility configurations using their CAD models (see Figure 4-3). The COMs of 2 DOF, 3 DOF, and 4 DOF Flex were positioned at 0.32 BL from their snouts and at 50% of their bodies' widths and heights. We also estimated the masses of the three configurations using their CAD models, which equaled 0.197 kg. This average agreed well with our physically measured masses of 0.190 kg, giving us confidence that the estimated COMs were accurate. Across all three configurations, the COMs and masses differed by less than 1.0 mm (0.0039 BL) and 0.005 kg, respectively, which we expected since few components differed between the configurations by design. This close agreement indicated that performance differences between the three body flexibility configurations did not result from variations in their COM or mass.

4.4.2 *Drag Forces and Coefficients*

Tunabot V5's dead-drag (Figure 4-9(A)) fit a quadratic polynomial, as expected of drag forces, with coefficients of determination (R^2) equaling at least 0.995 for all three body flexibility configurations. For speeds above 0.70 m/s, the drag of 4 DOF Flex was statistically greater than that of 3 DOF Flex. At 1.17 m/s, the drag between 3 DOF and 4 DOF Flex differed by 7.2%. Besides these and other lesser differences, the variations in drag between the three configurations were insignificant. Thus, the number and size of body gaps did not significantly contribute to overall performance differences between the three body flexibility configurations.

The maximum average dead-drag was 0.53 ± 0.01 N ($n = 3$) and corresponded to 4 DOF Flex at its highest self-propelled speed (1.17 m/s). The lateral snout tether and two power cables

were a significant source of drag (Figure 4-9(B)). At 1.17 m/s, the estimated drag force of the tether and power cables (0.22 N) was 41% of the measured dead-drag of 4 DOF Flex. This significant percentage increased to 86% as the speed decreased to 0.32 m/s. The two power cables contributed the majority of drag to the estimate due to their larger diameters compared to the thin tether; at 1.17 m/s, the power cables comprised 93% of the estimated drag force of the tether and power cables and 38% of the measured dead-drag. For an estimate of the dead-drag of

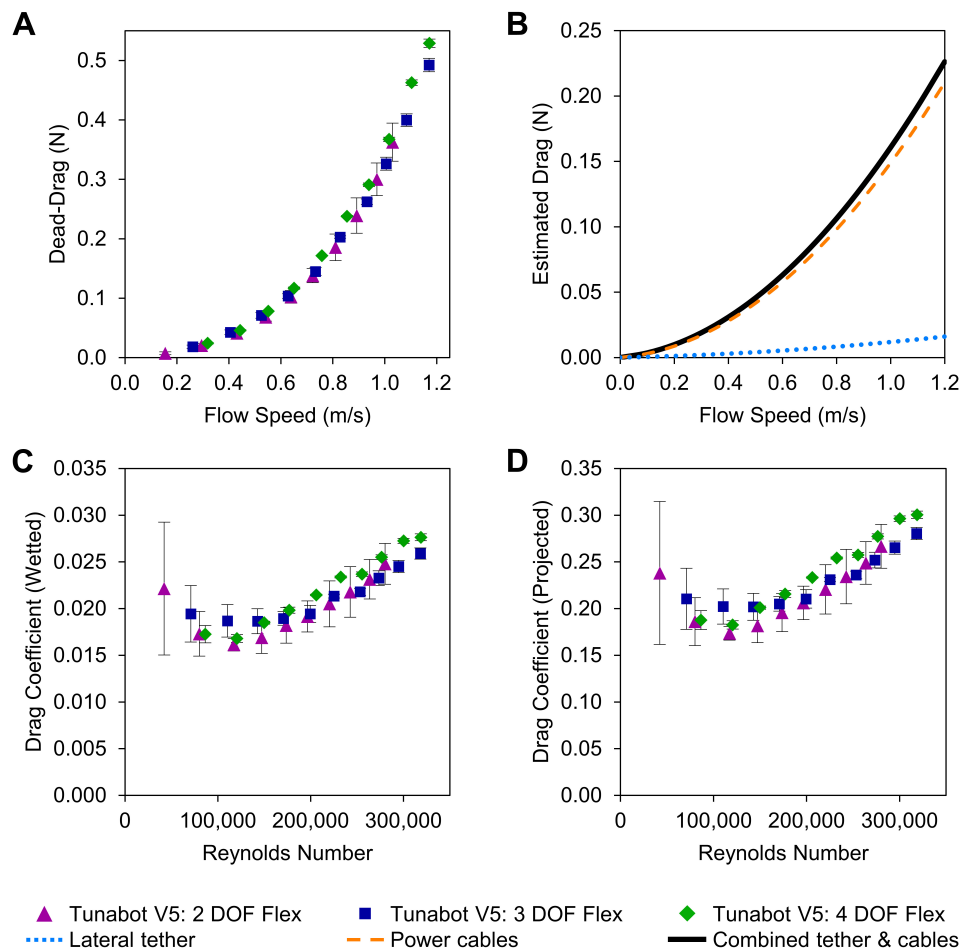


Figure 4-9: Drag forces and coefficients of Tunabot V5. (A) We measured the dead-drag (i.e., towed resistance) of Tunabot V5 in oncoming flow speeds that corresponded to self-propelled performance (see Figure 4-13). We tested all three body flexibility configurations (2 DOF, 3 DOF, and 4 DOF Flex) with straight, immobile midlines. (B) We estimated the drag forces of the lateral tether (dotted, blue line) and two power cables (dashed, orange line) before summing them to determine the combined drag of the tether and power cables (solid, black line). We calculated Tunabot V5’s drag coefficients using both the (C) wetted areas and (D) projected areas (see Table 4-2). Data points represent the mean \pm 95% CI ($n = 3$). We detail the measurements and calculations in Section 4.3.5.

Tunabot V5's body alone, we subtracted the estimated drag of the tether and power cables from the measured dead-drag. The body-only estimate of dead-drag for 4 DOF Flex at 1.17 m/s was 0.31 N, which was nearly half of the measured dead-drag. Because the estimated drag of the tether and power cables was a substantial component of the measured dead-drag across all speeds, we would expect a free-swimming Tunabot V5 to achieve significantly faster speeds.

Drag coefficients of Tunabot V5 (Figure 4-9(C)–(D)) ranged from 0.016 to 0.028 (wetted) and from 0.17 to 0.30 (projected) depending on the reference area of the body (see Table 4-2). We calculated these coefficients using the measured dead-drag. Both the wetted and projected drag coefficients of 4 DOF Flex were statistically greater than those of 3 DOF Flex for Reynolds numbers above 2.0×10^5 . For example, the drag coefficients of 3 DOF and 4 DOF Flex differed by 6.9% (projected) and 7.4% (wetted) at a Reynolds number of 3.2×10^5 . To estimate the drag coefficients of the body alone, we re-calculated the coefficients using the body-only estimate of dead-drag and then averaged them together ($n = 30$). The mean, body-only estimates of the drag coefficients were 0.008 ± 0.002 (wetted) and 0.09 ± 0.02 (projected). We later compare Tunabot V5's wetted drag coefficients against biological data for tunas and other relevant species in addition to discussing the general limitations of dead-drag measurements in Section 4.7.3.

4.4.3 *Swimming Kinematics*

We compared the swimming kinematics of Tunabot V5's three body flexibility configurations against each other and yellowfin tuna (Figure 4-10). We provide a single frame from the high-speed video data for each swimmer at similar points throughout their tail-beat periods (Figure 4-10(A)–(D)). The midlines of Tunabot V5 and yellowfin tuna demonstrated a

wave-like kinematic pattern (Figure 4-10(E)–(H)). The motion of Tunabot V5’s body joints caused its midlines to have visibly abrupt changes in displacement, which were most apparent for 2 DOF Flex. Tunabot V5’s wave-like motion became smoother as the number of body joints increased, resulting in 4 DOF Flex approaching the midline kinematics of yellowfin. All three of Tunabot V5’s configurations exhibited local peaks in midline curvature (Figure 4-10(I)–(K)) corresponding to the positions of the body joints (see Table 4-1). Conversely, the curvature of the yellowfin tuna smoothly increased from head to tail (Figure 4-10(L)).

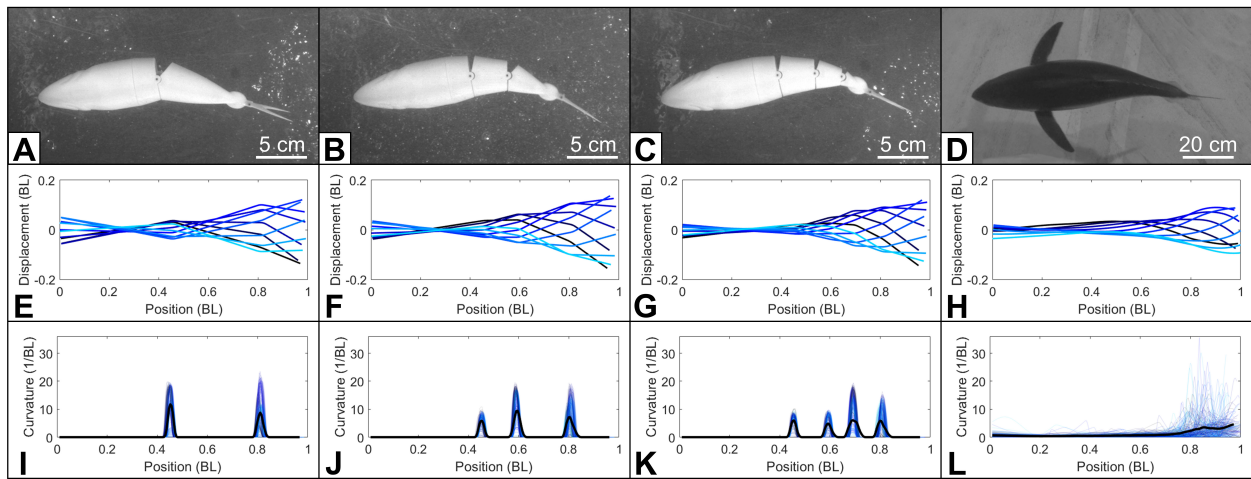


Figure 4-10: Swimming kinematics of Tunabot V5 and yellowfin tuna. We compared the swimming kinematics of Tunabot V5’s three body flexibility configurations and yellowfin tuna side-by-side. Ventral views of (A) 2 DOF Flex, (B) 3 DOF Flex, and (C) 4 DOF Flex. (D) Dorsal view of a yellowfin tuna steadily swimming (see Figure 3-4). (E–H) Corresponding midline kinematics of a single tail-beat period divided into 10 equally spaced time intervals. The provided views and kinematics are representative of the average and selected from the fastest trials: 4.07, 4.64, 4.66, and 1.0 BL/s, respectively. (I–L) Calculated curvatures along the body for $n = 300, 300, 300,$ and 200 midlines from all trials and swimming speeds, corresponding to 30, 30, 30, and 20 tail-beat periods, with the means indicated by thicker, black lines. High-speed videos of the yellowfin tuna were provided by Lauder Laboratory.

For each body flexibility configuration of Tunabot V5, the overall averages of head and tail-beat amplitudes varied depending on the degree of flexibility. The overall average head amplitude ($n = 30$) of Tunabot V5 decreased as flexibility increased: 0.11 ± 0.01 BL (2 DOF), 0.09 ± 0.01 BL (3 DOF), and 0.07 ± 0.01 BL (4 DOF). For tail-beat amplitude, the opposite

occurred; the overall average tail-beat amplitude ($n = 30$) increased with the number of joints: 0.26 ± 0.01 BL (2 DOF), 0.29 ± 0.01 BL (3 DOF), and 0.30 ± 0.01 BL (4 DOF). Our steadily swimming yellowfin tuna had average ($n = 20$) head and tail-beat amplitudes of 0.05 ± 0.01 BL and 0.19 ± 0.01 BL, respectively. The overall averages of Tunabot V5's head and tail-beat amplitudes for all three configurations statistically exceeded those of the yellowfin tuna.

The average ($n = 3$) head and tail-beat amplitudes of Tunabot V5's body flexibility configurations varied depending on the tail-beat frequency (Figure 4-11). The head amplitudes of 3 DOF and 4 DOF Flex decreased as the frequency increased. Interestingly, the head amplitude of 2 DOF Flex remained nearly constant despite the variable tail-beat amplitude. The intricate trends of Tunabot V5's head and tail-beat amplitudes were the result of complex interactions between the tail-beat frequency, body flexibility, body yaw, prescribed flapping motion of the tail, and peduncle stiffness.

The complex relationship between the amplitudes and tail-beat frequency was partly caused by the peduncle joint's spring, which provided constant torsional stiffness to the joint (see Section 4.2.1). The maximum rotation angle of the peduncle joint decreasingly increased as the

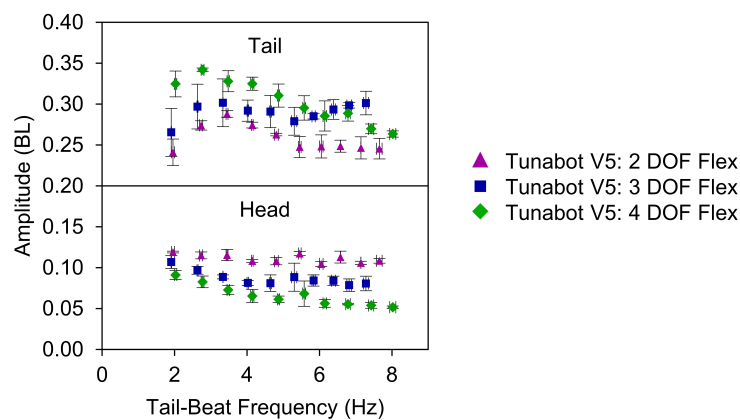


Figure 4-11: Head and tail-beat amplitudes of Tunabot V5. For Tunabot V5's three body flexibility configurations, the **(Top)** tail-beat amplitude and **(Bottom)** head amplitude varied with the tail-beat frequency and degree of body flexibility. Data points represent the mean \pm 95% CI ($n = 3$).

tail-beat frequency increased due to hydrodynamic forces on the caudal fin overcoming the spring's nonlinear stiffness. At higher tail-beat frequencies, the rotation angle eventually hit the joint's physical limit (18°). Through this changing rotation angle, the peduncle stiffness caused the phase difference between the peduncle joint and the caudal fin's tip to decrease with the tail-beat frequency (Figure 4-12). For 2 DOF Flex, this decrease was slight: $331 \pm 2^\circ$ to $324 \pm 3^\circ$ ($n = 3$). The phase difference of 2 DOF Flex diverged markedly from 3 DOF and 4 DOF Flex, whose phase differences decreased more significantly: $333 \pm 21^\circ$ to $303 \pm 4^\circ$ (3 DOF, $n = 3$) and $326 \pm 1^\circ$ to $291 \pm 2^\circ$ (4 DOF, $n = 3$). We further discuss peduncle stiffness and phase difference in Section 4.7.4.

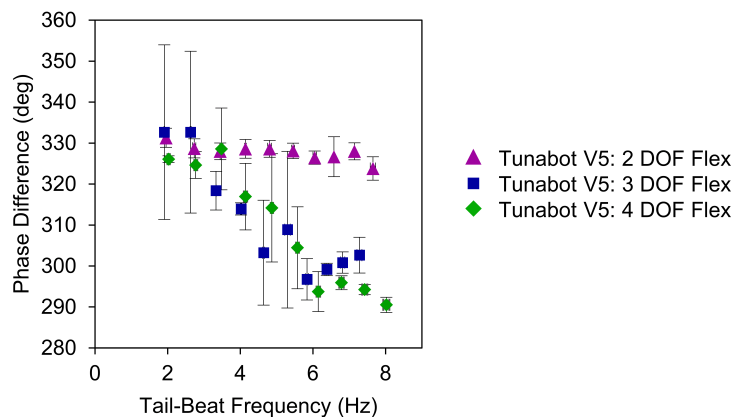


Figure 4-12: Phase difference of Tunabot V5. For Tunabot V5's three body flexibility configurations, the phase difference between the peduncle joint and the caudal fin's tip varied with the tail-beat frequency and the degree of body flexibility. Data points represent the mean \pm 95% CI ($n = 3$).

4.4.4 *Swimming Speed and Tail-Beat Frequency*

Swimming speed was linearly proportional to tail-beat frequency for the three body flexibility configurations of Tunabot V5 (Figure 4-13(A)) with coefficients of determination (R^2) ranging from 0.996 to 0.999. The linear slopes of 2 DOF, 3 DOF, and 4 DOF Flex were 0.60, 0.65, and 0.56 BL, respectively. The speed for a given frequency was statistically greater by

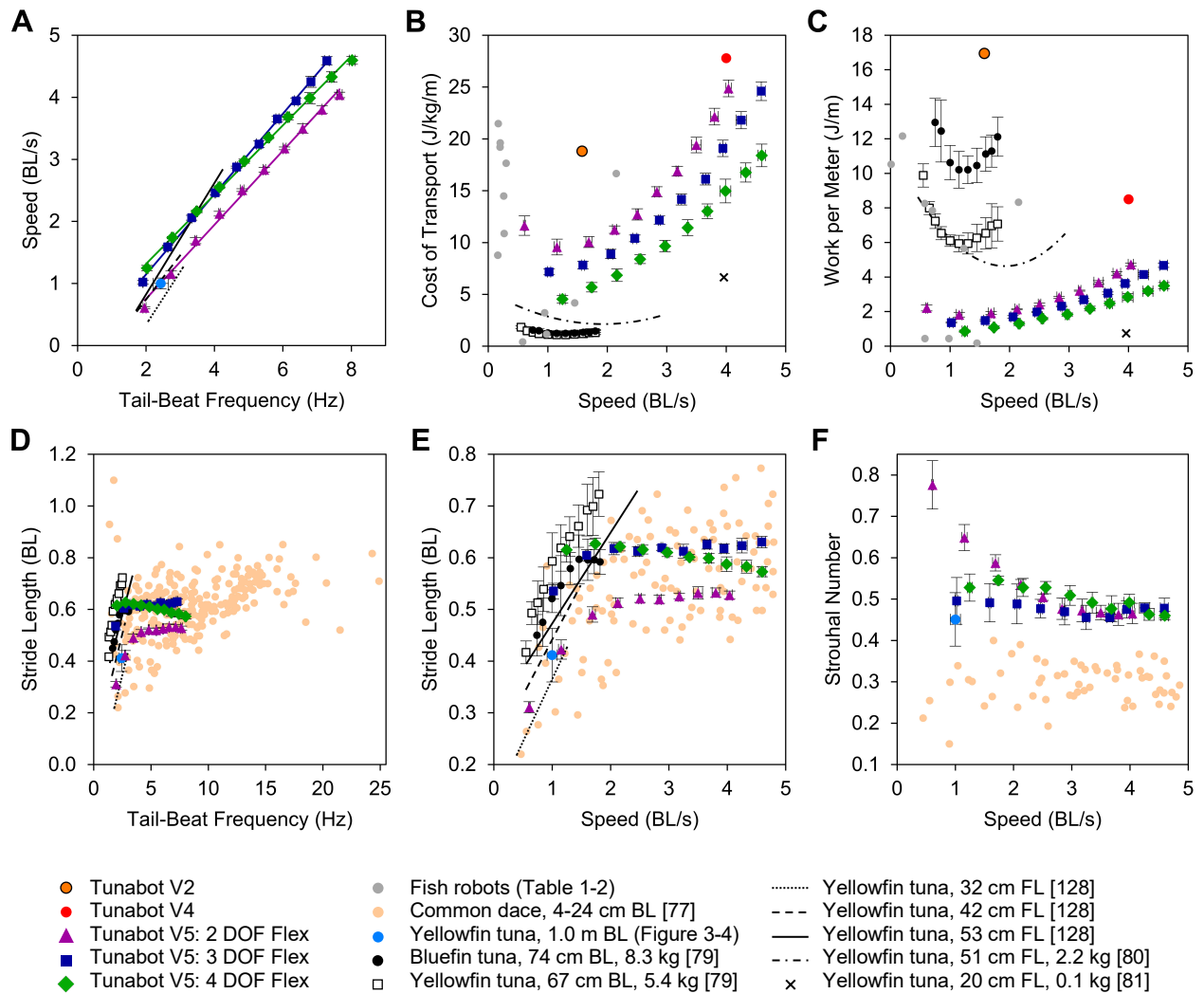


Figure 4-13: Performance results of Tunabot V5. We incrementally increased the body flexibility of Tunabot V5 by adding joints, or degrees of freedom (DOF), along the body. We quantified the performances of three body flexibility configurations (2 DOF, 3 DOF, and 4 DOF Flex) using several metrics: swimming speed, tail-beat frequency, cost of transport (COT), work per meter (WPM), stride length (SL), and Strouhal number (St). We compared the three configurations of Tunabot V5 with one another, with a diversity of fish species, and with the maximum speeds of Tunabot V2, Tunabot V4, and other robotic fish. Data points represent the mean \pm 95% CI ($n = 3$) for Tunabot V5's data points, and $n = 20$ for our steadily swimming yellowfin tuna (see Figure 3-4). **(A)** We provide linear fits of Tunabot V5's data. **(B)–(E)** For the sake of consistency, we converted the error bars reported by Blank et al. [79] from standard deviation to 95% CI (yellowfin $n = 5$ and bluefin $n = 6$ for both COT and WPM, assumed $n = 2$ for SL). **(D)** We calculated the SL vs. tail-beat frequency of yellowfin tuna using available data [128]. **(E)** We present a zoomed-in view, which cropped the dace data. **(E)–(F)** We calculated the SL vs. speed and the St vs. speed of dace using available data [77]. **(A)–(E)** Dewar & Graham [80], [128] and Sepulveda & Dickson [81] reported fish lengths in terms of fork length (FL) rather than body length (BL), but insufficient data were available for us to convert FL to BL. Despite this, we plotted lengths (FL) and speeds (FL/s) as if scaled by BL due to the short supply of tuna data available for comparing (see Section 4.7.1). All other data we present here are scaled by BL.

about 0.5 BL/s for 3 DOF and 4 DOF Flex compared to 2 DOF Flex across all tested frequencies. The performance difference was more subtle between 3 DOF and 4 DOF Flex, whose linear fits intersected at 3.9 Hz (2.4 BL/s). Below 3.9 Hz, the speed of 4 DOF Flex was higher for a given tail-beat frequency compared to 3 DOF Flex, and the opposite was true above 3.9 Hz. These differences were statistically significant except near the point of intersection. The linear fit of 2 DOF Flex intersected our data point for steadily swimming yellowfin tuna (Figure 4-13(A)). Tunabot V5's overall tail-beat frequency range of 1.9–8.0 Hz overlapped the 3–10 Hz range we obtained for feeding yellowfin tuna (see Section 3.3.3), which agreed with other observations of feeding yellowfin tuna (2–13 Hz, $n = 33$) [218]. For all three of Tunabot V5's configurations, the tail-beat frequency was linearly related ($R^2 \geq 0.999$) to the duty cycle of the PWM voltage input, confirming that varying the duty cycle was an effective methodology (see Section 4.3.2) for controlling swimming speed.

4.4.5 *Cost of Transport*

Increasing body flexibility improved Tunabot V5's energy efficiency. The COT statistically decreased by approximately 20% with each additional joint across all tested speeds (Figure 4-13(B)). 4 DOF Flex achieved the lowest COT of 4.5 ± 0.4 J/kg/m ($n = 3$) at a speed of 1.25 BL/s. At a similar speed of 1.15 BL/s, 2 DOF Flex's minimum COT was 9.6 ± 0.8 J/kg/m ($n = 3$). Thus, increasing body flexibility by two additional joints decreased the minimum COT by 53%. This trend also held true at higher speeds. At 4.0 BL/s, the COTs of 2 DOF and 4 DOF Flex were 24.9 ± 0.8 J/kg/m ($n = 3$) and 15.0 ± 1.2 J/kg/m ($n = 3$), respectively. This equated to a 40% decrease in COT as body flexibility increased by two additional joints. At its maximum tested speed of 4.60 ± 0.06 BL/s ($n = 3$), the COT of 4 DOF Flex measured 18.4 ± 1.1 J/kg/m.

The same trends in COT applied to the WPM as well (Figure 4-13(C)), but the specific values differed by a factor of 0.190 (i.e., Tunabot V5’s unsubmerged mass in kilograms). This was true, by definition, since the COT equals the WPM normalized by mass (see Section 4.3.4). For example, 4 DOF Flex achieved the lowest WPM of 0.9 ± 0.1 J/m ($n = 3$) at a speed of 1.25 BL/s. The WPM of 4 DOF Flex at its maximum tested speed (4.60 BL/s) was $(3.5 \pm 0.2$ J/m, $n = 3$). When comparing the energy efficiency of Tunabot V5 against other robotic systems and biological data, the plots of COT and WPM differed markedly (Figure 4-13(B) vs. (C)). This highlighted the importance of using mass-specific metrics when comparing energy efficiencies, which we further discuss in Section 4.7.7.

The electrical power consumption of all three body flexibility configurations quadratically increased with the tail-beat frequency (Figure 4-14); for 2 DOF, 3 DOF, and 4 DOF Flex, R^2 equaled 0.993, 0.994, and 0.999, respectively. Depending on the degree of flexibility, the ranges of power were 0.3–4.9 W (2 DOF), 0.4–5.5 W (3 DOF), and 0.3–4.1 W (4 DOF). Above a tail-beat frequency of ~ 3 Hz, the power curves statistically diverged from one another. The most flexible configuration (4 DOF) consumed the least amount of power for a

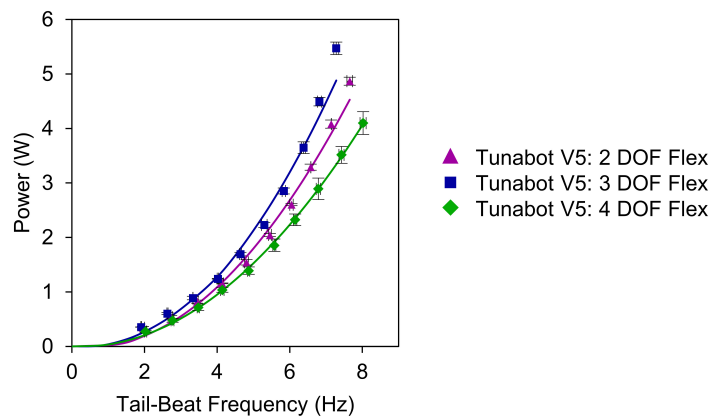


Figure 4-14: Electrical power consumption of Tunabot V5. For each body flexibility configuration of Tunabot V5, the electrical power consumption increased quadratically with the tail-beat frequency ($R^2 \geq 0.993$). Data points represent the mean \pm 95% CI ($n = 3$).

given tail-beat frequency. Interestingly, the moderately flexible configuration (3 DOF) consumed the highest power. We would have expected the least flexible configuration (2 DOF) to have had the highest power consumption since COT increased as flexibility decreased (Figure 4-13(B)). Recalling that COT contains the ratio of power to speed (see Equation (26)), the speed benefit from adding the third joint evidently resulted in 3 DOF Flex's COT being lower than 2 DOF Flex's COT despite consuming more power than 2 DOF Flex.

4.4.6 *Stride Length*

The ranges of Tunabot V5's average ($n = 3$) stride length (SL) were 0.31–0.53 BL (2 DOF Flex), 0.54–0.63 BL (3 DOF Flex), and 0.57–0.63 BL (4 DOF Flex). The SL of 2 DOF Flex was statistically less than that of 3 DOF and 4 DOF Flex across the tested range by 0.10 BL on average (Figure 4-13(D)–(E)). This translated to 3 DOF and 4 DOF Flex traveling about 2.5 cm further for a single tail-beat period than 2 DOF Flex. Both 3 DOF and 4 DOF Flex achieved a maximum SL of 0.63 BL, and their SL curves crossed over at 3.9 Hz (2.4 BL/s), corresponding to the intersection of their linear fits (Figure 4-13(A)). Due to this crossover, the configuration with the greatest SL depended on the operating tail-beat frequency and thus speed. Above 3.6 BL/s, the SL of 3 DOF Flex was statistically greater than that of 4 DOF Flex by as much as 0.06 BL. The opposite was true for speeds below 1.3 BL/s. 4 DOF Flex differed from the other two body flexibility configurations in that its SL decreased with tail-beat frequency and thus speed. This negative slope indicated a decline in performance, whereas 2 DOF and 3 DOF Flex maintained slightly positive SL slopes. The 0.41 ± 0.05 BL ($n = 20$) SL of steadily swimming yellowfin tuna was statistically similar to that of 2 DOF Flex near 1.0 BL/s as indicated by overlapping SEM.

4.4.7 *Strouhal Number*

The St of 2 DOF Flex was statistically greater than 3 DOF and 4 DOF Flex at swimming speeds below 2.0 BL/s (Figure 4-13(F)). For example, adding a third or fourth joint reduced the St by 25% at approximately 1.0 BL/s. At this speed, the St s of 3 DOF and 4 DOF Flex were also statistically similar to the estimated St of our steadily swimming yellowfin (0.45 ± 0.06 , $n = 20$), as indicated by overlapping SEM. The St of 4 DOF Flex was statistically greater than that of 3 DOF Flex at swimming speeds close to 2.5 BL/s. For speeds above 2.5 BL/s, nearly all the St s for 2 DOF, 3 DOF, and 4 DOF Flex were statistically similar as indicated by overlapping SEM. Interestingly, all configurations converged to the same average ($n = 3$) minimum St equal to 0.46, but this occurred at different speeds: 0.46 ± 0.03 at 3.80 BL/s (2 DOF), 0.46 ± 0.01 at 3.65 BL/s (3 DOF), and 0.46 ± 0.01 at 4.60 BL/s (4 DOF).

4.4.8 *Motor Efficiency*

We experimentally measured the efficiency of Tunabot V5's motor to quantify its impact on swimming performance. We replicated the hydrodynamic load on 4 DOF Flex's motor (see Section 4.3.6) so that the efficiency measurements corresponded to 4 DOF Flex's swimming performance during the body flexibility experiment (see Figure 4-13). The motor efficiency of 4 DOF Flex ranged from 26% to 45% (Figure 4-15). This result was extremely poor. For comparison, a motor with 75% efficiency is realistic and readily attainable for a similarly sized motor and gearbox (e.g., Maxon, Sachseln, CHE). Power consumption is a decisive variable of the COT (see Equation (26)); the low efficiency of Tunabot V5's motor directly and negatively impacted the COT. A higher quality motor with 75% efficiency would dramatically improve the swimming performance of Tunabot V5, which we further discuss in Section 5.2.2.

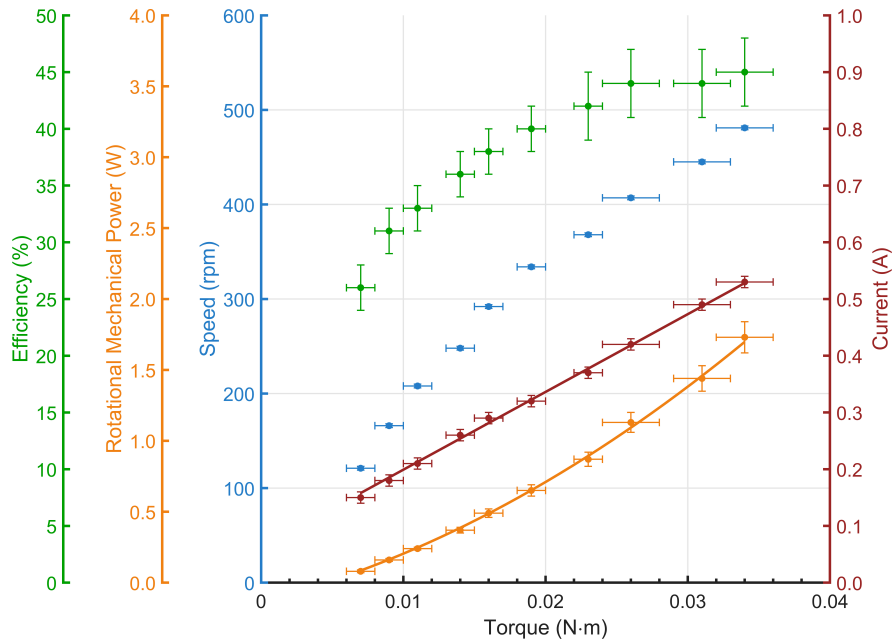


Figure 4-15: Motor characteristics of Tunabot V5 (4 DOF Flex). We experimentally measured the motor’s efficiency corresponding to the swimming conditions of 4 DOF Flex. For each data point, the motor’s speed (rpm) corresponds to exactly the same tail-beat frequency (Hz) as Figure 4-13, and voltage input (PWM duty cycle) is also identical. We loaded the motor until its speed matched the targeted tail-beat frequency for a particular voltage input. The current increased linearly with the torque ($R^2 = 0.999$), and the rotational mechanical power increased quadratically with the torque ($R^2 = 0.999$). Data points represent the mean \pm 95% CI ($n = 3$).

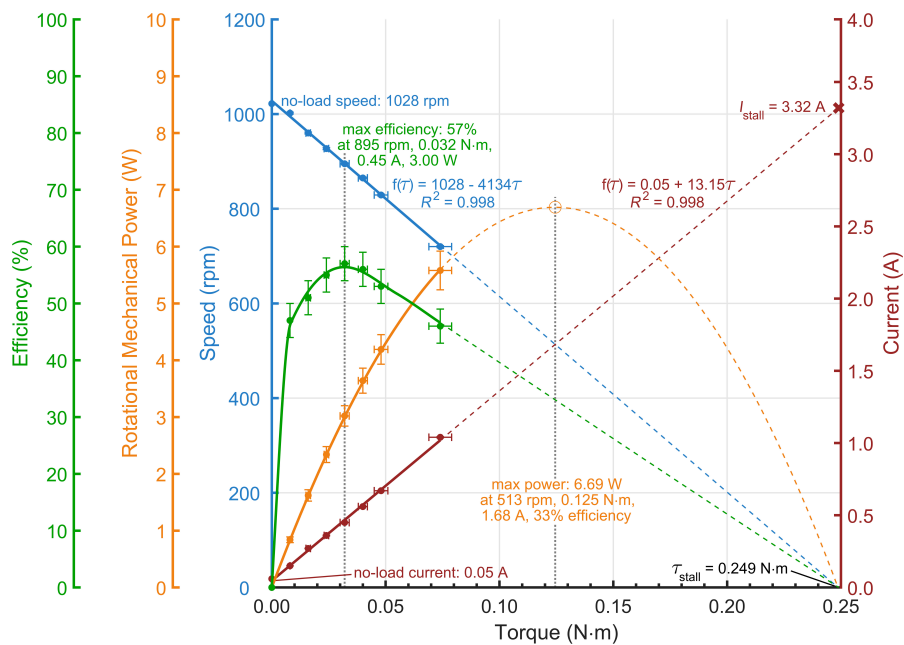


Figure 4-16: Maximum motor characteristics of Tunabots V4 and V5. We experimentally measured the maximum motor characteristics of the 12 V DC motor (Actobotics model 638358) that powered Tunabots V4 and V5. We incrementally increased the load on the motor while supplying a constant PWM voltage input of 100% duty cycle. Data points represent the mean \pm 95% CI ($n = 3$).

In addition to swimming conditions, we also fully characterized the motor's maximum performance (Figure 4-16) to better understand its performance envelopes. In this case, the duty cycle of the PWM voltage input was 100% for each mass lifted by the motor (see Section 4.3.6). We found that decreasing the duty cycle shifted the plotted speed line closer to the origin while remaining parallel to the original, diagonal line. We also found that decreasing the duty cycle shifted the plotted current's maximum value towards the origin along the same line, effectively shortening the line's length. Reducing the duty cycle decreased the time-averaged voltage, which resulted in the diminished speed envelope and lower current draw.

4.5 Tunabots V4 and V5 Comparison Experiment: Materials and Methods

4.5.1 *Specialized Configuration of Tunabot V5*

The body flexibility experiment demonstrated that tuna-like body flexibility enhanced the swimming performance of Tunabot V5 (see Section 4.4). However, we were still interested in quantifying the performance improvement resulting from Tunabot V5's novel mechanical design compared to the previous generation, Tunabot V4. We created a specialized configuration of Tunabot V5 (Figure 4-17) separately from the body flexibility experiment in order to directly compare its swimming performance against Tunabot V4. Doing so was necessary to ensure performance differences between Tunabots V4 and V5 were the result of their mechanical designs rather than kinematics such as body flexibility or tail-beat amplitude. This new configuration marked Tunabot V5's fourth configuration including its three body flexibility configurations (i.e., 2 DOF, 3 DOF, and 4 DOF Flex).

We designed Tunabot V5's specialized configuration by reducing the rotation angle of 2 DOF Flex's mid-body joint from 25° to 16° to match Tunabot V4's joint parameters (Table 4-3).

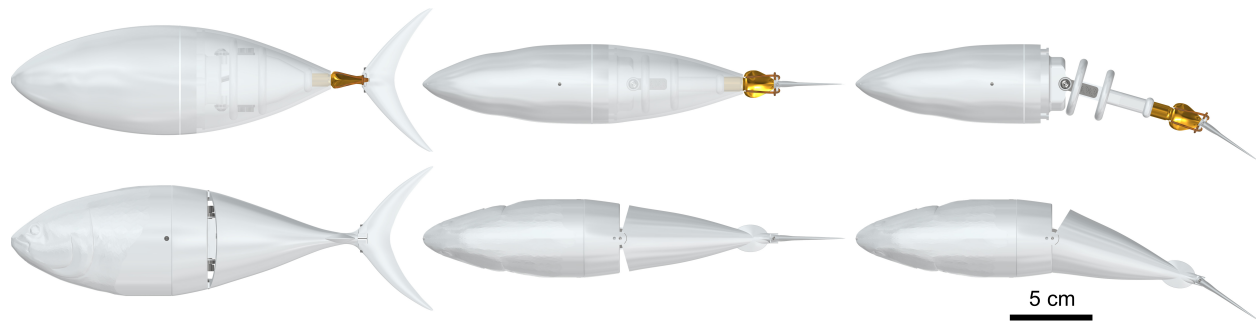


Figure 4-17: Design comparisons of Tunabots V4 and V5. Here we compare the designs of **(Top)** Tunabot V4 and **(Bottom)** Tunabot V5 by providing three different views of their CAD models: **(from Left to Right)** lateral views, dorsal views with straight midlines, and dorsal views with maximum tail deflections (with Tunabot V4’s skin removed for a clearer comparison). We designed this new two-jointed configuration of Tunabot V5 to deliberately mimic the key design parameters of Tunabot V4. Such parameters included its dimensions, joint positions, and joint rotation angles (Table 4-3). This ensured that tail-beat amplitude and body flexibility were not the cause of performance differences between Tunabots V4 and V5. Tethers and power cables are not shown for visualization purposes.

To implement this reduction, we swapped out 2 DOF Flex’s 25° body segment with a newly 3D-printed, 16° body segment. We accommodated the subsequent reduction of the tail-beat amplitude by modifying the bend angle θ of the actuation mechanism’s bent shaft (see Section 2.2.1). All else remained equal between the designs of Tunabot V5’s specialized configuration and 2 DOF Flex, including the unsubmerged mass (0.190 kg) and the COM (0.32 BL). Tunabot V4’s COM was 0.34 BL, which we determined by physically balancing the body. The similar COMs of Tunabots V4 and V5 (0.34 vs. 0.32 BL, respectively) indicated that performance variations were not the result of differences in their COMs.

Table 4-3: Comparison of design parameters between Tunabots V4 and V5. The specialized configuration of Tunabot V5 closely replicated Tunabot V4’s key design parameters. These parameters included the body length, the mid-body and peduncle joints’ angles of rotation (symmetrically away from a straight midline) and positions along the body’s length (as measured from the snout), and motor selection. We did so to compare the swimming performances of Tunabots V4 and V5 while ensuring that differences in performance were the result of mechanical design rather than kinematics. We designed Tunabot V5’s specialized configuration by reducing the rotation angle of 2 DOF Flex’s mid-body joint from 25° to 16° (see Table 4-1).

Generation	Body Length (cm)	Mass (kg)	Joint 1 (Mid-Body)		Joint 2 (Peduncle)		Motor Model No.
			Angle (°)	Position (BL)	Angle (°)	Position (BL)	
Tunabot V4	25.5	0.306	16	0.49	18	0.84	638358
Tunabot V5	25.5	0.190	16	0.47	18	0.84	638358

We deliberately balanced Tunabot V5's new features with previous ones from Tunabot V4 to ensure a fair comparison was possible while still advancing the state of the art. The following features were identical or nearly so between Tunabots V4 and V5: body morphology and dimensions; the shape, stiffness, and planform area of the caudal fin; the rotation angles and positions of their two joints; and the model of motor. We illustrate the physical similarities between Tunabots V4 and V5 by comparing their CAD models side-by-side in Figure 4-17. However, the unsubmerged mass of Tunabot V5 (0.190 kg) was significantly less than Tunabot V4's mass (0.306 kg); Tunabot V5's improved waterproofing methods did not require injecting bulky silicone (see Section 4.2.2), as was the case for Tunabot V4 (see Section 3.2.2). This difference in mass did not significantly affect our performance comparisons because the COM of Tunabots V4 and V5 were similarly positioned. Furthermore, the COT is normalized by mass.

4.5.2 *Performance Testing Protocol*

We tested Tunabot V5's specialized configuration in the flow tank at Harvard University by repeating Tunabot V4's testing protocol (see Section 3.3.1) with one difference: we added 10% duty cycle. This low amount of voltage was unable to turn over Tunabot V4's motor, which required a duty cycle input of at least 14%. Despite utilizing an identical motor, Tunabot V5's minimum duty cycle input was 10% resulting from its more efficient design. This 10% minimum was also less than the 15% minimum of 2 DOF Flex from the body flexibility experiment due to a smaller tail-beat amplitude; we designed Tunabot V5's specialized configuration by reducing the rotation angle of 2 DOF Flex's mid-body joint from 25° to 16°, which diminished the tail-beat amplitude. This also reduced Tunabot V5's stride length, enabling us to test 100% duty cycle without exceeding the flow tank's maximum speed, unlike the body flexibility experiment.

4.6 Tunabots V4 and V5 Comparison Experiment: Results

4.6.1 Drag Forces and Coefficients

Variation in body drag did not contribute to performance differences between Tunabots V4 and V5. We ensured that their wetted and projected areas were similar (Table 4-4). Their projected areas were identical (2570 mm²), and the wetted area of Tunabot V5 (28003 mm²) was only 3.8% less than that of Tunabot V4 (29087 mm²). Tunabot V5's wetted area was slightly less due to the physical gap in its body at the mid-body joint, whereas Tunabot V4's flexible skin was gapless (see Figure 4-17).

However, the drag forces due to tethers and power cables may have given Tunabot V5 a performance advantage. At Tunabot V4's maximum swimming speed (1.02 m/s) during performance testing (see Figure 3-11), the tethers and power cables generated 0.27 N according to our estimations (see Figure 3-9(B)). This included Tunabot V4's lateral snout tether, two vertical tethers, and two power cables. At the same speed (1.02 m/s), we estimated the drag force of Tunabot V5's singular tether and two power cables to be 0.17 N (see Figure 4-9(B)). Tunabot V5's power cables also functioned as vertical tethers, requiring fewer tethers and thus incurring less drag. We designed Tunabot V5 to have less tethered drag than Tunabot V4 in order to improve the experimental setup's likeness to untethered swimming (see Section 4.2.1).

Table 4-4: Comparison of wetted and projected areas between Tunabots V4 and V5. We compared the wetted and projected areas of Tunabot V4 and the specialized configuration of Tunabot V5. Their similar areas suggested that performance variations were not the result of drag differences. The gap in Tunabot V5's body caused its wetted area to be slightly less than that of Tunabot V4's gapless body (see Figure 4-17). The projected areas of Tunabots V4 and V5 were identical as a result of their deliberately similar dimensions. We calculated the wetted and projected areas from the CAD models.

Generation	Wetted Area (mm ²)	Projected Area (mm ²)
Tunabot V4	29087	2570
Tunabot V5	28003	2570

4.6.2 Swimming Kinematics

We compared the swimming kinematics of Tunabots V4 and V5 (Figure 4-18). The midline kinematics and curvatures of Tunabot V5 showed slightly more joint rotation than Tunabot V4. Despite this slight difference, the head and tail-beat amplitudes of Tunabots V4 and V5 were statistically similar. The average head and tail-beat amplitudes of Tunabot V4 were 0.05 ± 0.01 BL ($n = 27$) and 0.15 ± 0.01 BL ($n = 27$), respectively. The average head and tail-beat amplitudes of Tunabot V5 were 0.05 ± 0.01 BL ($n = 30$) and 0.16 ± 0.01 BL ($n = 30$),

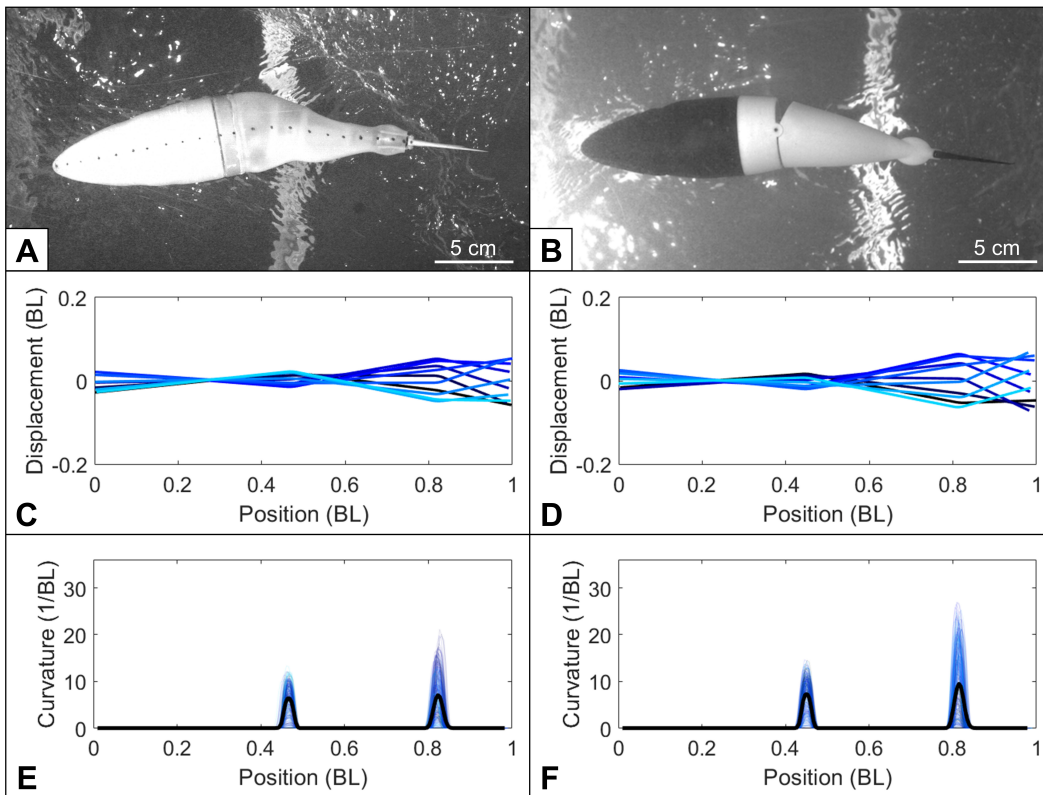


Figure 4-18: Swimming kinematics comparison between Tunabots V4 and V5. We compared the swimming kinematics of Tunabot V4 and Tunabot V5's specialized configuration side-by-side. Ventral views of (A) Tunabot V4 and (B) Tunabot V5. (C–D) Corresponding midline kinematics of a single tail-beat period divided into 10 equally spaced time intervals. The provided views and kinematics are representative of the average and selected for their similar swimming speeds: 3.92 and 3.97 BL/s, respectively, with 100% and 80% duty cycle voltage inputs. (E–F) Calculated curvatures along the body for $n = 270$ and 300 midlines from all trials and swimming speeds, corresponding to 27 and 30 tail-beat periods, with the means indicated by thicker, black lines. The head segment of Tunabot V5 was black to visually differentiate this specialized configuration from 2 DOF Flex, which had a larger tail-beat amplitude.

respectively. As expected, the intentionally similar designs of Tunabots V4 and V5 (see Section 4.5.1) produced nearly identical swimming kinematics. This gave us confidence that the following comparisons of swimming performance quantified the result of mechanical improvements rather than kinematic differences.

4.6.3 *Swimming Speed and Tail-Beat Frequency*

We thoroughly quantified and compared the swimming performance of Tunabots V4 and V5 using a variety of metrics beginning with the swimming speed and tail-beat frequency (Figure 4-19(A)). Using the same motor, Tunabot V5 was capable of a larger range of swimming speeds and tail-beat frequencies (0.31–4.70 BL/s and 1.4–15.3 Hz) compared to Tunabot V4 (0.37–4.00 BL/s and 2.5–14.8 Hz). Tunabot V5’s tail-beat frequency was also 0.6 Hz faster on average compared to Tunabot V4 for a given duty cycle of the PWM voltage input. For both Tunabots V4 and V5, the swimming speed was linearly proportional to the tail-beat frequency ($R^2 = 0.996$ and 0.994 , respectively) up to 10.2 Hz. Within this linear regime, Tunabot V5 swam 0.4 BL/s faster than Tunabot V4 on average for a given tail-beat frequency. At tail-beat frequencies above 10.2 Hz, both of their swimming speeds decreased, but the change in gradient was less abrupt for Tunabot V5.

4.6.4 *Cost of Transport*

Tunabot V5’s COT was statistically less than Tunabot V4’s COT by 7.7 J/kg/m on average across all tested speeds (Figure 4-19(B)). Tunabot V5’s minimum COT (6.3 ± 0.8 J/kg/m at 0.89 BL/s, $n = 3$) was 51% less than Tunabot V4’s minimum COT (12.9 ± 1.6 J/kg/m at 1.58 BL/s, $n = 3$). Furthermore, Tunabot V5’s COT increased less for speeds below 1.0 BL/s

compared to Tunabot V4. The COT is a mass-specific metric unlike the WPM (see Section 4.3.4), which disregards the different body masses of Tunabots V5 and V4 (0.190 vs. 0.306 kg, respectively). The minimum WPM of Tunabot V5 was 70% less than that of Tunabot V4. For both Tunabots V4 and V5, the electrical power consumption (Figure 4-19(C)) increased quadratically with the tail-beat frequency ($R^2 = 0.992$ and 0.999 , respectively). However, Tunabot V5 required 36–82% less power within the tail-beat frequency range of Tunabot V4 (2.5–14.8 Hz).

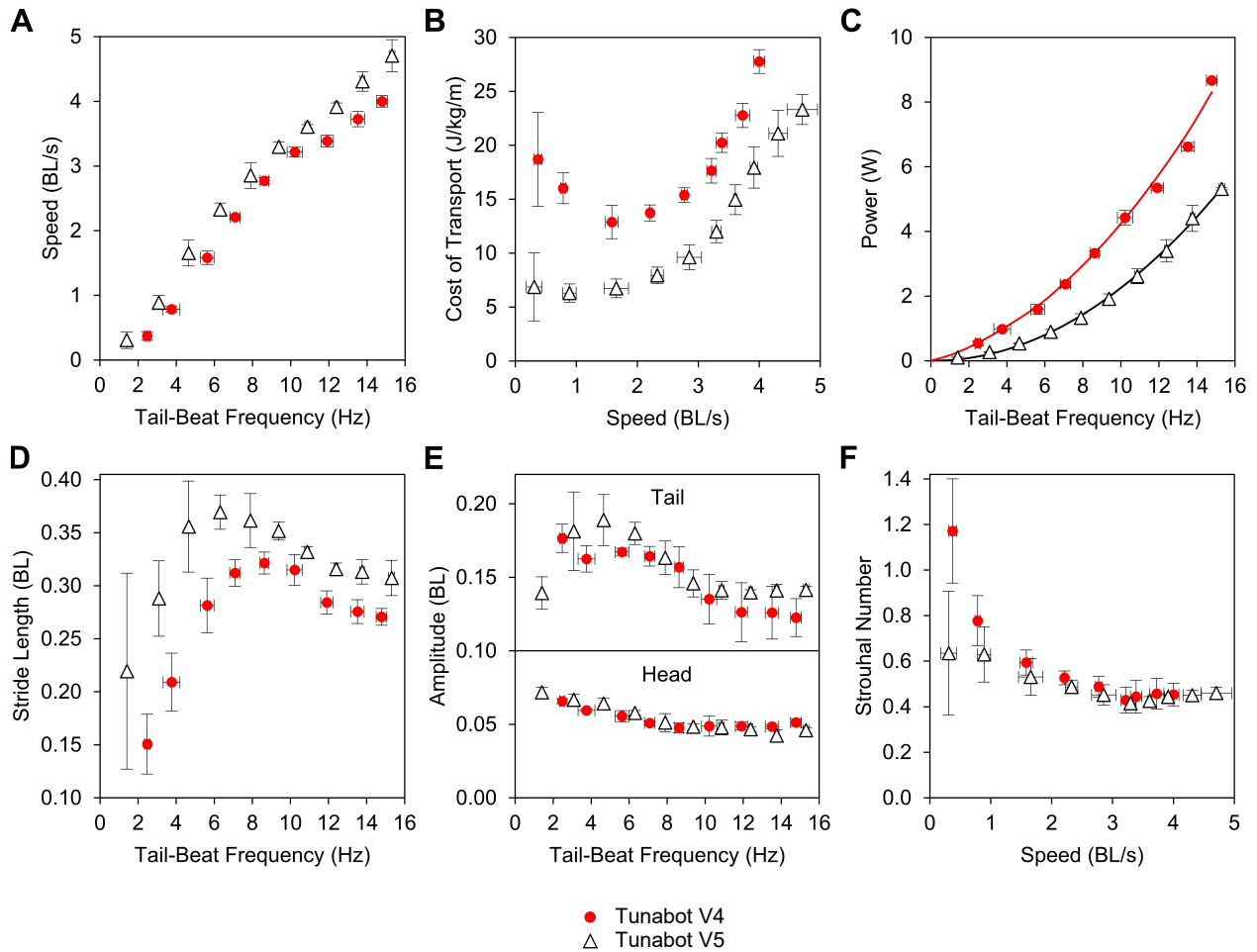


Figure 4-19: Performance results comparison between Tunabots V4 and V5. Here we compare the swimming performance of Tunabots V4 and V5. Tunabot V4’s data points are repeated from Figure 3-11. We designed a specialized configuration of Tunabot V5 specifically for this comparison and quantify its performance above. Data points represent the mean \pm 95% CI ($n = 3$).

4.6.5 *Stride Length*

Tunabot V5's stride length was statistically greater than that of Tunabot V4 for nearly all tail-beat frequencies (Figure 4-19(D)). Despite having different values, the profile of Tunabot V5's plotted stride length resembled that of Tunabot V4 if shifted upwards. This was because Tunabot V5's speed was 0.4 BL/s faster on average for a given tail-beat frequency compared to Tunabot V4 (see Section 4.6.3). The similarity of their stride length profiles indicated that the specialized configuration of Tunabot V5 replicated the swimming kinematics of Tunabot V4. This included the complex phenomena that resulted in the stride length's variable profile. Tunabot V5's specialized configuration successfully incorporated the key design parameters of Tunabot V4 in a way that allowed for reasonable comparison while still demonstrating improved performance.

4.6.6 *Head and Tail-Beat Amplitudes*

The head and tail-beat amplitudes of Tunabots V4 and V5 were similar in terms of their values and trends (Figure 4-19(E)). Using 2 DOF Flex to compare against Tunabot V4 would have been an unreasonable comparison due to their different tail-beat amplitudes, so we designed Tunabot V5's specialized configuration to match the tail-beat amplitude of Tunabot V4. Our results in Figure 4-19(E) confirm that the head and tail-beat amplitudes of Tunabots V4 and V5 were indeed similar in value and thus not the cause of performance differences. Additionally, the plotted head and tail-beat amplitudes of Tunabots V4 and V5 shared similar profiles. The dynamic trends in tail-beat amplitude of Tunabots V4 and V5 affected the profiles of their swimming speed (Figure 4-19(A)) and stride length (Figure 4-19(D)).

4.6.7 Strouhal Number

The St s of Tunabots V4 and V5 were similar for the majority of tested swimming speeds (Figure 4-19(F)). The minimum St of Tunabot V5 was 0.41 ± 0.03 ($n = 3$) at a speed of 3.30 BL/s. This result was statistically similar to the minimum St of Tunabot V4, which equaled 0.43 ± 0.06 at a speed of 3.22 BL/s ($n = 3$). The exception to this agreement occurred around 0.4 BL/s where the St of Tunabot V5 was statistically less than that of Tunabot V4. Tunabot V5's performance did not degrade at slower swimming speeds compared to Tunabot V4.

4.7 Biological Comparisons and Detailed Discussions

4.7.1 Normalizing by Length When Making Comparisons

We compared the swimming performance of Tunabot V5 with fishes using metrics normalized by length. These length-specific metrics included swimming speed, midline kinematics, head amplitude, tail-beat amplitude, midline curvature, and stride length. Body length and fork length are commonly used to normalize fish data. Body length, or 'total length', is the distance between the snout's tip and the end of the caudal fin's two lobes (i.e., the most anterior and posterior points of the body, respectively). Tunabot V5's results and much of the biological data presented in this chapter were normalized by body length. Fork length is the distance from the snout's tip to the end of the caudal fin's middle rays. Some of the speed and stride length data of yellowfin tuna was scaled by fork length [80], [81], [128]. Fork length and body length differ by the distance between the middle rays and longest lobe of the caudal fin. Because this distance is only a small percentage of overall body length, we compared values scaled by body length and fork length interchangeably (see Figure 4-13). Such comparisons were reasonable albeit approximate. In these instances, converting fork length to body length was not possible due to the

lack of reported information. Studies of tunas that plotted performance trends were also in short supply. For the sake of completeness, the third metric commonly used to quantify fish length is the standard length, which is the distance from the snout's tip to the end of the vertebral column. There is no single 'best' way to measure fish length since technique and consistency likely matter more than the method itself [273]. Irrespective of the preferred method, normalizing by length enabled us to make relative comparisons between Tunabot V5 and fishes of various sizes.

The following example demonstrates the importance of normalizing by length when comparing Tunabot V5 with biological data. Consider 4 DOF Flex (25.5 cm BL) and a yellowfin tuna about twice as long (53 cm FL) [128]. 4 DOF Flex swam 0.44 m/s with a stride length of 0.16 m. The tuna, however, swam twice as fast (0.92 m/s) with double the stride length (0.32 m). This valid comparison suggests that the tuna's performance was double that of 4 DOF Flex, and in an absolute sense, this is true. Normalizing these same data points by length yields a second conclusion. 4 DOF Flex swam 1.74 BL/s with a stride length of 0.63 BL, and the tuna similarly swam 1.74 FL/s with a stride length of 0.60 FL (see Figure 4-13(E)). Relative to their lengths, 4 DOF Flex and the yellowfin tuna performed nearly equally. The tuna's speed and stride length would be lesser if scaled by body length since fork length is shorter than body length for a given fish by definition. The example we presented here exemplifies how length-specific values are more informative and necessary when making relative comparisons.

For absolute comparisons, simply having a longer body would likely be faster and result in a larger stride length, although the performance would not necessarily scale linearly with size. The speed of fish is related to size through the tail-beat frequency, which decreases as fish size increases due to physiological limitations [77]. Similarly, a larger Tunabot would almost certainly outperform Tunabot V5 in an absolute sense but not relative to its size due to nonlinear

factors such as drag and mechanical losses. Taking inspiration from tuna by investigating the role of body flexibility improved the performance of Tunabot V5 relative to its size, and length-specific metrics enabled comparisons with biological data.

4.7.2 Center of Mass

Tunabot V5's COM (0.32 BL) was comparable to biological data. The COM of kawakawa tuna (*Euthynnus affinis*) was observed to be approximately 0.35 BL from the snout, which was determined by the position of minimum lateral displacement of the midline kinematics [183]. The COM of a fish can also be measured anatomically by finding the intersection of the body suspended by string in three different orientations [141]. For yellow perch (*Perca flavescens*), rock bass (*Ambloplites rupestris*), and bluegill sunfish (*Lepomis macrochirus*), the COM was reported to be located 0.34–0.41 BL from the snout [264]. Compared to these examples of tuna and non-Scombrid species, the COM of Tunabot V5 was similar but positioned slightly more towards the snout. Tunabot V5's mass distribution was concentrated in its head due to the heavy motor's anterior location and the posterior body's hollowness. Our use of CAD models to determine Tunabot V5's COM differed from the techniques used for fish measurements. In our case, we had already designed the necessary CAD models, and we were confident in their accuracy (see Section 4.4.1).

4.7.3 Dead-Drag Coefficients and Forces

Tunabot V5's drag coefficients were similar to those of tunas and other relevant fish species. We compared the drag coefficients of Tunabot V5 that we calculated using its wetted area rather than its projected area. Doing so enabled us to directly compare Tunabot V5 with fish

because the drag coefficients of fish are often calculated using their wetted areas. Tunabot V5's body modeled the morphology of yellowfin tuna (*Thunnus albacares*), which are members of the taxonomic family Scombridae. Other members of Scombridae include skipjack tuna (*Katsuwonus pelamis*), kawakawa tuna (*Euthynnus affinis*), and Pacific bluefin tuna (*Thunnus orientalis*). The drag coefficient of skipjack tuna was estimated to be 0.01 [134]. More broadly, the drag coefficient range of swimming *Euthynnus* (a genus in Scombridae) was estimated to be 0.01–0.03 [134]. Similarly, Tunabot V5's wetted drag coefficients were 0.016–0.028 depending on the Reynolds number (see Figure 4-9(C)). The Reynolds number of Tunabot V5 ranged from 4.2×10^4 to 3.2×10^5 . At slightly higher Reynolds numbers (5.0×10^5 – 1.3×10^6), the drag coefficient of kawakawa tuna was 0.009–0.044 depending on the method of calculation [134].

We also compared the drag coefficients of Tunabot V5 and rainbow trout [189], [265]. The trout's paired fins (i.e., pectoral and pelvic fins) were amputated, which resembled Tunabot V5's lack of paired fins. The trout's wetted area (342 cm^2) and body length (29.3 cm) were only slightly greater than those of 4 DOF Flex (279 cm^2 and 25.5 cm). The trout's drag coefficient was 0.015 at a Reynolds number of 1.73×10^5 . Similarly, 4 DOF Flex's body-only drag coefficient was 0.016 at a Reynolds number of 3.00×10^5 .

In addition to physical fish, the drag coefficient of a simulated Pacific bluefin tuna [266] was also comparable to Tunabot V5. CFD analysis of this bluefin tuna (20 cm BL) gliding at 1.2 BL/s ($Re = 4.8 \times 10^4$) yielded a drag coefficient of 0.015. The drag coefficient of 4 DOF Flex (25.5 cm BL) in 1.25 BL/s oncoming flow ($Re = 8.6 \times 10^4$) was 0.017 (see Figure 4-9(C)). The glide mode of the bluefin tuna with its straight, rigid body was essentially the same setup as Tunabot V5's dead-drag experiment in the flow tank (see Figure 4-8). When the simulated bluefin tuna beat its tail, the drag was twice that of the glide mode. This suggested that the drag

generated by a swimming, flapping fish was twice that of a towed, dead-body fish. The idea that undulatory swimming motion increases drag is referred to as the ‘Bone-Lighthill boundary-layer thinning hypothesis’ [120] and is a controversial topic [267]. Whether drag is enhanced or reduced by swimming motion is debated [267], [268].

The values of drag and comparisons between Tunabot V5 and biological data are not definitive for two reasons. First, the dead-drag is not equivalent to the self-propelled drag. This applies to Tunabot V5 and fish alike. Unlike dead-drag, the self-propelled drag of live fish accounts for body deformations during swimming and is consequently more challenging to measure [267]. To simplify drag measurements, rigid bodies are typically used. According to the ‘rigid-body analogy’, the flows around a swimming fish and rigid body are similar based on the observation that high-performance fish have streamlined bodies [189], [269]. For this reason, the exact self-propelled drag of Tunabot V5 remains unknown, but the measured dead-drag provided a conventional estimate. We also quantified and visualized the drag along Tunabot V5’s flapping body using PIV as it accelerated from rest [170].

Second, the dead-drag measurements of fish can vary by more than an order of magnitude due to the experiments themselves. The various methods for measuring fish drag can involve terminal velocity, deceleration in glide, towing-tanks, flow tanks, and wind tunnels [269]. Dead-drag measurements are also affected by the size of the fish and the passive fluttering of the flexible fins and posterior body [189]. Such fluttering like a flag in the wind is associated with a steep increase in drag [189], [270]. To further complicate matters, the numerous anatomical features of fish individually contribute to the total drag measurement and, therefore, must also be considered. For example, the body and caudal fin of a skipjack tuna comprised 57% [134] or 71% [265], [271] of the total estimated drag. These estimates did not include the gills,

paired fins, dorsal fins, or anal fin, which Tunabot V5's design physically omitted. Nevertheless, the comparisons we made using the biological data available indicated that the drag coefficients of Tunabot V5 were similar to those of tunas and other relevant fish species. Advanced applications of CFD [272] and PIV [170] techniques may be able to estimate the drag of live fish and bio-inspired systems with greater accuracy and uniformity than traditional dead-drag measurements.

4.7.4 *Swimming Kinematics*

The degree of body flexibility significantly affected the swimming kinematics of Tunabot V5. The joint angles and positions of Tunabot V5 (see Table 4-1) modeled the midline kinematics of yellowfin tuna (see Figure 4-10(H)). In particular, we designed the lateral displacement of Tunabot V5's body to increase posteriorly along the tail. For teleost fishes (which includes tunas), the lateral displacement of the midline decreases from the snout to a minimum located posterior to the neurocranium before increasing caudally to a maximum at the tail's tip [128], [183], [219]. The midlines of Tunabot V5 increasingly reflected this biological trend (see Figure 4-10(E)–(G) vs. (H)) as we added more body joints. This suggested that more joints would be better, but this is not necessarily the case (see Section 4.7.10). The midline curvature of teleost fishes gradually increases along the body [129], [219], [274] and is greatest in the anterior part of the tail (i.e., just behind the caudal peduncle) [184]. Our yellowfin tuna data (see Figure 4-10(L)) exemplified these trends, whereas Tunabot V5's curvature exhibited local peaks along the body and was essentially zero behind the peduncle (see Figure 4-10(I)–(K)). This was expected since Tunabot V5 consisted of rigid segments and a rigid caudal fin linked together by pinned joints.

We compared the head and tail-beat amplitudes of Tunabot V5's three body flexibility configurations with yellowfin tuna. The head amplitudes of Tunabot V5 (0.07–0.11 BL) were greater than the head amplitude of our yellowfin tuna (0.05 ± 0.01 BL, $n = 20$) in Figure 3-4. The tail-beat amplitude of our yellowfin tuna (0.19 ± 0.01 BL, $n = 20$) was similar to previously observed yellowfin whose amplitudes ranged from 0.17 to 0.20 FL [128]. More generally, teleost fishes had tail-beat amplitudes of 0.14–0.21 BL [77], 0.23 BL [78], and 0.11–0.21 BL [275]. Such similarity across species coincided with the 0.1–0.3 BL range of tail-beat amplitudes shown to minimize cruising energy expenditure [226]. The tail-beat amplitudes of Tunabot V5 (0.26–0.30 BL) lay within this range but exceeded the 0.19 BL amplitude of our yellowfin tuna. Nevertheless, the maximum tail-beat amplitude of Tunabot V5 (0.30 BL, 4 DOF Flex) was biologically realistic: skipjack tuna (*Katsuwonus pelamis*) were observed to have a tail-beat amplitude of 0.34 BL, although at nearly twice the speed (8.2 BL/s) [130].

Three characteristics of Tunabot V5 likely contributed to its larger head and tail-beat amplitudes compared to our yellowfin tuna. First, Tunabot V5's rigid head segment did not actively bend and orient itself upstream unlike the flexible heads of yellowfin tuna. Such active head yaw keeps the snout pointed ahead and thus directly reduces the head amplitude (see Figure 4-10(H)). We did not incorporate this component of yellowfin tuna kinematics into Tunabot V5 to simplify our biological model (see Section 4.7.10). Likewise, the positions and bend angles of Tunabot V5's body joints (see Table 4-1) might have modeled the body flexibility of yellowfin less accurately than we had originally expected, especially once dynamic swimming motions such as body yaw became involved. Second, the size and speed of our yellowfin tuna were different from Tunabot V5. The yellowfin were about four times longer (1.0 m) than Tunabot V5 (0.255 m), and only a very limited range of the yellowfin's achievable speeds was observed (1.0

BL/s) compared to Tunabot V5 (0.61–4.60 BL/s). Third, Tunabot V5’s caudal fin was rigid, whereas tuna caudal fins are flexible [82]. A flexible caudal fin would have reduced the lateral hydrodynamic forces on the fin, resulting in less body rotation about the center of mass. Less body yaw would have resulted in smaller head amplitudes. Caudal fin flexibility would have also altered the conformation of the tail’s trailing edge. Inward bending of the tail’s tip towards the body’s centerline, as exhibited by yellowfin tuna (see Figure 4-10(H)), would have reduced the lateral displacement of the tip. This displacement defined the tail-beat amplitude, so a flexible caudal fin would have reduced the tail-beat amplitude of Tunabot V5.

The variability of Tunabot V5’s tail-beat amplitude was unexpected since we designed the lateral displacement of the tail to be constant and equal across all three body flexibility configurations (see Figure 4-1(B)). In actuality, we designed the tail-beat amplitude to be constant from the head’s reference frame. Even this proved to not necessarily be true, however, since peduncle stiffness caused the tail-beat amplitude to increase with tail-beat frequency from the head’s reference frame. From the laboratory reference frame, which accounted for yawing motion of the body, the tail-beat amplitude rose and fell unexpectedly (see Figure 4-11). We attributed this to an involved combination of the degree of body flexibility, tail-beat frequency, body yaw, prescribed flapping motion of the tail, and peduncle stiffness.

The head’s reference frame is analogous to flow tank setups in which the head of a fish-inspired system is fixed by a rigid sting to always face directly upstream, and the posterior body rotates behind the stationary head (e.g., [276]–[278]). Such setups enable exceptional experimental control but omit the full-body yawing motion of swimming fish about their center of mass. We found body yaw to be important for several reasons. First, the power consumption of Tunabot V5 flapping in air dramatically increased when we firmly held the body by its head.

Doing so dampened the body's natural rotation about its center of mass. This suggested that the yaw component of fish kinematics improves swimming efficiency irrespective of fluid interactions. Second, body yaw directly affected the head and tail-beat amplitudes. The Strouhal number was also impacted since this metric is calculated using the tail-beat amplitude. Third, body yaw changed the orientation of the tail and subsequently the caudal fin's effective angle of attack. We showed in Section 3.3.6 that the effective angle of attack is a key variable of lift-based propulsion, and changing it would affect the thrust generated. The change in orientation would also likely affect the phase difference of the caudal fin, which is related to peduncle stiffness. Tunabot V5 demonstrated the importance of permitting the natural yaw motion of fish-like robotic systems when investigating kinematics; by restricting or eliminating body yaw, our results would have been less representative of free-swimming conditions and, therefore, less relevant to fish data.

The constant peduncle stiffness of Tunabot V5 resulted in the rotation angle of the peduncle joint increasing with tail-beat frequency before reaching its prescribed angle (see Table 4-1). Consequently, the phase difference between this joint and the caudal fin's tip decreased (see Figure 4-12). Recalling from earlier (see Section 3.3.6), phase differences around 270° and 330° maximize the propulsive efficiency and thrust, respectively, of a pitching and heaving airfoil [206]. With this in mind, the average phase difference of 2 DOF Flex ($328 \pm 2^\circ$, $n = 30$) may have maximized thrust over its tested range. For 3 DOF and 4 DOF Flex, the propulsive efficiency may have improved as tail-beat frequency increased since their phase differences decreased from $\sim 330^\circ$ towards 270° but only reached $\sim 295^\circ$. If the peduncle stiffness had the ability to vary instead of being constant, then a desired phase difference and tail-beat amplitude could be targeted and sustained across a range of tail-beat frequencies. This introduces

the idea of tuning the peduncle stiffness as fish do to optimize swimming performance across a range of speeds, which is an active area of research [132], [188], [279].

4.7.5 *Swimming Speed and Tail-Beat Frequency*

Tail-beat frequency is the major variable that fish modulate to obtain different swimming speeds [174]. Fish often do so at a specific ratio of wavelength to tail-beat amplitude [253]. But fish can also modulate their tail-beat amplitude to significantly affect speed [175]. We controlled the speed of Tunabot V5 through its tail-beat frequency, and the amplitude of the actuation mechanism's sweeping motion was constant (see Figure 2-1(B)). Tunabot V5's range of tail-beat frequencies (1.9–8.0 Hz) was limited by its internal motor on the low end and by the flow tank's maximum speed on the high end (see Section 4.3.1). Since the same model of motor achieved tail-beat frequencies of 14.8 Hz in the previous Tunabot V4, and because the tail-beat frequency of Tunabot V5 was 8.0 Hz with just 60% duty cycle of the PWM voltage input, we would expect Tunabot V5's untested maximum tail-beat frequency to be much greater. The tail-beat frequencies of 2 DOF, 3 DOF, and 4 DOF Flex were linearly related to the duty cycle ($R^2 = 0.994, 0.996, \text{ and } 0.999$), so we estimated their maximum tail-beat frequencies to be 12.9, 12.3, and 13.4 Hz, respectively. These were less than Tunabot V4's 14.8 Hz maximum tail-beat frequency because the tail-beat amplitudes of Tunabot V5's three body flexibility configurations were greater than Tunabot V4's tail-beat amplitude. The swimming speeds of 2 DOF, 3 DOF, and 4 DOF Flex were linearly related to tail-beat frequency as well ($R^2 = 0.996, 0.999, \text{ and } 0.998$), so we estimated their maximum speeds to be 7.3, 7.8, and 7.7 BL/s (i.e., 2.0 m/s), respectively, if unrestricted by the flow tank facility. The maximum speed of an autonomous Tunabot V5 would be even greater without the significant tethered drag (see Section 4.4.2).

The swimming speed of yellowfin tuna is linearly related to tail-beat frequency with positive slope [128], [280] as is the case for other tunas [183], [281], [282], other fish species [77], [78], [275], and cetaceans [283]. This was also the case for Tunabot V5 (see Figure 4-13(A)). The slopes of Tunabot V5 ranged from 0.56 to 0.65 BL depending on the body flexibility configuration. In Figure 4-13(A), we compared Tunabot V5's slopes with those of yellowfin tuna [128], which equaled 0.71, 0.86, and 0.92 FL depending on the tuna's size (42, 32, and 53 cm FL, respectively). Tunabot V5's slopes were less than the slopes of these yellowfin tuna. Since the slopes are indicative of stride length (see Equation (23)), which is a metric of swimming efficiency, Tunabot V5's smaller slope meant that it underperformed the yellowfin tuna. However, Tunabot V5's slopes overlapped the 0.57 FL slope observed of other yellowfin tuna (51.9 cm FL, $n = 33$) [218]. But these tuna were feeding rather than steadily swimming, which likely affected their slope. Linearly fitting the literature data of a diversity of fish species (see Figure 1-1(A)) yielded a slope of 0.71 BL ($R^2 = 0.93$). This was slightly less than the three slopes of yellowfin tuna [128] in Figure 4-13(A), which was consistent with previous work that found the slopes of tunas exceeded other species [128]. Overall, Tunabot V5's three body flexibility configurations overlapped the available yellowfin data in Figure 4-13(A), demonstrating favorable agreement between tail-beat frequencies of 2 and 4 Hz.

The Tunabot V5 platform enabled us to probe the largely unexplored high-performance space of fishes. The tested tail-beat frequencies of robotic fish are lower than Tunabot V5's specialized configuration (15.3 Hz) with two exceptions [21], [59], and perhaps none have higher length-specific, steady swimming speeds (4.70 BL/s). When robotic platforms do achieve high tail-beat frequencies, their corresponding swimming speed is often quite low compared to biological systems. Tunabot V5's three body flexibility configurations were centered in the fish

performance space up to 8.0 Hz (see Figure 4-13(A)). Despite this progress, fishes are capable of swimming speeds and tail-beat frequencies that are triple the tested performance of 4 DOF Flex (see Figure 5-1(A)). We would expect this difference to still be double even if we were able to test 4 DOF Flex's maximum performance in a faster flow tank. This disparity between fish and robotic platforms highlights the challenges and rewards of advancing the state-of-the-art in fish robotics.

4.7.6 *Cost of Transport*

The energy efficiency of Tunabot V5 aggressively closed the performance gap between robotic and biological systems, especially when considering Tunabot V5's broad speed range (1.25–4.60 BL/s). The COT of 4 DOF Flex was greater than the COT of tunas by less than half an order of magnitude across all tested speeds (see Figure 4-13(B)). For example, at a speed of 4.0 BL/s, the COT of 4 DOF Flex was 15.0 J/kg/m, whereas the COT of a yellowfin tuna was 6.6 J/kg/m [81]. Similarly, 4 DOF Flex's minimum COT (4.5 J/kg/m) was greater than the minimum COTs of tunas: 1.2 J/kg/m (bluefin) [79], 1.1 J/kg/m (yellowfin) [79], and 2.1 J/kg/m (yellowfin) [80]. However, the masses of these tunas (2.2–8.3 kg) with one exception (0.1 kg) were significantly greater than Tunabot V5's mass (0.190 kg). This highlighted the well-established trend in biology that more massive fishes have lower COTs. For example, the COT of minke whales (*Balaenoptera acutorostrata*) weighing 4,000 kg was estimated to be just 0.25 J/kg/m [284].

The defining challenge of developing high-performance robotic fish is the improvement of both speed *and* energy efficiency by taking inspiration from biological systems. We calculated the WPM and COT for the majority of robotic systems listed in Table 1-2 since fewer than half

directly reported either metric. When more than a single value was reported or calculable, we selected the COT corresponding to maximum swimming speed (as opposed to the minimum COT and corresponding speed). This approach emphasized how the COT of fish robots greatly varies (<1 to 5,000+ J/kg/m) despite having maximum speeds typically less than 2 BL/s. Figure 4-13(B) includes the 13 robotic fish from Table 1-2 whose COTs were less than or equal to the COT of Tunabot V4 at its maximum speed (27.8 J/kg/m). The COTs of at least four robots (see Table 1-2) were less than Tunabot V5's minimum COT (4.5 J/kg/m, 4 DOF Flex). Furthermore, there were at least ten robots (see Table 1-2) whose COTs were less than 4 DOF Flex's COT at its maximum tested speed (18.4 J/kg/m). However, the speeds of these robots did not exceed 2.2 BL/s, whereas the corresponding speed of 4 DOF Flex was 4.60 BL/s. This highlights our progress towards the development of a fish-like system demonstrating both high speed *and* energy efficiency.

The energetic costs of swimming fish vary nonlinearly with speed, resulting in J-shaped or U-shaped COT curves [111], [189], [221], [223]. As such, the minimum COT occurs at an intermediate speed. The COT curve of 2 DOF Flex was similarly U-shaped with its minimum occurring at 1.15 BL/s (see Figure 4-13(B)). Similarly, the speeds corresponding to the minimum COTs of tunas were 1.2 BL/s for bluefin [79], 1.2 BL/s for yellowfin [79], and 1.9 FL/s for yellowfin [80] (see Figure 4-13(B)). The COT curves of 3 DOF and 4 DOF Flex were not U-shaped because their COTs did not increase at their lowest tested swimming speeds. Consequently, it remains unknown if they reached their minimum COTs and at which speeds the minima would have occurred. If Tunabot V5's motor was capable of testing lower speeds (see Section 4.3.1), the COT curves of 3 DOF and 4 DOF Flex would have likely appeared U-shaped.

The COT of a U-shaped curve increases at the lowest swimming speeds. For fish, this increase is caused by the increasing relative contribution of the standard metabolic rate to the active metabolic rate [80]. Despite lacking a metabolism, 2 DOF Flex also produced a U-shaped COT curve that similarly increased at the lowest speeds (see Figure 4-13(B)). The increase in COT of 2 DOF Flex was potentially caused by higher costs due to stability and higher induced drag. Both were shown to increase at low speeds for fish [222]–[224]. However, stability was not likely a factor because 2 DOF Flex lacked active stability control, and we did not observe unusual kinematics. An example of unusual kinematics was the odd rolling of Tunabot V4 at its lowest tail-beat frequency (see Section 3.4.4). Higher induced drag was likely a factor because 2 DOF Flex’s airfoil-shaped caudal fin generated lift-based propulsion (see Section 3.3.6), and the induced drag of an airfoil becomes a substantial part of the drag coefficient at lower speeds [285]. A second likely cause of 2 DOF Flex’s increased COT at low speeds was the motor’s efficiency. In general, the efficiency of a DC motor increases with its rotational speed to a maximum before rapidly declining [286]. This trend applied to our experimentally obtained efficiency of Tunabot V5’s motor (see Figure 4-16). Consequently, the motor’s poor efficiency at slower swimming speeds contributed to the higher COT.

Tunabot V5’s COT increased with the tail-beat frequency (see Figure 4-13(B)). As the tail-beat frequency and thus swimming speed increased, so too did the hydrodynamic forces on Tunabot V5’s motor. This, in turn, caused the motor to consume more electrical power. Similarly, the COT of fish increases with swimming speed, but for a different reason. The COT of fish increases as the active metabolic rate rises with swimming speed [80]. This supports our view that the active metabolic rate is analogous to the total electrical power consumption (see Section 4.3.4).

We used Tunabot V5's unsubmerged mass when calculating its COT to be consistent with the COT calculations of fish, which also use unsubmerged mass (see Section 4.3.4). As a result, the 0.190 kg mass of Tunabot V5 did not include the volume of water that flooded its body cavity underwater through the joint gaps and immediately drained in air. We did not consider this water to be a part of Tunabot V5's discrete body since it freely flowed in and out, much the same as the water that drains from a fish's mouth on land. The mass of the internal water was 0.17 kg, which we estimated using Tunabot V5's CAD model (see Figure 4-2). Therefore, Tunabot V5's submerged mass was 0.36 kg, which was the sum of the unsubmerged mass and the internal water's mass. If we had used the submerged mass (0.36 kg) instead of the unsubmerged mass (0.190 kg) to calculate COT, all the values of Tunabot V5's COT would have been 47% lower. For example, this would have reduced 4 DOF Flex's minimum COT from 4.5 to 2.4 J/kg/m. The difference between submerged and unsubmerged masses would be less for an autonomous Tunabot V5 because the additional internal components would displace much of the internal water.

The optimal operating speed of Tunabot V5 would depend on mission requirements since COT was a function of swimming speed (see Figure 4-13(B)). The speed of minimum COT would result in the furthest swimming range, whereas the speed of maximum COT would produce the fastest performance. For example, 4 DOF Flex would cruise approximately 4.1 times further at a pace of 1.25 BL/s compared to 4.60 BL/s if powered by a finite energy source (i.e., battery). Holding all else equal, the additional mass of a battery would reduce Tunabot V5's COT by the battery's percentage of vehicle mass. For example, a 0.05 kg smartphone-sized battery would account for 21% of the new vehicle mass and thus decrease COT by 21%. In practice, such a straightforward improvement in efficiency is not guaranteed since incorporating

a battery might affect the center of mass and swimming performance. Furthermore, other components would be required to interface the battery, each with their own masses, so more than the battery's mass alone would affect the new vehicle's mass. In real-world applications, an AUV would likely utilize an adaptive, hybrid scheme that varies speed according to the task at hand.

4.7.7 *Work per Meter*

Accounting for body mass is important when comparing the energy efficiencies of differently sized systems. To highlight this, we compared the WPM of Tunabot V5 with tunas and fish robots (see Figure 4-13(C)). The WPM is a metric of efficiency that does not account for body mass unlike the COT, which is mass-specific (see Section 4.3.4). This difference between the COT and the WPM drastically impacted the appearance of their results (see Figure 4-13(B) vs. (C), respectively). Consequently, our comparisons of efficiency would have been quite different had we used the plot of WPM instead of COT. The WPMs of at least four robots (see Table 1-2) were less than Tunabot V5's minimum WPM (0.9 J/m, 4 DOF Flex). These same four robots were also less than 4 DOF Flex's WPM at its maximum tested speed (3.5 J/m). The minimum WPM of 4 DOF Flex (0.9 J/m) was 77% less than that of the previous Tunabot V4 (3.9 J/m). Most impressively, Tunabot V5's WPM was ~2–7 times lower than the WPM of tunas across all tested speeds (see Figure 4-13(C)) with one exception (0.7 J/m [81]). While WPM is a valid metric of energy efficiency, claiming to outperform the efficiency of tunas sevenfold would have been sensational but misleading. For this reason, we recommend using the COT instead of the WPM when making comparisons of energy efficiency, especially between robotic systems and their biological counterparts.

4.7.8 *Stride Length*

Tunabot V5's SL was similar in value to tunas and other species of fish. Figure 4-13(D) provides a broad-view comparison of SL between Tunabot V5 and biological data for common dace [77], bluefin tuna [79], and yellowfin tuna [79], [128]. The SL range of common dace was 0.22–1.10 [77]. Tunabot V5 overlapped this dace data having an SL range of 0.31–0.63 BL, which included all three body flexibility configurations. 3 DOF Flex was especially centered within the dace's SL data (see Figure 4-13(D)). The SL range of bluefin tuna was 0.45–0.60 [79], and the SL ranges of yellowfin tuna were 0.42–0.72 BL [79] and 0.22–0.73 FL [128]. The SL of our yellowfin tuna (see Figure 3-4) was 0.41 BL (see Section 4.4.6). Tunabot V5 also overlapped this tuna data. According to additional data that we did not plot, the SL of Atlantic bluefin tuna (*Thunnus thynnus*) ranged from 0.54 to 0.93 BL with a mean of 0.65 BL [287], and the average SL of a variety of fish species ranged from 0.53 to 1.04 BL [174]. All of these comparisons demonstrated that Tunabot V5's SL was similar in value to tunas and other fishes; however, Tunabot V5's SL range was more limited. This meant that fishes with higher SLs were capable of traveling further per tail-beat period than Tunabot V5.

The SLs of Tunabot V5 and fishes varied with swimming speed (see Figure 4-13(E)). At low swimming speeds, the SL of 2 DOF and 3 DOF Flex increased. This trend would likely have been apparent for 4 DOF Flex as well if its motor had been able to test lower speeds (see Section 4.3.1). The SL of common dace increased with speed as a whole, but the trends of individual fish were unclear because this data set combined seven differently sized specimens [77]. The SLs of bluefin and yellowfin tunas also increased with swimming speed [79], [128], overlapping the data of 2 DOF and 3 DOF Flex. As speed continued to increase, the SLs of 2 DOF and 3 DOF Flex leveled off at different values (~0.52 BL and ~0.62 BL, respectively).

At 1.5 BL/s, the SL of bluefin tuna [79] similarly leveled off at 0.60 BL, closely overlapping 3 DOF Flex (see Figure 4-13(E)). The SLs of yellowfin tuna [79], [128] did not level off but might have at higher, unobserved swimming speeds. After briefly increasing, the SL of 4 DOF Flex steadily decreased as swimming speed increased, which differed from all others. The negatively sloped SL of 4 DOF Flex would have fallen below the SL of dace if this trend continued at higher, untested tail-beat frequencies (see Figure 4-13(D)).

The values and trends of Tunabot V5's SL were similar to those of tunas and other species of fish. However, Tunabot V5 explored only a limited portion of the broad performance space of biological SLs (see Figure 4-13(D)). This illustrates the work that lies ahead to advance high-performance swimming platforms. Robotic fish that achieved high tail-beat frequencies often had low speeds (see Figure 1-1), which meant that they had shorter SLs compared to fishes. This demonstrates the importance of achieving and sustaining SLs greater than 0.6 in order to keep pace with biological systems, especially at higher swimming speeds.

4.7.9 *Strouhal Number*

We compared the trends and values of Tunabot V5's St with biological data. The St s of fishes and cetaceans decreased as their swimming speeds increased [225], [226]. Our results for 2 DOF Flex reflected this trend (see Figure 4-13(F)). The St s of 3 DOF and 4 DOF Flex would have likely increased for speeds below 1.0 BL/s as well if the motor were capable of testing such low speeds (see Section 4.3.1). The St s of cruising fishes are typically between 0.2 and 0.4 because this range optimizes propulsive efficiency [142], [226], [227], [229], [288]. Within this narrow range of values, the thrust of a pitching-heaving airfoil was maximized, and the thrust

was related to the duration of leading-edge vortex attachment [242]. The St of common dace [77] exemplified this 0.2–0.4 range (see Figure 4-13(F)). The minimum St of Tunabot V5's three body flexibility configurations was 0.46, which approached the upper limit of the 0.2–0.4 St range that is typical for fish. At slower speeds, however, Tunabot V5's St departed from this upper limit; Tunabot V5's highest St was 0.78 (2 DOF Flex) and occurred at 0.61 BL/s. This maximum value and corresponding speed were biologically realistic: dolphins were recorded as having a St of 0.78 at 0.63 BL/s [226]. The average ($n = 20$) St of steadily swimming yellowfin tuna was 0.45 ± 0.06 (see Section 3.3.3), which mostly exceeded the 0.2–0.4 St range that optimizes propulsive efficiency. This may have resulted from the slow swimming speeds (1.0 BL/s) of these tuna in captivity because propulsive efficiency is less important during slow locomotion than when cruising [142]. The St and propulsive efficiency are strongly correlated [289], so an optimal St is therefore important when cruising. The St dictates the conditions for undulatory locomotion that may surpass the propulsive efficiencies of traditional propellers [228]. For this reason, the St is a useful metric that we recommend quantifying when analyzing high-performance robotic fish.

4.7.10 *Optimal Number of Joints*

The degree of Tunabot V5's body flexibility affected the swimming speed, COT, stride length, and Strouhal number. Adding a third or fourth joint to Tunabot V5 improved speed by 0.5 BL/s for a given tail-beat frequency (see Figure 4-13(A)). A fourth joint diminished speeds by up to 0.3 BL/s compared to three joints for tail-beat frequencies above 3.9 Hz, but the reverse was true for tail-beat frequencies below 3.9 Hz. Despite this tradeoff, having four joints was clearly optimal after considering the energy efficiency; for each additional joint, the COT

decreased by 20% across all tested speeds (see Figure 4-13(B)). Having more than two joints was advantageous for the stride length; three or four joints increased the stride length by 0.10 BL on average compared to two joints (see Figure 4-13(E)). The stride length of four joints was greater than three joints for speeds below 1.3 BL/s, whereas the opposite occurred for speeds above 3.6 BL/s. In terms of the Strouhal number, having three or four joints was optimal; at speeds below 2 BL/s, having more than two joints reduced the Strouhal number by up to 25% (see Figure 4-13(F)). These results supported our hypothesis that increasing body flexibility improves swimming performance.

Overall, having four joints optimized the swimming performance of Tunabot V5 within the scope of this study. Utilizing three joints may actually be preferable to four joints if energy efficiency is not a concern or if other factors such as design simplicity are desired. The use of two joints is to be avoided. Beyond the scope of this study, having five or more joints may be optimal despite the diminishing returns on performance already present when adding Tunabot V5's fourth joint. The rotation angles of the joints could also be varied to optimize performance by tuning the tail-beat amplitude. While not the focus of our body flexibility study, we did reduce the tail-beat amplitude of 2 DOF Flex by nearly half in Section 4.6 with notable performance differences. In addition to the number of joints and their rotation angles, the positions of the joints could be selected to optimally model the kinematics of yellowfin tuna. For example, an actively driven joint positioned on the anterior half of Tunabot V5's body could mimic a tuna's ability to orient its head upstream (see Figure 4-10(H)). This would reduce Tunabot V5's head amplitude and likely improve swimming performance (see Section 4.7.4). For a flexible fish model, yawing motion of the head significantly reduced the COT when the phase angle between head and body movements fell within the range displayed by fish [290].

However, any gain in performance might not overcome the requisite mechanical inefficiencies for such a joint or be worth the additional design complexity. Tunabots V1–V5 had rigid head segments because we believed that active head yaw was a minor component of yellowfin tuna kinematics that insignificantly impacted performance compared to the tail’s kinematics.

Our results obtained with a tuna-inspired experimental platform suggested that high-performance fishes, of which yellowfin tuna are exemplary, benefit from body flexibility. Tuna exhibited flexibility surpassing that of Tunabot V5 (see Figure 4-10) partly as a result of their biological design; a jointed vertebral column with many segments is controlled by an array of both segmental and longitudinal musculature [82]. Such complexity is difficult to replicate in a robotic system but would increase body flexibility and generate a smooth, undulatory kinematic wave. The incorporation of compliant materials is a popular method of fish roboticists to smooth kinematics, but the rigid Tunabot V5 challenged the notion that these materials are necessary for high performance. An elastic skin may actually penalize performance, which we discuss in Section 4.7.11. One must consider how elastic energy is dissipated while deforming the material and the subsequent returns on performance.

Achieving biological performance in robotic systems is a challenging proposition that involves tradeoffs between design complexity and performance. Biological systems exhibit impressively complex morphologies and kinematics; consequently, only some biological features are approximated rather than exactly replicated to capture performance benefits. In this study, we modeled the body flexibility of yellowfin tuna to improve Tunabot V5’s swimming performance while omitting other features such as dorsal fins. In general, design complexity increases with the accuracy of the biological model, but returns on performance diminish after a certain point. This concept was demonstrated by our study; the design complexity of Tunabot V5 (i.e., the number

of joints) increased as the body flexibility approached that of tuna. However, the performance benefit from increasing the joint number from three to four was less than increasing the joint number from two to three.

This raises the question of what number of joints is optimal. Others recently developed algorithms that determined the arrangement of joints that optimally modeled the midline kinematics of a variety of fish species [291], [292]. To do so, these algorithms quantified the tradeoff between design complexity (i.e., number of joints) and biological accuracy. Our approach to designing the joints of Tunabots V1–V5 was more qualitative. For Tunabot V1, we manually traced the midlines of yellowfin tuna from dorsal-view footage and developed a two-joint model through trial and error (see Section 2.2.2). The footage was recorded by Lauder Laboratory (see Figure 3-4). Using the exact same footage as us, one of the recent algorithms systematically traced the midlines of yellowfin tuna and concluded that a two-joint model mimicked the midlines with more than 98% accuracy [292]. Interestingly, this highly accurate model was nearly identical to our own model that we developed five years prior; their algorithm positioned two joints at 0.49 BL and 0.83 BL, resembling Tunabot V1’s two joints located at 0.50 BL and 0.83 BL. This gave us confidence after the fact that our qualitative model was also quantitatively accurate. Tunabots V2–V4 applied Tunabot V1’s model (see Table 2-1), and we designed Tunabot V5’s three body flexibility configurations (see Table 4-1) by retracing the same footage of tuna. Quantitatively optimized models of biology are an invaluable resource during the initial design phase of bio-inspired systems. Our study encapsulated the difficult balance between model complexity and realized performance that is inherent to bio-inspired design.

4.7.11 Tunabot V5 Outperformed Tunabot V4: Design Improvements

We compared the swimming performance of Tunabots V4 and V5 in two ways. First, we compared Tunabot V4 with Tunabot V5's three body flexibility configurations (see Figure 3-11 vs. Figure 4-13, respectively). Second, we compared Tunabot V4 with the specialized configuration of Tunabot V5 that controlled for kinematic differences such as body flexibility and tail-beat amplitude (see Figure 4-19). In both cases, Tunabot V5 outperformed Tunabot V4.

Each of Tunabot V5's three body flexibility configurations swam faster than Tunabot V4 and with a lower COT across all tested tail-beat frequencies, especially 4 DOF Flex. Tunabot V4's maximum speed was 4.00 BL/s with 100% duty cycle of the PWM voltage input. The maximum tested speed of 4 DOF Flex (4.60 BL/s) was 15% faster than this with just 60% duty cycle of the PWM voltage input. At 4.00 BL/s, the COT of 4 DOF Flex (15.0 J/kg/m) was also 46% less than the COT of Tunabot V4 (27.8 J/kg/m). When comparing hypothetical swimming ranges, 4 DOF Flex would have traveled 4.6 times further than Tunabot V4 if both were powered by the same battery, resulting from 4 DOF Flex's 38% lighter mass (0.190 vs. 0.306 kg) and 65% lower minimum COT (4.5 vs. 12.9 J/kg/m).

However, Tunabot V5 had a larger tail-beat amplitude compared to Tunabot V4 and more body flexibility, and these kinematic differences could have caused Tunabot V5's significantly improved performance. To compare Tunabots V4 and V5 without kinematic differences, we designed a specialized configuration of Tunabot V5 that matched Tunabot V4's tail-beat amplitude and body flexibility (see Section 4.5.1). This specialized configuration of Tunabot V5 swam 0.4 BL/s faster than Tunabot V4 on average for a given tail-beat frequency. Furthermore, the minimum COT of Tunabot V5's specialized configuration (6.3 J/kg/m) was 51% less than that of Tunabot V4 (12.9 J/kg/m). These two highlights are from the detailed comparisons in

Section 4.6. The specialized configuration of Tunabot V5 demonstrated that the mechanical design of Tunabot V5 outperformed Tunabot V4. Therefore, the kinematic differences of Tunabot V5's three body flexibility configurations further improved an already higher-performing baseline.

Seven aspects of Tunabot V5's design contributed to its performance improvements over Tunabot V4. First, we replaced Tunabot V4's flexible skin with rigid body segments in order to incrementally test body flexibility. We also did not design a skin for Tunabot V5 due to its detrimental effects on performance (see Section 3.5.1). Despite its drawbacks, however, the skin would still offer advantages for an autonomous Tunabot V5; the skin's continuous surface would prevent floating debris from jamming the joint gaps or from entering the body. Second, Tunabot V5's single-motor actuation mechanism was capable of driving multiple body joints instead of just a single mid-body joint like Tunabots V1-V4. This capability was necessary for flapping the segmented tails of Tunabot V5's different body flexibility configurations. Third, we waterproofed Tunabot V5's motor with 3D-printed nylon. Doing so avoided the weight and internal space penalties of the silicone-injection technique (see Section 3.2.2). The massive bulk of silicone inside Tunabot V4's head also caused the body to oddly roll and bounce on its vertical tethers. Conversely, Tunabot V5 demonstrated stable swimming kinematics across all tested speeds. Tunabot V5's 3D-printed nylon also enabled us to waterproof the motor without preventing access to it for removal, whereas Tunabot V4's motor was unremovable. Fourth, Tunabot V5's improved tethering system reduced streamwise drag to more closely resemble untethered swimming conditions. Because Tunabot V5's two power cables also functioned as vertical tethers, Tunabot V5 required two fewer tethers than Tunabot V4, incurring less drag. Fifth, to reduce Tunabot V5's power consumption, we selected lightweight materials that

minimized the rotational inertia of the actuation mechanism and tail. The keeled peduncle of Tunabot V5 was made of ABS polymer, which weighed significantly less than Tunabot V4's gold-plated, stainless-steel spar. Tunabot V4's spar and caudal fin had to be made of stronger materials (i.e., stainless steel and VeroWhite resin, respectively) to prevent the peduncle joint from breaking. But we designed Tunabot V5's keeled body segment and caudal fin to be sufficiently strong despite both being made of ABS plastic. Sixth, the design of Tunabot V5's stiffened peduncle joint was more compact and streamlined than that of Tunabot V4. A single, internal spring wire provided torsional stiffness to Tunabot V5's peduncle joint that returned the caudal fin to a 0° neutral position with a passive restoring force. This new design imitated the function of lateral tuna tendons [126], [131], [252] just like the bilateral elastic bands of Tunabots V1–V4. The seventh aspect of Tunabot V5's design that improved its performance was the stuffing tube that waterproofed the actuation mechanism's rotating bent shaft. The stuffing tube generated less frictional resistance than Tunabot V4's solid silicone seal. The lesser friction of Tunabot V5's stuffing tube reduced power consumption and broadened the range of tail-beat frequencies. Altogether, these mechanical design improvements contributed towards closing the performance gap between high-performance fish and fish-like robotic systems.

4.7.12 Performance Implications: Closing the Performance Gap

There remains a significant performance gap between high-performance fish swimming and fish-like robotic systems despite progress in developing such systems. This study [106] utilized two approaches to close the performance gap. For the first approach, we used biology to inform the design of Tunabot V5, specifically tuna-inspired body flexibility. The most flexible configuration of Tunabot V5 steadily swam at 4.60 BL/s with a tail-beat frequency of 8.0 Hz and

a COT measuring 18.4 J/kg/m (see Figure 4-13). For the second approach, we advanced the mechanical design of Tunabot V5 from an engineering standpoint building upon Tunabots V1–V4. The specialized configuration of Tunabot V5, which we specifically created to compare against Tunabot V4, steadily swam at 4.70 BL/s with a tail-beat frequency of 15.3 Hz and a COT measuring 23.3 J/kg/m (see Figure 4-19). These results of both approaches represented an approach to fish-like performance. The enhancements of both bio-inspired and mechanical designs occurred in tandem to form a unified effort towards closing the performance gap. Led by Dr. Robin Thandiackal, we later investigated Tunabot V5’s linear acceleration from rest in December 2019 to further understand the extreme, high-performance capabilities of tunas and other pelagic fishes [170].

4.7.13 Tethered Tunabots

We designed and tested tethered Tunabots with the ultimate goal of improving untethered swimming performance. Both Tunabot V1 and the free-swimming configuration of Tunabot V2 were untethered systems that we tested in a stationary water tank. It became apparent from these tests that free-swimming systems were not ideal for rigorously studying the fundamentals of fast and efficient propulsion. We realized that these fundamentals should be understood first before applying them to an autonomous system. The physical constraints of the stationary water tank would have limited an autonomous Tunabot, making high-speed experiments impractical. Tunabot V2 was already swimming the length of the stationary water tank in a matter of seconds. Alternatively, if we had tested a free-swimming Tunabot in a flow tank, then autonomous control would have become the focus, especially at the high speeds we were exploring. An autonomous Tunabot capable of staying centered in a flow tank’s test section at high speeds was

certainly of great interest to us but would have distracted from our original objectives. We focused on speed and efficiency rather than control, so an autonomous Tunabot would have needlessly complicated experiments in a flow tank. For these reasons, we redesigned Tunabot V2 with tethers and quantified its performance in a flow tank. Due to the tethered setup's effectiveness, Tunabots V3–V5 were all tethered systems that we tested exclusively in flow tanks. Tethered testing in flow tanks provided exceptional experimental control as we explored the high-performance space of fish, especially in regard to high speed and low cost of transport. Autonomous control, which includes navigation and maneuverability, is also a core feature of high-performance fish swimming but was outside the scope of this dissertation. Our work here informs the future development of an autonomous, high-performance Tunabot.

Chapter 5

Concluding Remarks

5.1 Closing the Gap: Robotic vs. Biological Swimming Performance

Our research goal was to close the gap in performance between bio-inspired robotic swimmers and high-performance fish. Current robotic fish are unable to access the high-speed, high-frequency performance space of fish with three exceptions: [12], [59], [66] (Figure 5-1(A)). Regarding efficiency, the COT of fish robots is one to four orders of magnitude higher than that of tunas with four exceptions: [5], [31], [37], [44] (Figure 5-1(B)). There is no overlap between these exceptions. In other words, there is no *single* fish robot capable of matching both the swimming speed *and* energy efficiency of high-performance fish to our knowledge.

To address this disparity, we developed five generations of fish robots modeling the morphology and kinematics of yellowfin tuna (*Thunnus albacares*). We selected tuna as our biological model for their extraordinary speed and endurance. Our close collaboration with biologists from Harvard University's Lauder Laboratory was fundamental to the success of this dissertation. Our tuna-inspired robots, or Tunabots, approached the swimming speed *and* energy efficiency of high-performance fish with each successive generation (Figure 5-1). The fifth generation, Tunabot V5, swam 4.60 BL/s with a tail-beat frequency of 8.0 Hz and a COT

measuring 18.4 J/kg/m. We highlight the speed and efficiency of the Tunabots in Table 5-1 and Table 5-2, respectively. To compare our work with the state of the art, we provide a uniquely comprehensive literature review of the field of bio-inspired underwater robots in Table 1-1.

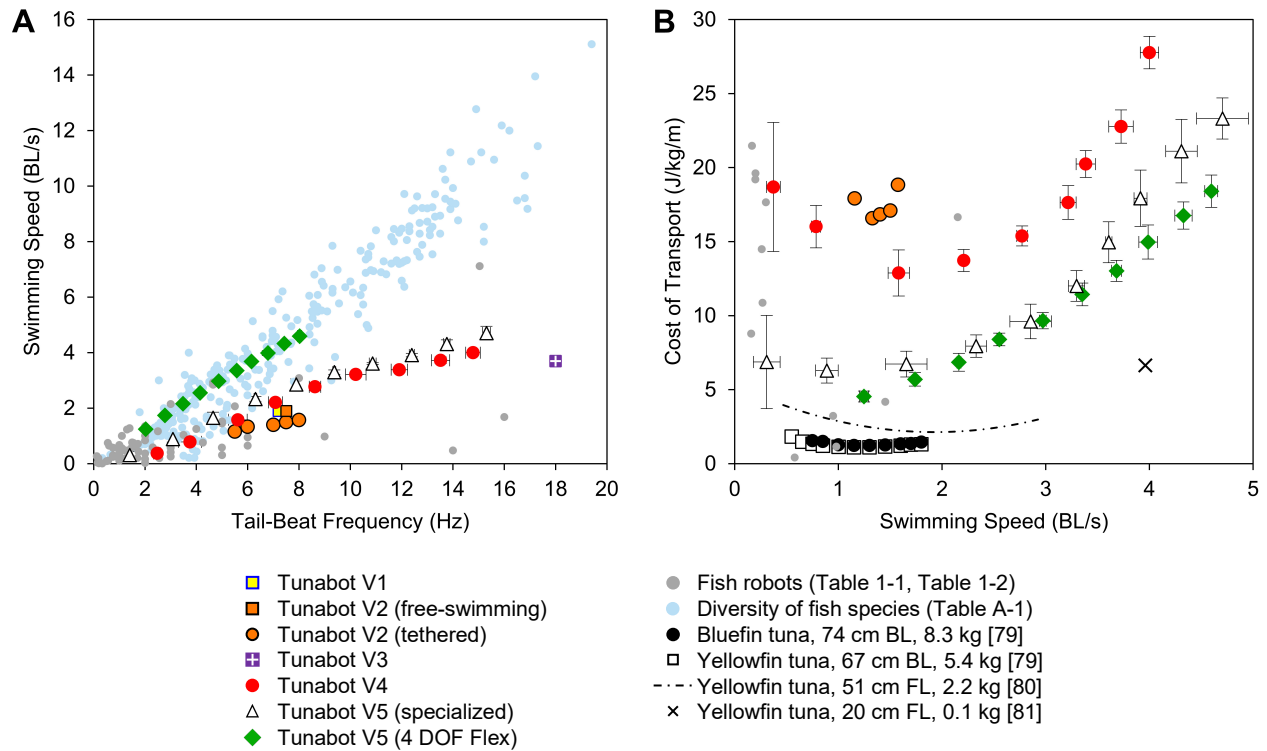


Figure 5-1: Closing the performance gap between fish robots and high-performance fish. This dissertation significantly reduced the gap in performance between bio-inspired fish robots and high-performance fish. Here we summarize our progress towards developing a *single* system with both the (A) swimming speed and (B) energy efficiency of high-performance fish. We advanced the designs and methodologies required to do so over five generations of tuna-inspired experimental platforms (Tunabots V1–V5). Data points represent the mean \pm 95% CI. We provide data summaries in Table 5-1 and Table 5-2.

Additionally, we provide an unprecedented literature review of all bio-inspired underwater robots from 1999 to the time of this dissertation’s defense that, to our knowledge, directly reported COT (Table 1-2). Investigations of energy efficiency are rare within the field of bio-inspired underwater robots. We select COT to quantify the energy efficiency of the Tunabots because COT is a common metric of fish performance. The active metabolic rate of fish is

analogous to the total electrical power consumption of the Tunabots. We demonstrate how to directly compare the two with identical units using an oxycalorific coefficient. We also address the literature’s inconsistent units of COT by proposing that COT be normalized by body mass. Doing so reasonably compares systems of different sizes. We measure the power consumption of the Tunabots using a custom system of external electronics. This system is widely applicable to underwater vehicles driven by PWM-controlled DC motors, making it possible for future vehicles to investigate their COT.

Table 5-1: Maximum swimming speed of Tunabots V1–V5. Maximum swimming speed and corresponding tail-beat frequency and cost of transport (COT) of all Tunabot generations and configurations in this dissertation. We provide mean values (white columns) and their 95% confidence intervals (CI, gray columns) for results with multiple trials ($n = 3$). The COT was unmeasurable for Tunabots V1 and V2 (free-swimming) and untested for Tunabot V3. Tunabot V5’s specialized configuration was for direct comparison with Tunabot V4. Tunabot V5’s configuration with the greatest body flexibility (4 DOF Flex) was the highest-performing system in terms of speed *and* efficiency. *We estimated Tunabot V1’s unmeasured performance to equal that of Tunabot V2 since both systems differed only in their waterproofing. **We predicted Tunabot V3’s untested performance based on Tunabot V2’s tethered performance.

Generation	Setup	Max. Speed (BL/s)	Speed 95% CI (BL/s)	Tail-Beat Frequency (Hz)	Freq. 95% CI (Hz)	COT (J/kg/m)	COT 95% CI (J/kg/m)
Tunabot V1	Free-swimming	1.9*	-	7.5*	-	-	-
Tunabot V2	Free-swimming	1.9	-	7.5	-	-	-
Tunabot V2	Tethered	1.6	-	8.0	-	18.8	-
Tunabot V3	Tethered	3.7**	-	18**	-	-	-
Tunabot V4	Tethered	4.00	± 0.09	14.8	± 0.3	27.8	± 1.1
Tunabot V5 (Specialized)	Tethered	4.70	± 0.25	15.3	± 0.2	23.3	± 1.4
Tunabot V5 (4 DOF Flex)	Tethered	4.60	± 0.06	8.0	± 0.1	18.4	± 1.1

Table 5-2: Minimum cost of transport (COT) of Tunabots V4 and V5. Minimum COT and corresponding swimming speed and tail-beat frequency of Tunabots V4 and V5. We provide mean values (white columns) and their 95% confidence intervals (CI, gray columns) of the multiple trials ($n = 3$). Tunabot V5’s specialized configuration was for direct comparison with Tunabot V4. Tunabot V5’s configuration with the greatest body flexibility (4 DOF Flex) achieved the lowest COT.

Generation	Min. COT (J/kg/m)	COT 95% CI (J/kg/m)	Speed (BL/s)	Speed 95% CI (BL/s)	Tail-Beat Frequency (Hz)	Freq. 95% CI (Hz)
Tunabot V4	12.9	± 1.6	1.58	± 0.10	5.6	± 0.4
Tunabot V5 (Specialized)	6.3	± 0.8	0.89	± 0.11	3.1	± 0.1
Tunabot V5 (4 DOF Flex)	4.5	± 0.4	1.25	± 0.04	2.0	± 0.1

We quantify the swimming performance of our tuna-inspired robots by applying the same metrics and testing facilities used for researching fish performance. Doing so enables us to directly compare our systems with fish to demonstrate our progress towards fish-like performance. We compare the swimming speed, tail-beat frequency, COT, stride length, midline kinematics, midline curvature, head amplitude, tail-beat amplitude, Strouhal number, dead-drag force, dead-drag coefficients, wake flow via PIV, and phase difference of the caudal fin. Our comprehensive analyses are important for the field of bio-inspired underwater robots where data presentation is inconsistent. Furthermore, comparisons of fish robots with their sources of biological inspiration are rare, making it difficult for these systems and thus the overall field to quantify progress. To elevate this standard, we rigorously compare the Tunabots with data of their species-specific inspiration (i.e., yellowfin tuna) in addition to a diversity of fish species.

The Tunabots are able to explore the high-performance space of fish (Figure 5-1(A)) more effectively as we refine both their design and testing methodology. To generate the high, requisite tail-beat frequencies, the Tunabots establish an actuation mechanism that converts the rotary motion of a single DC motor into flapping motion. This mechanism demonstrates tail-beat frequencies ranging from 1.4 to 22.4 Hz. The subsequent swimming speeds quickly cover the length of our stationary water tank, so we transition from free-swimming Tunabots to ones tethered in flow tanks. Flow tanks enable the Tunabots to steadily swim in a straight path indefinitely and at higher speeds. The tethered setup does not restrict the body's natural yawing motion and, with the exception of streamwise drag, is representative of free swimming. This novel tethered setup may be useful to others testing systems with sensitive body kinematics while requiring exceptional experimental control.

We extend the tethered setup from the flow tank to the stationary water tank to measure the static thrust of the fourth generation, Tunabot V4. Our experimental setup quantifies the propulsive force output of Tunabot V4 as it flapped in place with unconstrained body yaw. This unique setup provides a non-computational alternative to PIV for measuring the thrust of undulatory swimmers without restricting the head's natural yawing motion. We show that thrust is generated, in part, by a lift force on the caudal fin. To characterize this lift-based propulsion, we model the caudal fins of fish and Tunabots as pitching-heaving airfoils and apply airfoil theory. We focus on the effective angle of attack, which accounts for both the caudal fin's angle of attack and the relative flow velocity seen by the caudal fin. We mathematically show how the effective angle of attack determines the amount of lift-based propulsion generated. We also discuss how the effective angle of attack determines the behavior of leading-edge vortices during dynamic stall and hence thrust generation. For these reasons, we propose that the caudal fin's effective angle of attack is a more appropriate metric of thrust than simply the angle of attack when studying pitching-heaving locomotion.

The Tunabots are research platforms for testing hypotheses related to high-performance fish swimming. The two-jointed designs of Tunabots V1–V4 produce midline kinematics lacking the smooth curvature exhibited by yellowfin tuna, so we hypothesize that modeling such curvature in a tuna-inspired system would improve swimming performance. Tunabot V5 ('Tunabot Flex') demonstrates that body flexibility improves swimming speed and lowers COT, advancing our understanding of high-performance fish swimming. This dissertation informs the development of state-of-the-art underwater vehicles that aim to explore a fish-like, high-performance space and close the gap between robotic systems and fish swimming ability.

5.2 Future Work

5.2.1 *Demonstrate Tunabot V5's Full Capabilities*

We were unable to test Tunabot V5's full range of performance. Testing duty cycles above 60% was not possible because Tunabot V5's self-propelled swimming speed exceeded the maximum speed (1.25 m/s) of the flow tank (see Section 4.3.1). Previously, we delayed this limitation with the smaller dimensions of Tunabot V4 (see Section 2.5.3). The dimensions of Tunabots V4 and V5 were identical. While further miniaturization is possible, a faster flow tank would be more appropriate based on the progress of our work. We predict that the maximum (i.e., 100% duty cycle) tail-beat frequency 4 DOF Flex is 13.4 Hz based on the linear relationship ($R^2 = 0.999$) between the tail-beat frequency and duty cycle. This tail-beat frequency would correspond to a maximum swimming speed of 7.7 BL/s (2.0 m/s), which we predicted by extrapolating the linear slope ($R^2 = 0.998$) of 4 DOF Flex in Figure 5-1(A). However, this prediction is a best-case scenario since the stride length may decrease at higher tail-beat frequencies due to the caudal fin's decreasing phase difference (see Section 4.4.3). We require a faster flow tank facility in order to continue exploring the high-performance space of fish and advancing the state of the art.

5.2.2 *Improve Motor Efficiency*

A higher quality motor would dramatically and immediately improve the swimming performance of Tunabot V5. Tunabot V5 utilized the same motor as Tunabot V4 so that we were able to directly compare their performance. This motor's efficiency ranged from 26% to 45% based on our measurements (see Section 4.4.8). Having a motor efficiency of 75% is realistic and readily attainable for a similarly sized motor and gearbox (e.g., Maxon). A higher quality motor

with 75% efficiency would dramatically improve the swimming performance of Tunabot V5. For example, the minimum COT of 4 DOF Flex would decrease from 4.5 to 1.6 J/kg/m, corresponding to a swimming speed of 1.25 BL/s. This result would match both the swimming speed and COT of tuna (see Figure 5-1(B)). Additionally, the COT of 4 DOF Flex at its maximum tested speed of 4.60 BL/s would decrease from 18.4 to 11.1 J/kg/m. Such a result would significantly close the performance gap between high-performance fish and fish-like robotics even further.

5.2.3 Investigate Fin-Fin Interactions

Hypothesis: The first and second dorsal fins, anal fin, and finlets improve performance through fluid interactions between their surfaces and the caudal fin.

Until this point, Tunabots V1–V5 have reflected a simplified version of tuna morphology. We omitted all fins except for the caudal fin to focus on the propulsive contributions of the body and tail (see Section 2.2.2). These omitted fins would enhance the bio-inspired design of Tunabot V5 and enable us to investigate their impact on swimming performance. We added first and second dorsal fins, an anal fin, and finlets to Tunabot V5 (4 DOF Flex) based on reference videos and images of yellowfin tuna (Figure 5-2). These new features match tuna in terms of morphology and placement. The modular fins snap into place, enabling us to test different shapes and stiffnesses by swapping out fins. We are able to rapidly prototype various fin designs since they are 3D printed, and the designs can even be nonbiological in shape. PIV data will enable us to assess the hydrodynamic interactions between the dorsal fins, anal fin, finlets, and caudal fin. These fin-fin interactions are a feature of high-performance fish that have yet to be explored at

higher swimming speeds, which are accessible by Tunabot V5. We detailed this investigation of fin-fin interactions in our Doctoral Thesis Proposal in December 2019.

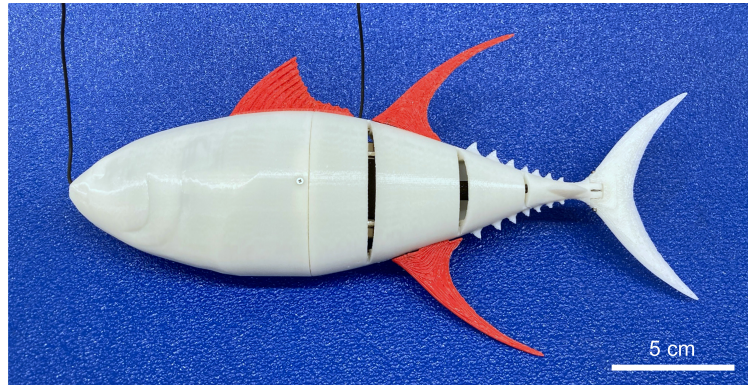


Figure 5-2: Tunabot Fin. This configuration of Tunabot V5 (4 DOF Flex) features first and second dorsal fins, an anal fin, and finlets to explore their impact on swimming performance. The modular, 3D-printed fins are removable, enabling us to test a variety of fins with different shapes and stiffnesses.

5.2.4 Explore Caudal Fin Flexibility

Hypothesis: A flexible caudal fin improves the cost of transport at the expense of swimming speed compared to a rigid caudal fin.

Until this point, the caudal fins of Tunabots V1–V5 have consisted of a single piece of rigid material. This contrasts the complex anatomy of tuna caudal fins and their anisotropic flexibility with both stiff and compliant bending axes (see Section 3.5.3). This difference in flexibility was apparent when comparing the swimming kinematics of Tunabot V5 with those of yellowfin tuna (see Figure 4-10(E)–(H)). Introducing a flexible caudal fin to Tunabot V5 would enhance its bio-inspired design and enable us to investigate the impact of caudal fin flexibility on swimming performance. Tunabot V5’s modular caudal fin is removable, enabling us to test a variety of caudal fins with different stiffnesses. To isolate the effects of flexibility,

these caudal fins would share identical morphologies including planform area and aspect ratio. We detailed this investigation of caudal fin flexibility in our Doctoral Thesis Proposal in December 2019.

Besides flexibility, a promising area of research is the effect of caudal fin morphology on swimming performance. As with caudal fin flexibility, Tunabot V5's modular design enables us to test differently shaped caudal fins. Interestingly, we could apply shapes from any species to our tuna-inspired system. We could also test caudal fins with nonbiological shapes, such as rectangular airfoils, that might not exist naturally. Unlike fish, the Tunabots are neither constrained by evolutionary pressure nor limited by biological material properties. This enables us to rapidly evolve our design with 'beyond-bio' body parts and perhaps surpass fish performance.

5.2.5 Investigate Peduncle Stiffness with Tunabot V5

Hypothesis: No single stiffness of the peduncle joint is optimal across the full range of swimming speeds; rather, actively tuning the stiffness for each particular speed optimizes performance.

A formal investigation of peduncle stiffness using Tunabot V5 remains. With a higher quality motor, we predict that the minimum COT of Tunabot V5 will match the COT of tuna at the same swimming speed (see Section 5.2.2). However, at Tunabot V5's maximum speed, Tunabot V5's COT will still exceed the COT of tuna despite the upgraded motor. This is because Tunabot V5's COT increases with swimming speed more dramatically than the COT of tunas (see Figure 5-1(B)). Previously, we found that tuning the peduncle stiffnesses of Tunabots V2 and V4 sustained lower COTs at higher swimming speeds. By applying this concept to Tunabot

V5, tuning the peduncle stiffness of Tunabot V5 would decrease the COT at higher speeds. Reducing COT would further close the gap in performance between Tunabot V5 and tunas. Additionally, Tunabot V5 would be able to swim further for a given battery while at a faster speed (see Section 4.7.6).

Tunabot V2 demonstrated that peduncle stiffness impacted swimming performance (see Section 2.3.6). The rigid peduncle's faster speed suggested that higher stiffness is desirable for high-frequency swimming but perhaps at the cost of higher power consumption. Thus, a tradeoff exists between efficiency and speed depending on the peduncle stiffness and tail-beat frequency. These results support the previous findings of Gregory Lewis [132], who inspired our experiment.

Varying Tunabot V4's peduncle stiffness yielded similar results. We found that a stiffer peduncle was able to access higher swimming speeds but with a higher COT. This supported our conclusions with Tunabot V2, except this time we were able to quantify COT; we had not yet developed the system to measure power consumption and thus COT (see Section 2.4.2) when testing Tunabot V2's free-swimming performance. We detailed this investigation of peduncle stiffness using Tunabot V4 in our Doctoral Thesis Proposal in December 2019.

5.2.6 *Apply Bio-Inspired Flow Sensing*

This dissertation informs the development of future bio-inspired underwater vehicles. AUVs require the ability to self-navigate and thus sense their surroundings. The lateral-line system of fish offers a bio-inspired solution to the development of an autonomous sensory system. The lateral line consists of hair-like, epidermal organs termed 'neuromasts'. Neuromasts enable fish to sense obstacles, flow velocity, and approaching predators and prey. For our

undergraduate thesis, we fabricated flow sensors inspired by neuromasts with similar functionality (Figure 5-3) [293], [294]. Applying an array of these sensors along Tunabot V5's lateral line would demonstrate their capabilities during high-speed swimming at high tail-beat frequencies. This bio-inspired array of artificial flow sensors offers a unique sensory system for state-of-the-art AUVs.

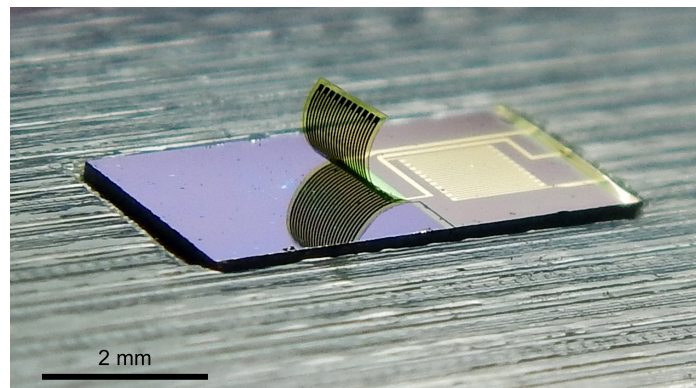


Figure 5-3: Artificial flow sensor inspired by fish neuromasts. Neuromasts are hair-like, epidermal organs located along the lateral line of fish that sense obstacles, flow velocity, and approaching predators and prey. Artificial sensors with such functionality would lend automated systems the acute awareness of the lateralis system to sense and react to their environment. We fabricated flow sensors inspired by neuromasts, including the one pictured above, for our undergraduate thesis [293], [294].

References

- [1] A. N. Ahmad Mazlan, “A Fully Actuated Tail Propulsion System for a Biomimetic Autonomous Underwater Vehicle,” Ph.D. Dissertation, University of Glasgow, Glasgow, United Kingdom, 2015.
- [2] J. M. Anderson and N. K. Chhabra, “Maneuvering and stability performance of a robotic tuna,” *Integr. Comp. Biol.*, vol. 42, no. 1, pp. 118–126, Feb. 2002, doi: 10.1093/icb/42.1.118.
- [3] D. S. Barrett, M. S. Triantafyllou, D. K. P. Yue, M. A. Grosenbaugh, and M. J. Wolfgang, “Drag reduction in fish-like locomotion,” *J. Fluid Mech.*, vol. 392, pp. 183–212, 1999, doi: 10.1017/S0022112099005455.
- [4] F. Berlinger, M. Gauci, and R. Nagpal, “Implicit coordination for 3D underwater collective behaviors in a fish-inspired robot swarm,” *Sci. Robot.*, vol. 6, no. 50, p. eabd8668, 2021, doi: 10.1126/scirobotics.abd8668.
- [5] T. Bujard, F. Giorgio-Serchi, and G. D. Weymouth, “A resonant squid-inspired robot unlocks biological propulsive efficiency,” *Sci. Robot.*, vol. 6, p. eabd2971, Jan. 2021, doi: 10.1126/scirobotics.abd2971.
- [6] S. Butail, N. Abaid, S. Macrì, and M. Porfiri, “Chapter 12: Fish–robot interactions: robot fish in animal behavioral studies,” in *Robot Fish*, R. Du, Z. Li, K. Youcef-Toumi, and P. Valdivia y Alvarado, Eds., in Springer Tracts in Mechanical Engineering. Springer, Berlin, Heidelberg, 2015, pp. 359–377. doi: 10.1007/978-3-662-46870-8_12.
- [7] Y. Cai, S. Bi, and L. Zheng, “Design and experiments of a robotic fish imitating cow-nosed ray,” *J. Bionic. Eng.*, vol. 7, pp. 120–126, 2010, doi: 10.1016/S1672-6529(09)60204-3.
- [8] Y. Cai, S. Bi, and H. Ma, “Chapter 5: Research on robotic fish propelled by oscillating pectoral fins,” in *Robot Fish*, R. Du, Z. Li, K. Youcef-Toumi, and P. Valdivia y Alvarado, Eds., in Springer Tracts in Mechanical Engineering. Springer, Berlin, Heidelberg, 2015, pp. 119–160. doi: 10.1007/978-3-662-46870-8_5.
- [9] B. Chen and H. Jiang, “Swimming performance of a tensegrity robotic fish,” *Soft Robotics*, vol. 6, no. 4, pp. 520–531, 2019, doi: 10.1089/soro.2018.0079.
- [10] Z. Chen, H. Bart-Smith, and X. Tan, “Chapter 8: IPMC-actuated robotic fish,” in *Robot Fish*, R. Du, Z. Li, K. Youcef-Toumi, and P. Valdivia y Alvarado, Eds., in Springer Tracts

- in Mechanical Engineering. Springer, Berlin, Heidelberg, 2015, pp. 219–253. doi: 10.1007/978-3-662-46870-8_8.
- [11] Z. Chen, P. Hou, and Z. Ye, “Robotic fish propelled by a servo motor and ionic polymer-metal composite hybrid tail,” *Journal of Dynamic Systems, Measurement, and Control*, vol. 141, no. 7, p. 071001, Jul. 2019, doi: 10.1115/1.4043101.
- [12] D. Chen, Z. Wu, P. Zhang, M. Tan, and J. Yu, “Performance improvement of a high-speed swimming robot for fish-like leaping,” *IEEE Robotics and Automation Letters*, vol. 7, no. 2, pp. 1936–1943, Apr. 2022, doi: 10.1109/LRA.2022.3142409.
- [13] C. Christianson, N. N. Goldberg, D. D. Deheyn, S. Cai, and M. T. Tolley, “Translucent soft robots driven by frameless fluid electrode dielectric elastomer actuators,” *Sci. Robot.*, vol. 3, no. 17, p. eaat1893, Apr. 2018, doi: 10.1126/scirobotics.aat1893.
- [14] C. Christianson *et al.*, “Jellyfish-inspired soft robot driven by fluid electrode dielectric organic robotic actuators,” *Front. Robot. AI*, vol. 6, no. 126, pp. 1–11, Nov. 2019, doi: 10.3389/frobt.2019.00126.
- [15] M. Cianchetti, M. Calisti, L. Margheri, M. Kuba, and C. Laschi, “Bioinspired locomotion and grasping in water: the soft eight-arm OCTOPUS robot,” *Bioinspir. Biomim.*, vol. 10, no. 035003, pp. 1–19, 2015, doi: 10.1088/1748-3190/10/3/035003.
- [16] O. M. Curet, N. A. Patankar, G. V. Lauder, and M. A. MacIver, “Mechanical properties of a bio-inspired robotic knifefish with an undulatory propulsor,” *Bioinspir. Biomim.*, vol. 6, no. 2, p. 026004, Jun. 2011, doi: 10.1088/1748-3182/6/2/026004.
- [17] S. Du, Z. Wu, J. Wang, S. Qi, and J. Yu, “Design and control of a two-motor-actuated tuna-inspired robot system,” *IEEE Trans. Syst. Man Cybern, Syst.*, pp. 1–11, 2019, doi: 10.1109/TSMC.2019.2944786.
- [18] A. Erturk, “Chapter 9: Macro-fiber composite actuated piezoelectric robotic fish,” in *Robot Fish*, R. Du, Z. Li, K. Youcef-Toumi, and P. Valdivia y Alvarado, Eds., in Springer Tracts in Mechanical Engineering. Springer, Berlin, Heidelberg, 2015, pp. 255–283. doi: 10.1007/978-3-662-46870-8_9.
- [19] S. Farideddin Masoomi, S. Gutschmidt, X. Chen, and M. Sellier, “The kinematics and dynamics of undulatory motion of a tuna-mimetic robot,” *Int J Adv Robot Syst*, vol. 12, no. 83, pp. 1–11, 2014, doi: 10.5772/60059.
- [20] F. E. Fish, H. Dong, J. Zhu, and H. Bart-Smith, “Kinematics and hydrodynamics of mouliform swimming: oscillatory winged propulsion by large pelagic batoids,” *Marine Technology Society Journal*, vol. 51, no. 5, pp. 35–47, 2017.
- [21] S. Fujiwara and S. Yamaguchi, “Development of fishlike robot that imitates carangiform and subcarangiform swimming motions,” *J. Aero Aqua Bio-Mechanisms*, vol. 6, no. 1, pp. 1–8, Mar. 2017, doi: 10.5226/jabmech.6.1.

- [22] F. Gibouin, C. Raufaste, Y. Bouret, and M. Argentina, “Study of the thrust–drag balance with a swimming robotic fish,” *Physics of Fluids*, vol. 30, no. 9, p. 091901, Sep. 2018, doi: 10.1063/1.5043137.
- [23] K. Hirata, T. Takimoto, and K. Tamura, “Study of turning performance of a fish robot,” *Proc. 1st Int. Symp. Aqua Bio-Mechanisms*, pp. 287–292, 2000.
- [24] A. Jusufi, D. M. Vogt, R. J. Wood, and G. V. Lauder, “Undulatory swimming performance and body stiffness modulation in a soft robotic fish-inspired physical model,” *Soft Robotics*, vol. 4, no. 3, pp. 202–210, 2017, doi: 10.1089/soro.2016.0053.
- [25] R. K. Katzschmann, J. DelPreto, R. MacCurdy, and D. Rus, “Exploration of underwater life with an acoustically controlled soft robotic fish,” *Science Robotics*, vol. 3, no. 16, p. eaar3449, Mar. 2018, doi: 10.1126/scirobotics.aar3449.
- [26] J. M. Kumph, “Maneuvering of a robotic pike,” Master of Science Thesis, Massachusetts Institute of Technology, Cambridge, MA, USA, 2000.
- [27] B. Kwak and J. Bae, “Toward fast and efficient mobility in aquatic environment: a robot with compliant swimming appendages inspired by a water beetle,” *J. Bionic. Eng.*, vol. 14, no. 2, pp. 260–271, Jun. 2017, doi: 10.1016/S1672-6529(16)60396-7.
- [28] M. C. Leftwich and A. J. Smits, “Thrust production by a mechanical swimming lamprey,” *Exp Fluids*, vol. 50, no. 5, pp. 1349–1355, May 2011, doi: 10.1007/s00348-010-0994-x.
- [29] M. C. Leftwich, E. D. Tytell, A. H. Cohen, and A. J. Smits, “Wake structures behind a swimming robotic lamprey with a passively flexible tail,” *Journal of Experimental Biology*, vol. 215, no. 3, pp. 416–425, Feb. 2012, doi: 10.1242/jeb.061440.
- [30] Z. Li, Y. Zhong, and R. Du, “A novel underactuated wire-driven robot fish with vector propulsion,” in *2013 IEEE/RSJ International Conference on Intelligent Robots and Systems (IROS)*, Tokyo, Japan: IEEE, Nov. 2013, pp. 941–946. doi: 10.1109/IROS.2013.6696463.
- [31] T. Li *et al.*, “Fast-moving soft electronic fish,” *Sci. Adv.*, vol. 3, p. e1602045, 2017.
- [32] L. Li *et al.*, “Bottom-level motion control for robotic fish to swim in groups: modeling and experiments,” *Bioinspir. Biomim.*, vol. 14, no. 4, p. 046001, May 2019, doi: 10.1088/1748-3190/ab1052.
- [33] G. Li *et al.*, “Self-powered soft robot in the Mariana Trench,” *Nature*, vol. 591, pp. 66–71, 2021, doi: 10.1038/s41586-020-03153-z.
- [34] B. Liao, Z. Li, and R. Du, “Robot fish with a novel biomimetic wire-driven flapping propulsor,” *Advanced Robotics*, vol. 28, no. 5, pp. 339–349, Mar. 2014, doi: 10.1080/01691864.2013.867288.

- [35] H. Liu and O. Curet, “Swimming performance of a bio-inspired robotic vessel with undulating fin propulsion,” *Bioinspir. Biomim.*, vol. 13, p. 056006, 2018, doi: 10.1088/1748-3190/aacd26.
- [36] J. H. Long *et al.*, “Biomimetic evolutionary analysis: testing the adaptive value of vertebrate tail stiffness in autonomous swimming robots,” *Journal of Experimental Biology*, vol. 209, no. 23, pp. 4732–4746, Dec. 2006, doi: 10.1242/jeb.02559.
- [37] J. H. Long Jr., J. Schumacher, N. Livingston, and M. Kemp, “Four flippers or two? Tetrapodal swimming with an aquatic robot,” *Bioinspir. Biomim.*, vol. 1, no. 1, pp. 20–29, Mar. 2006, doi: 10.1088/1748-3182/1/1/003.
- [38] A. Mazumdar, P. V. Y. Alvarado, and K. Youcef-Toumi, “Maneuverability of a robotic tuna with compliant body,” in *2008 IEEE International Conference on Robotics and Automation*, Pasadena, CA, USA: IEEE, 2008, pp. 683–688. doi: 10.1109/ROBOT.2008.4543284.
- [39] S. McGovern, G. Alici, V.-T. Truong, and G. Spinks, “Finding NEMO (novel electromaterial muscle oscillator): a polypyrrole powered robotic fish with real-time wireless speed and directional control,” *Smart Mater. Struct.*, vol. 18, no. 9, p. 095009, 2009, doi: 10.1088/0964-1726/18/9/095009.
- [40] D. Mohammadshahi, A. Yousefi-Koma, S. Bahmanyar, and H. Maleki, “Design, fabrication and hydrodynamic analysis of a biomimetic robot fish,” presented at the 10th WSEAS Int. Conf. on Automatic Control, Modelling & Simulation (ACMOS), Istanbul, Turkey, May 2008, pp. 249–254.
- [41] L. Neely, J. Gaiennie, N. Noble, and J. C. Erickson, “Stingray-inspired robot with simply actuated intermediate motion,” in *Proceedings Volume 9797, Bioinspiration, Biomimetics, and Bioreplication 2016*, R. J. Martín-Palma, A. Lakhtakia, and M. Knez, Eds., Las Vegas, NV, USA, 2016. doi: 10.1117/12.2219494.
- [42] D. Q. Nguyen and V. A. Ho, “Anguilliform swimming performance of an eel-inspired soft robot,” *Soft Robotics*, vol. 9, no. 3, pp. 425–439, Jun. 2022, doi: 10.1089/soro.2020.0093.
- [43] T. Paschal, J. Shintake, S. Mintchev, and D. Floreano, “Development of bio-inspired underwater robot with adaptive morphology capable of multiple swimming modes,” in *2017 IEEE/RSJ International Conference on Intelligent Robots and Systems (IROS)*, Vancouver, Canada: IEEE, Sep. 2017, pp. 4197–4202. doi: 10.1109/IROS.2017.8206281.
- [44] V. A. Pham, T. T. Nguyen, B. R. Lee, and T. Q. Vo, “Dynamic analysis of a robotic fish propelled by flexible folding pectoral fins,” *Robotica*, pp. 1–20, Jul. 2019, doi: 10.1017/S0263574719000997.
- [45] M. A. Robertson, F. Efremov, and J. Paik, “RoboScallop: a bivalve inspired swimming robot,” *IEEE Robot. Autom. Lett.*, vol. 4, no. 2, pp. 2078–2085, Apr. 2019, doi: 10.1109/LRA.2019.2897144.

- [46] M. Saadat, F. Berlinger, A. Sheshmani, R. Nagpal, G. V. Lauder, and H. Haj-Hariri, “Hydrodynamic advantages of in-line schooling,” *Bioinspir. Biomim.*, vol. 16, p. 046002, 2021, doi: 10.1088/1748-3190/abe137.
- [47] M. Sfakiotakis, A. Kazakidi, and D. P. Tsakiris, “Octopus-inspired multi-arm robotic swimming,” *Bioinspir. Biomim.*, vol. 10, no. 035005, pp. 1–22, 2015, doi: 10.1088/1748-3190/10/3/035005.
- [48] W. Shao and C. Xu, “Pitch motion control of a soft bionic robot fish based on centroid adjustment,” in *2019 IEEE International Conference on Mechatronics and Automation (ICMA)*, Tianjin, China: IEEE, Aug. 2019, pp. 1883–1888. doi: 10.1109/ICMA.2019.8816287.
- [49] J. Shintake, V. Cacucciolo, H. Shea, and D. Floreano, “Soft biomimetic fish robot made of dielectric elastomer actuators,” *Soft Robotics*, vol. 5, no. 4, pp. 466–474, Aug. 2018, doi: 10.1089/soro.2017.0062.
- [50] J. Shintake, D. Zappetti, T. Peter, Y. Ikemoto, and D. Floreano, “Bio-inspired tensegrity fish robot,” in *IEEE International Conference on Robotics and Automation (ICRA)*, Paris, France: IEEE, 2020, pp. 2887–2892. doi: 10.1109/ICRA40945.2020.9196675.
- [51] X. Tan *et al.*, “An autonomous robotic fish for mobile sensing,” in *2006 IEEE/RSJ International Conference on Intelligent Robots and Systems*, Beijing, China, Oct. 2006, pp. 5424–5429. doi: 10.1109/IROS.2006.282110.
- [52] P. Valdivia y Alvarado and K. Youcef-Toumi, “Chapter 6: Soft-body robot fish,” in *Robot Fish. Bio-inspired Fishlike Underwater Robots.*, R. Du, Z. Li, K. Youcef-Toumi, and P. Valdivia y Alvarado, Eds., in Springer Tracts in Mechanical Engineering. Springer, Berlin, Heidelberg, 2015, pp. 161–191. doi: 10.1007/978-3-662-46870-8_6.
- [53] S. C. van den Berg, “Design of a high speed soft robotic fish,” Master of Science Thesis, Delft University of Technology, Delft, Netherlands, 2019.
- [54] A. Villanueva, C. Smith, and S. Priya, “A biomimetic robotic jellyfish (Robojelly) actuated by shape memory alloy composite actuators,” *Bioinspir. Biomim.*, vol. 6, no. 036004, pp. 1–16, 2011, doi: 10.1088/1748-3182/6/3/036004.
- [55] A. A. Villanueva, K. J. Marut, T. Michael, and S. Priya, “Biomimetic autonomous robot inspired by the *Cyanea capillata* (Cyro),” *Bioinspir. Biomim.*, vol. 8, no. 046005, pp. 1–18, 2013, doi: 10.1088/1748-3182/8/4/046005.
- [56] T. Wang, L. Wen, J. Liang, and G. Wu, “Fuzzy vorticity control of a biomimetic robotic fish using a flapping lunata tail,” *J. Bionic. Eng.*, vol. 7, pp. 56–65, Mar. 2010, doi: 10.1016/S1672-6529(09)60183-9.
- [57] S. Wang, B. Huang, D. McCoul, M. Li, L. Mu, and J. Zhao, “A soft breaststroke-inspired swimming robot actuated by dielectric elastomers,” *Smart Mater. Struct.*, vol. 28, no. 4, p. 045006, 2019a, doi: 10.1088/1361-665X/ab0a7a.

- [58] W. Wang, D. Gu, and G. Xie, “Autonomous optimization of swimming gait in a fish robot with multiple onboard sensors,” *IEEE Trans. Syst. Man Cybern, Syst.*, vol. 49, no. 5, pp. 891–903, 2019b, doi: 10.1109/TSMC.2017.2683524.
- [59] T. Wang, Z. Ren, W. Hu, M. Li, and M. Sitti, “Effect of body stiffness distribution on larval fish-like efficient undulatory swimming,” *Sci. Adv.*, vol. 7, no. 19, p. eabf7364, 2021, doi: 10.1126/sciadv.abf7364.
- [60] L. Wen *et al.*, “Understanding fish linear acceleration using an undulatory biorobotic model with soft fluidic elastomer actuated morphing median fins,” *Soft Robotics*, vol. 5, no. 4, pp. 375–388, Aug. 2018, doi: 10.1089/soro.2017.0085.
- [61] Z. Wu, J. Yu, Z. Su, M. Tan, and Z. Li, “Towards an *Esox lucius* inspired multimodal robotic fish,” *Sci. China Inf. Sci.*, vol. 58, pp. 1–13, May 2015, doi: 10.1007/s11432-014-5202-9.
- [62] F. Xie, Z. Li, Y. Ding, Y. Zhong, and R. Du, “An experimental study on the fish body flapping patterns by using a biomimetic robot fish,” *IEEE Robot. Autom. Lett.*, vol. 5, no. 1, pp. 64–71, Jan. 2020, doi: 10.1109/LRA.2019.2941827.
- [63] Z. Yang, D. Chen, D. J. Levine, and C. Sung, “Origami-inspired robot that swims via jet propulsion,” *IEEE Robotics and Automation Letters*, vol. 6, no. 4, pp. 7145–7152, Oct. 2021, doi: 10.1109/LRA.2021.3097757.
- [64] J. Yu and M. Tan, “Chapter 4: Design and control of a multi-joint robotic fish,” in *Robot Fish*, R. Du, Z. Li, K. Youcef-Toumi, and P. Valdivia y Alvarado, Eds., in Springer Tracts in Mechanical Engineering. Springer, Berlin, Heidelberg, 2015, pp. 93–117. doi: 10.1007/978-3-662-46870-8_4.
- [65] J. Yu, Z. Su, Z. Wu, and M. Tan, “Development of a fast-swimming dolphin robot capable of leaping,” *IEEE/ASME Trans. Mechatron.*, vol. 21, no. 5, pp. 2307–2316, 2016a, doi: 10.1109/TMECH.2016.2572720.
- [66] J. Yu, C. Zhang, and L. Liu, “Design and control of a single-motor-actuated robotic fish capable of fast swimming and maneuverability,” *IEEE/ASME Trans. Mechatron.*, vol. 21, no. 3, pp. 1711–1719, 2016b, doi: 10.1109/TMECH.2016.2517931.
- [67] J. Yu, Z. Wu, Z. Su, T. Wang, and S. Qi, “Motion control strategies for a repetitive leaping robotic dolphin,” *IEEE/ASME Trans. Mechatron.*, vol. 24, no. 3, pp. 913–923, Jun. 2019, doi: 10.1109/TMECH.2019.2908082.
- [68] Y. Zhong, Z. Li, and R. Du, “The design and prototyping of a wire-driven robot fish with pectoral fins,” in *Proceedings of the IEEE*, Shenzhen, China: IEEE, Dec. 2013, pp. 1918–1923. doi: 10.1109/ROBIO.2013.6739749.
- [69] Y. Zhong, Z. Li, and R. Du, “A novel robot fish with wire-driven active body and compliant tail,” *IEEE/ASME Trans. Mechatron.*, vol. 22, no. 4, pp. 1633–1643, Aug. 2017, doi: 10.1109/TMECH.2017.2712820.

- [70] Y. Zhong, J. Song, H. Yu, and R. Du, “A study on kinematic pattern of fish undulatory locomotion using a robot fish,” *Journal of Mechanisms and Robotics*, vol. 10, p. 041013, 2018, doi: 10.1115/1.4040434.
- [71] N. Gravish and G. V. Lauder, “Robotics-inspired biology,” *J. Exp. Biol.*, vol. 221, no. 7, p. 138438, Apr. 2018, doi: 10.1242/jeb.138438.
- [72] G. V. Lauder, “Fish locomotion: recent advances and new directions,” *Ann. Rev. Mar. Sci.*, vol. 7, no. 1, pp. 521–545, Jan. 2015, doi: 10.1146/annurev-marine-010814-015614.
- [73] M. J. Lighthill, “Hydromechanics of aquatic animal propulsion,” *Annu. Rev. Fluid Mech.*, vol. 1, pp. 413–446, 1969.
- [74] U. K. Müller, B. L. E. van den Heuvel, E. J. Stamhuis, and J. J. Videler, “Fish foot prints: morphology and energetics of the wake behind a continuously swimming mullet (*Chelon labrosus* Risso),” *Journal of Experimental Biology*, vol. 200, pp. 2893–2906, 1997.
- [75] J. C. Nauen and G. V. Lauder, “Hydrodynamics of caudal fin locomotion by chub mackerel, *Scomber japonicus* (Scombridae),” *Journal of Experimental Biology*, vol. 205, pp. 1709–1724, 2002.
- [76] T. von Kármán and J. M. Burgers, “Theory of the wake,” in *General aerodynamic theory-Perfect fluids*, W. F. Durand, Ed., Berlin: Julius Springer, 1935, pp. 330–352. doi: 10.1007/978-3-642-91485-0.
- [77] R. Bainbridge, “The speed of swimming of fish as related to size and to the frequency and amplitude of the tail beat,” *Journal of Experimental Biology*, vol. 35, pp. 109–133, 1958.
- [78] J. R. Hunter and J. R. Zweifel, “Swimming speed, tail beat frequency, tail beat amplitude, and size in jack mackerel, *Trachurus symmetricus*, and other fishes,” *Fish. Bull.*, vol. 69, no. 2, pp. 253–266, 1971.
- [79] J. M. Blank, C. J. Farwell, J. M. Morrissette, R. J. Schallert, and B. A. Block, “Influence of swimming speed on metabolic rates of juvenile Pacific bluefin tuna and yellowfin tuna,” *Physiol. Biochem. Zool.*, vol. 80, pp. 167–177, 2007, doi: 10.1086/510637.
- [80] H. Dewar and J. B. Graham, “Studies of tropical tuna swimming performance in a large water tunnel: I. Energetics,” *Journal of Experimental Biology*, vol. 192, pp. 13–31, 1994a, doi: 10.1242/jeb.192.1.13.
- [81] C. Sepulveda and K. A. Dickson, “Maximum sustainable speeds and cost of swimming in juvenile kawakawa tuna (*Euthynnus affinis*) and chub mackerel (*Scomber japonicus*),” *Journal of Experimental Biology*, vol. 203, pp. 3089–3101, 2000, doi: 10.1242/jeb.203.20.3089.
- [82] D. K. Wainwright and G. V. Lauder, “Tunas as a high-performance fish platform for inspiring the next generation of autonomous underwater vehicles,” *Bioinspir. Biomim.*, vol. 15, p. 035007, 2020, doi: 10.1088/1748-3190/ab75f7.

- [83] L. Harding *et al.*, “Endothermy makes fishes faster but does not expand their thermal niche,” *Funct Ecol*, vol. 35, pp. 1951–1959, 2021, doi: 10.1111/1365-2435.13869.
- [84] F. Azarsina, “Designing a hydrodynamic shape and thrust mechanism for a batoid underwater robot,” *Mar. Technol. Soc. J.*, vol. 50, no. 5, pp. 45–58, 2016, doi: 10.4031/MTSJ.50.5.6.
- [85] R. M. Shelton, P. J. M. Thornycroft, and G. V. Lauder, “Undulatory locomotion of flexible foils as biomimetic models for understanding fish propulsion,” *J. Exp. Biol.*, vol. 217, no. 12, pp. 2110–2120, Jun. 2014, doi: 10.1242/jeb.098046.
- [86] K. W. Moored, P. A. Dewey, M. C. Leftwich, H. Bart-Smith, and A. J. Smits, “Bioinspired propulsion mechanisms based on manta ray locomotion,” *Mar. Tech. Soc. J.*, vol. 45, no. 4, pp. 110–118, 2011, doi: 10.4031/MTSJ.45.4.3.
- [87] J. A. Tuhtan, G. Toming, T. Ruuben, and M. Kruusmaa, “A method to improve instationary force error estimates for undulatory swimmers,” *Underwater Technology*, vol. 33, no. 3, pp. 141–151, 2016, doi: 10.3723/ut.33.141.
- [88] M. Sharifzadeh, Y. Jiang, A. S. Lafmejani, K. Nichols, and D. Aukes, “Maneuverable gait selection for a novel fish-inspired robot using a CMA-ES-assisted workflow,” *Bioinspir. Biomim.*, vol. 16, p. 056017, 2021, doi: 10.1088/1748-3190/ac165d.
- [89] S. P. Howe, A. R. Duff, and H. C. Astley, “Comparing the turn performance of different motor control schemes in multilink fish-inspired robots,” *Bioinspir. Biomim.*, vol. 16, p. 036010, 2021, doi: 10.1088/1748-3190/abe7cc.
- [90] J. Liu and H. Hu, “A 3D simulator for autonomous robotic fish,” *International Journal of Automation and Computing*, vol. 1, pp. 42–50, 2004.
- [91] M. Sfakiotakis, A. Kazakidi, A. Chatzidaki, T. Evdaimon, and D. P. Tsakiris, “Multi-arm robotic swimming with octopus-inspired compliant web,” in *2014 IEEE/RSJ International Conference on Intelligent Robots and Systems*, Chicago, IL, USA: IEEE, Sep. 2014, pp. 302–308. doi: 10.1109/IROS.2014.6942576.
- [92] P. Valdivia y Alvarado and K. Youcef-Toumi, “Modeling and design methodology of an efficient underwater propulsion system,” in *Proceedings of the IASTED International Conference on Robotics and Applications*, Salzburg, Austria, 2003, pp. 1–6.
- [93] G. Liu, Y. Ren, J. Zhu, H. Bart-Smith, and H. Dong, “Thrust producing mechanisms in ray-inspired underwater vehicle propulsion,” *Theoretical and Applied Mechanics Letters*, vol. 5, pp. 54–57, 2015, doi: 10.1016/j.taml.2014.12.004.
- [94] L. Li, J. Lv, W. Chen, W. Wang, X. Zhang, and G. Xie, “Application of Taguchi method in the optimization of swimming capability for robotic fish,” *Int J Adv Robot Syst*, vol. 13, no. 102, pp. 1–11, 2016, doi: 10.5772/64039.

- [95] W. Zhao, A. Ming, and M. Shimojo, “Development of high-performance soft robotic fish by numerical coupling analysis,” *Applied Bionics and Biomechanics*, vol. 2018, pp. 1–12, 2018, doi: 10.1155/2018/5697408.
- [96] Z. Lei, D. Yongchao, L. Kunlun, and Q. Linchuan, “A new type of biomimetic fish with oscillatory propulsion method,” *MATEC Web of Conferences*, vol. 139, no. 3, p. 00194, 2017, doi: 10.1051/mateconf/201713900194.
- [97] G. H. Kwon, J. Y. Park, J. Y. Kim, M. L. Frisk, D. J. Beebe, and S.-H. Lee, “Biomimetic soft multifunctional miniature aquabots,” *Small*, vol. 4, no. 12, pp. 2148–2153, 2008, doi: 10.1002/sml.200800315.
- [98] T. Fukuda, H. Hosokai, and I. Kikuchi, “Distributed type of actuators by shape memory alloy and its application to underwater mobile robotic mechanism,” in *IEEE International Conference on Robotics and Automation*, Cincinnati, OH, USA, 1990, pp. 1316–1321. doi: 10.1109/ROBOT.1990.126182.
- [99] J. C. Nawroth *et al.*, “A tissue-engineered jellyfish with biomimetic propulsion,” *Nat. Biotechnol.*, vol. 30, no. 8, pp. 792–797, 2012, doi: 10.1038/nbt.2269.
- [100] S.-J. Park *et al.*, “Phototactic guidance of a tissue-engineered soft-robotic ray,” *Science*, vol. 353, no. 6295, pp. 158–162, 2016, doi: 10.1126/science.aaf4292.
- [101] K. Y. Lee *et al.*, “An autonomously swimming biohybrid fish designed with human cardiac biophysics,” *Science*, vol. 375, no. 6581, pp. 639–647, 2022, doi: 10.1126/science.abh0474.
- [102] N. W. Xu and J. O. Dabiri, “Low-power microelectronics embedded in live jellyfish enhance propulsion,” *Sci. Adv.*, vol. 6, p. eaaz3194, 2020, doi: 10.1126/sciadv.aaz3194.
- [103] N. W. Xu, J. P. Townsend, J. H. Costello, S. P. Colin, B. J. Gemmell, and J. O. Dabiri, “Field testing of biohybrid robotic jellyfish to demonstrate enhanced swimming speeds,” *Biomimetics*, vol. 5, no. 4, p. 64, 2020, doi: 10.3390/biomimetics5040064.
- [104] R. J. Clapham and H. Hu, “iSplash-II: realizing fast carangiform swimming to outperform a real fish,” in *2014 IEEE/RSJ International Conference on Intelligent Robots and Systems*, Chicago, IL, USA: IEEE, 2014, pp. 1080–1086. doi: 10.1109/IROS.2014.6942692.
- [105] A. B. Phillips *et al.*, “Nature in engineering for monitoring the oceans: comparison of the energetic costs of marine animals and AUVs,” in *Further Advances in Unmanned Marine Vehicles*, G. N. Roberts and R. Sutton, Eds., in IET Control Engineering Series, no. 77. Institution of Engineering and Technology, 2012, pp. 373–405. doi: 10.1049/PBCE077E_ch17.
- [106] C. H. White, G. V. Lauder, and H. Bart-Smith, “Tunabot Flex: a tuna-inspired robot with body flexibility improves high-performance swimming,” *Bioinspir. Biomim.*, vol. 16, no. 2, p. 026019, Sep. 2020, doi: 10.1088/1748-3190/abb86d.

- [107] R. W. Blake, L. M. Chatters, and P. Domenici, “Turning radius of yellowfin tuna (*Thunnus albacares*) in unsteady swimming manoeuvres,” *J. Fish Biology*, vol. 46, pp. 536–538, 1995, doi: 10.1111/j.1095-8649.1995.tb05994.x.
- [108] G. V. Lauder and J. L. Tangorra, “Fish Locomotion: Biology and Robotics of Body and Fin-Based Movements,” in *Robot Fish. Bio-inspired Fishlike Underwater Robots*, R. Du, Z. Li, K. Youcef-Toumi, and P. Valdivia y Alvarado, Eds., in Springer Tracts in Mechanical Engineering. Berlin: Springer Verlag, 2015, pp. 25–49. doi: 10.1007/978-3-662-46870-8_2.
- [109] G. V. Lauder, B. E. Flammang, and S. Alben, “Passive robotic models of propulsion by the bodies and caudal fins of fish,” *Integr. Comp. Biol.*, vol. 52, no. 5, pp. 576–587, Nov. 2012, doi: 10.1093/icb/ics096.
- [110] U. K. Müller, E. J. Stamhuis, and J. J. Videler, “Riding the waves: the role of the body wave in undulatory swimming,” *Integr. Comp. Biol.*, vol. 42, no. 5, pp. 981–987, Nov. 2002, doi: 10.1093/icb/42.5.981.
- [111] J. J. Videler, *Fish Swimming*, vol. 10. in Chapman & Hall Fish and Fisheries, vol. 10. London: Springer, 1993. doi: 10.1007/978-94-011-1580-3.
- [112] C. S. Wardle, J. J. Videler, and J. D. Altringham, “Tuning in to fish swimming waves: body form, swimming mode and muscle function,” *Journal of Experimental Biology*, vol. 198, pp. 1629–1636, 1995.
- [113] J. Gray, “Studies in animal locomotion. I. The movement of fish with special reference to the eel,” *J. Exp. Biol.*, vol. 10, pp. 88–104, 1933, doi: 10.1242/jeb.10.1.88.
- [114] G. V. Lauder and E. D. Tytell, “Three Gray classics on the biomechanics of animal movement,” *J. Exp. Biol.*, vol. 207, no. 10, pp. 1597–1599, 2004, doi: 10.1242/jeb.00921.
- [115] G. I. Taylor, “Analysis of the swimming of long and narrow animals,” *Proc. R. Soc. Lond. A*, vol. 214, no. 1117, pp. 158–183, 1952, doi: 10.1098/rspa.1952.0159.
- [116] D. Paniccia, G. Graziani, C. Lugni, and R. Piva, “On the role of added mass and vorticity release for self-propelled aquatic locomotion,” *J. Fluid Mech.*, vol. 918, p. A45, 2021, doi: 10.1017/jfm.2021.375.
- [117] M. J. Lighthill, “Note on the swimming of slender fish,” *J. Fluid Mech.*, vol. 9, pp. 305–317, 1960, doi: 10.1017/S0022112060001110.
- [118] M. J. Lighthill, “Hydromechanics of aquatic animal propulsion,” *Annu. Rev. Fluid Mech.*, vol. 1, no. 1, pp. 413–446, 1969, doi: 10.1146/annurev.fl.01.010169.002213.
- [119] M. J. Lighthill, “Aquatic animal propulsion of high hydromechanical efficiency,” *J. Fluid Mech.*, vol. 44, no. 2, pp. 265–301, 1970, doi: doi:10.1017/s0022112070001830.
- [120] M. J. Lighthill, “Large-amplitude elongated-body theory of fish locomotion,” *Proc. R. Soc. Lond. B.*, vol. 179, pp. 125–138, 1971, doi: 10.1098/rspb.1971.0085.

- [121] T. Y.-T. Wu, “Swimming of a waving plate,” *J. Fluid Mech.*, vol. 10, no. 3, pp. 321–344, 1961, doi: 10.1017/s0022112061000949.
- [122] K. H. Low and C. W. Chong, “Parametric study of the swimming performance of a fish robot propelled by a flexible caudal fin,” *Bioinspir. Biomim.*, vol. 5, p. 046002, 2010, doi: 10.1088/1748-3182/5/4/046002.
- [123] Y. Zhong, J. Song, H. Yu, and R. Du, “Toward a transform method from Lighthill fish swimming model to biomimetic robot fish,” *IEEE Robot. Autom. Lett.*, vol. 3, no. 3, pp. 2632–2639, 2018, doi: 10.1109/LRA.2018.2822310.
- [124] X. An, D. Floryan, and C. W. Rowley, “Optimal gaits of fish-like swimming,” in *AIAA Scitech 2021 Forum*, Virtual Event: American Institute of Aeronautics and Astronautics, 2021. doi: 10.2514/6.2021-1083.
- [125] T. Van Buren, D. Floryan, D. Quinn, and A. J. Smits, “Nonsinusoidal gaits for unsteady propulsion,” *Phys. Rev. Fluids*, vol. 2, no. 5, p. 053101, 2017, doi: 10.1103/PhysRevFluids.2.053101.
- [126] M. W. Westneat and S. A. Wainwright, “Mechanical design for swimming: muscle, tendon, and bone,” in *Tuna: Physiology, Ecology, and Evolution*, B. Block and E. Stevens, Eds., in *Fish Physiology*, vol. 19. San Diego: Academic Press, 2001, pp. 271–311. doi: 10.1016/S1546-5098(01)19008-4.
- [127] J. B. Graham, F. J. Koehn, and K. A. Dickson, “Distribution and relative proportions of red muscle in scombrid fishes: consequences of body size and relationships to locomotion and endothermy,” *Can. J. Zool.*, vol. 61, pp. 2087–2096, 1983, doi: 10.1139/z83-274.
- [128] H. Dewar and J. B. Graham, “Studies of tropical tuna swimming performance in a large water tunnel: III. Kinematics,” *Journal of Experimental Biology*, vol. 192, pp. 45–59, 1994b.
- [129] R. E. Shadwick and S. Gemballa, “Structure, kinematics, and muscle dynamics in undulatory swimming,” R. E. Shadwick and G. V. Lauder, Eds., in *Fish Physiology*, vol. 23 *Fish Biomechanics*. San Diego: Academic Press, 2006, pp. 241–280. doi: 10.1016/S1546-5098(05)23007-8.
- [130] H. L. Fierstine and V. Walters, “Studies in locomotion and anatomy of scombroid fishes,” *Mem. So. Cal. Acad. Sci.*, vol. 6, pp. 1–31, 1968.
- [131] R. E. Shadwick and D. A. Syme, “Thunniform swimming: muscle dynamics and mechanical power production of aerobic fibres in yellowfin tuna (*Thunnus albacares*),” *J. Exp. Biol.*, vol. 211, no. 10, pp. 1603–1611, May 2008, doi: 10.1242/jeb.013250.
- [132] G. Lewis, “The influence of the peduncle on swimming performance in biological tuna and tuna-inspired artificial propulsors,” Master of Science Thesis, University of Virginia, Charlottesville, VA, USA, 2017.

- [133] Seafood Analysts, “Yellowfin tuna *Thunnus albacares* Trinidad and Tobago Pelagic Longline,” Blue Ocean Institute, School of Marine & Atmospheric Sciences at Stony Brook University, Long Island, NY, USA, Monterey Bay Aquarium Seafood Report, Apr. 2013.
- [134] J. J. Magnuson, “Locomotion by scombrid fishes: hydromechanics, morphology, and behavior,” W. S. Hoar and D. J. Randall, Eds., in *Fish Physiology*, vol. VII Locomotion. New York: Academic Press, 1978, pp. 239–313. doi: 10.1016/S1546-5098(08)60166-1.
- [135] T. Kemp, “Investigating Batoid-Inspired Propulsion: The Development, Testing, and Performance Analysis of a Tensegrity-Based Robotic Fin for Underwater Locomotion,” Ph.D. Dissertation, University of Virginia, Charlottesville, VA, USA, 2014. doi: 10.18130/V3CJ88.
- [136] Z. Chen, T. I. Um, and H. Bart-Smith, “Bio-inspired robotic manta ray powered by ionic polymer–metal composite artificial muscles,” *International Journal of Smart and Nano Materials*, vol. 3, no. 4, pp. 296–308, 2012, doi: 10.1080/19475411.2012.686458.
- [137] K. W. Moored, “The Design of a Novel Tensegrity-Based Synthetic Pectoral Fin for Bio-Inspired Propulsion,” Ph.D. Dissertation, University of Virginia, Charlottesville, VA, USA, 2010.
- [138] G. Perrotta, F. E. Fish, D. S. Adams, A. M. Leahy, A. M. Downs, and M. C. Leftwich, “Velocity field measurements of the California sea lion propulsive stroke using bubble PIV,” *Fluids*, vol. 7, no. 3, pp. 1–11, 2022, doi: 10.3390/fluids7010003.
- [139] F. E. Fish, P. Legac, T. M. Williams, and T. Wei, “Measurement of hydrodynamic force generation by swimming dolphins using bubble DPIV,” *J. Exp. Biol.*, vol. 217, pp. 252–260, 2014, doi: 10.1242/jeb.087924.
- [140] J. D. Anderson, “Applied aerodynamics: the flow over a circular cylinder—the real case,” in *Fundamentals of aerodynamics*, 5th ed. in McGraw-Hill Series in Aeronautical and Aerospace Engineering. 2011, pp. 292–300.
- [141] G. Xiong and G. V. Lauder, “Center of mass motion in swimming fish: effects of speed and locomotor mode during undulatory propulsion,” *Zool.*, vol. 117, no. 4, pp. 269–281, Aug. 2014, doi: 10.1016/j.zool.2014.03.002.
- [142] G. K. Taylor, R. L. Nudds, and A. L. R. Thomas, “Flying and swimming animals cruise at a Strouhal number tuned for high power efficiency,” *Nature*, vol. 425, no. 6959, pp. 707–711, Oct. 2003, doi: 10.1038/nature02000.
- [143] E. M. Standen and G. V. Lauder, “Dorsal and anal fin function in bluegill sunfish *Lepomis macrochirus*: three-dimensional kinematics during propulsion and maneuvering,” *Journal of Experimental Biology*, vol. 208, pp. 2753–2763, 2005, doi: 10.1242/jeb.01706.
- [144] S. P. Thompson, “A little more about curvature of curves,” in *Calculus made easy*, 2nd ed. Palgrave, London: Macmillan Company, 1914, pp. 249–265.

- [145] W. J. McCroskey, “The phenomenon of dynamic stall,” National Aeronautics and Space Administration, Ames Research Center, NASA, and AVRADCOM Research and Technology Laboratories, Moffett Field, CA, USA, Report No. NASA TM-81264, AD-A098191, 1981.
- [146] L. L. van Dommelen and S. F. Shen, “The spontaneous generation of the singularity in a separating laminar boundary layer,” *Journal of Computational Physics*, vol. 38, pp. 125–140, 1980, doi: 10.1016/0021-9991(80)90049-2.
- [147] N. D. Ham, “Aerodynamic loading on a two-dimensional airfoil during dynamic stall,” *AIAA Journal*, vol. 6, no. 10, pp. 1927–1934, 1968, doi: 10.2514/3.4902.
- [148] N. D. Ham and M. S. Garelick, “Dynamic stall considerations in helicopter rotors,” *J Am Helicopter Soc*, vol. 13, no. 2, pp. 49–55, Apr. 1968, doi: 10.4050/JAHS.13.49.
- [149] W. Johnson, “The effect of dynamic stall on the response and airloading of helicopter rotor blades,” *J Am Helicopter Soc*, vol. 14, no. 2, pp. 68–79, 1969, doi: 10.4050/JAHS.14.68.
- [150] L. Lourenco, A. Krothapalli, L. L. van Dommelen, and C. Shih, “Unsteady flow past a NACA 0012 airfoil pitching at constant rates,” Air Force Office of Scientific Research Division of Aerospace Sciences, Bolling Air Force Base, VA, USA, Report No. AD-A265159, 1993.
- [151] M. Raffel, J. Kompenhans, and P. Wernert, “Investigation of the unsteady flow velocity field above an airfoil pitching under deep dynamic stall conditions,” *Exp Fluids*, vol. 19, no. 2, pp. 103–111, Jun. 1995, doi: 10.1007/BF00193856.
- [152] G. Chang, H. R. Karbasian, S. Zhang, Y. Yan, B. Chen, and K. C. Kim, “The influence of kinematics of blades on the flow structure in deep dynamic stall,” *J. Mech. Sci. Technol.*, vol. 34, no. 7, pp. 2855–2868, 2020, doi: 10.1007/s12206-020-0618-1.
- [153] I. Tuncer, R. Walz, and M. Platzer, “A computational study on the dynamic stall of a flapping airfoil,” in *16th AIAA Applied Aerodynamics Conference*, Albuquerque, NM, USA: American Institute of Aeronautics and Astronautics, 1998, pp. 219–225. doi: 10.2514/6.1998-2519.
- [154] I. Borazjani and M. Daghooghi, “The fish tail motion forms an attached leading edge vortex,” *Proc. R. Soc. Lond. B*, vol. 280, Apr. 2013, doi: 10.1098/rspb.2012.2071.
- [155] M. H. Dickinson, “Unsteady mechanisms of force generation in aquatic and aerial locomotion,” *Amer. Zool.*, vol. 36, no. 6, pp. 537–554, Dec. 1996, doi: 10.1093/icb/36.6.537.
- [156] J. D. Anderson, “Applied aerodynamics: the flow over an airfoil—the real case,” in *Fundamentals of aerodynamics*, 5th ed. in McGraw-Hill Series in Aeronautical and Aerospace Engineering. 2011, pp. 387–398.

- [157] G. V. Foster and R. F. Griner, “Low-speed longitudinal characteristics of a circular-arc 52-degree sweptback wing of aspect ratio 2.84 with and without leading-edge and trailing-edge flaps at Reynolds numbers from 1.6E6 to 9.7E6,” Langley Aeronautical Laboratory, Langley Air Force Base, VA, USA, National Advisory Committee for Aeronautics Report No. NACA-RM-L50F16a, 1950.
- [158] J. E. Colgate and K. M. Lynch, “Mechanics and control of swimming: a review,” *IEEE J. Oceanic Eng.*, vol. 29, no. 3, pp. 660–673, Jul. 2004, doi: 10.1109/JOE.2004.833208.
- [159] T. Maxworthy, “Experiments on the Weis-Fogh mechanism of lift generation by insects in hovering flight. Part 1. Dynamics of the ‘fling,’” *J. Fluid Mech.*, vol. 93, pp. 47–63, 1979, doi: 10.1017/S0022112079001774.
- [160] J. M. Birch and M. H. Dickinson, “Spanwise flow and the attachment of the leading-edge vortex on insect wings,” *Nature*, vol. 412, pp. 729–733, Aug. 2001, doi: 10.1038/35089071.
- [161] S. P. Sane, “The aerodynamics of insect flight,” *J. Exp. Biol.*, vol. 206, pp. 4191–4208, 2003, doi: 10.1242/jeb.00663.
- [162] F. T. Muijres, L. C. Johansson, R. Barfield, M. Wolf, G. R. Spedding, and A. Hedenström, “Leading-edge vortex improves lift in slow-flying bats,” *Science*, vol. 319, no. 5867, pp. 1250–1253, 2008, doi: 10.1126/science.1153019.
- [163] D. D. Chin and D. Lentink, “Flapping wing aerodynamics: from insects to vertebrates,” *J. Exp. Biol.*, vol. 219, no. 7, pp. 920–932, Apr. 2016, doi: 10.1242/jeb.042317.
- [164] C. P. Ellington, C. van den Berg, A. P. Willmott, and A. L. R. Thomas, “Leading-edge vortices in insect flight,” *Nature*, vol. 384, pp. 626–630, Dec. 1996, doi: 10.1038/384626a0.
- [165] M. H. Dickinson, F.-O. Lehmann, and S. P. Sane, “Wing rotation and the aerodynamic basis of insect flight,” *Science*, vol. 284, pp. 1954–1960, Jun. 1999, doi: 10.1126/science.284.5422.1954.
- [166] J. D. Anderson, “Airfoil characteristics,” in *Fundamentals of aerodynamics*, 5th ed. in McGraw-Hill Series in Aeronautical and Aerospace Engineering. 2011, pp. 320–325.
- [167] G. V. Lauder and E. G. Drucker, “Forces, fishes, and fluids: hydrodynamic mechanisms of aquatic locomotion,” *News Physiol. Sci.*, vol. 17, no. 6, pp. 235–240, Dec. 2002, doi: 10.1152/nips.01398.2002.
- [168] H. Levy and S. G. Hooker, “On the vortex system in the wake of a cylinder in a fluid,” *Phil. Mag.*, vol. 7, no. 9, pp. 489–502, 1930, doi: 10.1080/14786443008565020.
- [169] E. G. Drucker, “Experimental hydrodynamics of fish locomotion: functional insights from wake visualization,” *Integr. Comp. Biol.*, vol. 42, no. 2, pp. 243–257, 2002, doi: 10.1093/icb/42.2.243.

- [170] R. Thandiackal, C. H. White, H. Bart-Smith, and G. V. Lauder, “Tuna robotics: hydrodynamics of rapid linear accelerations,” *Proc. R. Soc. Lond. B*, vol. 288, no. 1945, p. 20202726, Feb. 2021, doi: 10.1098/rspb.2020.2726.
- [171] R. M. Alexander, “The history of fish mechanics,” in *Fish biomechanics*, P. W. Webb and D. Weihs, Eds., New York: Praeger, 1983, pp. 1–35.
- [172] J. R. Brett, “The respiratory metabolism and swimming performance of young sockeye salmon,” *J. Fish. Res. Bd. Can.*, vol. 21, no. 5, pp. 1183–1226, 1964, doi: 10.1139/f64-103.
- [173] P. Blazka, M. Volf, and M. Cepala, “A new type of respirometer for the determination of metabolism of fish in an active state,” *Physiol. Bohemoslov.*, vol. 9, pp. 553–558, 1960.
- [174] J. J. Videler and C. S. Wardle, “Fish swimming stride by stride: speed limits and endurance,” *Rev Fish Biol Fisheries*, vol. 1, no. 1, pp. 23–40, Sep. 1991, doi: 10.1007/BF00042660.
- [175] G. V. Lauder, “Locomotion,” in *The Physiology of Fishes*, D. H. Evans and J. B. Claiborne, Eds., 3rd ed. Boca Raton, FL, USA: CRC Press, 2006, pp. 3–46.
- [176] A. Hughes, *Electric motors and drives: fundamentals, types, and applications*, 3rd ed. Burlington, MA: Newnes (an imprint of Elsevier Ltd.), 2006.
- [177] T. Bliss, T. Iwasaki, and H. Bart-Smith, “Central pattern generator control of a tensegrity swimmer,” *IEEE/ASME Trans. Mechatron.*, vol. 18, no. 2, pp. 586–597, 2013, doi: 10.1109/TMECH.2012.2210905.
- [178] G. V. Lauder, E. J. Anderson, J. Tangorra, and P. G. A. Madden, “Fish biorobotics: kinematics and hydrodynamics of self-propulsion,” *Journal of Experimental Biology*, vol. 210, pp. 2767–2780, 2007, doi: 10.1242/jeb.000265.
- [179] P. Webb, “Bainbridge sets the stage on scaling in fish swimming,” *Journal of Experimental Biology*, vol. 209, no. 10, pp. 1789–1790, 2006, doi: 10.1242/jeb.02232.
- [180] P. W. Webb, “Stability and Maneuverability,” in *Fish Physiology*, Elsevier Ltd., 2005, pp. 281–332. doi: 10.1016/S1546-5098(05)23008-X.
- [181] J. J. Magnuson, “Comparative study of adaptations for continuous swimming and hydrostatic equilibrium of scombrid and xiphoid fishes,” *U.S. Fish Wild. Serv., Fish. Bull.*, vol. 71, no. 2, pp. 337–356, 1973.
- [182] J. Zhu, C. H. White, D. K. Wainwright, V. Di Santo, G. V. Lauder, and H. Bart-Smith, “Tuna robotics: a high-frequency experimental platform exploring the performance space of swimming fishes,” *Sci. Robot.*, vol. 4, no. 34, p. eaax4615, Sep. 2019, doi: 10.1126/scirobotics.aax4615.

- [183] J. M. Donley and K. A. Dickson, “Swimming kinematics of juvenile kawakawa tuna (*Euthynnus affinis*) and chub mackerel (*Scomber japonicus*),” *J. Exp. Biol.*, vol. 203, pp. 3103–3116, 2000.
- [184] J. J. Videler and F. Hess, “Fast continuous swimming of two pelagic predators, saithe (*Pollachius virens*) and mackerel (*Scomber scombrus*): a kinematic analysis,” *J. Exp. Biol.*, vol. 109, pp. 209–228, 1984.
- [185] B. C. Jayne and G. V. Lauder, “Are muscle fibers within fish myotomes activated synchronously? Patterns of recruitment within deep myomeric musculature during swimming in largemouth bass,” *J. Exp. Biol.*, vol. 198, pp. 805–815, 1995.
- [186] E. G. Drucker and G. V. Lauder, “Locomotor forces on a swimming fish: three-dimensional vortex wake dynamics quantified using digital particle image velocimetry,” *J. Exp. Biol.*, vol. 202, pp. 2393–2412, 1999.
- [187] V. Di Santo, E. L. Blevins, and G. V. Lauder, “Batoid locomotion: effects of speed on pectoral fin deformation in the little skate, *Leucoraja erinacea*,” *J. Exp. Biol.*, vol. 220, no. 4, pp. 705–712, Feb. 2017, doi: 10.1242/jeb.148767.
- [188] R. Zhu, “Effects of non-uniform stiffness on propulsive performance of canonical and bio-inspired foils,” Ph.D. Dissertation, University of Virginia, Charlottesville, VA, USA, 2020.
- [189] P. W. Webb, “Hydrodynamics and energetics of fish propulsion,” *Bull. Fish. Res. Bd. Can.*, vol. 190, pp. 1–159, 1975.
- [190] T. V. Buren, D. Floryan, and A. J. Smits, “Bioinspired Underwater Propulsors,” in *Bioinspired Structures and Design*, W. Soboyejo and L. Daniel, Eds., 1st ed. Cambridge University Press, 2020, pp. 113–139. doi: 10.1017/9781139058995.006.
- [191] M. I. Northway and A. S. Mackenzie, “On the period of a rod vibrating in a liquid,” *Phys. Rev. (Series I)*, vol. 13, no. 3, pp. 145–164, 1901, doi: 10.1103/PhysRevSeriesI.13.145.
- [192] J. Pantaleone, “The increasing added mass of a bouncing ball,” *Eur. J. Phys.*, vol. 43, p. 035006, 2022, doi: 10.1088/1361-6404/ac5633.
- [193] C. E. Brennen, “A review of added mass and fluid inertial forces,” Naval Civil Engineering Laboratory, Port Hueneme, CA, USA, Report No. CR 82.010, 1982.
- [194] G. Su, H. Shen, N. Li, Y. Zhu, and Y. Su, “Numerical investigation of the hydrodynamics of stingray swimming under self-propulsion,” *Journal of Fluids and Structures*, vol. 106, p. 103383, 2021, doi: 10.1016/j.jfluidstructs.2021.103383.
- [195] G. Tokić and D. K. P. Yue, “Optimal shape and motion of undulatory swimming organisms,” *Proc. R. Soc. Lond. B*, vol. 279, pp. 3065–3074, 2012, doi: 10.1098/rspb.2012.0057.

- [196] E. Limacher, C. Morton, and D. Wood, “Generalized derivation of the added-mass and circulatory forces for viscous flows,” *Phys. Rev. Fluids*, vol. 3, no. 1, p. 014701, 2018, doi: 10.1103/PhysRevFluids.3.014701.
- [197] D. Floryan, T. Van Buren, and A. J. Smits, “Efficient cruising for swimming and flying animals is dictated by fluid drag,” *Proc. Natl. Acad. Sci.*, vol. 115, no. 32, pp. 8116–8118, Aug. 2018, doi: 10.1073/pnas.1805941115.
- [198] D. Paniccia, L. Padovani, G. Graziani, and R. Piva, “The performance of a flapping foil for a self-propelled fishlike body,” *Sci. Rep.*, vol. 11, no. 22297, pp. 1–7, Dec. 2021, doi: 10.1038/s41598-021-01730-4.
- [199] C. M. Breder, “The locomotion of fishes,” *Zoologica*, vol. 4, no. 5, pp. 159–297, 1926, doi: 10.5962/p.203769.
- [200] J. Gray, “Studies in animal locomotion. III. The propulsive mechanism of the whiting (*Gadus merlangus*),” *J. Exp. Biol.*, vol. 10, pp. 391–400, 1933, doi: 10.1242/jeb.10.4.391.
- [201] K. D. Jones, C. M. Dohring, and M. F. Platzer, “Experimental and computational investigation of the Knoller-Betz effect,” *AIAA Journal*, vol. 36, no. 7, pp. 1240–1246, 1998, doi: 10.2514/2.505.
- [202] C. Eloy, “Optimal Strouhal number for swimming animals,” *J. Fluids & Struct.*, vol. 30, pp. 205–218, 2012, doi: 10.1016/j.jfluidstructs.2012.02.008.
- [203] T. Y. Wu, “Fish swimming and bird/insect flight,” *Annu. Rev. Fluid Mech.*, vol. 43, pp. 25–58, 2010, doi: 10.1146/annurev-fluid-122109-160648.
- [204] D. Lentink, F. T. Muijres, F. J. Donker-Duyvis, and J. L. van Leeuwen, “Vortex-wake interactions of a flapping foil that models animal swimming and flight,” *J. Exp. Biol.*, vol. 211, no. 2, pp. 267–273, Jan. 2008, doi: 10.1242/jeb.006155.
- [205] D. Floryan, T. Van Buren, C. W. Rowley, and A. J. Smits, “Scaling the propulsive performance of heaving and pitching foils,” *J. Fluid Mech.*, vol. 822, pp. 386–397, 2017, doi: 10.1017/jfm.2017.302.
- [206] T. Van Buren, D. Floryan, and A. J. Smits, “Scaling and performance of simultaneously heaving and pitching foils,” *AIAA Journal*, vol. 57, no. 9, pp. 3666–3677, 2019, doi: 10.2514/1.J056635.
- [207] R. Knoller, “Die Gesetze des Luftwiderstandes,” *Flug und Motortechnik*, vol. 3, no. 21, pp. 1–7, 1909.
- [208] A. Betz, “Ein Beitrag zur Erklärung des Segelfluges,” *Zeitschrift für Flugtechnik und Motorluftschiffahrt*, vol. 3, pp. 269–272, 1912.
- [209] R. Katzmayr, “Effect of periodic changes of angle of attack on behavior of airfoils (translated from *Zeitschrift für Flugtechnik und Motorluftschiffahrt*, March 31, pp. 80–82,

- and April 13, 1922, pp. 95–101),” National Advisory Committee for Aeronautics Report No. NACA-TM-147, Oct. 1922.
- [210] D. B. Quinn, G. V. Lauder, and A. J. Smits, “Maximizing the efficiency of a flexible propulsor using experimental optimization,” *J. Fluid Mech.*, vol. 767, pp. 430–448, 2015, doi: 10.1017/jfm.2015.35.
- [211] M. Xu and M. Wei, “Using adjoint-based optimization to study kinematics and deformation of flapping wings,” *J. Fluid Mech.*, vol. 799, pp. 56–99, 2016, doi: 10.1017/jfm.2016.351.
- [212] T. Van Buren, D. Floryan, A. Smits, P. Han, A. T. Bode-Oke, and H. Dong, “Optimizing foil shape for efficient unsteady propulsion,” in *AIAA SciTech 2019 Forum*, San Diego, CA, USA: American Institute of Aeronautics and Astronautics, 2019. doi: 10.2514/6.2019-1379.
- [213] E. G. Drucker and G. V. Lauder, “A hydrodynamic analysis of fish swimming speed: wake structure and locomotor force in slow and fast labriform swimmers,” *J. Exp. Biol.*, vol. 203, pp. 2379–2393, 2000.
- [214] E. G. Drucker and G. V. Lauder, “Locomotor function of the dorsal fin in teleost fishes: experimental analysis of wake forces in sunfish,” *J. Exp. Biol.*, vol. 204, pp. 2943–2958, 2001.
- [215] J. R. Taylor, *An introduction to error analysis*, 2nd ed. Sausalito, CA: University Science Books, 1997.
- [216] R. Peck, C. Olsen, and J. Devore, *Introduction to statistics and data analysis*, 3rd ed. Belmont, CA, USA: Thomson Brooks/Cole, 2008.
- [217] P. W. Webb, “Hydrodynamics: nonscombroid fish,” W. S. Hoar and D. J. Randall, Eds., in *Fish Physiology*, vol. VII Locomotion. New York: Academic Press, 1978, pp. 189–237. doi: 10.1016/S1546-5098(08)60165-X.
- [218] H. S. H. Yuen, “Swimming speeds of yellowfin and skipjack tuna,” *Trans. Am. Fish. Soc.*, vol. 95, pp. 203–209, 1966, doi: 10.1577/1548-8659(1966)95[203:SSOYAS]2.0.CO;2.
- [219] B. C. Jayne and G. V. Lauder, “Speed effects on midline kinematics during steady undulatory swimming of largemouth bass, *Micropterus salmoides*,” *Journal of Experimental Biology*, vol. 198, pp. 585–602, 1995.
- [220] A. C. Gibb, K. A. Dickson, and G. V. Lauder, “Tail kinematics of the chub mackerel *Scomber japonicus*: testing the homocercal tail model of fish propulsion,” *J. Exp. Biol.*, vol. 202, pp. 2433–2447, 1999.
- [221] K. E. Korsmeyer, J. F. Steffensen, and J. Herskin, “Energetics of median and paired fin swimming, body and caudal fin swimming, and gait transition in parrotfish (*Scarus schlegeli*) and triggerfish (*Rhinecanthus aculeatus*),” *J. Exp. Biol.*, vol. 205, pp. 1253–1263, 2002.

- [222] C. A. Sepulveda, K. A. Dickson, and J. B. Graham, “Swimming performance studies on the eastern Pacific bonito *Sarda chiliensis*, a close relative of the tunas (family Scombridae) I. Energetics,” *J. Exp. Biol.*, vol. 206, no. 16, pp. 2739–2748, Aug. 2003, doi: 10.1242/jeb.00497.
- [223] V. Di Santo, C. P. Kenaley, and G. V. Lauder, “High postural costs and anaerobic metabolism during swimming support the hypothesis of a U-shaped metabolism–speed curve in fishes,” *Proc. Natl. Acad. Sci. U.S.A.*, vol. 114, no. 49, pp. 13048–13053, Dec. 2017, doi: 10.1073/pnas.1715141114.
- [224] P. W. Webb, “Swimming,” in *The Physiology of Fishes, Second Edition*, D. H. Evans, Ed., 2nd ed. Boca Raton, FL, USA: CRC Press, 1998, pp. 3–24.
- [225] G. V. Lauder and E. D. Tytell, “Hydrodynamics of undulatory propulsion,” in *Fish Biomechanics Volume 23 in Fish Physiology*, R. E. Shadwick and G. V. Lauder, Eds., in *Fish Physiology*, vol. 23. San Diego: Academic Press, 2006, pp. 425–468. doi: 10.1016/S1546-5098(05)23011-X.
- [226] M. Saadat, F. E. Fish, A. G. Domel, V. Di Santo, G. V. Lauder, and H. Haj-Hariri, “On the rules for aquatic locomotion,” *Phys. Rev. Fluids*, vol. 2, no. 8, p. 083102, Aug. 2017, doi: 10.1103/PhysRevFluids.2.083102.
- [227] G. S. Triantafyllou, M. S. Triantafyllou, and M. A. Grosenbaugh, “Optimal thrust development in oscillating foils with application to fish propulsion,” *J. Fluids Struct.*, vol. 7, pp. 205–224, 1993.
- [228] M. S. Triantafyllou and G. S. Triantafyllou, “An efficient swimming machine,” *Sci. Am.*, vol. 272, no. 3, pp. 64–70, Mar. 1995, doi: 10.1038/scientificamerican0395-64.
- [229] M. S. Triantafyllou, G. S. Triantafyllou, and D. K. P. Yue, “Hydrodynamics of fishlike swimming,” *Annu. Rev. Fluid Mech.*, vol. 32, pp. 33–53, Jan. 2000, doi: 10.1146/annurev.fluid.32.1.33.
- [230] J. Wang *et al.*, “Hydrodynamics and flow characterization of tuna-inspired propulsion in forward swimming,” in *Proceedings of the ASME-JSME-KSME 2019*, San Francisco, CA, USA: ASME, 2019, pp. AJKFluids2019-5472. doi: 10.1115/AJKFluids2019-5472.
- [231] D. N. Beal, F. S. Hover, M. S. Triantafyllou, J. C. Liao, and G. V. Lauder, “Passive propulsion in vortex wakes,” *J. Fluid Mech.*, vol. 549, pp. 385–402, 2006, doi: 10.1017/S0022112005007925.
- [232] R. Bainbridge, “Caudal fin and body movement in the propulsion of some fish,” *J. Exp. Biol.*, vol. 40, no. 1, pp. 23–56, 1963, doi: 10.1242/jeb.40.1.23.
- [233] B. E. Flammang and G. V. Lauder, “Caudal fin shape modulation and control during acceleration, braking and backing maneuvers in bluegill sunfish, *Lepomis macrochirus*,” *J. Exp. Biol.*, vol. 212, pp. 277–286, 2009, doi: 10.1242/jeb.021360.

- [234] G. Liu, Y. Ren, H. Dong, O. Akanyeti, J. C. Liao, and G. V. Lauder, “Computational analysis of vortex dynamics and performance enhancement due to body–fin and fin–fin interactions in fish-like locomotion,” *J. Fluid Mech.*, vol. 829, pp. 65–88, 2017, doi: 10.1017/jfm.2017.533.
- [235] E. D. Tytell, “Median fin function in bluegill sunfish *Lepomis macrochirus*: streamwise vortex structure during steady swimming,” *J. Exp. Biol.*, vol. 209, pp. 1516–1534, 2006, doi: 10.1242/jeb.02154.
- [236] J. Wang, D. K. Wainwright, R. E. Lindengren, G. V. Lauder, and H. Dong, “Tuna locomotion: a computational hydrodynamic analysis of finlet function,” *J. R. Soc. Interface*, vol. 17, p. 20190590, 2020, doi: 10.1098/rsif.2019.0590.
- [237] Q. Zhu and K. Shoele, “Propulsion performance of a skeleton-strengthened fin,” *J. Exp. Biol.*, vol. 211, pp. 2087–2100, 2008, doi: 10.1242/jeb.016279.
- [238] C. J. Esposito, J. L. Tangorra, B. E. Flammang, and G. V. Lauder, “A robotic fish caudal fin: effects of stiffness and motor program on locomotor performance,” *Journal of Experimental Biology*, vol. 215, no. 1, pp. 56–67, Jan. 2012, doi: 10.1242/jeb.062711.
- [239] G. B. Gillis, “Anguilliform locomotion in an elongate salamander (*Siren intermedia*): effects of speed on axial undulatory movements,” *J. Exp. Biol.*, vol. 200, pp. 767–784, 1997.
- [240] J. Yu, T. Wang, Z. Wu, and M. Tan, “Design of a miniature underwater angle-of-attack sensor and its application to a self-propelled robotic fish,” *IEEE J. Oceanic Eng.*, pp. 1–13, Oct. 2019, doi: 10.1109/JOE.2019.2940800.
- [241] J. Wang, P. Han, X. Deng, and H. Dong, “A versatile level set based immersed boundary reconstruction for bio-inspired flow applications,” in *AIAA Scitech 2020 Forum*, Orlando, FL, USA: American Institute of Aeronautics and Astronautics, 2020. doi: 10.2514/6.2020-2235.
- [242] Z. J. Wang, “Vortex shedding and frequency selection in flapping flight,” *J. Fluid Mech.*, vol. 410, pp. 323–341, 2000, doi: 10.1017/S0022112099008071.
- [243] J. Wang, G. V. Lauder, and H. Dong, “Effect of tunable stiffness on the hydrodynamic performance of a tuna tail informed flexible propulsor,” in *AIAA SCITECH 2022 Forum*, San Diego, CA, USA: American Institute of Aeronautics and Astronautics, 2022. doi: 10.2514/6.2022-0729.
- [244] K. N. Lucas, G. V. Lauder, and E. D. Tytell, “Airfoil-like mechanics generate thrust on the anterior body of swimming fishes,” *Proc. Natl. Acad. Sci. U.S.A.*, vol. 117, no. 19, pp. 10585–10592, 2020, doi: 10.1073/pnas.1919055117.
- [245] M. W. Westneat, W. Hoese, C. A. Pell, and S. A. Wainwright, “The horizontal septum: mechanisms of force transfer in locomotion of scombrid fishes (Scombridae, Perciformes),” *J. Morphol.*, vol. 217, pp. 183–204, 1993, doi: 10.1002/jmor.1052170207.

- [246] K. W. Moored, F. E. Fish, T. H. Kemp, and H. Bart-Smith, “Batoid fishes: inspiration for the next generation of underwater robots,” *Mar. Tech. Soc. J.*, vol. 45, no. 4, pp. 99–109, Jul. 2011, doi: 10.4031/MTSJ.45.4.10.
- [247] K. W. Moored, T. H. Kemp, N. E. Houle, and H. Bart-Smith, “Analytical predictions, optimization, and design of a tensegrity-based artificial pectoral fin,” *Int. J. Solids Struct.*, vol. 48, no. 22–23, pp. 3142–3159, 2011, doi: 10.1016/j.ijsolstr.2011.07.008.
- [248] J. H. Long and K. S. Nipper, “The importance of body stiffness in undulatory propulsion,” *Amer. Zool.*, vol. 36, no. 6, pp. 678–694, Dec. 1996, doi: 10.1093/icb/36.6.678.
- [249] J. H. Long Jr., “Muscles, elastic energy, and the dynamics of body stiffness in swimming eels,” *Amer. Zool.*, vol. 38, no. 4, pp. 771–792, Sep. 1998, doi: 10.1093/icb/38.4.771.
- [250] E. D. Tytell, C. Y. Hsu, T. L. Williams, A. H. Cohen, and L. J. Fauci, “Interactions between internal forces, body stiffness, and fluid environment in a neuromechanical model of lamprey swimming,” *Proc. Natl. Acad. Sci. U.S.A.*, vol. 107, no. 46, pp. 19832–19837, Nov. 2010, doi: 10.1073/pnas.1011564107.
- [251] E. D. Tytell *et al.*, “Body stiffness and damping depend sensitively on the timing of muscle activation in lampreys,” *Integr. Comp. Biol.*, vol. 58, no. 5, pp. 860–873, Jun. 2018, doi: 10.1093/icb/icy042.
- [252] T. Knowler, R. E. Shadwick, A. A. Biewener, K. E. Korsmeyer, and J. B. Graham, “Direct measurement of tail tendon forces in swimming tuna,” *Amer Zool*, vol. 3, p. 30A, 1993.
- [253] N. Nangia, R. Bale, N. Chen, Y. Hanna, and N. A. Patankar, “Optimal specific wavelength for maximum thrust production in undulatory propulsion,” *PLOS ONE*, vol. 12, no. 6, p. e0179727, Jun. 2017, doi: 10.1371/journal.pone.0179727.
- [254] R. W. Brill, “The effect of body size on the standard metabolic rate of skipjack tuna, *Katsuwonus pelamis*,” *Fish. Bull.*, vol. 77, no. 2, pp. 494–498, 1979.
- [255] D. L. McPhee and D. M. Janz, “Dietary selenomethionine exposure alters swimming performance, metabolic capacity and energy homeostasis in juvenile fathead minnow,” *Aquatic Toxicology*, vol. 155, pp. 91–100, 2014, doi: 10.1016/j.aquatox.2014.06.012.
- [256] K. Yanase, N. A. Herbert, and J. C. Montgomery, “Disrupted flow sensing impairs hydrodynamic performance and increases the metabolic cost of swimming in the yellowtail kingfish, *Seriola lalandi*,” *Journal of Experimental Biology*, vol. 215, pp. 3944–3954, 2012, doi: 10.1242/jeb.082107.
- [257] G. Claireaux, C. Couturier, and A. L. Groison, “Effect of temperature on maximum swimming speed and cost of transport in juvenile European sea bass (*Dicentrarchus labrax*),” *Journal of Experimental Biology*, vol. 209, pp. 3420–3428, 2006, doi: 10.1242/jeb.02346.

- [258] T. Norin and H. Malte, “Repeatability of standard metabolic rate, active metabolic rate and aerobic scope in young brown trout during a period of moderate food availability,” *J. Exp. Biol.*, vol. 214, pp. 1668–1675, 2011, doi: 10.1242/jeb.054205.
- [259] J. R. Brett and T. D. D. Groves, “Physiological energetics,” in *Fish Physiology, Vol. VII, Bioenergetics and growth*, W. S. Hoar, D. J. Randall, and J. R. Brett, Eds., in Bioenergetics and growth, vol. 7. London: Academic Press, 1979, pp. 279–352.
- [260] J. Ohlberger, G. Staaks, and F. Hölker, “Swimming efficiency and the influence of morphology on swimming costs in fishes,” *J. Comp. Physiol. B*, vol. 176, pp. 17–25, 2006, doi: 10.1007/s00360-005-0024-0.
- [261] R. Williams and D. P. Noren, “Swimming speed, respiration rate, and estimated cost of transport in adult killer whales,” *Marine Mammal Science*, vol. 25, no. 2, pp. 327–350, 2009, doi: 10.1111/j.1748-7692.2008.00255.x.
- [262] G. Cumming, F. Fidler, and D. L. Vaux, “Error bars in experimental biology,” *Journal of Cell Biology*, vol. 177, no. 1, pp. 7–11, Apr. 2007, doi: 10.1083/jcb.200611141.
- [263] D. S. Fay and K. Gerow, “A biologist’s guide to statistical thinking and analysis,” in *WormBook*, The *C. elegans* Research Community, 2013, pp. 1–54.
- [264] P. W. Webb and D. Weihs, “Hydrostatic stability of fish with swim bladders: not all fish are unstable,” *Can. J. Zool.*, vol. 72, pp. 1149–1154, 1994, doi: 10.1139/z94-153.
- [265] P. W. Webb, “Some aspects of the energetics of swimming of fish with special reference to the cruising performance of rainbow trout,” Ph.D. Dissertation, University of Bristol, Bristol, England, 1970.
- [266] T. Takagi, Y. Tamura, and D. Weihs, “Hydrodynamics and energy-saving swimming techniques of Pacific bluefin tuna,” *Journal of Theoretical Biology*, vol. 336, pp. 158–172, 2013, doi: 10.1016/j.jtbi.2013.07.018.
- [267] A. P. Maertens, M. S. Triantafyllou, and D. K. P. Yue, “Efficiency of fish propulsion,” *Bioinspir. Biomim.*, vol. 10, no. 046013, pp. 1–11, 2015, doi: 10.1088/1748-3190/10/4/046013.
- [268] F. E. Fish and G. V. Lauder, “Passive and active flow control by swimming fishes and mammals,” *Annu. Rev. Fluid Mech.*, vol. 38, pp. 193–224, 2006, doi: 10.1146/annurev.fluid.38.050304.092201.
- [269] R. W. Blake, *Fish Locomotion*. University of Cambridge, Cambridge, UK: Cambridge University Press, 1983.
- [270] H. Hertel, *Structure, form, and movement*. New York: Reinhold Publishing Corporation, 1966.

- [271] C. E. Brown and B. S. Muir, “Analysis of ram ventilation of fish gills with application to skipjack tuna (*Katsuwonus pelamis*),” *J. Fish. Res. Bd. Can.*, vol. 27, no. 9, pp. 1637–1652, 1970, doi: 10.1139/f70-184.
- [272] G. Liu, B. Geng, X. Zheng, Q. Xue, H. Dong, and G. V. Lauder, “An image-guided computational approach to inversely determine *in vivo* material properties and model flow-structure interactions of fish fins,” *Journal of Computational Physics*, vol. 392, pp. 578–593, 2019, doi: 10.1016/j.jcp.2019.04.062.
- [273] R. G. Kahn, D. E. Pearson, and E. J. Dick, “Comparison of standard length, fork length, and total length for measuring West Coast marine fishes,” *Marine Fisheries Review*, vol. 66, no. 1, pp. 31–33, 2004.
- [274] S. L. Katz and R. E. Shadwick, “Curvature of swimming fish midlines as an index of muscle strain suggests swimming muscle produces net positive work,” *J. Theor. Biol.*, vol. 193, no. 2, pp. 243–256, Jul. 1998, doi: 10.1006/jtbi.1998.0696.
- [275] P. W. Webb, P. T. Kostecki, and E. D. Stevens, “The effect of size and swimming speed on locomotor kinematics of rainbow trout,” *Journal of Experimental Biology*, vol. 109, pp. 77–95, 1984.
- [276] A. Matta, J. Bayandor, F. Battaglia, and H. Pendar, “Effects of fish caudal fin sweep angle and kinematics on thrust production during low-speed thunniform swimming,” *Biology Open*, vol. 8, no. bio040626, pp. 1–9, 2019, doi: 10.1242/bio.040626.
- [277] L. Wen, T. M. Wang, G. H. Wu, and J. H. Liang, “Hydrodynamic investigation of a self-propelled robotic fish based on a force-feedback control method,” *Bioinspir. Biomim.*, vol. 7, p. 036012, 2012, doi: 10.1088/1748-3182/7/3/036012.
- [278] Q. Zhong *et al.*, “Tunable stiffness enables fast and efficient swimming in fish-like robots,” *Sci. Robot.*, vol. 6, p. eabe4088, 2021, doi: 10.1126/scirobotics.abe4088.
- [279] D. Quinn and G. Lauder, “Tunable stiffness in fish robotics: mechanisms and advantages,” *Bioinspir. Biomim.*, vol. 17, p. 011002, 2022, doi: 10.1088/1748-3190/ac3ca5.
- [280] T. Knowler, R. E. Shadwick, S. L. Katz, J. B. Graham, and C. S. Wardle, “Red muscle activation patterns in yellowfin (*Thunnus albacares*) and skipjack (*Katsuwonus pelamis*) tunas during steady swimming,” *Journal of Experimental Biology*, vol. 202, pp. 2127–2138, 1999.
- [281] A. C. Gleiss, R. J. Schallert, J. J. Dale, S. G. Wilson, and B. A. Block, “Direct measurement of swimming and diving kinematics of giant Atlantic bluefin tuna (*Thunnus thynnus*),” *R. Soc. Open Sci.*, vol. 6, p. 190203, May 2019, doi: 10.1098/rsos.190203.
- [282] K. Takagi and S. Kimura, Eds., “Swimming performance of Pacific bluefin tuna,” in *Biology and ecology of bluefin tuna*, CRC Press, 2015, pp. 274–291.

- [283] J. J. Rohr and F. E. Fish, “Strouhal numbers and optimization of swimming by odontocete cetaceans,” *Journal of Experimental Biology*, vol. 207, pp. 1633–1642, 2004, doi: 10.1242/jeb.00948.
- [284] A. S. Blix and L. P. Folkow, “Daily energy expenditure in free living minke whales,” *Acta Physiol Scand*, vol. 153, no. 1, pp. 61–66, 1995, doi: 10.1111/j.1748-1716.1995.tb09834.x.
- [285] J. D. Anderson, “Prandtl’s classical lifting-line theory,” in *Fundamentals of aerodynamics*, 5th ed. in McGraw-Hill Series in Aeronautical and Aerospace Engineering. 2011, pp. 424–453.
- [286] J. Yu, T. Zhang, and J. Qian, “Testing methods for electric motors,” in *Electrical motor products: International energy-efficient standards and testing methods*, Woodhead Publishing, 2011, pp. 95–172. doi: 10.1533/9780857093813.95.
- [287] C. S. Wardle, J. J. Videler, T. Arimoto, J. M. Franco, and P. He, “The muscle twitch and the maximum swimming speed of giant bluefin tuna, *Thunnus thynnus* L.,” *J. Fish Biol.*, vol. 35, pp. 129–137, 1989, doi: 10.1111/j.1095-8649.1989.tb03399.x.
- [288] F. E. Fish, “Advantages of aquatic animals as models for bio-inspired drones over present AUV technology,” *Bioinspir. Biomim.*, vol. 15, no. 2, p. 025001, Feb. 2020, doi: 10.1088/1748-3190/ab5a34.
- [289] J. M. Anderson, K. Streitlien, D. S. Barrett, and M. S. Triantafyllou, “Oscillating foils of high propulsive efficiency,” *J. Fluid Mech.*, vol. 360, pp. 41–72, 1998, doi: 10.1017/S0022112097008392.
- [290] O. Akanyeti, P. J. M. Thornycroft, G. V. Lauder, Y. R. Yanagitsuru, A. N. Peterson, and J. C. Liao, “Fish optimize sensing and respiration during undulatory swimming,” *Nat Commun*, vol. 7, no. 11044, pp. 1–8, 2016, doi: 10.1038/ncomms11044.
- [291] S. E. A. W. Fetherstonhaugh, Q. Shen, and O. Akanyeti, “Automatic segmentation of fish midlines for optimizing robot design,” *Bioinspir. Biomim.*, vol. 16, p. 046005, 2021, doi: 10.1088/1748-3190/abf031.
- [292] O. Akanyeti *et al.*, “Fish-inspired segment models for undulatory steady swimming,” *Bioinspir. Biomim.*, vol. 17, p. 046007, 2022, doi: 10.1088/1748-3190/ac6bd6.
- [293] C. H. White, J. Zhu, and H. Bart-Smith, “Bio-inspired superficial self-rolled flow sensor: design, manufacturing, and testing,” *University of Virginia Library*, May 2016.
- [294] J. Zhu, H. Bart-Smith, and C. H. White, “Flexible, self-rolled superficial flow sensor,” Patent No. US10782164B2, Sep. 22, 2020

Appendix

Table A-1: Performance space of a diversity of fish species. Here we review the literature data of a diversity of fish species [77], [78], [219] in addition to data provided by Lauder Laboratory. Fishes occupy a wide performance space with 15 BL/s swimming speeds and tail-beat frequencies close to 20 Hz. To illustrate this high-performance range, we plot all 300 data points in Figure 1-1(A). We also compare our results with this data set in Figure 5-1. Entries are alphabetized by author then species.

Reference	Species	Speed (m/s)	Body Length, BL (m)	Speed (BL/s)	Tail-Beat Frequency (Hz)	Source
Bainbridge (1958)	<i>Carassius auratus</i>	0.13	0.23	0.57	1.64	Fig. 12
Bainbridge (1958)	<i>Carassius auratus</i>	0.17	0.23	0.76	2.17	Fig. 12
Bainbridge (1958)	<i>Carassius auratus</i>	0.24	0.23	1.04	2.22	Fig. 12
Bainbridge (1958)	<i>Carassius auratus</i>	0.26	0.23	1.17	2.27	Fig. 12
Bainbridge (1958)	<i>Carassius auratus</i>	0.23	0.23	1.01	2.44	Fig. 12
Bainbridge (1958)	<i>Carassius auratus</i>	0.33	0.23	1.48	2.61	Fig. 12
Bainbridge (1958)	<i>Carassius auratus</i>	0.27	0.23	1.19	2.76	Fig. 12
Bainbridge (1958)	<i>Carassius auratus</i>	0.29	0.23	1.30	2.83	Fig. 12
Bainbridge (1958)	<i>Carassius auratus</i>	0.35	0.23	1.57	3.03	Fig. 12
Bainbridge (1958)	<i>Carassius auratus</i>	0.37	0.23	1.65	3.05	Fig. 12
Bainbridge (1958)	<i>Carassius auratus</i>	0.55	0.23	2.43	3.41	Fig. 12
Bainbridge (1958)	<i>Carassius auratus</i>	0.63	0.23	2.80	3.68	Fig. 12
Bainbridge (1958)	<i>Carassius auratus</i>	0.60	0.23	2.68	3.73	Fig. 12
Bainbridge (1958)	<i>Carassius auratus</i>	0.67	0.23	2.97	3.80	Fig. 12
Bainbridge (1958)	<i>Carassius auratus</i>	0.69	0.23	3.08	3.82	Fig. 12
Bainbridge (1958)	<i>Carassius auratus</i>	0.58	0.23	2.57	3.90	Fig. 12
Bainbridge (1958)	<i>Carassius auratus</i>	0.71	0.23	3.14	4.63	Fig. 12
Bainbridge (1958)	<i>Carassius auratus</i>	0.72	0.23	3.18	4.68	Fig. 12
Bainbridge (1958)	<i>Carassius auratus</i>	0.76	0.23	3.39	4.70	Fig. 12
Bainbridge (1958)	<i>Carassius auratus</i>	0.76	0.23	3.39	5.22	Fig. 12
Bainbridge (1958)	<i>Carassius auratus</i>	0.80	0.23	3.57	5.31	Fig. 12
Bainbridge (1958)	<i>Leuciscus leuciscus</i>	0.22	0.24	0.90	2.10	Fig. 3
Bainbridge (1958)	<i>Leuciscus leuciscus</i>	0.25	0.24	1.05	2.57	Fig. 3
Bainbridge (1958)	<i>Leuciscus leuciscus</i>	0.40	0.24	1.65	3.04	Fig. 3
Bainbridge (1958)	<i>Leuciscus leuciscus</i>	0.43	0.24	1.78	3.35	Fig. 3
Bainbridge (1958)	<i>Leuciscus leuciscus</i>	0.58	0.24	2.43	3.55	Fig. 3
Bainbridge (1958)	<i>Leuciscus leuciscus</i>	0.47	0.24	1.96	3.58	Fig. 3
Bainbridge (1958)	<i>Leuciscus leuciscus</i>	0.51	0.24	2.12	3.70	Fig. 3
Bainbridge (1958)	<i>Leuciscus leuciscus</i>	0.61	0.24	2.53	4.13	Fig. 3
Bainbridge (1958)	<i>Leuciscus leuciscus</i>	0.66	0.24	2.74	4.25	Fig. 3
Bainbridge (1958)	<i>Leuciscus leuciscus</i>	0.58	0.24	2.40	4.56	Fig. 3
Bainbridge (1958)	<i>Leuciscus leuciscus</i>	0.77	0.24	3.22	4.56	Fig. 3
Bainbridge (1958)	<i>Leuciscus leuciscus</i>	0.69	0.24	2.88	4.60	Fig. 3
Bainbridge (1958)	<i>Leuciscus leuciscus</i>	0.75	0.24	3.12	4.71	Fig. 3
Bainbridge (1958)	<i>Leuciscus leuciscus</i>	0.78	0.24	3.27	4.79	Fig. 3
Bainbridge (1958)	<i>Leuciscus leuciscus</i>	0.80	0.24	3.31	4.79	Fig. 3
Bainbridge (1958)	<i>Leuciscus leuciscus</i>	0.76	0.24	3.15	5.03	Fig. 3
Bainbridge (1958)	<i>Leuciscus leuciscus</i>	0.94	0.24	3.90	5.26	Fig. 3
Bainbridge (1958)	<i>Leuciscus leuciscus</i>	0.86	0.24	3.59	5.45	Fig. 3

Bainbridge (1958)	<i>Leuciscus leuciscus</i>	0.91	0.24	3.79	5.49	Fig. 3
Bainbridge (1958)	<i>Leuciscus leuciscus</i>	0.91	0.24	3.77	5.81	Fig. 3
Bainbridge (1958)	<i>Leuciscus leuciscus</i>	0.95	0.24	3.97	6.00	Fig. 3
Bainbridge (1958)	<i>Leuciscus leuciscus</i>	1.09	0.24	4.54	6.58	Fig. 3
Bainbridge (1958)	<i>Leuciscus leuciscus</i>	1.10	0.24	4.58	6.58	Fig. 3
Bainbridge (1958)	<i>Leuciscus leuciscus</i>	1.01	0.24	4.21	6.74	Fig. 3
Bainbridge (1958)	<i>Leuciscus leuciscus</i>	0.82	0.24	3.40	6.90	Fig. 3
Bainbridge (1958)	<i>Leuciscus leuciscus</i>	1.06	0.24	4.42	6.94	Fig. 3
Bainbridge (1958)	<i>Leuciscus leuciscus</i>	1.11	0.24	4.63	6.97	Fig. 3
Bainbridge (1958)	<i>Leuciscus leuciscus</i>	1.15	0.24	4.79	6.97	Fig. 3
Bainbridge (1958)	<i>Leuciscus leuciscus</i>	1.32	0.24	5.50	6.97	Fig. 3
Bainbridge (1958)	<i>Leuciscus leuciscus</i>	1.03	0.24	4.29	7.17	Fig. 3
Bainbridge (1958)	<i>Leuciscus leuciscus</i>	1.49	0.24	6.21	7.36	Fig. 3
Bainbridge (1958)	<i>Leuciscus leuciscus</i>	1.04	0.24	4.33	7.44	Fig. 3
Bainbridge (1958)	<i>Leuciscus leuciscus</i>	1.26	0.24	5.25	8.53	Fig. 3
Bainbridge (1958)	<i>Leuciscus leuciscus</i>	1.46	0.24	6.08	8.73	Fig. 3
Bainbridge (1958)	<i>Leuciscus leuciscus</i>	1.69	0.24	7.04	8.88	Fig. 3
Bainbridge (1958)	<i>Leuciscus leuciscus</i>	1.54	0.24	6.42	8.96	Fig. 3
Bainbridge (1958)	<i>Leuciscus leuciscus</i>	1.65	0.24	6.88	10.60	Fig. 3
Bainbridge (1958)	<i>Leuciscus leuciscus</i>	1.88	0.24	7.83	10.80	Fig. 3
Bainbridge (1958)	<i>Leuciscus leuciscus</i>	1.76	0.24	7.33	12.20	Fig. 3
Bainbridge (1958)	<i>Leuciscus leuciscus</i>	2.19	0.24	9.13	12.40	Fig. 3
Bainbridge (1958)	<i>Leuciscus leuciscus</i>	2.21	0.24	9.21	12.80	Fig. 3
Bainbridge (1958)	<i>Leuciscus leuciscus</i>	0.17	0.09	1.86	1.79	Fig. 3
Bainbridge (1958)	<i>Leuciscus leuciscus</i>	0.12	0.09	1.33	2.45	Fig. 3
Bainbridge (1958)	<i>Leuciscus leuciscus</i>	0.13	0.09	1.42	2.92	Fig. 3
Bainbridge (1958)	<i>Leuciscus leuciscus</i>	0.14	0.09	1.51	3.00	Fig. 3
Bainbridge (1958)	<i>Leuciscus leuciscus</i>	0.10	0.09	1.16	3.11	Fig. 3
Bainbridge (1958)	<i>Leuciscus leuciscus</i>	0.15	0.09	1.63	3.54	Fig. 3
Bainbridge (1958)	<i>Leuciscus leuciscus</i>	0.26	0.09	2.93	5.02	Fig. 3
Bainbridge (1958)	<i>Leuciscus leuciscus</i>	0.28	0.09	3.07	5.72	Fig. 3
Bainbridge (1958)	<i>Leuciscus leuciscus</i>	0.33	0.09	3.71	5.92	Fig. 3
Bainbridge (1958)	<i>Leuciscus leuciscus</i>	0.26	0.09	2.84	6.42	Fig. 3
Bainbridge (1958)	<i>Leuciscus leuciscus</i>	0.38	0.09	4.23	7.40	Fig. 3
Bainbridge (1958)	<i>Leuciscus leuciscus</i>	0.33	0.09	3.67	7.59	Fig. 3
Bainbridge (1958)	<i>Leuciscus leuciscus</i>	0.39	0.09	4.31	7.67	Fig. 3
Bainbridge (1958)	<i>Leuciscus leuciscus</i>	0.42	0.09	4.66	8.41	Fig. 3
Bainbridge (1958)	<i>Leuciscus leuciscus</i>	0.44	0.09	4.92	8.41	Fig. 3
Bainbridge (1958)	<i>Leuciscus leuciscus</i>	0.52	0.09	5.74	8.57	Fig. 3
Bainbridge (1958)	<i>Leuciscus leuciscus</i>	0.45	0.09	5.04	8.72	Fig. 3
Bainbridge (1958)	<i>Leuciscus leuciscus</i>	0.49	0.09	5.48	8.72	Fig. 3
Bainbridge (1958)	<i>Leuciscus leuciscus</i>	0.51	0.09	5.66	8.72	Fig. 3
Bainbridge (1958)	<i>Leuciscus leuciscus</i>	0.50	0.09	5.52	8.88	Fig. 3
Bainbridge (1958)	<i>Leuciscus leuciscus</i>	0.57	0.09	6.30	9.31	Fig. 3
Bainbridge (1958)	<i>Leuciscus leuciscus</i>	0.59	0.09	6.57	10.00	Fig. 3
Bainbridge (1958)	<i>Leuciscus leuciscus</i>	0.56	0.09	6.17	10.10	Fig. 3
Bainbridge (1958)	<i>Leuciscus leuciscus</i>	0.67	0.09	7.43	10.70	Fig. 3
Bainbridge (1958)	<i>Leuciscus leuciscus</i>	0.68	0.09	7.56	10.70	Fig. 3
Bainbridge (1958)	<i>Leuciscus leuciscus</i>	0.62	0.09	6.90	11.20	Fig. 3
Bainbridge (1958)	<i>Leuciscus leuciscus</i>	0.65	0.09	7.21	11.60	Fig. 3
Bainbridge (1958)	<i>Leuciscus leuciscus</i>	0.74	0.09	8.17	11.60	Fig. 3
Bainbridge (1958)	<i>Leuciscus leuciscus</i>	0.66	0.09	7.29	11.80	Fig. 3
Bainbridge (1958)	<i>Leuciscus leuciscus</i>	0.76	0.09	8.47	12.00	Fig. 3
Bainbridge (1958)	<i>Leuciscus leuciscus</i>	0.75	0.09	8.38	12.30	Fig. 3
Bainbridge (1958)	<i>Leuciscus leuciscus</i>	0.77	0.09	8.56	12.30	Fig. 3
Bainbridge (1958)	<i>Leuciscus leuciscus</i>	0.83	0.09	9.20	12.50	Fig. 3

Bainbridge (1958)	<i>Leuciscus leuciscus</i>	0.69	0.09	7.63	12.60	Fig. 3
Bainbridge (1958)	<i>Leuciscus leuciscus</i>	0.87	0.09	9.63	12.60	Fig. 3
Bainbridge (1958)	<i>Leuciscus leuciscus</i>	0.75	0.09	8.29	12.70	Fig. 3
Bainbridge (1958)	<i>Leuciscus leuciscus</i>	0.78	0.09	8.68	12.70	Fig. 3
Bainbridge (1958)	<i>Leuciscus leuciscus</i>	0.79	0.09	8.72	13.00	Fig. 3
Bainbridge (1958)	<i>Leuciscus leuciscus</i>	0.83	0.09	9.20	13.00	Fig. 3
Bainbridge (1958)	<i>Leuciscus leuciscus</i>	0.76	0.09	8.42	13.10	Fig. 3
Bainbridge (1958)	<i>Leuciscus leuciscus</i>	0.80	0.09	8.90	13.30	Fig. 3
Bainbridge (1958)	<i>Leuciscus leuciscus</i>	0.75	0.09	8.29	13.50	Fig. 3
Bainbridge (1958)	<i>Leuciscus leuciscus</i>	0.80	0.09	8.93	13.50	Fig. 3
Bainbridge (1958)	<i>Leuciscus leuciscus</i>	0.86	0.09	9.54	13.70	Fig. 3
Bainbridge (1958)	<i>Leuciscus leuciscus</i>	0.92	0.09	10.23	13.70	Fig. 3
Bainbridge (1958)	<i>Leuciscus leuciscus</i>	0.89	0.09	9.93	14.00	Fig. 3
Bainbridge (1958)	<i>Leuciscus leuciscus</i>	0.84	0.09	9.37	14.10	Fig. 3
Bainbridge (1958)	<i>Leuciscus leuciscus</i>	0.79	0.09	8.77	14.20	Fig. 3
Bainbridge (1958)	<i>Leuciscus leuciscus</i>	0.98	0.09	10.89	14.70	Fig. 3
Bainbridge (1958)	<i>Leuciscus leuciscus</i>	1.08	0.09	12.00	16.20	Fig. 3
Bainbridge (1958)	<i>Leuciscus leuciscus</i>	1.03	0.09	11.44	17.30	Fig. 3
Bainbridge (1958)	<i>Leuciscus leuciscus</i>	1.30	0.09	14.44	20.40	Fig. 3
Bainbridge (1958)	<i>Leuciscus leuciscus</i>	1.63	0.09	18.11	25.00	Fig. 3
Bainbridge (1958)	<i>Salmo irideus</i>	0.238	0.23	1.03	2.07	Fig. 8
Bainbridge (1958)	<i>Salmo irideus</i>	0.296	0.23	1.28	2.56	Fig. 8
Bainbridge (1958)	<i>Salmo irideus</i>	0.202	0.23	0.87	3.28	Fig. 8
Bainbridge (1958)	<i>Salmo irideus</i>	0.458	0.23	1.97	3.46	Fig. 8
Bainbridge (1958)	<i>Salmo irideus</i>	0.516	0.23	2.22	3.86	Fig. 8
Bainbridge (1958)	<i>Salmo irideus</i>	0.354	0.23	1.53	3.91	Fig. 8
Bainbridge (1958)	<i>Salmo irideus</i>	0.494	0.23	2.13	3.96	Fig. 8
Bainbridge (1958)	<i>Salmo irideus</i>	0.669	0.23	2.88	4.13	Fig. 8
Bainbridge (1958)	<i>Salmo irideus</i>	0.822	0.23	3.54	4.81	Fig. 8
Bainbridge (1958)	<i>Salmo irideus</i>	1.06	0.23	4.57	7.10	Fig. 8
Bainbridge (1958)	<i>Salmo irideus</i>	1.52	0.23	6.55	8.89	Fig. 8
Bainbridge (1958)	<i>Salmo irideus</i>	1.43	0.23	6.16	9.30	Fig. 8
Bainbridge (1958)	<i>Salmo irideus</i>	1.25	0.23	5.39	10.30	Fig. 8
Bainbridge (1958)	<i>Salmo irideus</i>	1.78	0.23	7.67	10.40	Fig. 8
Bainbridge (1958)	<i>Salmo irideus</i>	1.41	0.23	6.08	10.40	Fig. 8
Bainbridge (1958)	<i>Salmo irideus</i>	1.61	0.23	6.94	10.90	Fig. 8
Bainbridge (1958)	<i>Salmo irideus</i>	1.7	0.23	7.33	11.80	Fig. 8
Bainbridge (1958)	<i>Salmo irideus</i>	1.67	0.23	7.20	11.90	Fig. 8
Bainbridge (1958)	<i>Salmo irideus</i>	1.53	0.23	6.59	12.00	Fig. 8
Bainbridge (1958)	<i>Salmo irideus</i>	1.68	0.23	7.24	12.00	Fig. 8
Bainbridge (1958)	<i>Salmo irideus</i>	1.87	0.23	8.06	12.20	Fig. 8
Bainbridge (1958)	<i>Salmo irideus</i>	1.73	0.23	7.46	12.70	Fig. 8
Bainbridge (1958)	<i>Salmo irideus</i>	1.83	0.23	7.89	12.80	Fig. 8
Bainbridge (1958)	<i>Salmo irideus</i>	1.91	0.23	8.23	13.10	Fig. 8
Bainbridge (1958)	<i>Salmo irideus</i>	1.75	0.23	7.54	13.20	Fig. 8
Bainbridge (1958)	<i>Salmo irideus</i>	1.98	0.23	8.53	13.20	Fig. 8
Bainbridge (1958)	<i>Salmo irideus</i>	2.19	0.23	9.44	13.90	Fig. 8
Bainbridge (1958)	<i>Salmo irideus</i>	1.98	0.23	8.53	15.20	Fig. 8
Bainbridge (1958)	<i>Salmo irideus</i>	2.2	0.23	9.48	16.50	Fig. 8
Bainbridge (1958)	<i>Salmo irideus</i>	2.22	0.23	9.57	16.80	Fig. 8
Bainbridge (1958)	<i>Salmo irideus</i>	2.13	0.23	9.18	16.90	Fig. 8
Bainbridge (1958)	<i>Salmo irideus</i>	0.01	0.04	0.29	3.50	Fig. 8
Bainbridge (1958)	<i>Salmo irideus</i>	0.01	0.04	0.21	3.71	Fig. 8
Bainbridge (1958)	<i>Salmo irideus</i>	0.02	0.04	0.52	3.86	Fig. 8
Bainbridge (1958)	<i>Salmo irideus</i>	0.04	0.04	0.89	3.92	Fig. 8
Bainbridge (1958)	<i>Salmo irideus</i>	0.01	0.04	0.21	3.92	Fig. 8

Bainbridge (1958)	<i>Salmo irideus</i>	0.02	0.04	0.44	4.01	Fig. 8
Bainbridge (1958)	<i>Salmo irideus</i>	0.03	0.04	0.82	4.07	Fig. 8
Bainbridge (1958)	<i>Salmo irideus</i>	0.03	0.04	0.82	4.25	Fig. 8
Bainbridge (1958)	<i>Salmo irideus</i>	0.04	0.04	1.04	4.52	Fig. 8
Bainbridge (1958)	<i>Salmo irideus</i>	0.05	0.04	1.34	4.67	Fig. 8
Bainbridge (1958)	<i>Salmo irideus</i>	0.07	0.04	1.79	5.03	Fig. 8
Bainbridge (1958)	<i>Salmo irideus</i>	0.05	0.04	1.19	5.06	Fig. 8
Bainbridge (1958)	<i>Salmo irideus</i>	0.06	0.04	1.57	5.12	Fig. 8
Bainbridge (1958)	<i>Salmo irideus</i>	0.06	0.04	1.57	5.30	Fig. 8
Bainbridge (1958)	<i>Salmo irideus</i>	0.10	0.04	2.55	5.48	Fig. 8
Bainbridge (1958)	<i>Salmo irideus</i>	0.11	0.04	2.78	5.99	Fig. 8
Bainbridge (1958)	<i>Salmo irideus</i>	0.10	0.04	2.47	5.99	Fig. 8
Bainbridge (1958)	<i>Salmo irideus</i>	0.13	0.04	3.15	5.99	Fig. 8
Bainbridge (1958)	<i>Salmo irideus</i>	0.14	0.04	3.38	6.44	Fig. 8
Bainbridge (1958)	<i>Salmo irideus</i>	0.13	0.04	3.23	6.86	Fig. 8
Bainbridge (1958)	<i>Salmo irideus</i>	0.16	0.04	4.05	7.13	Fig. 8
Bainbridge (1958)	<i>Salmo irideus</i>	0.16	0.04	4.05	7.25	Fig. 8
Bainbridge (1958)	<i>Salmo irideus</i>	0.20	0.04	4.95	7.70	Fig. 8
Bainbridge (1958)	<i>Salmo irideus</i>	0.21	0.04	5.18	7.94	Fig. 8
Bainbridge (1958)	<i>Salmo irideus</i>	0.23	0.04	5.78	9.56	Fig. 8
Bainbridge (1958)	<i>Salmo irideus</i>	0.28	0.04	6.98	10.80	Fig. 8
Bainbridge (1958)	<i>Salmo irideus</i>	0.27	0.04	6.83	11.40	Fig. 8
Bainbridge (1958)	<i>Salmo irideus</i>	0.33	0.04	8.33	11.90	Fig. 8
Bainbridge (1958)	<i>Salmo irideus</i>	0.44	0.04	10.95	15.60	Fig. 8
Bainbridge (1958)	<i>Salmo irideus</i>	0.72	0.04	17.93	23.60	Fig. 8
Hunter & Zweifel (1971)	<i>Trachurus symmetricus</i>	0.13	0.05	2.96	7.80	Fig. 4
Hunter & Zweifel (1971)	<i>Trachurus symmetricus</i>	0.17	0.05	3.84	9.40	Fig. 4
Hunter & Zweifel (1971)	<i>Trachurus symmetricus</i>	0.22	0.05	4.89	10.70	Fig. 4
Hunter & Zweifel (1971)	<i>Trachurus symmetricus</i>	0.29	0.05	6.38	12.10	Fig. 4
Hunter & Zweifel (1971)	<i>Trachurus symmetricus</i>	0.36	0.05	8.00	15.20	Fig. 4
Hunter & Zweifel (1971)	<i>Trachurus symmetricus</i>	0.47	0.05	10.38	16.80	Fig. 4
Hunter & Zweifel (1971)	<i>Trachurus symmetricus</i>	0.68	0.05	15.11	19.40	Fig. 4
Hunter & Zweifel (1971)	<i>Trachurus symmetricus</i>	0.59	0.05	13.18	20.60	Fig. 4
Hunter & Zweifel (1971)	<i>Trachurus symmetricus</i>	0.17	0.06	2.61	6.60	Fig. 4
Hunter & Zweifel (1971)	<i>Trachurus symmetricus</i>	0.22	0.06	3.44	8.40	Fig. 4
Hunter & Zweifel (1971)	<i>Trachurus symmetricus</i>	0.28	0.06	4.38	8.60	Fig. 4
Hunter & Zweifel (1971)	<i>Trachurus symmetricus</i>	0.37	0.06	5.73	10.50	Fig. 4
Hunter & Zweifel (1971)	<i>Trachurus symmetricus</i>	0.47	0.06	7.30	12.10	Fig. 4
Hunter & Zweifel (1971)	<i>Trachurus symmetricus</i>	0.68	0.06	10.63	13.60	Fig. 4
Hunter & Zweifel (1971)	<i>Trachurus symmetricus</i>	0.59	0.06	9.17	13.90	Fig. 4
Hunter & Zweifel (1971)	<i>Trachurus symmetricus</i>	0.78	0.06	12.19	15.90	Fig. 4
Hunter & Zweifel (1971)	<i>Trachurus symmetricus</i>	0.89	0.06	13.95	17.20	Fig. 4
Hunter & Zweifel (1971)	<i>Trachurus symmetricus</i>	0.13	0.11	1.24	4.20	Fig. 4
Hunter & Zweifel (1971)	<i>Trachurus symmetricus</i>	0.17	0.11	1.62	4.40	Fig. 4
Hunter & Zweifel (1971)	<i>Trachurus symmetricus</i>	0.23	0.11	2.12	5.20	Fig. 4
Hunter & Zweifel (1971)	<i>Trachurus symmetricus</i>	0.29	0.11	2.68	5.30	Fig. 4
Hunter & Zweifel (1971)	<i>Trachurus symmetricus</i>	0.37	0.11	3.43	7.00	Fig. 4
Hunter & Zweifel (1971)	<i>Trachurus symmetricus</i>	0.47	0.11	4.36	7.70	Fig. 4
Hunter & Zweifel (1971)	<i>Trachurus symmetricus</i>	0.59	0.11	5.49	9.10	Fig. 4
Hunter & Zweifel (1971)	<i>Trachurus symmetricus</i>	0.68	0.11	6.36	9.80	Fig. 4
Hunter & Zweifel (1971)	<i>Trachurus symmetricus</i>	0.90	0.11	8.41	11.00	Fig. 4
Hunter & Zweifel (1971)	<i>Trachurus symmetricus</i>	0.78	0.11	7.29	11.30	Fig. 4
Hunter & Zweifel (1971)	<i>Trachurus symmetricus</i>	1.04	0.11	9.72	12.10	Fig. 4
Hunter & Zweifel (1971)	<i>Trachurus symmetricus</i>	1.37	0.11	12.78	14.90	Fig. 4
Hunter & Zweifel (1971)	<i>Trachurus symmetricus</i>	1.20	0.11	11.21	15.10	Fig. 4
Hunter & Zweifel (1971)	<i>Trachurus symmetricus</i>	0.17	0.16	1.05	3.60	Fig. 4

Hunter & Zweifel (1971)	<i>Trachurus symmetricus</i>	0.23	0.16	1.38	4.10	Fig. 4
Hunter & Zweifel (1971)	<i>Trachurus symmetricus</i>	0.28	0.16	1.71	4.40	Fig. 4
Hunter & Zweifel (1971)	<i>Trachurus symmetricus</i>	0.37	0.16	2.24	4.90	Fig. 4
Hunter & Zweifel (1971)	<i>Trachurus symmetricus</i>	0.68	0.16	4.15	5.90	Fig. 4
Hunter & Zweifel (1971)	<i>Trachurus symmetricus</i>	0.47	0.16	2.85	5.90	Fig. 4
Hunter & Zweifel (1971)	<i>Trachurus symmetricus</i>	0.59	0.16	3.58	6.80	Fig. 4
Hunter & Zweifel (1971)	<i>Trachurus symmetricus</i>	0.90	0.16	5.49	8.50	Fig. 4
Hunter & Zweifel (1971)	<i>Trachurus symmetricus</i>	1.04	0.16	6.34	10.50	Fig. 4
Hunter & Zweifel (1971)	<i>Trachurus symmetricus</i>	1.21	0.16	7.36	10.60	Fig. 4
Hunter & Zweifel (1971)	<i>Trachurus symmetricus</i>	1.39	0.16	8.46	11.70	Fig. 4
Hunter & Zweifel (1971)	<i>Trachurus symmetricus</i>	1.59	0.16	9.71	13.30	Fig. 4
Hunter & Zweifel (1971)	<i>Trachurus symmetricus</i>	1.84	0.16	11.22	13.90	Fig. 4
Hunter & Zweifel (1971)	<i>Trachurus symmetricus</i>	0.17	0.23	0.73	2.20	Fig. 4
Hunter & Zweifel (1971)	<i>Trachurus symmetricus</i>	0.22	0.23	0.96	2.30	Fig. 4
Hunter & Zweifel (1971)	<i>Trachurus symmetricus</i>	0.29	0.23	1.26	2.60	Fig. 4
Hunter & Zweifel (1971)	<i>Trachurus symmetricus</i>	0.47	0.23	2.05	3.10	Fig. 4
Hunter & Zweifel (1971)	<i>Trachurus symmetricus</i>	0.37	0.23	1.61	3.40	Fig. 4
Hunter & Zweifel (1971)	<i>Trachurus symmetricus</i>	0.59	0.23	2.57	4.10	Fig. 4
Hunter & Zweifel (1971)	<i>Trachurus symmetricus</i>	0.67	0.23	2.95	4.50	Fig. 4
Hunter & Zweifel (1971)	<i>Trachurus symmetricus</i>	0.77	0.23	3.39	6.30	Fig. 4
Hunter & Zweifel (1971)	<i>Trachurus symmetricus</i>	0.89	0.23	3.89	6.90	Fig. 4
Hunter & Zweifel (1971)	<i>Trachurus symmetricus</i>	1.03	0.23	4.53	7.00	Fig. 4
Hunter & Zweifel (1971)	<i>Trachurus symmetricus</i>	1.20	0.23	5.26	7.50	Fig. 4
Hunter & Zweifel (1971)	<i>Trachurus symmetricus</i>	1.38	0.23	6.05	8.40	Fig. 4
Hunter & Zweifel (1971)	<i>Trachurus symmetricus</i>	1.59	0.23	6.99	9.50	Fig. 4
Hunter & Zweifel (1971)	<i>Trachurus symmetricus</i>	1.83	0.23	8.01	11.70	Fig. 4
Hunter & Zweifel (1971)	<i>Trachurus symmetricus</i>	2.11	0.23	9.24	13.20	Fig. 4
Hunter & Zweifel (1971)	<i>Trachurus symmetricus</i>	0.29	0.27	1.09	2.20	Fig. 4
Hunter & Zweifel (1971)	<i>Trachurus symmetricus</i>	0.37	0.27	1.38	2.50	Fig. 4
Hunter & Zweifel (1971)	<i>Trachurus symmetricus</i>	0.48	0.27	1.78	2.70	Fig. 4
Hunter & Zweifel (1971)	<i>Trachurus symmetricus</i>	0.60	0.27	2.22	3.50	Fig. 4
Hunter & Zweifel (1971)	<i>Trachurus symmetricus</i>	0.69	0.27	2.54	3.70	Fig. 4
Hunter & Zweifel (1971)	<i>Trachurus symmetricus</i>	0.79	0.27	2.91	4.80	Fig. 4
Hunter & Zweifel (1971)	<i>Trachurus symmetricus</i>	0.91	0.27	3.36	4.90	Fig. 4
Hunter & Zweifel (1971)	<i>Trachurus symmetricus</i>	1.05	0.27	3.90	5.30	Fig. 4
Hunter & Zweifel (1971)	<i>Trachurus symmetricus</i>	1.39	0.27	5.14	6.20	Fig. 4
Hunter & Zweifel (1971)	<i>Trachurus symmetricus</i>	1.21	0.27	4.49	7.00	Fig. 4
Hunter & Zweifel (1971)	<i>Trachurus symmetricus</i>	1.60	0.27	5.93	7.20	Fig. 4
Hunter & Zweifel (1971)	<i>Trachurus symmetricus</i>	1.84	0.27	6.81	8.60	Fig. 4
Hunter & Zweifel (1971)	<i>Trachurus symmetricus</i>	2.12	0.27	7.85	9.30	Fig. 4
Jayne & Lauder (1995)	<i>Micropterus salmoides</i>	0.17	0.25	0.70	1.89	Table 5
Jayne & Lauder (1995)	<i>Micropterus salmoides</i>	0.29	0.25	1.20	2.53	Table 5
Jayne & Lauder (1995)	<i>Micropterus salmoides</i>	0.39	0.25	1.60	3.04	Table 5
Jayne & Lauder (1995)	<i>Micropterus salmoides</i>	0.49	0.25	2.00	3.55	Table 5
Jayne & Lauder (1995)	<i>Micropterus salmoides</i>	0.59	0.25	2.40	4.06	Table 5
Jayne & Lauder (1995)	<i>Oncorhynchus mykiss</i>	0.17	0.25	0.70	2.00	Table 5
Jayne & Lauder (1995)	<i>Oncorhynchus mykiss</i>	0.29	0.25	1.20	2.58	Table 5
Jayne & Lauder (1995)	<i>Oncorhynchus mykiss</i>	0.39	0.25	1.60	3.04	Table 5
Jayne & Lauder (1995)	<i>Oncorhynchus mykiss</i>	0.49	0.25	2.00	3.50	Table 5
Jayne & Lauder (1995)	<i>Oncorhynchus mykiss</i>	0.59	0.245	2.40	4.0	Table 5
Lauder Laboratory	<i>amphioxus</i>	0.01	0.04	0.20	0.34	
Lauder Laboratory	<i>amphioxus</i>	0.01	0.04	0.17	0.25	
Lauder Laboratory	<i>amphioxus</i>	0.01	0.04	0.16	0.32	
Lauder Laboratory	<i>amphioxus</i>	0.01	0.04	0.13	0.30	
Lauder Laboratory	<i>Anguilla rostrata</i>	0.13	0.38	0.33	0.65	
Lauder Laboratory	<i>Anguilla rostrata</i>	0.27	0.38	0.71	2.00	

Lauder Laboratory	<i>Anguilla rostrata</i>	0.30	0.38	0.79	2.14
Lauder Laboratory	<i>Anguilla rostrata</i>	0.38	0.38	1.00	2.23
Lauder Laboratory	<i>Devario aequipinnatus</i>	0.05	0.05	1.00	3.45
Lauder Laboratory	<i>Devario aequipinnatus</i>	0.10	0.05	2.00	6.17
Lauder Laboratory	<i>Devario aequipinnatus</i>	0.15	0.05	3.00	6.76
Lauder Laboratory	<i>Devario aequipinnatus</i>	0.25	0.05	5.00	10.64
Lauder Laboratory	<i>Devario aequipinnatus</i>	0.50	0.05	10.00	21.74
Lauder Laboratory	lamprey ammocoete	0.13	0.13	1.00	2.28
Lauder Laboratory	lamprey ammocoete	0.26	0.13	2.00	2.95
Lauder Laboratory	lamprey ammocoete	0.39	0.13	3.00	2.54
Lauder Laboratory	lamprey transformer	0.13	0.13	1.00	3.14
Lauder Laboratory	lamprey transformer	0.26	0.13	2.00	5.18
Lauder Laboratory	lamprey transformer	0.39	0.13	3.00	9.26
Lauder Laboratory	<i>Lepomis macrochirus</i>	0.29	0.12	2.50	4.12
Lauder Laboratory	<i>Lepomis macrochirus</i>	0.20	0.20	1.00	2.60
Lauder Laboratory	lungfish	0.15	0.30	0.50	2.25
Lauder Laboratory	<i>Micropterus salmoides</i>	0.15	0.15	1.00	2.12
Lauder Laboratory	<i>Micropterus salmoides</i>	0.30	0.15	2.00	3.38
Lauder Laboratory	<i>Noturus insignis</i>	0.11	0.11	1.00	2.63
Lauder Laboratory	<i>Noturus insignis</i>	0.17	0.11	1.50	3.09
Lauder Laboratory	<i>Noturus insignis</i>	0.22	0.11	2.00	3.33
Lauder Laboratory	<i>Oncorhynchus mykiss</i>	0.09	0.09	1.00	2.07
Lauder Laboratory	<i>Oncorhynchus mykiss</i>	0.18	0.09	2.00	3.14
Lauder Laboratory	<i>Oncorhynchus mykiss</i>	0.27	0.09	3.00	3.94
Lauder Laboratory	<i>Oncorhynchus mykiss</i>	0.36	0.09	4.00	3.70
Lauder Laboratory	<i>Perca flavescens</i>	0.15	0.15	1.00	3.62
Lauder Laboratory	<i>Perca flavescens</i>	0.15	0.15	1.00	2.87
Lauder Laboratory	<i>Polypterus</i>	0.19	0.19	1.00	3.36
Lauder Laboratory	<i>Polypterus</i>	0.37	0.19	2.00	2.73
Lauder Laboratory	<i>Polypterus</i>	0.56	0.19	3.00	5.15
Lauder Laboratory	<i>Salvelinus fontinalis</i>	0.11	0.20	0.57	1.72
Lauder Laboratory	<i>Salvelinus fontinalis</i>	0.29	0.22	1.30	2.37
Lauder Laboratory	<i>Salvelinus fontinalis</i>	0.70	0.22	3.20	3.55
Lauder Laboratory	<i>Salvelinus fontinalis</i>	0.39	0.22	1.75	3.07
Lauder Laboratory	<i>Scomber scombrus</i>	0.30	0.23	1.30	3.45
Lauder Laboratory	<i>Scomber scombrus</i>	0.23	0.23	1.00	3.01
Lauder Laboratory	<i>Squalus acanthias</i>	0.41	0.27	1.50	1.61